IN-47-CR

P-189

Final Report

NAGW-1855

Microwave (SSM/I) Estimates of the Precipitation Rate to Improve Numerical Atmospheric Model Forecasts

PRIMARY

Abstract

In this study it is shown that the delay in the spin-up of precipitation early in numerical atmospheric forecasts is a deficiency that can be corrected by diabatic initialization combined with diabatic forcing. For either to be effective requires some knowledge of the magnitude and vertical placement of the latent heating fields. Until recently the best source of cloud and rain water data has been the remotely sensed vertically integrated precipitation rate or liquid water content. Still, the vertical placement of the condensation (heating) remains unknown. However, some information about the vertical distribution of the heating rates and precipitating liquid water and ice can be obtained from retrieval techniques that use a physical model of precipitating clouds to refine and improve the interpretation of the remotely sensed data. A description of this procedure and an examination of its three dimensional liquid water products, along with improved modeling methods that enhance or speed-up storm development and precipitation early in the forecast, are the subject of this report.

The first chapter in our final report contains a description of the spin-up problem. Included is an examination of diabatic initialization and diabatic forcing methodologies that help enhance the spin-up of precipitation in numerical atmospheric forecasts. The potential usefulness of remotely retrieved liquid water data is also discussed. Chapters two and three of the final report describe a retrieval procedure that uses a physical model to help improve and interpret remotely sensed data. Highlighted are the physical model and the retrieval procedure, its accuracy and ability to produce three dimensional spatial liquid water fields using data from the Special Sensor Microwave/Imager (SSM/I). Retrievals from the SSM/I, qualified by information from a cloud model, are found to verify well against independent estimates of the liquid water. Chapter four describes an application in numerical model forecasts of these remotely retrieved three dimensional data sets. In the fifth and final chapter of the report, the governing equations for the kinematic moisture and heat flux are introduced, along with an examination of the influences of mesoscale diabatic processes on the large scale atmospheric dynamics.

Final Report

NAGW-1855

Microwave (SSM/I) Estimates of the Precipitation Rate to Improve Numerical Atmospheric Model Forecasts

By

William H. Raymond and William S. Olson

Cooperative Institute for Meteorological Satellite Studies
1225 West Dayton Street
University of Wisconsin
Madison, Wisconsin 53706

Table of Contents

Chapter

Abstract

Introduction

Diabatic Forcing and Initialization with Assimilation of Cloud and Rain Water in a Forecast Model: Methodology..... 1 - 1

Physical Retrieval of Precipitation Water Contents from Special Sensor Microwave/Imager (SSM/I) Data- Part I: A Cloud Ensemble/Radiative Parameterization for Sensor Response..... 2 2

Physical Retrieval of Precipitation Water Content from Special Sensor Microwave/Imager Data- Part II: Retrieval Method and Applications..... 3 3

Forecast Model Applications of Retrieved Three Dimensional Liquid Water Fields..... 4 - 4

Moist Wind Relationships..... 5 - 5

Conference Reports

ABSTRACTS OF PAPERS

I. Introduction

Grant NAGW-1855 supported research for atmospheric forecast model diabatic initialization studies and for the development of physical retrieval methods for the Special Sensor Microwave/Imager (SSM/I). Funding was split evenly between these two efforts. Results from our research are presented in chapters 1 through 5 of this report. A brief description/summary to each of the five chapters is presented next.

1. Diabatic Forcing and Initialization with Assimilation of Cloud and Rainwater in a Forecast Model: Methodology

The focus of this part of the investigation is to find one or more general modeling techniques that will help reduce the time taken by numerical forecast models to initiate or spin-up precipitation processes and enhance storm intensity. If the conventional data base could explain the atmospheric mesoscale flow in detail, then much of our problem would be eliminated. But the data base is primarily synoptic scale, requiring that a solution must be sought either in nonconventional data, in methods to initialize mesoscale circulations, or in ways of retaining between forecasts the model generated mesoscale dynamics and precipitation fields. All three methods are investigated in this study.

Herein we examine the initialization and assimilation of explicit cloud and rainwater quantities computed from conservation equations in a mesoscale regional model. The physical processes include condensation, evaporation, autoconversion, accretion and the removal of rainwater by fallout. The question of how to initialize the explicit liquid water calculations in numerical models and how to retain information about precipitation processes during the 4-D assimilation cycle are important issues that will be addressed. The explicit cloud calculations have purposely been kept simple so that different initialization techniques can be easily and economically tested. Precipitation spin-up processes associated with three different types of weather phenomena are

examined.

Our findings show that diabatic initialization, or a diabatic initialization in combination with a new diabatic forcing procedure, work effectively to enhance the spin-up of precipitation in a mesoscale numerical weather prediction forecast. Also, the retention of cloud and rain water during the analysis phase of the 4-D data assimilation procedure is shown to be valuable. Without detailed observations, the vertical placement of the diabatic heating remains a critical problem.

2. Physical Retrieval of Precipitation Water Contents from Special Sensor Microwave/Imager (SSM/I) Data- Part I: A Cloud Ensemble/Radiative Parameterization for Sensor Response

The physical retrieval of geophysical parameters based upon remotely sensed data requires a sensor response model which relates the upwelling radiances that the sensor observes to the parameters to be retrieved. In the retrieval of precipitation water contents from satellite passive microwave observations, the sensor response model has two basic components. First, a description of the radiative transfer of microwaves through a precipitating atmosphere must be considered, because it is necessary to establish the physical relationship between precipitation water content and upwelling microwave brightness temperature. Also the spatial response of the satellite microwave sensor (or antenna pattern) must be included in the description of sensor response, since precipitation and the associated brightness temperature field can vary over a typical microwave sensor resolution footprint.

In the current study a "population" of convective cells, as well as stratiform clouds, are simulated using a computationally-efficient multi-cylinder cloud model. Ensembles of clouds selected at random from the population, distributed over a 25 km x 25 km model domain, serve as the basis for radiative transfer calculations of upwelling brightness temperatures at the SSM/I frequencies. Sensor spatial response is treated explicitly by convolving the upwelling brightness temperature by the domain-integrated SSM/I antenna patterns. The sensor response model is

utilized in precipitation water content retrievals, which is the subject of chapter 3 in this series.

3. Physical Retrieval of Precipitation Water Content from Special Sensor Microwave/Imager Data- Part II: Retrieval Method and Applications

A physical retrieval method for estimating precipitating water distributions and other geophysical parameters based upon measurements from the DMSP-F8 SSM/I is developed. Three unique features of the retrieval method are (1) sensor antenna patterns are explicitly included to accommodate varying channel resolution, (2) precipitation-brightness temperature relationships are quantified using the cloud ensemble/radiative parameterization described in chapter 3, and (3) spatial constraints are imposed for certain background parameters, such as humidity, which vary more slowly in the horizontal than the cloud and precipitation water contents. The general framework of the method will facilitate the incorporation of measurements from the SSM/T, SSM/T-2 and geostationary infrared measurements, as well as information from conventional sources (e.g., radiosondes) or numerical forecast model fields.

4. Forecast Model Applications of Retrieved Three Dimensional Liquid Water Fields

Forecasts are made for tropical storm Emily using heating rates derived from the SSM/I physical retrievals described in chapters 2 and 3. Average values of the latent heating rates from the convective and stratiform cloud simulations, used in the physical retrieval, are obtained for individual 1.1 km thick vertical layers. Then, the layer-mean latent heating rates are regressed against the slant path-integrated liquid and ice precipitation water contents to determine the best fit two parameter regression coefficients for each layer. The regression formulae and retrieved precipitation water contents are utilized to infer the vertical distribution of heating rates for forecast model applications. In the forecast model, diabatic temperature contributions are calculated and used in a diabatic initialization, or in a diabatic initialization combined with a diabatic forcing procedure. Our forecasts

show that the time needed to spin-up precipitation processes in tropical storm Emily is greatly accelerated through the application of the data.

5. Moist Wind Relationships

We have identified the equations describing the temporal and spatial behavior of the kinematic moisture and heat flux. In these nonlinear equations, the contribution by diabatic processes to the large-scale flux is composed of two parts. One part is associated with a Rayleigh damping term while the other arises from temporal and spatial changes in the pressure gradient term. Given below are some findings from the manuscript accepted for publication in *Mon . Wea. Rev.*.

We have found that the influence of diabatic processes on large-scale moisture fluxes depends greatly on the degree of balance between forcing and damping terms in the governing kinematic flux equations. The existence of a near balance requires a reduction in the large-scale horizontal geostrophic wind speed. Based on an examination of the moisture flux equations, it is argued that reductions in the large-scale horizontal wind speed observed within major cumulus cloud systems help conserve large-scale moisture fluxes. The deviation of the wind from geostrophic conditions is easily estimated for a near balanced state. This wind modification induces secondary vertical circulations that contribute to convergence, creating or supporting long-lived mesoscale flows. We believe this process to be a major supporter of the mesoscale circulations observed in severe storms and squall lines. In the tropics the wind modification has an antitriptic relationship.

These diagnostic findings suggest possible modifications to the wind field in the application of a cumulus parameterization, and may be important in diabatic initialization of numerical weather prediction models.

Diabatic Forcing and Initialization with Assimilation of Cloud and Rain Water in a Forecast Model: Methodology

By

William H. Raymond*, William S. Olson* and Geary Callan+

*Cooperative Institute for Meteorological Satellite Studies
1225 West Dayton Street
University of Wisconsin
Madison, Wisconsin 53706

+ National Environmental Satellite Data and Information Service (NOAA)
Madison, Wisconsin 53706

Submitted to *Mon. Wea. Rev.*

Abstract

In this study diabatic initialization and assimilation techniques are tested in a semi-implicit hydrostatic forecast model containing explicit representations of cloud and rain water. Diabatic vertical mode initialization and a diabatic forcing process are combined to strengthen the diabatic signal and to help the forecast keep the modification. In some experiments explicit cloud and rain water fields are retained through the analysis/initialization phase of the forecast cycle, i.e., from the end of one forecast to the beginning of the next sequential forecast, to help reduce the spin-up time of major precipitating events. This is only possible when these variables are explicitly computed and retained for use in prognostic cloud and rain water calculations. Deficiencies in the forecast model's production of precipitation can be reduced provided liquid cloud and rain water data are available.

Numerical experiments for a wide range of grid scale sizes, varying from 150 to 40 km, illustrate the adaptability of the diabatic initialization, diabatic forcing and liquid water assimilation procedures in combination with explicit cloud and rain water calculations. Particulars include information about the simple explicit cloud scheme and the diabatic initialization and diabatic forcing procedure. Presented also are comparisons between forecasts computed with the diabatic initialization, diabatic forcing and retained cloud and rain water fields and those obtained by the traditional adiabatic approach.

1. Introduction

In this investigation the primary goal is to identify one or more general procedures that will help reduce the time taken by numerical weather prediction models containing explicit cloud and rain water formulations to initiate or spin-up precipitation processes. These precipitation intensifying procedures also assist in enhancing the storm intensity. If the conventional data base could explain the atmospheric mesoscale flow in detail, then much of our problem would be eliminated. But the data base is primarily synoptic scale, requiring that a solution must be sought either in nonconventional data, in methods to initialize mesoscale circulations or by procedures that retain the model generated mesoscale dynamics and precipitation fields between the end of a forecast and the beginning of the next sequential forecast. All three methods are investigated in this study. These methods would allow the existing nonconventional data base, including satellite estimates of precipitation rate, to become more valuable for fine tuning and correcting model inaccuracies and conventional data shortcomings.

In this study we examine in a mesoscale regional model the initialization and assimilation of explicit cloud and rain water quantities. Parameterizations of the physical processes of condensation, evaporation, autoconversion, accretion and the removal of rain water by fallout are all included as source and sink terms in the liquid water conservation equations. The question of how to initialize the explicit liquid water calculations in numerical models and how to retain information about precipitation processes during the 4-D assimilation cycle are important issues that will be addressed. The explicit cloud model has purposely been kept simple so that different initialization techniques can be easily and economically tested.

With increasing computer speed there has been a slow but steady enhancement in model horizontal grid resolution. Current global numerical weather prediction models are approaching the spatial resolution where time-dependent cloud variables are physically relevant. The time to study the feasibility of initializing and assimilating cloud and rain water using explicit cloud conservation equations within a regional mesoscale model is now. The knowledge of explicitly

calculated cloud and rain water fields as a function of time and space provides information, such as model heating rates and vertical distributions, that are more difficult to obtain from conventional cloud parameterization approaches where cloud properties are not retained or used in a prognostic manner.

Cloud and rain water are the cumulative products of the transport of atmospheric moisture, both vapor and liquid, plus the physical processes included in cloud development and decay. By their very nature cumulative processes are difficult to initiate in numerical models, and it is common for precipitation to be absent during the first few hours of a numerical forecast. One reason for this deficiency is the resolution of the data. Conventional surface and upper air reports are frequently unable to capture the essence of mesoscale circulations with their enhanced convergence which supports the mesoscale precipitation process. The analysis of the irrotational wind component in the tropics is especially poor (Mizzi and Kasahara 1989). In mid-latitudes the large scale part of the irrotational wind can be estimated fairly accurately (Kasahara et al. 1992) but the mesoscale component depends a great deal upon the diabatic term (Tarbell et al 1981). The missing mesoscale circulations also influence the moisture and thermal fields (e.g., Krishnamurti et al 1984; Turpeinen 1990). Consequently, in order to initiate precipitation and assimilate cloud parameters it is necessary to know additional information beyond the conventional synoptic data base. This might include accurate estimates of the vertical heating rates and the low level convergence and/or the high level divergence that produces the cloud-sustaining vertical motion field. These also include the supporting mesoscale circulations that help produce long-lived disturbances. The incorporation of this data into model simulations is further complicated by inaccuracies or shortcomings in the forecast, e.g., phase errors.

When the heating rates are known or can be approximated, then either diabatic (Errico and Rasch 1988) or cumulus initialization (Donner 1988) is possible. These initialization procedures help establish circulation patterns consistent with latent heating processes that are otherwise not resolved in synoptic scale data. For a review of some studies using diabatic initialization schemes, see Table 1 in Turpeinen et al. (1990) and the introduction of Mathur et al (1992). Without the

heating rate information each forecast must go through a short time period where the mesoscale circulations that support precipitation processes must 'spin-up' before rainfall can be produced. In regional mesoscale models this spin-up usually occurs during the first 2 to 6 hours. Diabatic initialization should reduce the degree and duration of the spin-up, but this procedure is not always completely successful (Errico and Rasch 1988; Kasahara et al. 1992). In contrast, normal mode or dynamic initialization procedures, designed to help with the removal of gravity waves during initialization, only provide slight or no assistance in speeding up precipitation processes (Lejenas 1980).

Cloud and rain water data are generally not available. Rain gauge reports imply information about the total amount of liquid water reaching the surface, but no knowledge about the instantaneous vertical distribution is recoverable. Most microwave satellite measurements of instantaneous cloud quantities only resolve the vertically integrated cloud and/or integrated rain water. Thus it is necessary to make some assumption about the vertical distribution of the heating rate. New retrieval methods that combine observed microwave satellite radiances with cloud models should provide some insight into the vertical partitioning of the liquid water. These techniques are just beginning to be examined (Olson 1993).

The use of diabatic initialization requires an answer to the question of how the latent heating is going to be distributed in the vertical. Some studies have used representative profiles (Fiorino and Warner 1981; Puri and Miller 1990) others assume a general parabolic profile (Tarbell et al 1981; Salmon and Warner 1986, etc.) while some have tried to use the forecast model itself in some fashion with observations (Wergen 1988; Danard 1985; Turpeinen et al. 1990; Donner and Rasch 1989; Puri and Miller 1990; Heckley 1990). Donner (1988) used a variational formulation to optimize the vertical distribution with respect to the methodology of the Kuo cumulus parameterization. In all but the Donner study, it has been customary to use either the diabatic omega equation or a diabatic form of the normal mode initialization scheme. In contrast, Donner used a variational optimization.

Early pioneering work by Krishnamurti et al. (1984) suggested that in addition to the diabatic heating a re-analysis of the moisture and wind field is needed. Even earlier studies by Perkey (1976) and Wolcott and Warner (1981) enhanced the moisture field in cloudy regions. To produce the observed rainfall, Donner (1988) made slight modifications in the temperature field and relatively large changes to the humidity field. Donner and Rasch (1989) found that the divergence, temperature and moisture must all be adjusted to produce the proper precipitation. The necessity of moisture initialization to reduce the spin-up problem has also been noted in Turpeinen (1990) and Puri and Miller (1990).

The cumulus initialization used by Donner (1988) is effective in dealing with cumulus convective situations. However, improvements are still needed in the initialization of grid scale precipitation processes. In this study we use diabatic initialization, diabatic forcing, allow for moisture modification and in some experiments assimilate cloud water and rain water predicted by a forecast beginning 12 hours earlier. For the latter cases, non-zero cloud and rain water are carried through the 4-D data assimilation process from the end of one forecast to the beginning of the next forecast. The diabatic initialization is installed to work with the vertical mode initialization scheme of Bourke and McGregor (1983). Diabatic forcing is formulated in a new design to represent a natural continuation of the diabatic initialization. Together, diabatic initialization and diabatic forcing form a powerful system to reduce the time needed to spin-up precipitation processes and enhance storm development.

Theoretically, if precipitation data were always available then cloud and rain water could be treated much like other meteorological variables, i.e., updated and modified during the 4D assimilation process. However, caution is required when making large changes to existing model cloud fields, or to the dynamics that support the precipitation process. Testing and experience with explicit cloud initialization will dictate what the correct procedure should be. The problem goes far beyond any single study, and must be addressed in an operational setting where a large number of cases and situations can be examined over a long time period. Because of resource limitation

this study tests specific parts of the proposed initialization procedures separately, and then only on a few cases. The sensitivity of the initialization to the vertical distribution of the diabatic heating is appraised. Emphasized are procedures that have the potential to reduce the spin-up time and assist with enhancing storm development.

2. Modeling Considerations

A modified version of the Bureau of Meteorology Research Centre (BMRC) operational incremental O/I analysis (Mills and Seaman 1990), vertical mode initialization (Bourke and McGregor 1983), and semi-implicit forecast model (Leslie, et al. 1985) are used in this investigation. The incremental analysis is set to preserve the irrotational wind field while the rotational component of the differences between data and model guess wind and other fields are evaluated by the O/I. In this study the horizontal grid configuration varies from 40 to 150 km, while the vertical sigma coordinate is subdivided into 15 levels. The horizontal wind components, temperature and mixing ratio fields are smoothed with the 6th order implicit low-pass tangential filter (Raymond 1988), with a filter parameter setting sufficiently large enough to provide some horizontal mixing. Cloud and rain water quantities are not filtered, nor is horizontal diffusion applied to these fields.

Explicit conservation equations for cloud water and rain water are inserted in the model. The explicit cloud physics contain processes modeled using a modified Kessler type scheme (Kessler 1974), while the condensation and fall velocity calculations are similar to those described in Anthes, et al. (1987) and Liu and Orville (1969). The 'fallout' term is calculated by a semi-Lagrangian method to allow for the larger time steps used in the semi-implicit model calculations. Ice phase cloud physics have not yet been explicitly included in the model, but modifications are incorporated to increase the life time of high clouds and and to enhance anvil structures.

In sigma coordinates the frictionless explicit conservation equations for water vapor, cloud and rain water satisfy

(1a)

$$\partial(p^* q_v)/\partial t + \partial(up^* q_v)/\partial x + \partial(vp^* q_v)/\partial y + \partial(\dot{\sigma} p^* q_v)/\partial \sigma = p^*(P_{EVAP} - P_{CON}) + F_z ,$$

(1b)

$$\partial(p^* q_c)/\partial t + \partial(up^* q_c)/\partial x + \partial(vp^* q_c)/\partial y + \partial(\dot{\sigma} p^* q_c)/\partial \sigma = - p^*(P_{ACC} + P_{AUTO} - P_{CON}) + F_z ,$$

(1c)

$$\partial(p^* q_r)/\partial t + \partial(up^* q_r)/\partial x + \partial(vp^* q_r)/\partial y + \partial(\dot{\sigma} p^* q_r)/\partial \sigma = p^*(P_{ACC} + P_{AUTO} - P_{CON}) - g\partial(\rho q_r v_t)/\partial \sigma + F_z .$$

Here q_v, q_c and q_r are the water vapor, cloud water and rain water mixing ratios. P_{EVAP} is the evaporation of raindrops, P_{CON} is the condensation of water vapor (Asai 1965) or evaporation of cloud droplets, P_{ACC} is the accretion of cloud droplets by raindrops and P_{AUTO} represents the autoconversion of cloud droplets into raindrops. The acceleration of gravity is g, p^* is the surface pressure, ρ is the density of dry air and v_t is the mean terminal velocity of the raindrops. The independent variables t, x, y, and σ have their standard definitions. F_z represents the vertical diffusion. The map factor is omitted in the above equations.

Because of horizontal scale considerations, our explicit cloud calculations do not model individual clouds but yield approximate average values for a system or complex of clouds. This was the motivation behind the modifications made to the cloud physics formulation. It is known that the lifetime of individual convective clouds is less than one hour while a cloud complex exists for many hours with remnants lasting for days. Thus Kessler's (1974) accretion (collection) process was modified to slow the conversion from cloud to rain water when the cloud water q_c is below a preset critical value $q_c = C_{crit}$. Also incorporated into the accretion process is a vertical dependence on temperature that follows the scheme suggested by Schlesinger (1990). These changes help retain and enhance anvil or cloud top features. In addition to explicitly modeling

cloud complexes, the consequences of convection are parameterized by a modified Kuo-type cumulus parameterization scheme (Sundqvist et al 1989). However, in some cases the cumulus parameterization scheme is intentionally turned off to assist in the study of the spin-up of grid scale precipitation.

In mixing ratio units (gg^{-1}), the formula for the rate of change from accretion is

$$P_{ACC} \equiv 0.88 C_1 C_2 q_c q_r^{0.875} , \tag{2}$$

where

$$C_1 = \min[1.0,\ 1.0 - (C_{crit} - q_c)/C_{crit}]$$

$$C_2 = \max[0.0, \min(1.0, (T - 233)/40)] .$$

Here T is the temperature in degrees Kelvin, and $C_{crit}=1$ gkg^{-1}. Comparisons between model cloud water fields and infrared VISSR Atmospheric Sounder (VAS) images of cloud patterns and categories of low or high clouds, and SSM/I retrieved precipitation rates indicate acceptable ranges of cloud and rain water predicted by the explicit formulation. This will be shown later.

The autoconversion process is described by

$$P_{AUTO} = k_1 (q_c - q_{co}) , \quad q_c \geq q_{co} ,$$

$$P_{AUTO} = 0 , \quad q_c < q_{co} . \tag{3}$$

The parameters $k_1=10^{-3}$ s^{-1} and the onset of autoconversion depends on the critical value q_{co} which has the value of 0.2 g kg^{-1}.

To facilitate the large time step used in the semi-implicit forecast model the fallout term in (1c) is rewritten as two terms, one of which represents vertical advection, i. e.,

$$g\partial(\rho v_t\, q_r)/\partial\sigma \equiv A\partial(p^* q_r)/\partial\sigma + (p^* q_r g/p^*)\partial(\rho v_t)/\partial\sigma\,. \qquad (4)$$

Here A (s^{-1}) is equivalent to a velocity in the vertical σ coordinate system, that is

$$A = g\rho v_t/p^*\,. \qquad (5)$$

Thus, the time tendency for $p^* q_r$ in (1c) is found by semi-Lagrangian procedures using (4) and (5).

3. The Diabatic Initialization and Diabatic Forcing Formulation

The diabatic initialization is installed into the forecast model to take full advantage of the semi-implicit method. This is accomplished by modifying the semi-implicit representation of the average temperature $T^{2\tau}$, computed from the thermodynamic equation (McGregor et al 1978; Leslie et al 1985), by adding the temperature contribution T_{EX} from a measured or approximated diabatic heat source. This redefines the average temperature at the appropriate grid points using

$$T^{2\tau} \equiv T^{2\tau} + T_{EX}\,. \qquad (6)$$

(This is approximately equivalent to adding to the thermodynamic equation a forcing term $T_{EX}/\Delta t$, and including it in the semi-implicit formulation.) This modified temperature is then used in the semi-implicit calculations of the finite difference averaged horizontal wind components and surface pressure. To avoid excessive evaporation, some upward adjustment of the relative humidity may be required during this process . The amount of moisture needed to satisfy the expected condensation requirements is $c_p T_{EX}/L$, where c_p is the specific heat for constant pressure and L is

the latent heat of condensation. When cloud and rain water are assimilated it is especially important to retain saturation at the appropriate levels. During the vertical mode initialization procedure (Bourke and McGregor 1983), T_{EX} is held constant at the selected grid points. Recall, that the averaging in (6) for the semi-implicit method, with any variable χ, is defined by

$$\chi^{2\tau} = [\chi^{\tau+1} + \chi^{\tau-1}]/2 \ . \tag{7}$$

Following the initialization, the immediate application of an external diabatic forcing represents a natural extension of the diabatic initialization. Wang and Warner (1988) showed that this was useful. To keep the forcing from becoming excessive, the grid point average temperature is modified by the difference between the external contribution T_{EX} and the model produced or internal diabatic temperature change $T_{IN}=\Delta t LQ/c_p$, yielding

$$T^{2\tau} \equiv T^{2\tau} + (T_{EX} - T_{IN}) . \tag{8}$$

Here Q is the model produced condensed rate and Δt the time step. In our study the quantity in parenthesis in (8) is taken to be non-negative. If T_{IN} exceeds T_{EX} at a given grid location and timestep, then the forcing is reduced to zero. At some time in the forecast this would be the desired result but, it is not explicitly required before the termination of the forcing at a preselected forecast time. Too much forcing can over-develop the updraft and the liquid water content and/or create excessive gravity waves. The inclusion of the internally generated latent heating in (8) helps reduce over-development.

Note that (6) and (8) are similar, except that in (8) model produced condensation reduces the external forcing. This diabatic forcing is a natural continuation of the diabatic contributions used in the initialization. Thus, it is applied starting with the first time step after the vertical mode initialization and continued until the model produces an equivalent temperature change or until the

termination time is exceeded. This procedure is illustrated in Fig 1a.

To simulate the movement associated with a disturbance, T_{EX} is advected by the model horizontal winds according to

$$\partial(T_{EX})/\partial t + u\partial(T_{EX})/\partial x + v\partial(T_{EX})/\partial y = 0. \tag{9}$$

In regions with strong vertical shear it may be advantageous to advect T_{EX} using a vertically averaged horizontal wind. The advection process will ultimately smooth and diffuse the heating if (9) is used over a sufficiently large time period. Normally, the diabatic forcing is not applied long enough for this to become a problem. Albeit, to avoid noise some tapering is required to terminate the diabatic forcing, provided (8) is not reduced to zero by model generated condensation processes. Remotely sensed time variations in T_{EX} could also be specified if these were known. In their absence, the advection of T_{EX} is necessary to approximately locate the condensation. In our calculations T_{EX} remains unchanged except for horizontal advection. Thus, in this study the application of the external forcing is somewhat different from the procedure used in Newtonian nudging (Hoke and Anthes 1976).

An alternative approach, examined in this study, is to apply the external diabatic forcing at the satellite observation time without reinitializing the model, i.e., with no diabatic initialization. Then, during the forecast, a gradual transition into and exit from the external forcing greatly avoids the production of noise and gravity waves. This is shown graphically in Fig 1b to contrast how this procedure differs from diabatic initialization. The time span needed to produce gradual changes depends upon the magnitude of the external forcing. The length of the time period used in the forcing can be varied to achieve the desired result. Excessively long periods of forcing should be avoided since they can can lead to some negative consequences. For example, overproduction of precipitating liquid in the atmospheric column leads to down bursts accompanied by low-level divergence, ultimately choking off the moisture source.

In any event, the horizontal distribution of the forcing is determined using the grid

configuration and knowledge of the location of the storm or liquid precipitating water. In the absence of measurements, the best vertical placement of the forcing remains unknown and is a function of several factors, including the nature of the disturbance. For example, hurricanes are known to be warm core; warming extends to surface, while most middle-latitude disturbances have upper level lows with warming that does not extend to the surface (Wallace and Hobbs 1977).

Raymond (1993) has identified diabatic wind modifications that induce secondary vertical circulations that contribute to the convergence, helping to create or support long-lived mesoscale flows. An approximate representation for the secondary flow within the diabatically active part of the disturbance, based on near conservation of the large scale kinematic moisture flux, requires that the x and y coordinate horizontal wind components u and v be modified by the addition of a perturbation term of the form

$$u_{pert} = R_1 v_g - R_1^2 u_g + \cdots \quad , \tag{10}$$

$$v_{pert} = -R_1 u_g - R_1^2 v_g + \cdots \quad . \tag{11}$$

Here $R_1 = -|Q/(fq)|$, Q is the condensation rate, f is the Coriolis parameter, q the mixing ratio and u_g and v_g are the geostrophic wind components for u and v respectively. Generally R_1 is small, say, $0 < R_1 < -0.50$. Because (10) and (11) only describe the modifications within the updraft, they represent only part of an unbalanced ageostrophic approximation of the mesoscale circulation. Theoretically, a balanced and complete flow can be determined, but this requires additional computational resources to solve a vorticity equation. In our calculations, R_1 in (10) and (11) is used as an independent gauge to measure the production of latent heating, but the wind field is not modified.

4. Precipitation Events

Precipitation spin-up processes associated with three different weather phenomena are examined. The first situation includes a tropical disturbance known as Emily. The initial conditions are taken from NMC's initialized global data set beginning at OOOO UTC 21 Sept. 1987. At that time Emily was a tropical storm located among the Windward Islands a little ways south of the Island of Martinique, just north of the Venezuelan coast in the Atlantic Ocean. The model calculations are performed on a 65 x 65 horizontal grid with 40 km grid spacing, having 15 vertical sigma levels. The time step size used in the semi-implicit model is 300 s.

The second major precipitation study examines rapid cyclonic development in the North Atlantic. Intensive observation period number five (IOP-5) is selected from the Experiment on Rapidly Intensifying Cyclones over the Atlantic (ERICA). It represents a case where a major cyclone over water experiences a rapid pressure deepening. Our examination extends from 0000 UTC 19 January 1989 through 0000 UTC on the 20th. For this part of the study the forecast model uses a horizontal grid resolution of 120 km. The initial meteorological fields for our ERICA IOP-5 case study are obtained from NMC's initialized global analyses. Conventional data are limited because the disturbance is located over water. However, observations during ERICA have documented the cyclone's path, pressure and provided an assortment of other atmospheric measurements using dropsondes and aircraft. Also, the microwave measurements of the precipitation rates retrieved from the Special Sensor Microwave/Imager (SSM/I) provide a product of major importance in verifying the precipitating liquid in the forecast.

The final precipitation event used to study model spin-up comes from a time period that includes frontal development associated with strong wind jets over the US. Specifically, 24h forecasts are made for the period beginning 1200 UTC 21 April 1988. This case over North America was selected because of its large conventional data bases including surface, upper air and aircraft winds. The horizontal grid scale used in this part of the modelling effort is 150 km on a 35 x 35 grid with 15 vertical sigma levels.

5. Discussion of Results

A. Tropical Storm Emily

Super-imposed over the validating GOES infrared (IR) image of tropical storm Emily in Figs 2 and 3 are the 700 mb geopotential height and divergence fields, respectively, from a fourteen hour forecast beginning at 1000 UTC 21 September 1987. The forecast uses an adiabatic initialization with four vertical modes and the initial meteorological fields come from a ten hour preforecast. Decreasing the number of modes by one or two makes no significant difference in the adiabatic initialization. Note in Figs 2 and 3 that the height and divergence fields show very little development whatsoever in the immediate vicinity of Emily. A small trough is located to the east of Emily in Fig 2, but no precipitation is produced over any water surface, although moderate amounts of precipitation fall in some elevated regions.

In the absence of the model's inability to produce any diabatic heating in the vicinity of Emily during a 10 h preforecast beginning 0000 UTC 21 Sept 1987, a proxy latent heating field is assigned based on the approximate position of Emily in the 1001 UTC satellite image. (In a separate study that will be presented elsewhere, data from SSM/I estimates of the precipitating liquid and ice at 1000 UTC 21 Sept 1987 are used in initialization experiments) In this study highly simplistic initial conditions are used to test our basic diabatic forcing procedure. Previous investigators have also used simplified approaches to describe the vertical distribution of the latent heating, including Tarbell et al (1981), Salmon and Warner (1986), Ninomiya and Kurihara (1987), and Wang and Warner (1988). Our proxy temperature distribution is described by the product of vertical and horizontal sine functions, viz.,

$$T_{EX}=K \sin(a\pi)\sin(b\pi)\sin(c\pi) \qquad (12)$$

where K is the maximum magnitude of T_{EX} and $a=(k-k_T)/(k_B-k_T)$, $b=(j-j_S)/(j_N-j_S)$ and $c=(i-i_E)/(i_W-j_E)$. The independent coordinates i, j, and k are associated with the x, y and σ variables, respectively. At 1001 UTC 21 September 1987, Emily was approximately centered

near grid point location (40.5,30.5) in our 65 x 65 horizontal grid. Assigning j_S=26, j_N=35, i_E=37, i_W=44 and setting K=0.5 gives the distribution shown at 500 mb in Fig 4, provided the sigma levels are between 0.25 and 0.80. This vertical distribution is compatible with pre-hurricane/tropical wave observations (Kuo and Raymond 1980; Shapiro and Stevens 1980). In general, the values for k_B and k_T are varied to test the impact of heating at different vertical heights.

Figures 5 through 7 contain fields from a fourteen hour forecast using the diabatic initialization and a two hour application of diabatic forcing as described in (6) through (12), and illustrated in Fig 1a. For convenience, diabatic initialization will be denoted by DI, while DF(K) will identify diabatic forcing with a maximum temperature perturbation of K degrees. The 700 mb height field from the fourteen hour forecast, Fig 5, contains closed contours of small magnitude over the southern extent of tropical storm Emily, indicating that the forecasted disturbance still has a cold core. The 700 mb vorticity, with maximum in excess of 2 x 10^{-4} s^{-1} is similarly located (Fig 6), while the 700 mb divergence (Fig 7) is positive directly behind the disturbance and negative (convergence) within the vicinity of the storm and to the southwest. The diabatic temperature perturbation used in these calculations has a maximum value of K=0.5 C per time step of 300 s. Six iterations (iter=6) are used in the vertical mode initialization (Bourke and McGregor 1983), each having a time step of 50s, requiring that K be modified appropriately in the initialization, i.e., K=0.5/iter. In (12), the parameters describing the vertical depth of the perturbation are assigned k_B=9 and k_T=3, i.e., the forcing occurs between sigma levels 0.25 and 0.80. Also, the diabatic forcing, which is applied over a time period of two hours, is ramped linearly to zero during the second hour.

Four vertical wave numbers are used in the initialization shown in Fig. 8. Included in this figure are curves describing the number of grid scale condensation points per time step for adiabatic, diabatic initialization (DI), and for two different time periods of diabatic forcing (DF). Note that, without the diabatic forcing, the diabatic initialization is unable to produce sustained condensation activity over the fourteen hour forecast. This is true for vertical modes 2 and 3 also.

Adding additional moisture during the initialization at all locations influenced by the diabatic heating does not enhance the long term development. However, strong diabatic activity occurs when the diabatic initialization is combined with diabatic forcing, where the forcing is applied for a duration of either two or three hours. In Fig 8 note that the longer the diabatic forcing is applied, the more intense is the storm development as gauged by the production of precipitation. Both the diabatic initialization and diabatic forcing are restricted to the immediate Emily region which is entirely over water, as illustrated in Fig 4. Thus, the difference between the adiabatic and other curves represent development in the Emily region. In fact, the development wants to become too extreme, partially because of the large availability of moist air in this tropical location, and partially because the natural tropical storm circulation, feedback and balancing processes, developed over several days, are difficult for the model to duplicate in a few hours. To keep the storm from over developing or developing too rapidly, the maximum amount condensed at any one time step at any grid location is restricted by requiring that $-0.5<R_1<0$. Conservation of moisture is retained since the excess is carried in the slightly super saturated mixing ratio. This is thought to be a better alternative than applying artificial diffusion which is non-conservative. It is also consistent with the fact that small sub-grid scale moist and dry downdrafts exist within the cloud environment, limiting to some extent the updraft while enhancing mixing, thereby reducing the condensation amount. Except for the K-theory vertical diffusion, these processes are not explicitly included in the conservation equations (1a,b,c) or in the condensation calculation, but should be parameterized in some way.

In our calculations the horizontal wind is required to spin-up through time since the disturbance is initially absent, and since no bogus tropical storm wind field is inserted during the initialization. At non-tropical latitudes it has been shown that a perturbation spiral feature associated with a mean converging flow has an e-folding times in excess of 22 hours (Raymond 1989) as a consequence of vortex stretching (mean divergence of 10^{-5} s). Still, in model simulations performed by Kurihara and Tuleya (1981), the development of a deep vortex

characteristic of a tropical storm from a shallow easterly wave required three to five days.

The mesoscale circulation pattern associated with the tropical storm also influences the diabatic activity. When the relative vorticity is of the same order as the planetary vorticity, then the surface pressure tendencies are influenced very little by diabatic heating (Delden 1989). But, the more intense the vortex, the greater the response to a given heat source (Schubert and Hack 1982; Delden 1989).

Figure 9 shows that when diabatic forcing is used, the number of vertical modes in the initialization has little influence on the grid scale condensation. But the magnitude of the forcing is shown to be influential, as illustrated by the difference between the DF(0.3) and DF(0.5) curves. Clearly, the greater the forcing the greater the response. Also in Fig 9 it is seen that when the forcing is closer to the surface, i.e., between sigma levels 0.4 and 0.95, the response is greater, presumedly because more moisture is transported vertically.

In Fig 10 a maximum of 14.26 cm of precipitation is recorded over fourteen hours when the forcing DF(0.5), centered between sigma levels 0.25 and 0.80, is applied for two hours. Approximately fifty percent more rainfall is recorded when the forcing is extended in duration from two to three hours. As expected, reducing the maximum magnitude of the forcing from K=0.5 C per 300 s time step to 0.3 C reduces the rainfall, yielding a maximum of 4.59 cm for DF(0.3). When the forcing is placed lower in the atmosphere, i.e., between sigma levels 0.4 and 0.95, then more moisture condenses and more total precipitation falls, but for this case the maximum rainfall is nevertheless reduced. Generally, Fig 10 shows that a high degree of correlation exists between the number of grid scale condensation points, shown in Figs 7 and 8, and the maximum rainfall. To help visualize the precipitation pattern the rainfall recorded on the surface, associated with a two hour application of DF(0.5), is shown in Fig 11. The convective rainfall resulting from the cumulus parameterization is small in this region (not shown), although the 40 km grid resolution is somewhat boarder line for the effective use of a Kuo-type cumulus parameterization scheme.

The diabatic forcing can also be used at any time during a forecast as shown graphically in

Fig 1b. For example, results from an application of diabatic forcing beginning ten hours into a twenty-four hour forecast, as the sole means to enhance the spin-up of tropical storm Emily, are illustrated in Figs 12 through 15. Beginning the application of diabatic forcing DF(0.25) in nearly the middle of a forecast at the satellite observation time, with the forcing centered between $0.25 < \sigma < 0.80$, requires a gradual approach into and decline out of the forcing regime to avoid introducing noise. A time period of one and one-half hours (time steps 120 to 138) is selected for linearly introducing the forcing, which remains constant for one and one quarter hours (time steps 138 to 153), while one hour (time steps 153 to 165) is used to turn off the diabatic forcing. The resulting geopotential heights contain closed contours (Fig 12), while significant vorticity ($>2.5 \times 10^{-4}$) and convergence are revealed in Figs 13 and 14 respectively. Convergence even exists in the region containing the spiral arm in the satellite image. The placement of these features is fairly good. A maximum rainfall of 94.5 mm is indicated in Fig 15. In the control, no rainfall is produced in the region containing Emily, but over 90 mm falls on the mountain slopes. Figure 15 also shows that doubling the forcing doubles the rainfall while low-level forcing gives a large maximum of 277.2 mm. The areal distribution of the precipitation produced by the twenty four hour forecast, using DF(0.25) (solid line), and the low level forcing (dashed line), is given in Fig 16 and are somewhat reduced in comparison with the precipitation from the fourteen hour forecast shown in Fig 11.

The number of grid scale condensation points as a function of time is shown in Fig 17 for the control (no forcing), and for three different vertical distributions and two different magnitudes of diabatic forcings. The grid scale condensation points occurring in the control case are associated with convection over elevated topography, none occurs in the vicinity of Emily. Differences then between the control and forced cases are associated with Emily. Figure 17 clearly shows that the magnitude of the forcing is important.

Presented in Fig. 18 is the integrated precipitating water, in kgm^{-2}, predicted by the fourteen hour forecast. It can be compared with the SSM/I retrieved estimates (Olson 1993) given in Fig 19. Note the latter is distributed over a much larger area and contains a comma shaped pattern,

while the forecasted amount has concentric contours much like the shape of the forcing. The maximum produced by the forecast is slightly too far south. Enlarging the initial areal size of the diabatic heating results in a proportional increase in the integrated rain water in the fourteen hour forecast. When the initial conditions are shifted to the north, then the development in the forecast responds in a corresponding manner (not shown).

B. ERICA IOP-5

This case differs from the Emily situation in that the 12 hour preforecast produces diabatic activity over the region of interest. However, diabatic heating fields from the last time step of the 12 hour preforecast are thought to be unrepresentative enough that they should not be used directly in the diabatic initialization and diabatic forcing formulation. Consequently, the T_{EX} fields, with a maximum of <1 C during a 600 s time step, are set proportional to the coverage and vertical distribution of the cloud water fields (not shown) predicted by the 12h preforecast. It is assumed that the distribution of cloud water is more representative of the distribution of heating than the larger size rain water particles which fall out as precipitation.

Figure 20 illustrates, for a grid resolution of 120 km at 0000 UTC 20 1988, that the diabatic initialization produces a doubling of the negative omega values (solid lines) found at 700 and 400 mb in the global analysis. This initialization did enhance slightly the storm development and rainfall distribution in the 12h forecast, but the predicted 988 mb low pressure is far from the observed 968 mb measured in this rapidly deepening storm (IOP-5), as indicated in the ERICA Field Phase Summary (Hartnett et al. 1989). Thus, given the model's 120 km horizontal resolution, additional measures are required to better forecast this intensely developing storm.

Results from a 24h forecast, ending at 1200 UTC 20 Jan 1988, are compared in Figs 21, 22 and 23 against a control twelve hour forecast and with two diabatically forced cases. The diabatic forcing is applied to the global initial conditions, and in all calculations the cumulus parameterization scheme has been turned off to isolate the spin-up process for the grid scale

calculations. In Fig 21 the wind speed at 500 mb is shown. Note that the jet develops a maximum speed of 40^{+} ms^{-1} in all cases except the lower right figure, which is from a forecast using four hours of diabatic forcing. This forecast produces 50^{+} ms^{-1} wind speeds in the dry slot just behind the upper part of the comma. Note that two hours of diabatic forcing did increase the area under the 40 ms^{-1} curve (lower left). The change in the wind field can be directly associated with the enhancement in the comma shape of the mixing ratio shown at the 700 mb level in Fig 22. Note also in the two and four hour diabatically forced forecasts, that the gradients of mixing ratio are largest to the rear of the storm.

Fig 23 shows the precipitation (mm) accumulated during a twelve hour period. The final twelve hours of the twenty four hour forecast produced a small region with a maximum in excess of 70 mm, while the diabatically forced forecasts show a slight reduction in the maximum precipitation from 30^{+} mm (upper right) to 20^{+} mm. This small and temporary reduction is thought to occur because the continual diabatic forcing builds a deeper system containing more precipitating liquid aloft. If, however, the forcing is too strong or applied too long, then the upward vertical motion becomes large, causing an excessive amount of water to be suspended in the atmospheric column. Then, the eventual fallout of this rain water can lead to negative consequences, and possibly the premature death of the storm.

The area averaged precipitation rate as a function of time is presented in Fig 24 for five forecasts and from satellite measurements. The latter is computed using a technique (Martin et al 1990) that estimates the hourly precipitation rate from satellite infrared image cloud-top temperatures by a regression power-law formula. The coefficients in the power-law formula are obtained using maximum-likelihood correlations of relationships between cloud-top temperatures and a large number of raingauge precipitation rate observations (B. Goodman, personal communication). The variations seen in Fig 24 for the observations are small, but the extra time needed to spin-up the precipitation in the model is clear. In the legend in Fig. 24 "large scale" refers to the traditional method of instantaneously removing from the atmosphere water vapor in

excess of saturation. Clearly, this procedure needs less time to produce precipitation than the grid scale explicit cloud category which requires time for the different cloud processes to react and for the rain water to reach the earth's surface. Retaining cloud and rain water unaltered through an assimilation cycle (heavy solid line) allows the precipitation to continue at the same rate as it had previously, denoted by "hot start" in the legend. Note that all methods come close to converging to the average precipitation rate seen in the satellite measurements. The forecast that uses diabatic forcing for four hours (not shown) produces just slightly less rainfall than the explicit category with no diabatic forcing (open circle).

Super-imposed over the GOES 7 IR image at 1201 UTC 20 Jan. 1989 in Fig. 25 is the surface pressure field. This field is from a 12 h forecast that uses diabatic initialization (DI), consequently it deepens to only 988 mb instead of the observed 968 mb. In contrast, using the diabatic initialization (DI) and diabatic forcing (DF) over a 4 hour period, where during the last two hours the forcing is linearly tapered to zero, produces a 968 mb contour as shown in Fig 26. However, some gravity wave noise is also produced as can be seen by the waviness of the contours near the US coast and elsewhere.

C. US Forecasts (1200 UTC 21-22 April 1988)

The final case involves a meteorological situation where surface and upper air reports are plentiful. This situation was chosen to test how conventional data effects the assimilation of cloud and rain water quantities. Rainfall and other meteorological information for this time period is available in the Daily Weather Maps[1]. Generally, a stationary front is located over Colorado, Wyoming, and Montana, with the center of the surface low over Kansas. Another stationary front lying directly east of the surface low. The heaviest concentration of clouds are found to the north of the front. Rainfall amounts are generally light to moderate, with less than one-half of an inch over the last twenty-four hours. Upper level moisture and a band of high clouds have moved

[1] Daily Weather Maps, Weekly Series April 18-24, 1988, National Oceanic and Atmospheric Administration, National Weather Service, National Meteorological Center Climate Analysis Center.

across Mexico and into the southern US. Only a small amount of precipitation is associated with this upper level system. The integrated cloud water (x 100 kg m^{-2}) from our 12 hour forecast is shown in Fig 27, valid for 1200 UTC 22 April 1988. The predicted cloud cover is surprising good for the region north of the front, given the 150 km horizontal resolution use in the forecast. Boundary conditions influence the cloud development along the eastern, western and southern boundaries. The high level clouds along the southern part of the US are not predicted, partially because the southern boundary condition in our regional model calculations did not supply enough moisture. Initial conditions for this forecast used surface and upper air observations, along with the traditional model produced guess fields plus cloud and rain water information supplied by the 12 hour preforecast. These liquid water quantities helped reduce the time needed for precipitation to develop, as illustrated below.

Figure 28 illustrates the sensitivity of the vertical mode initialization procedure. Note that for two vertical modes the number of condensation points, in the grid scale calculations for a one time step forecast, change little when the magnitude of the heating is increased by a factor of four. However, the number of condensation points increases dramatically as the number of modes in the vertical mode initialization is increased. This requires that care must be exercised in selecting the proper number of vertical modes. When diabatic forcing is combined with the diabatic initialization, the importance of selecting the proper vertical modes is less important, as has been illustrated earlier. In the above calculations the T_{EX} fields are generated using cloud water information from the 12 hour preforecast.

Changes in the grid averaged precipitation rate resulting from the inclusion of data inserted during the assimilation cycle are contrasted in Fig 29 with the contribution from the cumulus parameterization process. Here MG stands for the preforecast model generated 150 km resolution fields used in the initial conditions, and represents a forecast that does not use cumulus parameterization unless so stated. Note in Fig 29 that the largest difference in precipitation production between the MG simulation with cumulus (thin line) and without cumulus (circle) exists

early in the forecast. Also clear in Fig 29 is the fact that precipitation contributions added by the cumulus parameterization are larger than the precipitation changes induced by the addition of the surface, upper air and air craft data (thick line). To really understand the impact of data, i.e., temperatures, pressures, mixing ratios, and winds upon the assimilation of cloud and rain water will require an examination of a large number of cases. Such a study must be conducted within an operational environment.

The number of grid scale condensation points (Fig 30) and the grid averaged precipitation rate (Fig 31) indicate large differences which exist between the global no data + DI and the other MG categories. For this particular case, at the 150 km resolution, the inclusion of cloud, cloud and rain, or cloud and rain water plus diabatic initialization (DI) makes a difference during the first half of the 12 hour forecast. These differences are still much less than those found between the global and the higher resolution MG data sets. Nevertheless, even in this situation which contains weak to moderate precipitation events, there are some positive benefits, seen especially in Fig 31, from including the cloud water in the assimilation cycle. Their inclusion also temporarily increases the total moisture supply, until it all is rained out. Also, diabatic initialization is usually required in the assimilation of cloud and rain water to help sustain or add to the supporting mesoscale circulation.

The amount of mesoscale resolution in the initial model fields makes a difference 12 hours later in the vertical distribution of the area averaged cloud and rain water, as shown in Fig 32 and 33. Note that the MG higher resolution initial fields produce cloud water in the 12 hour forecast that has a larger percentage of its total contribution at elevated sigma levels (Fig 32). Similar comments apply to the rain water displayed in Fig 33. This would seem to be a natural consequence of having enhanced vertical motions and larger magnitudes of convergence. The differences illustrated in Fig 32 and 33 also imply that diabatic temperature initialization, used with the global data is not able to correct for missing diabatic mesoscale circulation deficiencies.

VI Summary

In this study several methods are shown to enhance the development and reduce the spin-up of precipitation when explicit cloud and rain water calculations are used. These include diabatic initialization, diabatic forcing and the assimilation of cloud and rain water fields from one forecast to the next sequential forecast. To statistically validate any of the precipitation enhancing procedures requires an operational setting where a large number of cases can be tested.

Diabatic initialization can be given an assist by a short period of diabatic forcing following the initialization. This is also beneficial for enhancing storm intensity. The forcing procedure can be constructed to be a natural continuation of the diabatic initialization, but can be applied at any time provided care is taken to avoid introducing noise. Advection of the external heating field helps with the proper horizontal placement of the forcing provided the forecast wind field is approximately correct. Extra moisture can also be added to help encourage diabatic development. When explicit cloud schemes are employed, the assimilation of cloud and rain water from one forecast to the next sequential forecast has the potential to be a useful method for encouraging the early development of precipitation, especially in major disturbances. Improved modeling techniques using diabatic forcing and cloud and rain water assimilation are thus able to help reduce the spin-up of grid-scale precipitation and enhance mesoscale circulations, which in turn provide the support necessary to sustain continued diabatic activity.

The vertical placement of the diabatic forcing remains a difficult problem. Using the vertical levels and proportions of the cloud development in the preforecast provides some vertical information, but difficulties remain in regions that lack cloud development. Most of the time the lack of cloud development can be traced to the lack of information in initial conditions. This study shows that data assimilation, diabatic initialization and diabatic forcing procedures can be used with explicit cloud and rain water formulations to encourage, enhance and modify the cloud and rain water fields, and to intensify the forecasted storm development. A major problem is the lack of data to initialize the cloud and rain water fields and an incomplete knowledge of the correct vertical

profile of latent heating. Promising satellite retrieval techniques, that combine standard remote sensing procedures with physical models to estimate the precipitating liquid water and ice distributions, may also be able to estimate the vertical placement of the latent heating fields. This holds great promise for providing data for the assimilation of the initial cloud and rain water fields, especially over water surfaces.

Acknowledgments. This work was supported by NASA Grant NAGW-1855. One author (WHR) was supported in part by National Science Foundation Grant ATM-8920508.

References

Anthes, R. A., E-Y Hsie and Y-H Kuo, 1987: Description of the Penn State/NCAR mesoscale model version 4 (MM4). NCAR Technical Note NCAR/TN-282+STR. National Center for Atmospheric Research, Boulder, Colorado, 66pp.

Asai, T., 1965: A numerical study of the air-mass transformation over the Japan Sea in winter. *J. Meteor. Soc. Japan*, **43**, 1-15.

Bourke, W. and J. L. McGregor, 1983: A nonlinear vertical mode initialization scheme for a limited area prediction model. *Mon. Wea. Rev.*, **111**, 2285-2297.

Danard, M., 1985: On the use of satellite estimates of precipitation in initial analyses for numerical weather prediction. *Atmosphere-Ocean*, **23**, 23-42.

Delden, A. van., 1989: On the deepening and filling of balanced cyclones by diabatic heating. *Meteorol. Atmos. Phys.*, **41**, 127-145.

Donner, L. J., 1988: An initialization for cumulus convection in numerical weather prediction models. *Mon. Wea. Rev.*, **116**, 377-385.

_____, and P. J. Rasch, 1989: Cumulus initialization in a global model for numerical weather prediction. *Mon. Wea. Rev.*, **117**, 2654-2671.

Errico, R. and P. J. Rasch, 1988: A comparison of various normal-mode initialization schemes and the inclusion of diabatic processes. *Tellus*, **40A**, 1-25.

Fiorino, M and T.T. Warner, 1981: Incorporating surface winds and rainfall rates into the initialization of a mesoscale hurricane model. *Mon. Wea. Rev.*, **109**, 1914-1929.

Hartnett, E., G. Forbes and R. Hadlock, 1989: ERICA Experiment on Rapidly Intensifying Cyclones over the Atlantic: Field Phase Summary. Available from ERICA Data Center, Drexal University.

Heckley, A. H., G. Kelly, and M. Tiedtke, 1990: On the use of satellite-derived heating rates for data assimilation within the tropics. *Mon. Wea. Rev.*, **118**, 1743-1757.

Hoke, J. E. R. A. Anthes, 1976: The initialization of numerical models by a dynamical initialization technique. *Mon. Wea. Rev.*, **104**, 1551-1556.

Kasahara, A., A. Mizzi, and L. J. Donner, 1992: Impact of cumulus initialization on the spinup of precipitation forecasts in the tropics. *Mon. Wea. Rev.*, **120**, 1360-1380.

Kessler, E., 1974: Model of precipitation and vertical air currents. *Tellus*, **26**, 519-542.

Krishnamurti, T. N., K. Ingles, S. Cocke, R. Pasch, and T. Kitade, 1984: Details of low latitude medium range weather prediction using a global spectral model II. Effect of orography and physical initialization. *J Meteor. Soc. Japan*, **62**, 613-649.

Kurihara, Y. and R. E. Tuleya, 1981: A numerical simulation study on the genesis of a tropical storm. *Mon. Wea. Rev.*, **109**, 1629-1653.

Kuo, H. L. and W. H. Raymond, 1980: A quasi-one-dimensional cumulus cloud model and parameterization of cumulus heating and mixing effects. *Mon. Wea. Rev.*, **108**, 991-1009

Lejenas, H., 1980: On the influence of the technique of nonlinear normal mode initialization on the nonconvective precipitation rate. *Mon. Wea. Rev.*, **108**, 1465-1468.

Leslie, L. M., G. A. Mills, L. W. Logan, D. J. Gauntlett, G. A. Kelly, J. L. McGregor and M. J. Manton, 1985: A high resolution primitive equation NWP model for operations and research. *Aust. Meteor. Mag.*, **33**, 11-35.

Liu, J. Y. and H. D. Orville, 1969: Numerical modeling of precipitation and cloud shadow effects on mountain- induced cumuli. *J. Atmos. Sci.*, **26**, 1283-1298.

Martin, D. W., B. M. Goodman, T. J. Schmit and E. C. Cutrine, 1990: Estimates of daily rainfall over the Amazon basin. *J. G. R.*, **95**, 17043-17050.

Mathur, M. B., H. S. Bedi, T. N. Krishnamurti, M. Kanamitsu and J. S. Woollen, 1992: Use of satellite-derived rainfall for improving tropical forecasts. *Mon. Wea. Rev.*, **120**, 2540-2560.

McGregor, J. L., L. M. Leslie and D. J. Gauntlett, 1978: The ANMRC limited-area model: consolidated formulation and operational results. *Mon. Wea. Rev.*, **106**, 427-438.

Mills, G. A. and R. S. Seaman, 1990: The BMRC regional data assimilation system. *Mon. Wea. Rev.*, **118**, 1217-1237.

Mizzi, A., P., and A. Kasahara, 1989: Intercomparison of daily values of atmospheric variables, including diabatic heating rates, from the ECMWF, GFDL and Goddard Laboratory for Atmospheres FGGE level IIIb analyses. *J. Geophys. Res.*, **44**, 14717-14748.

Olson, William S., 1993: Physical retrieval of precipitation water contents from special sensor microwave/Imager (SSM/I) Data-Part II: Retrieval method and applications. To be submitted to *J. Appl. Meteor.*

Perkey, D. J., 1976: A description of preliminary results from a fine-mesh model for forecasting quantitative precipitation. *Mon. Wea. Rev.*, **104**, 1513-1526.

Puri, K., and M. J. Miller, 1990: The use of satellite data in the specification of convective heating for diabatic initialization and moisture adjustment in numerical weather prediction models. *Mon.Wea. Rev.*, **118**, 67-93.

Raymond, W. H., 1988: High-order low-pass implicit tangent filters for use in finite area calculations. *Mon. Wea. Rev.*, **116**, 2132-2141.

_____, 1989: Theoretical investigation of spiral features in mesolow circulations. *Polar and Arctic Lows*, Editors P. F. Twitchell, E. A. Rasmussen and K. L. Davidson, DEEPAK Publishing, 191-200.

_____, 1993: Moist wind relationships. *Mon. Wea. Rev.*, **121**, 1992-2003.

Salmon, E. M., and T. T. Warner, 1986: Short-term numerical precipitation forecasts initialized using a diagnosed divergent-wind component. *Mon. Wea. Rev.*, **114**, 2122-2132.

Schlesinger, R. E., 1990: Feedback of deep moist convection to its near environment as diagnosed from three-dimensional numerical model output: Results from an early experiment. *J. Atmos. Sci.*, **47**, 1390-1412.

Schubert, W. H. and J. J. Hack, 1982: Inertial stability and tropical cyclone development. *J. Atmos. Sci.*, **39**, 1687-1697.

Shapiro, L. J., and D. E. Stevens, 1980: Parameterization of convective effects on the momentum and vorticity budgets of synoptic-scale Atlantic tropical waves. *Mon. Wea. Rev.*, **108**, 1816-1826.

Sundqvist, H., E. Berge and J. E. Kristjansson, 1989: Condensation and cloud parameterization studies with a mesoscale numerical weather prediction model. *Mon. Wea. Rev.*, **117**, 1641-1657.

Tarbell, T. C., T. T. Warner and R. A. Anthes, 1981: An example of the initialization of the divergent wind component in a mesoscale numerical weather prediction model. *Mon. Wea. Rev.*, **109**, 77-95.

Turpeinen, O. M., L. Garand, R. Benoit and M. Roch, 1990: Diabatic initialization of the Canadian regional finite-element (RFE) model using satellite data. Part I: Methodology and application to a winter storm. *Mon. Wea. Rev.*, **118**, 1381-1395.

Wallace, J. M. and P. V. Hobbs, 1977: *Atmospheric Science, An Introductory Survey.* Academic Press, New York, 467pp.

Wang, W. and T. T. Warner, 1988: Use of four-dimensional data assimilation by newtonian relaxation and latent-heat forcing to improve a mesoscale-model precipitation forecast: A case study. *Mon. Wea. Rev.*, **116**, 2593-2613.

Wergen, W., 1988: The diabatic ECMWF normal mode initialization scheme. *Beitr. Phys. Atmosph.*, **61**, 274-302.

Wolcott, S. W., and T. T. Warner: 1981: A humidity initialization utilizing surface and satellite data. *Mon. Wea. Rev.*, **109**, 1989-1998.

List of Figures

Fig. 1. A schematic showing in (a) that the diabatic forcing follows immediately after the diabatic initialization, while in (b) the diabatic forcing is applied later in the forecast.

Fig. 2. Presented are the 700 mb heights from the fourteen hour forecast in the absence of diabatic forcing or diabatic initialization.

Fig. 3. Same as Fig 2 but for divergence field.

Fig. 4 Initial temperature perturbation field at 500 mb for T_{EX} as obtained from (12) with K=0.5C.

Fig. 5 Height field at 700 mb from a fourteen hour forecast containing both diabatic initialization and diabatic forcing DF(0.5). Contour interval is every 4 m.

Fig. 6 Same as Fig. 5 but for vorticity. Contour interval is 4.0×10^{-5} s^{-1}.

Fig. 7 Same as Fig. 5 but for divergence. Contour interval is 1.0×10^{-5} s^{-1}.

Fig. 8 The number of grid scale condensations as a function of time step is illustrated for adiabatic and diabatic initialization with and without diabatic forcing.

Fig. 9 Same as Fig. 8 but showing the variation as a function of the number of vertical modes, vertical position and magnitude.

Fig. 10 Bar graph of maximum rainfall for a select number of simulations.

Fig. 11 Total rainfall (cm) from the fourteen hour forecast with diabatic forcing. The maximum amount is in excess of 14 cm. Contour interval is 2 cm.

Fig. 12 Height field from the twenty four hour forecast with diabatic forcing DF(0.25) inserted gently at time step 120 (hour 10) and removed gently by step 165 (hour 13.75). Contour interval is 4 m.

Fig. 13. Same as Fig. 12 but for vorticity. Contour interval is 4.0×10^{-5} s^{-1}.

Fig. 14 Same as Fig. 12 but for divergence. Contour interval is 1.0×10^{-5} s^{-1}.

Fig. 15 Bar graph of maximum rainfall as a function of the diabatic forcing. Control case contains no rainfall in the vicinity of Emily but does have significant rainfall over elevated regions.

Fig. 16 Total rainfall is shown for two cases having different diabatic forcing in the vertical. Dashed lines are associated with lower level forcing while the elevated forcing gives the solid line. Contour interval is 4 cm.

Fig. 17 The number of grid scale condensations are shown as a function of the diabatic forcing which varies in its vertical distribution or magnitude.

Fig. 18 Shown is the integrated rain water (kg m^{-2} x 10) from the fourteen hour forecast.

Fig. 19 Retrieved estimates of the integrated precipitating liquid and ice from SSM/I radiances (Olson, 1993).

Fig. 20 Presented are the omega distributions in the adiabatic (top) and diabatic (bottom) initialized fields associated with ERICA IOP-5. Left-hand panels show the 700 mb distributions, while the right-hand panels give the 400 mb distribution.

Fig. 21 Presented are the 500 mb wind speed from the twenty four hour (control) forecast (upper left), twelve hour forecast with adiabatic initial conditions (upper right), twelve hour forecast with 2 hours of diabatic forcing (lower left), and twelve hour forecast with 4 hours of diabatic forcing (lower right).

Fig. 22 Same as in Fig 21 but for the 700 mb mixing ratio.

Fig. 23 Same as in Fig 21 but showing the rainfall.

Fig. 24 Shown is the grid averaged precipitation rate (mm h^{-1}) during a twenty four hour period ending at 1200 UTC 20 Jan 1988. The grid scale calculations with no clouds are labeled large scale while explicit cloud calculations, with and without a diabatic initialization and initialized cloud and rain water, can be compared against estimates of the hourly precipitation rate obtained from satellite infrared image cloud-top temperatures.

Fig. 25 Mean sea level pressure from a 12 h forecast beginning with a diabatic initialization. Contour interval is 4 mb.

Fig. 26 Mean sea level from a 12 h forecast that uses diabatic initialization and diabatic forcing. Contour interval is 4 mb.

Fig. 27 The vertically integrated cloud water (x 100 kg m^{-2}) at 1200 UTC 22 April 1988 from a 12 hour forecast initialized with cloud and rain water from the 12 hour preforecast. Contour interval is 3 .

Fig. 28 The response in the grid scale condensations, as a function of vertical modes, to changes in the magnitude of the diabatic initialization.

Fig. 29 Shown is the average precipitation per time step, using in the assimilation the model generated (MG) fields from the preforecast, with and without the cumulus parameterization scheme and the surface and upper air data.

Fig. 30 The number of grid scale condensations are shown as a function of cloud water (Cl), rain water (Rn), diabatic initialization (DI) and whether the model generated fields (MG) or global fields are used in the assimilation process.

Fig. 31 Same as Fig. 30 but showing the average precipitation rate.

Fig. 32 The per cent of the total cloud water at each vertical level at the end of a 12 h forecast is shown for two forecasts that have different amounts of data in the initialization.

Fig. 33 Same as Fig. 32 but for total rain water.

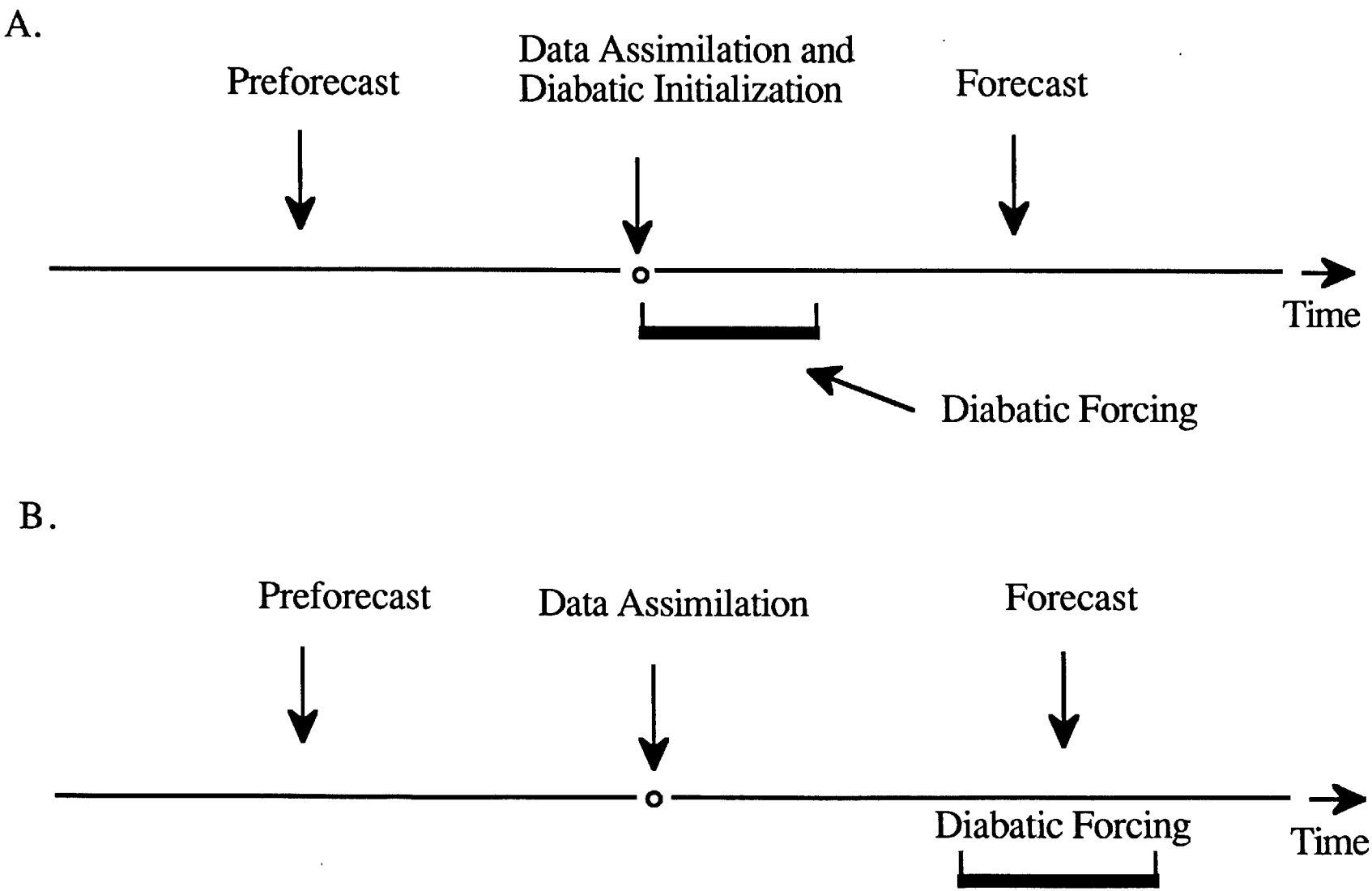
A.
Preforecast
Data Assimilation and
Diabatic Initialization
Forecast
Time
Diabatic Forcing
B.
Preforecast
Data Assimilation
Forecast
Diabatic Forcing
Time

Fig. 1

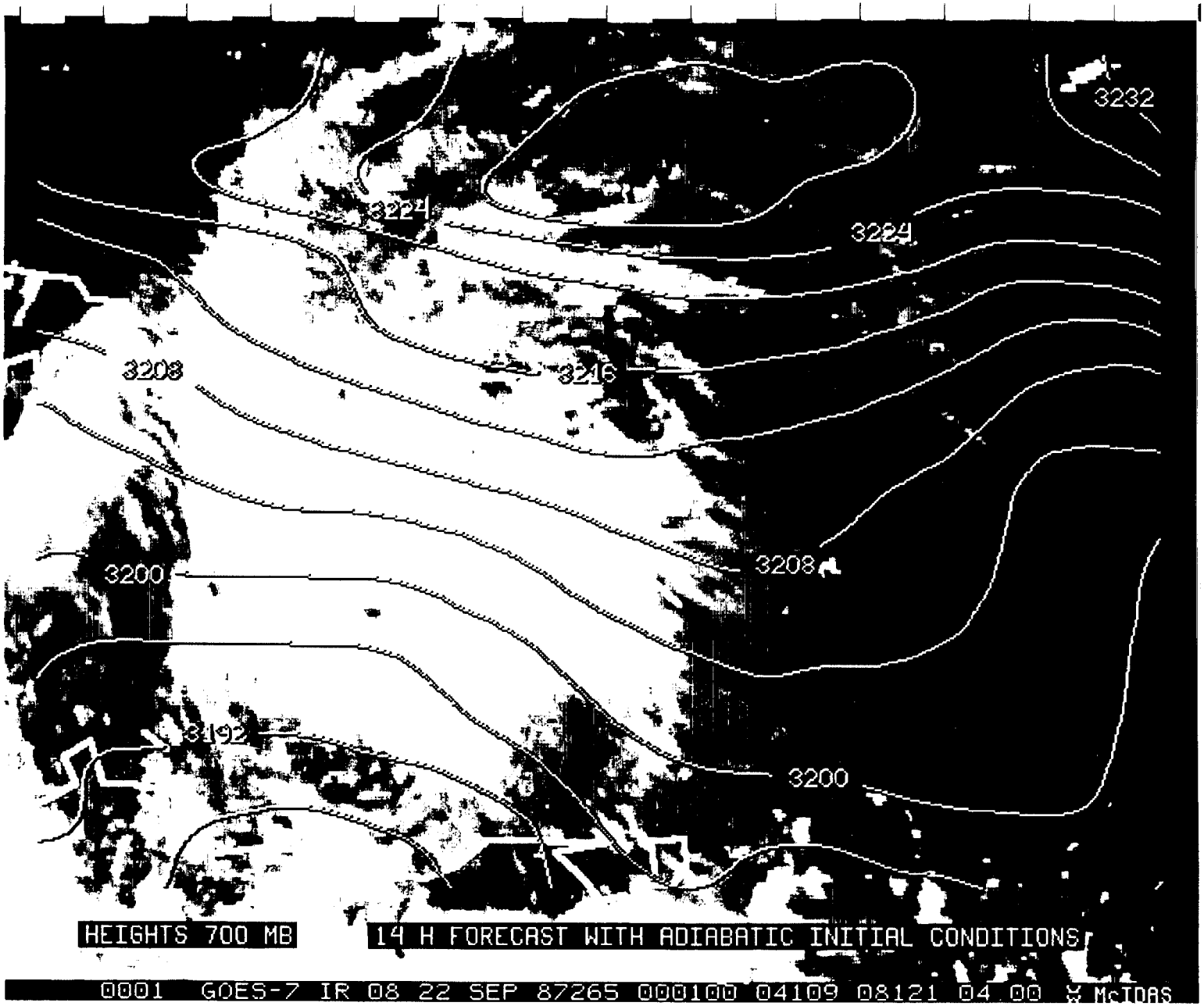
3232
3224
3224
3208
3216
3208
3200
3192
3200
HEIGHTS 700 MB
14 H FORECAST WITH ADIABATIC INITIAL CONDITIONS
0001 GOES-7 IR 08 22 SEP 87265 000100 04109 08121 04 00 McIDAS

Fig 2

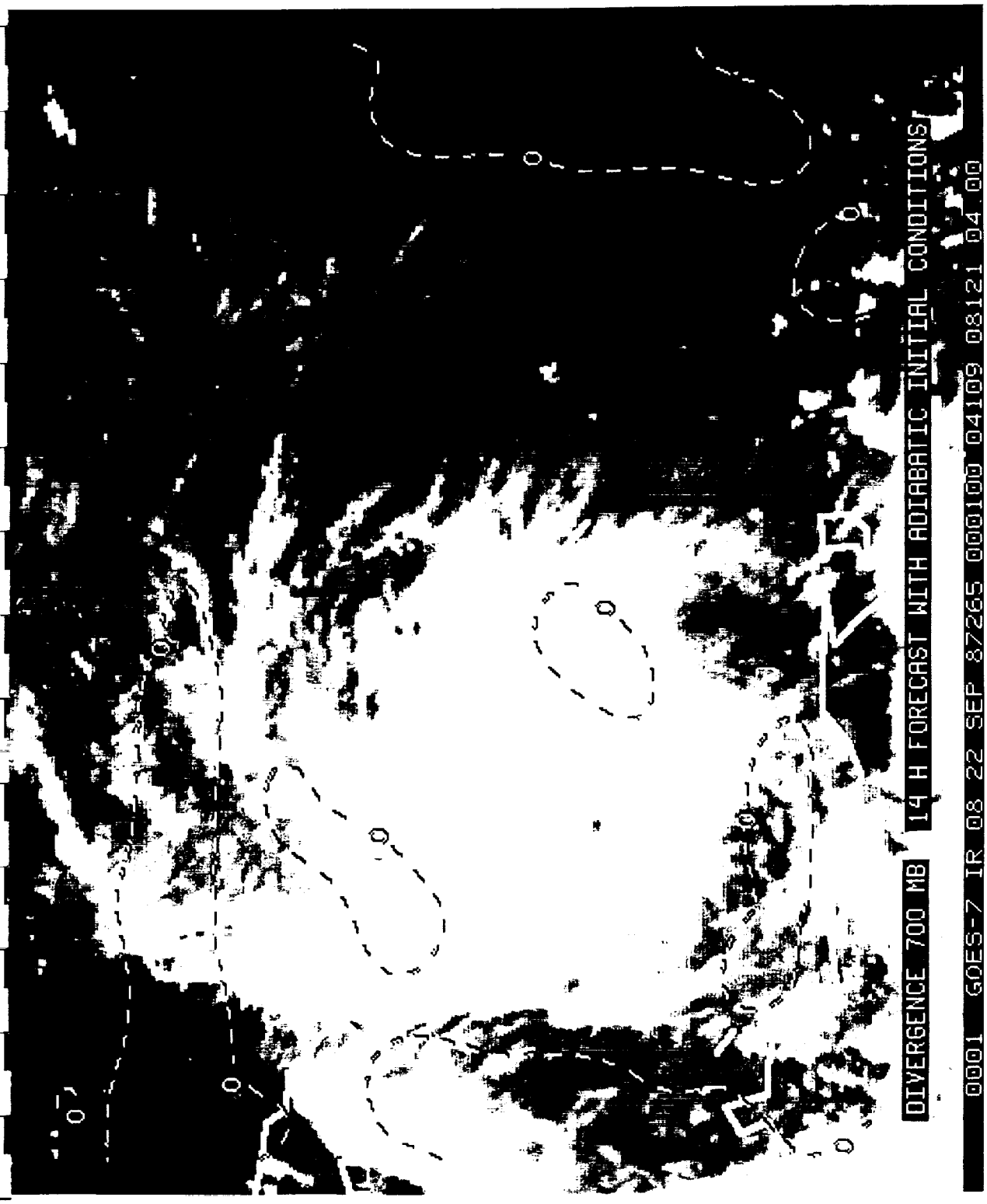
DIVERGENCE 700 MB
14 H FORECAST WITH ADIABATIC INITIAL CONDITIONS
0001 GOES-7 IR 08 22 SEP 87265 000100 04109 08121 04 00

Fig 3

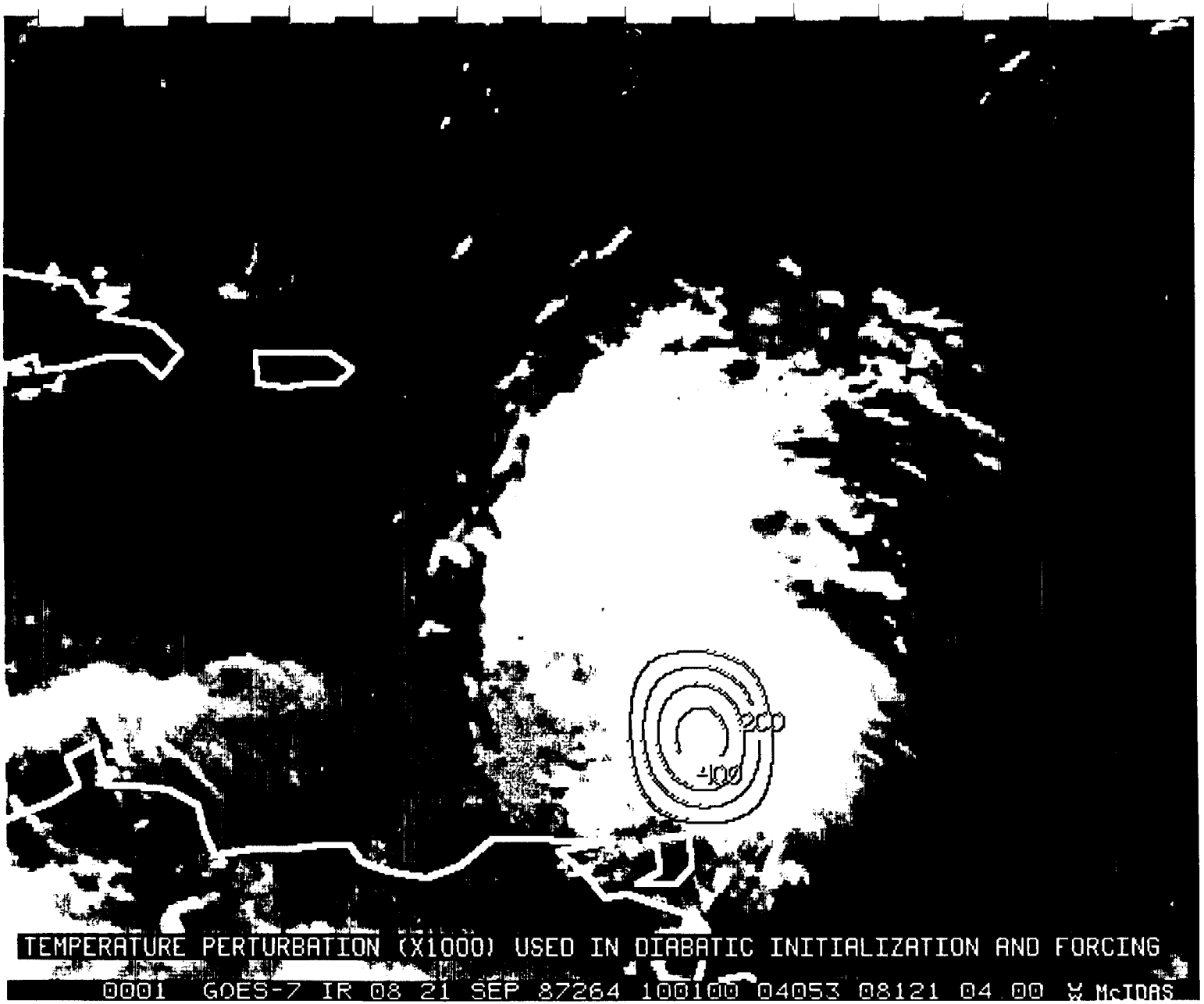
TEMPERATURE PERTURBATION (X1000) USED IN DIABATIC INITIALIZATION AND FORCING
0001 GOES-7 IR 08 21 SEP 87264 100100 04053 08121 04 00 W McIDAS

Fig 4

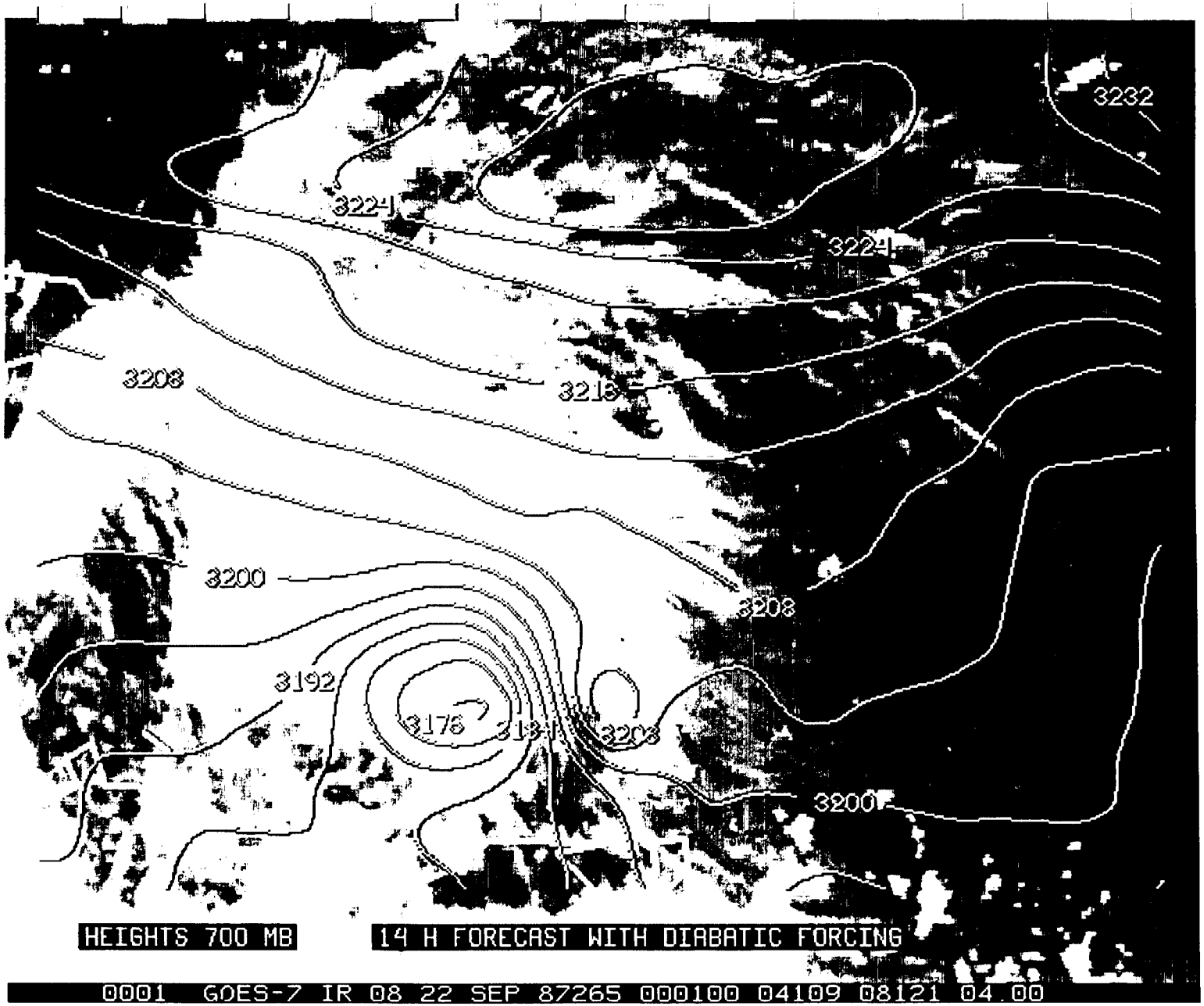
3232
3224
3224
3208
3216
3200
3208
3192
3176
3208
3200
HEIGHTS 700 MB
14 H FORECAST WITH DIABATIC FORCING
0001 GOES-7 IR 08 22 SEP 87265 000100 04109 08121 04.00

Fig 5

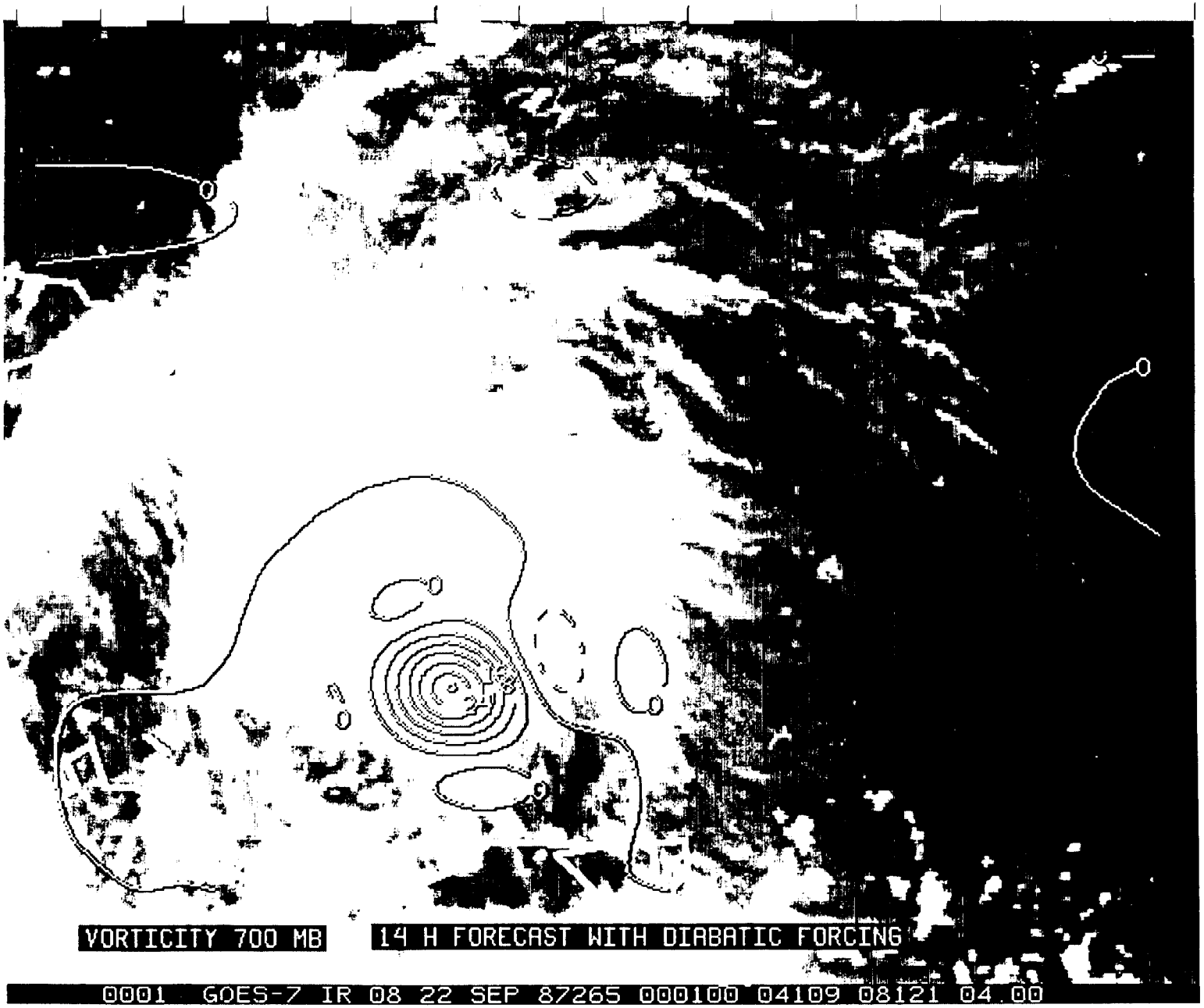
VORTICITY 700 MB
14 H FORECAST WITH DIABATIC FORCING
0001 GOES-7 IR 08 22 SEP 87265 000100 04109 08121 04 00

Fig 6

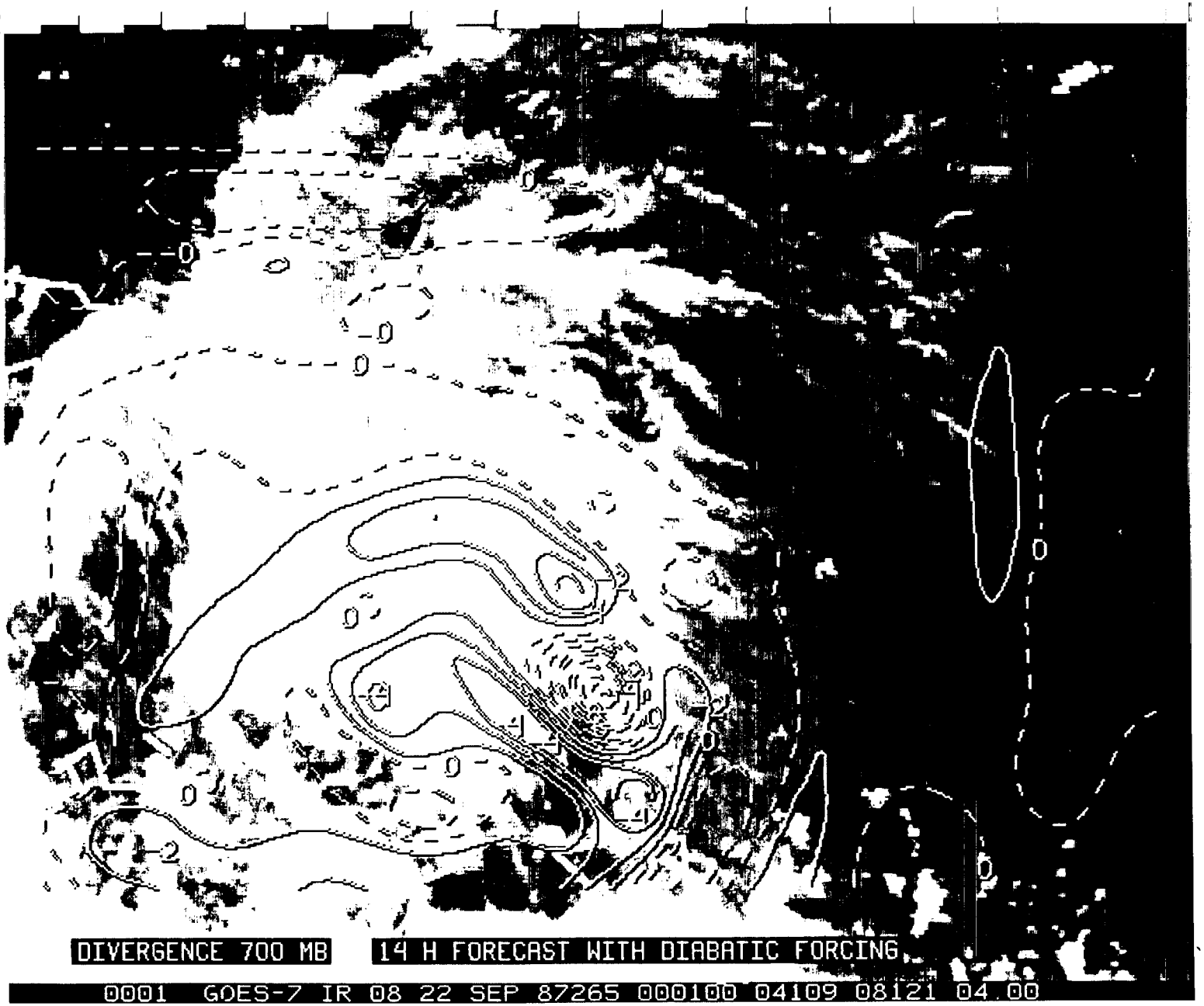
DIVERGENCE 700 MB
14 H FORECAST WITH DIABATIC FORCING
0001 GOES-7 IR 08 22 SEP 87265 000100 04109 08121 04.00

Fig 7

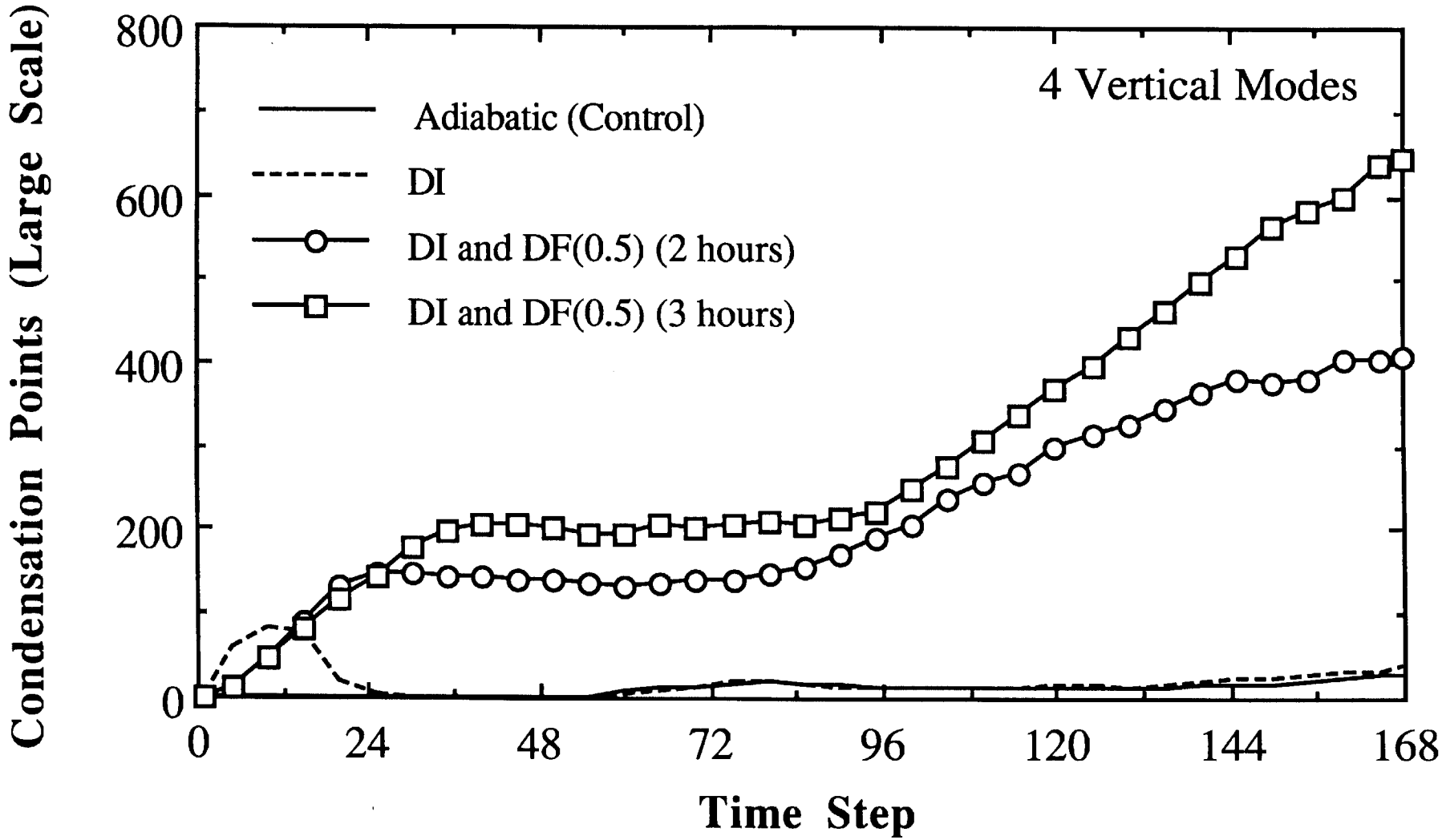
Condensation Points (Large Scale)
800
600
400
200
0
0
24
48
72
96
120
144
168
Time Step
4 Vertical Modes
Adiabatic (Control)
DI
DI and DF(0.5) (2 hours)
DI and DF(0.5) (3 hours)

Fig. 8

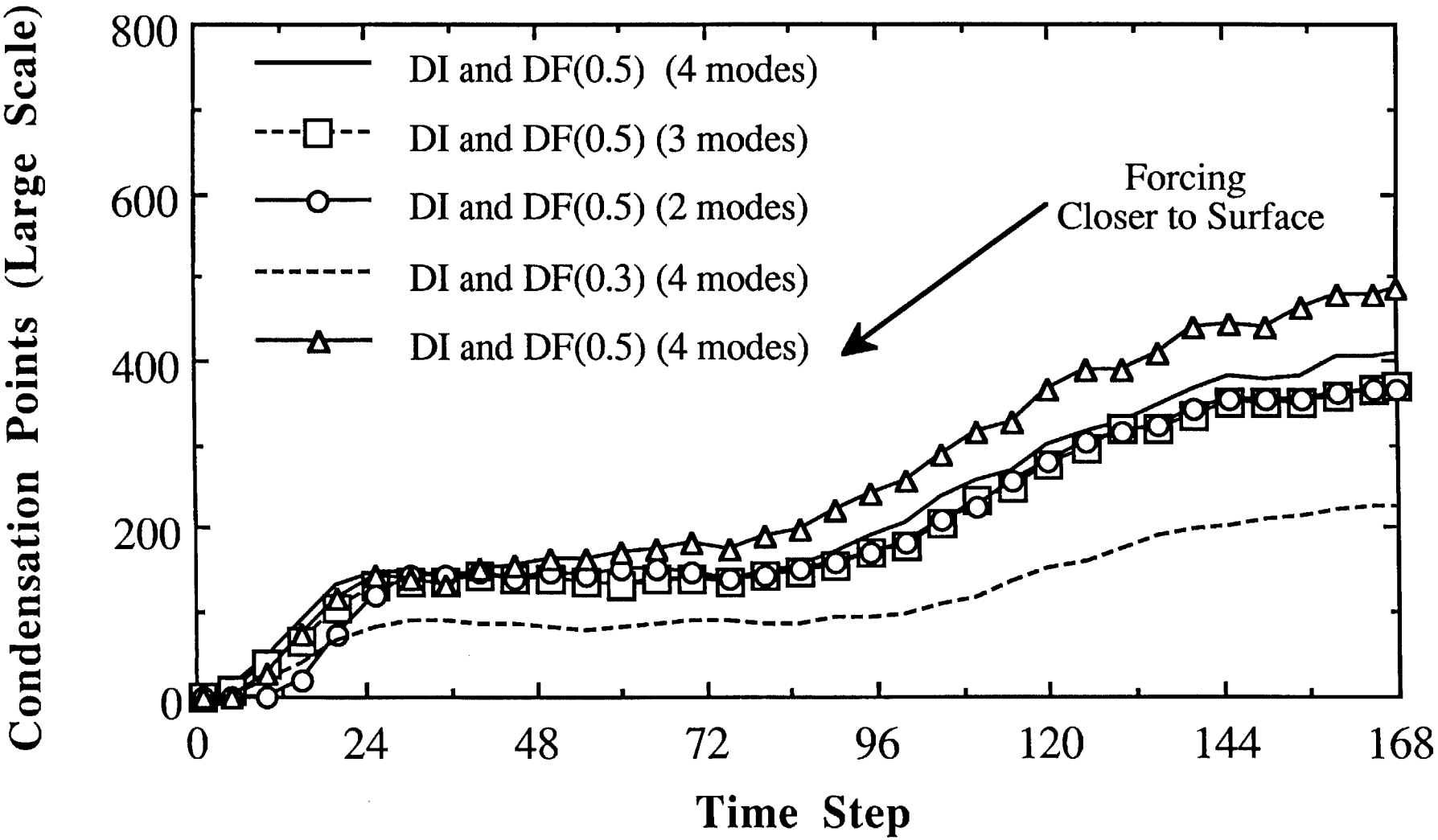
Condensation Points (Large Scale)
800
600
400
200
0
0
24
48
72
96
120
144
168
Time Step
DI and DF(0.5) (4 modes)
DI and DF(0.5) (3 modes)
DI and DF(0.5) (2 modes)
DI and DF(0.3) (4 modes)
DI and DF(0.5) (4 modes)
Forcing
Closer to Surface

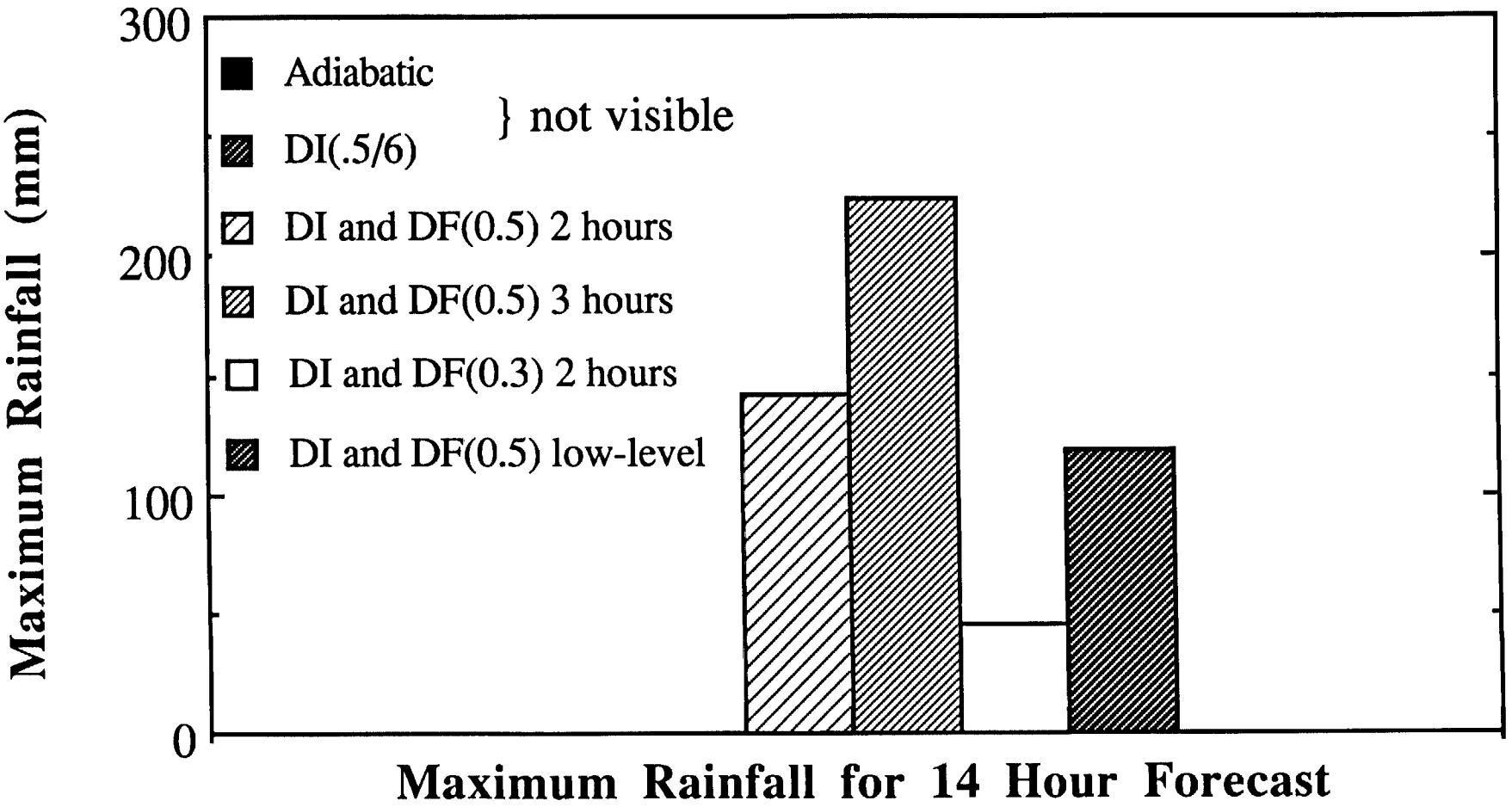
300
200
100
0
Maximum Rainfall (mm)
Adiabatic
DI(.5/6)
} not visible
DI and DF(0.5) 2 hours
DI and DF(0.5) 3 hours
DI and DF(0.3) 2 hours
DI and DF(0.5) low-level
Maximum Rainfall for 14 Hour Forecast

Fig 10

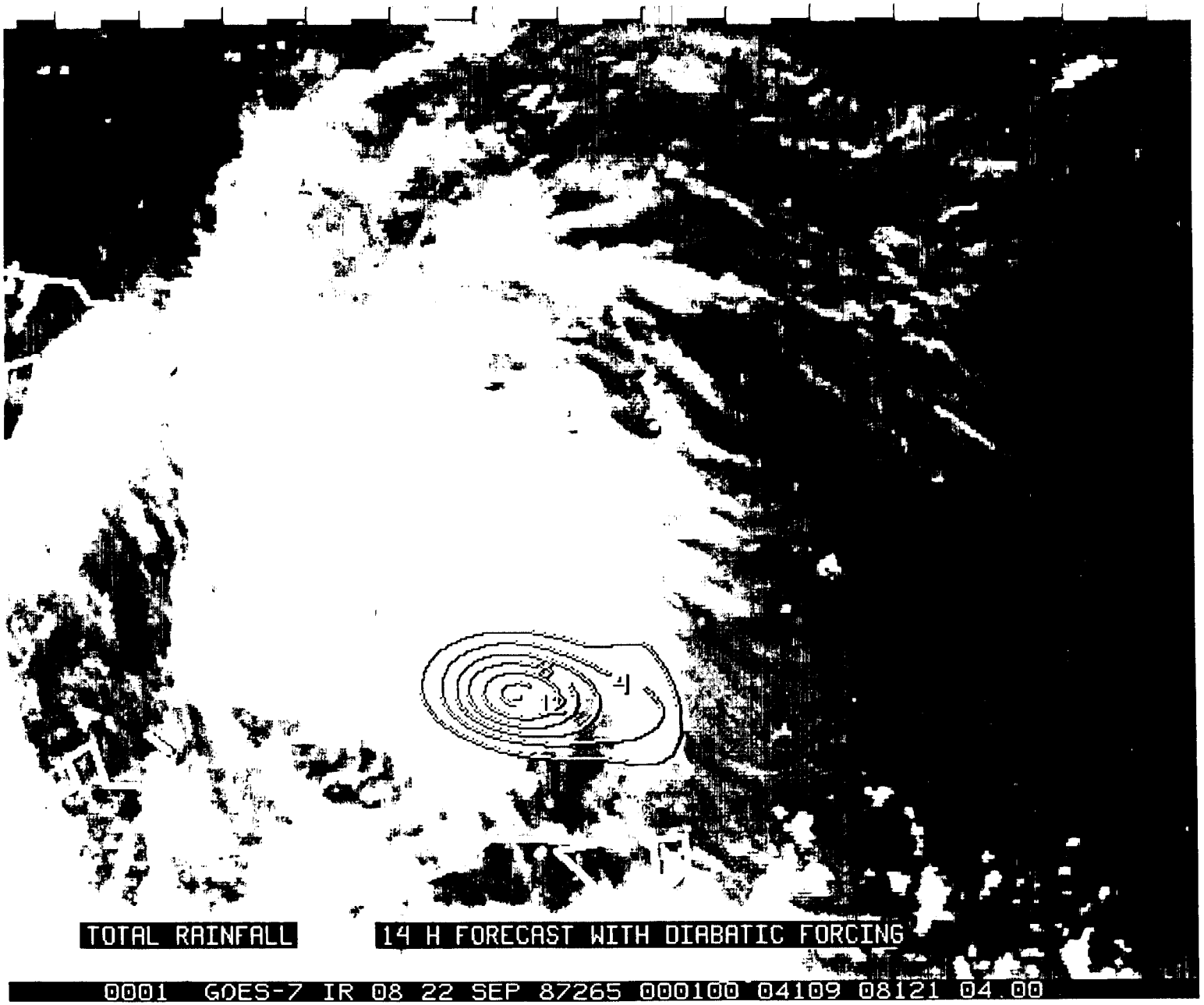
TOTAL RAINFALL
14 H FORECAST WITH DIABATIC FORCING
0001 GOES-7 IR 08 22 SEP 87265 000100 04109 08121 04 00

Fig 11

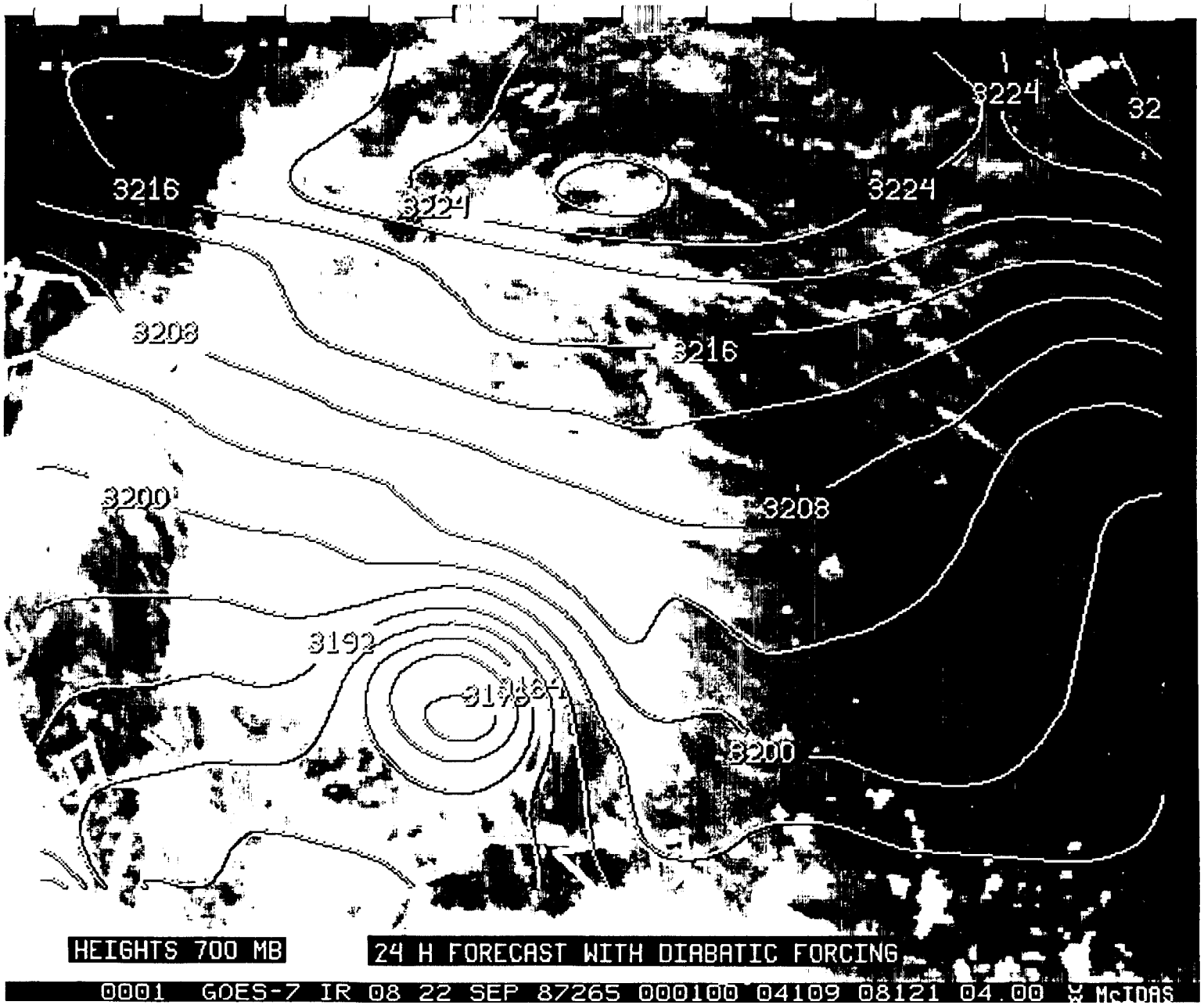
3224
32
3216
3224
3224
3208
3216
3200
3208
3192
3184
3200
HEIGHTS 700 MB
24 H FORECAST WITH DIABATIC FORCING
0001 GOES-7 IR 08 22 SEP 87265 000100 04109 08121 04.00 ※ McIDAS

Fig 12

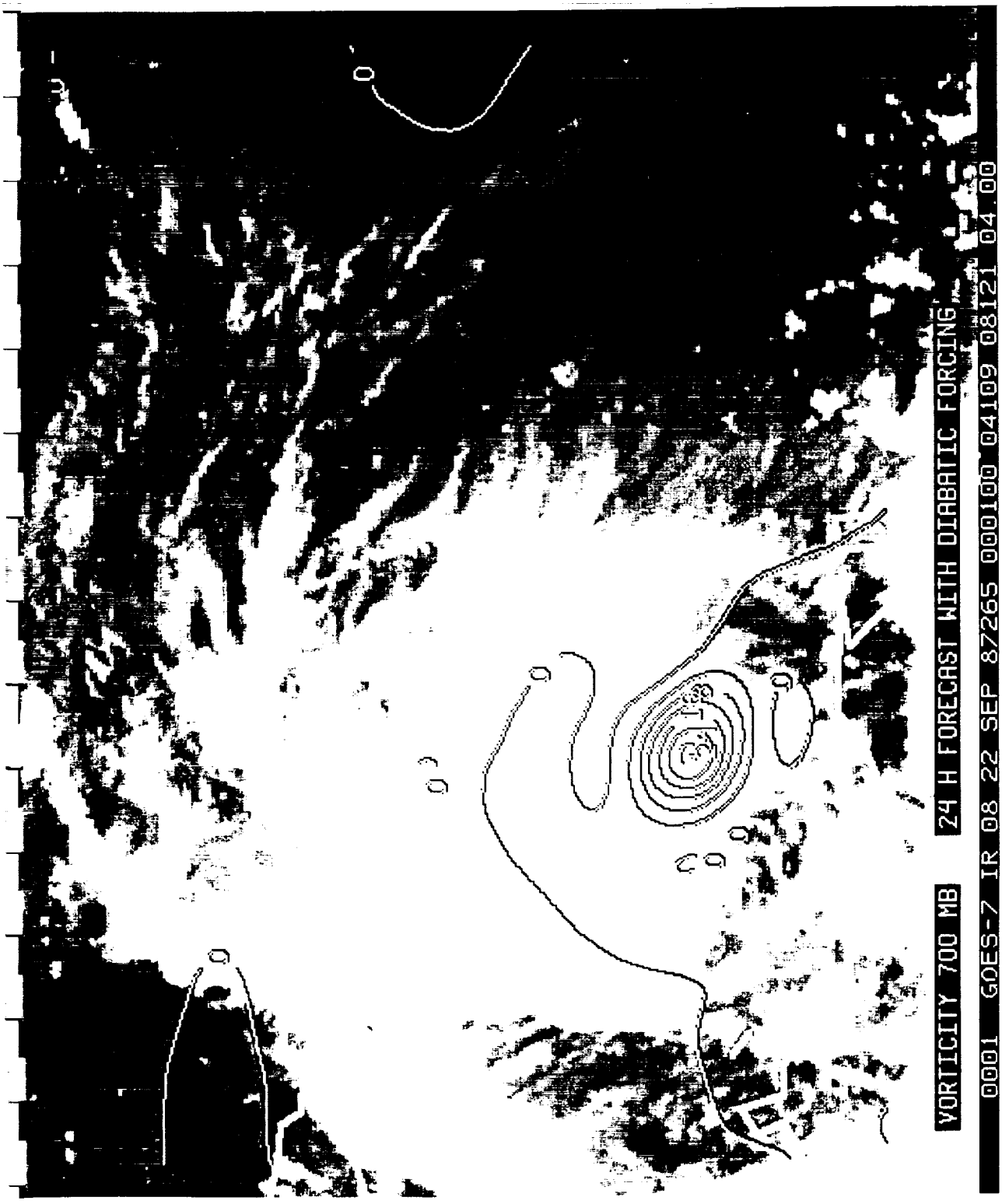
VORTICITY 700 MB
24 H FORECAST WITH DIABATIC FORCING
0001 GOES-7 IR 08 22 SEP 87265 000100 04109 08121 04 00

Fig 13

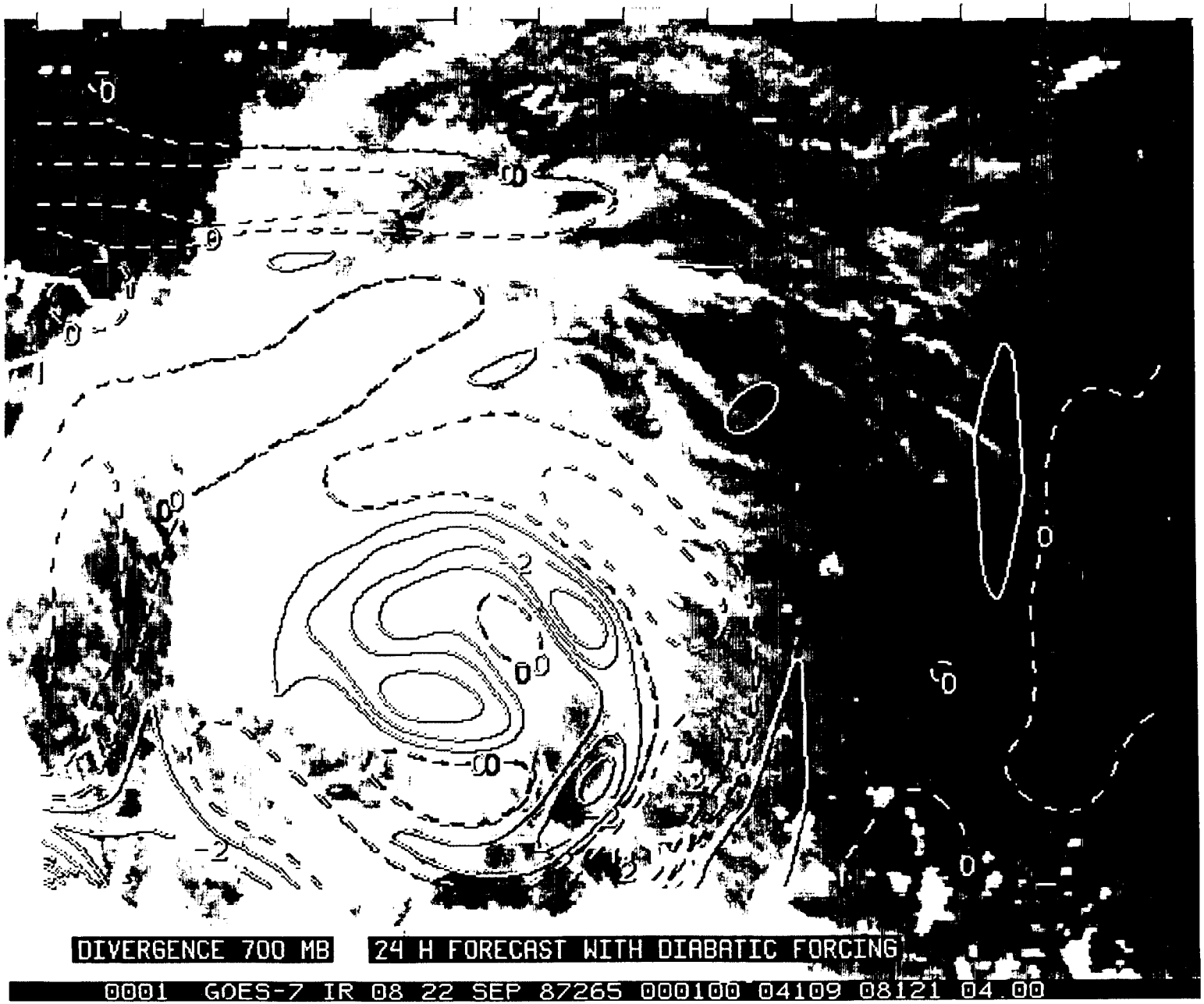
DIVERGENCE 700 MB
24 H FORECAST WITH DIABATIC FORCING
0001 GOES-7 IR 08 22 SEP 87265 000100 04109 08121 04 00

Fig. 14

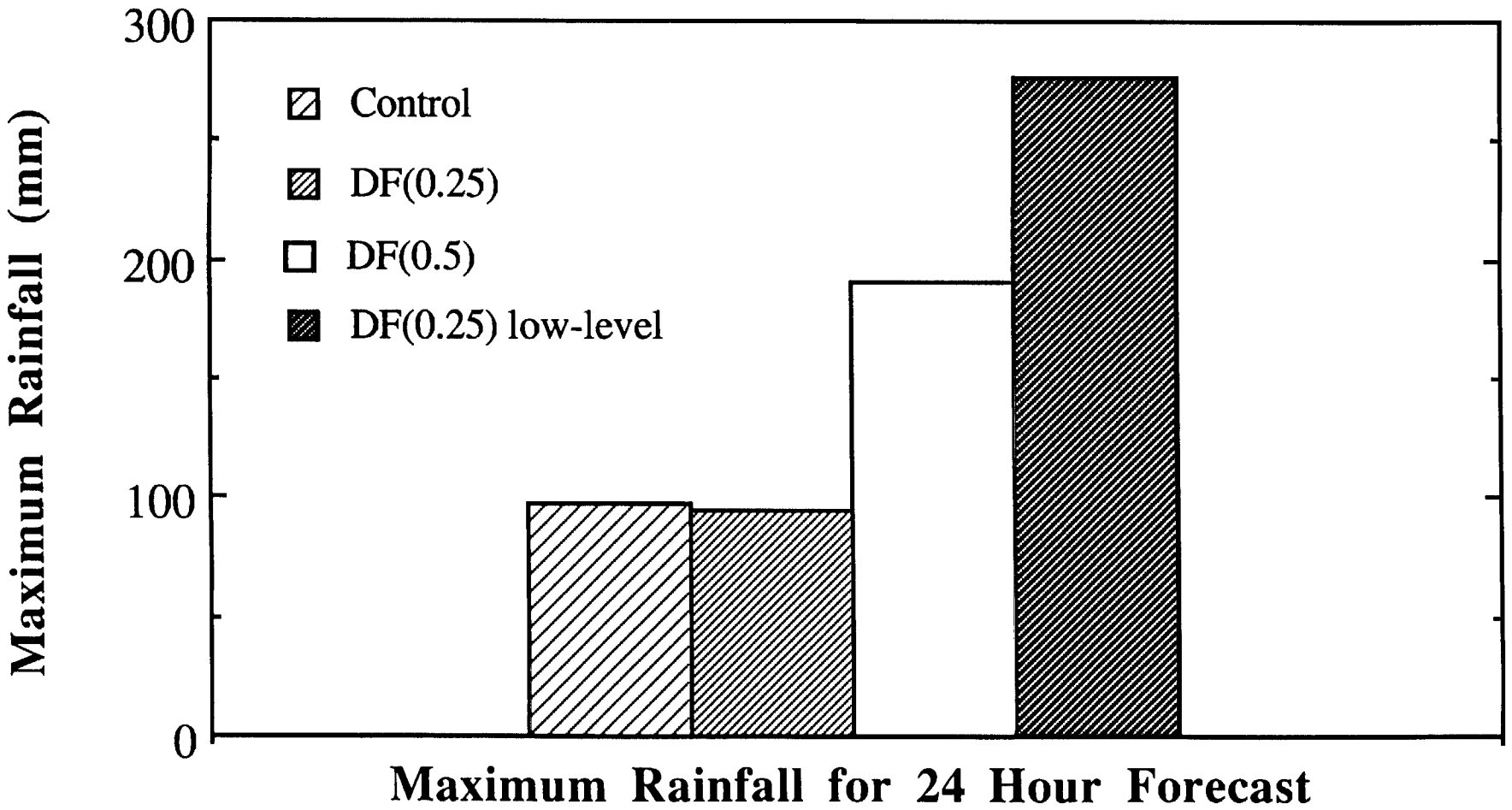
300
200
100
0
Maximum Rainfall (mm)
Control
DF(0.25)
DF(0.5)
DF(0.25) low-level
Maximum Rainfall for 24 Hour Forecast

Fig 15

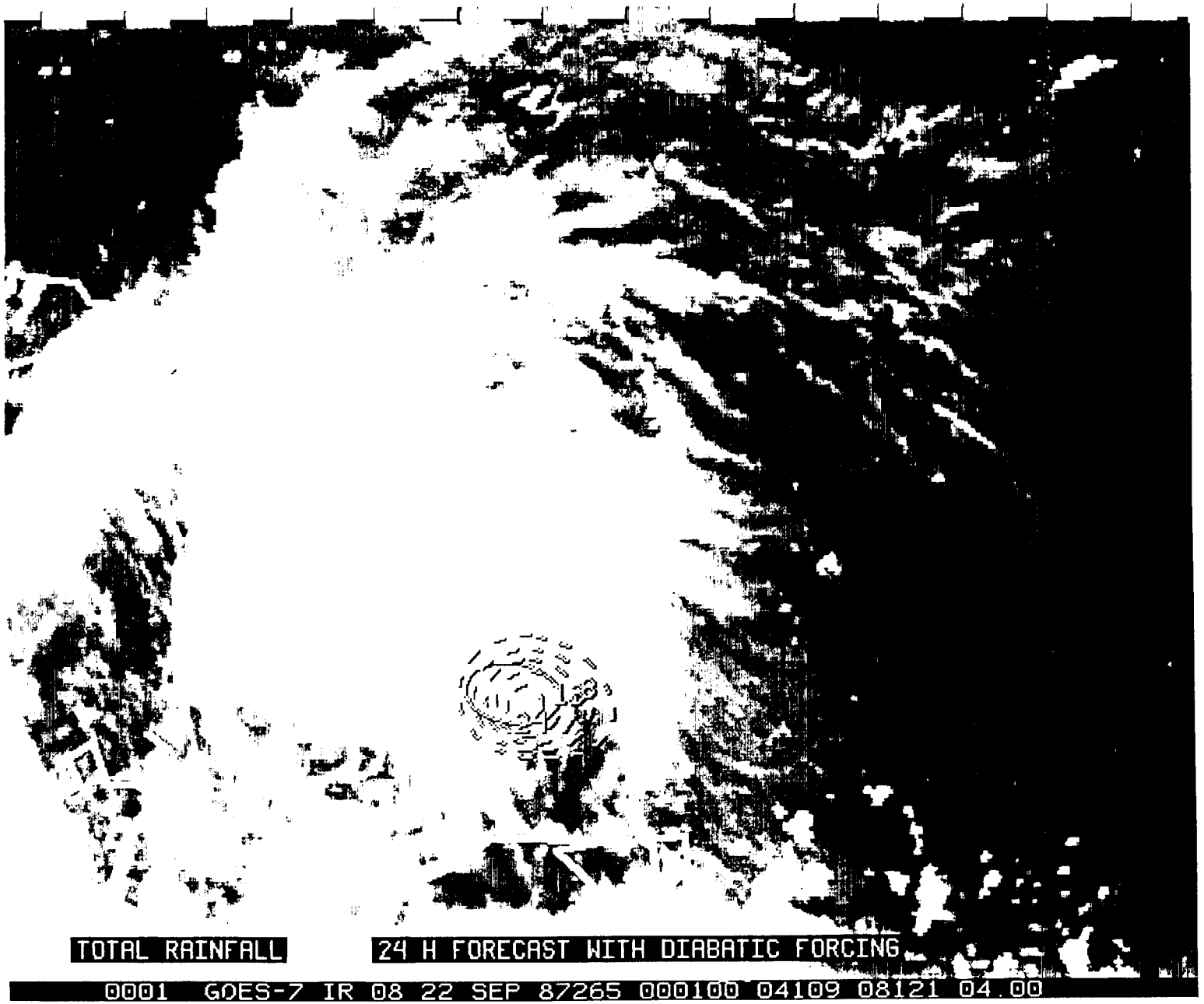
TOTAL RAINFALL
24 H FORECAST WITH DIABATIC FORCING
0001 GOES-7 IR 08 22 SEP 87265 000100 04109 08121 04.00

Fig 16

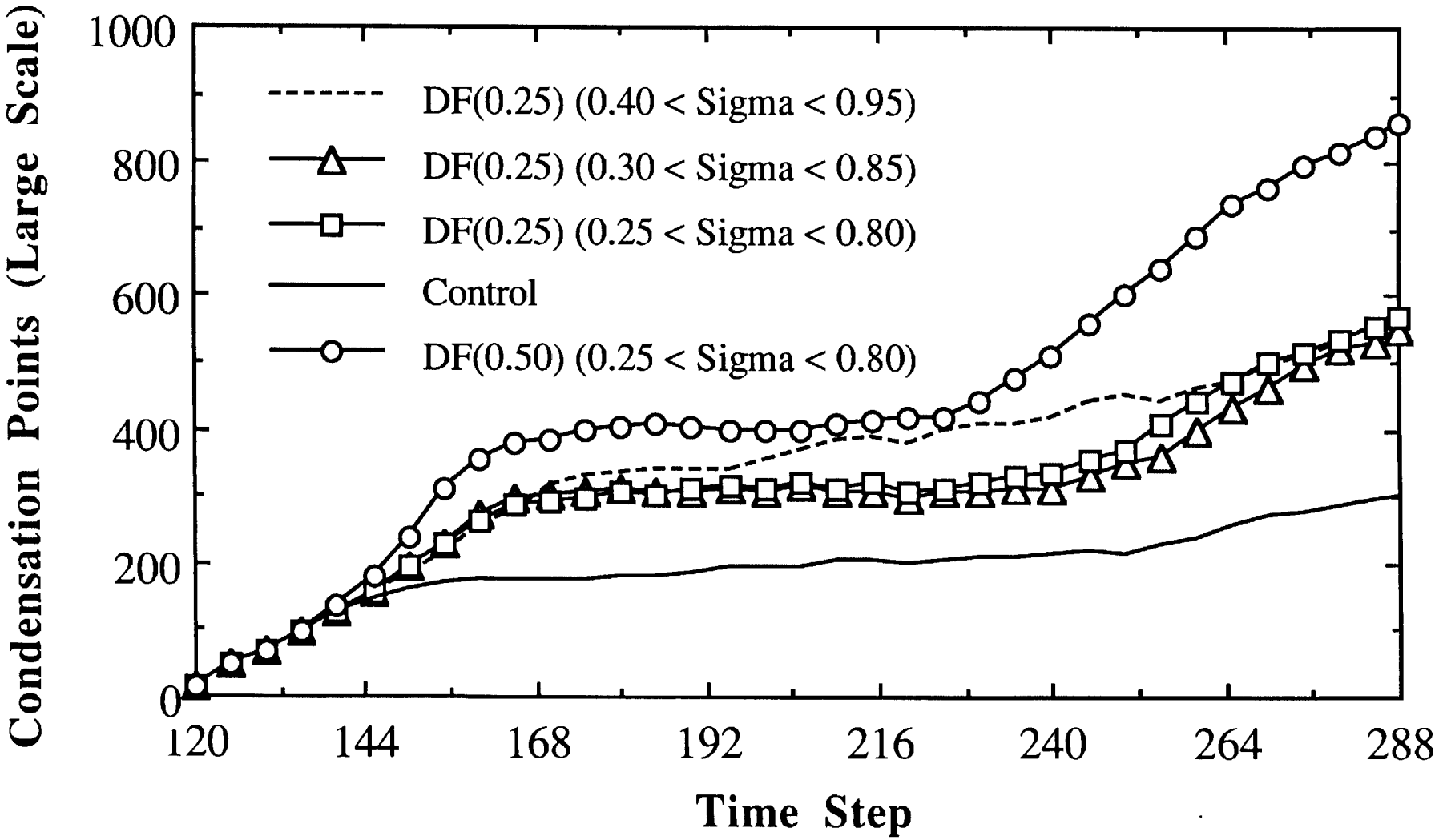
Condensation Points (Large Scale)
1000
800
600
400
200
0
120
144
168
192
216
240
264
288
Time Step
DF(0.25) (0.40 < Sigma < 0.95)
DF(0.25) (0.30 < Sigma < 0.85)
DF(0.25) (0.25 < Sigma < 0.80)
Control
DF(0.50) (0.25 < Sigma < 0.80)

Fig 11

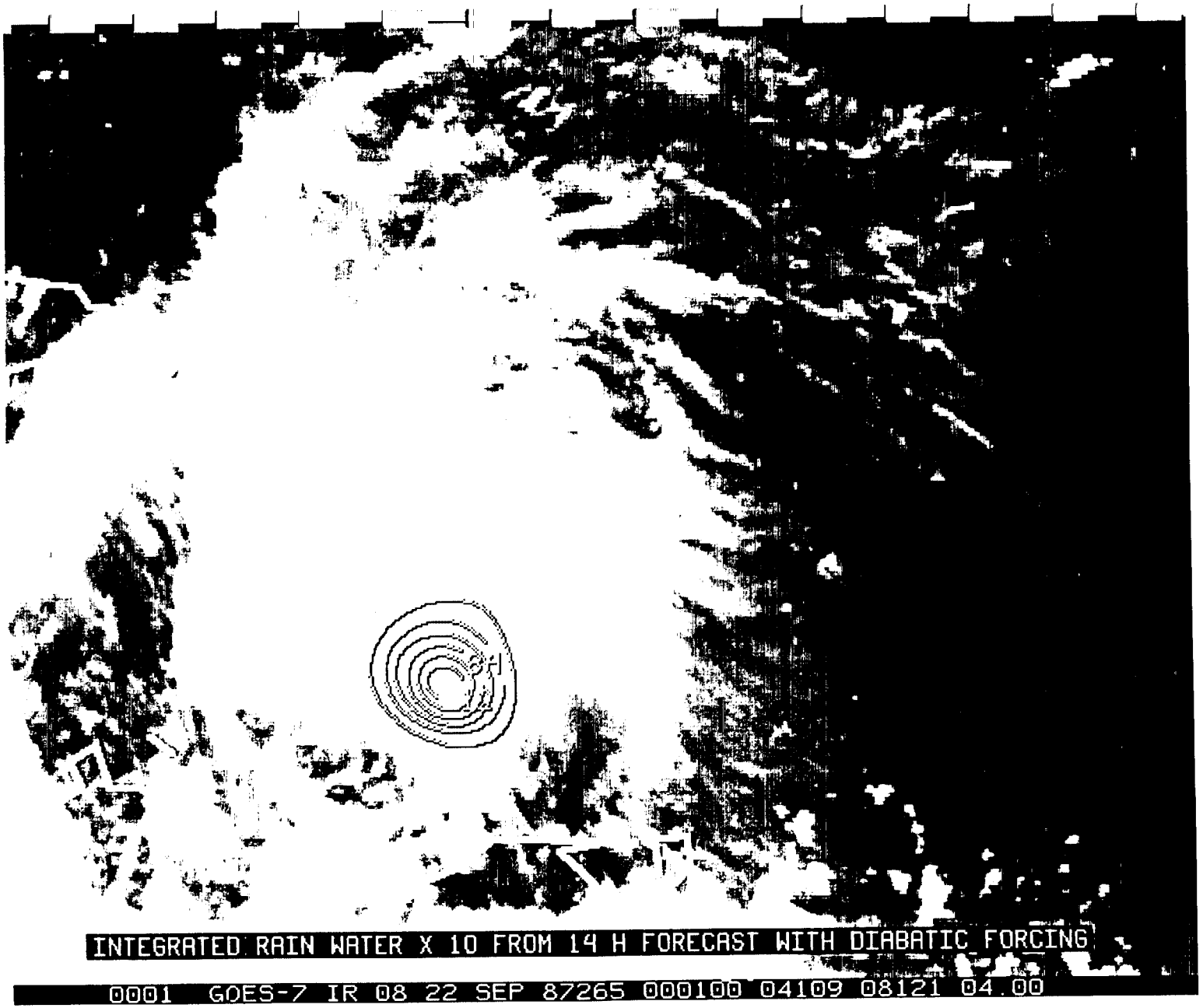
INTEGRATED RAIN WATER X 10 FROM 14 H FORECAST WITH DIABATIC FORCING
0001 GOES-7 IR 08 22 SEP 87265 000100 04109 08121 04.00

Fig 18

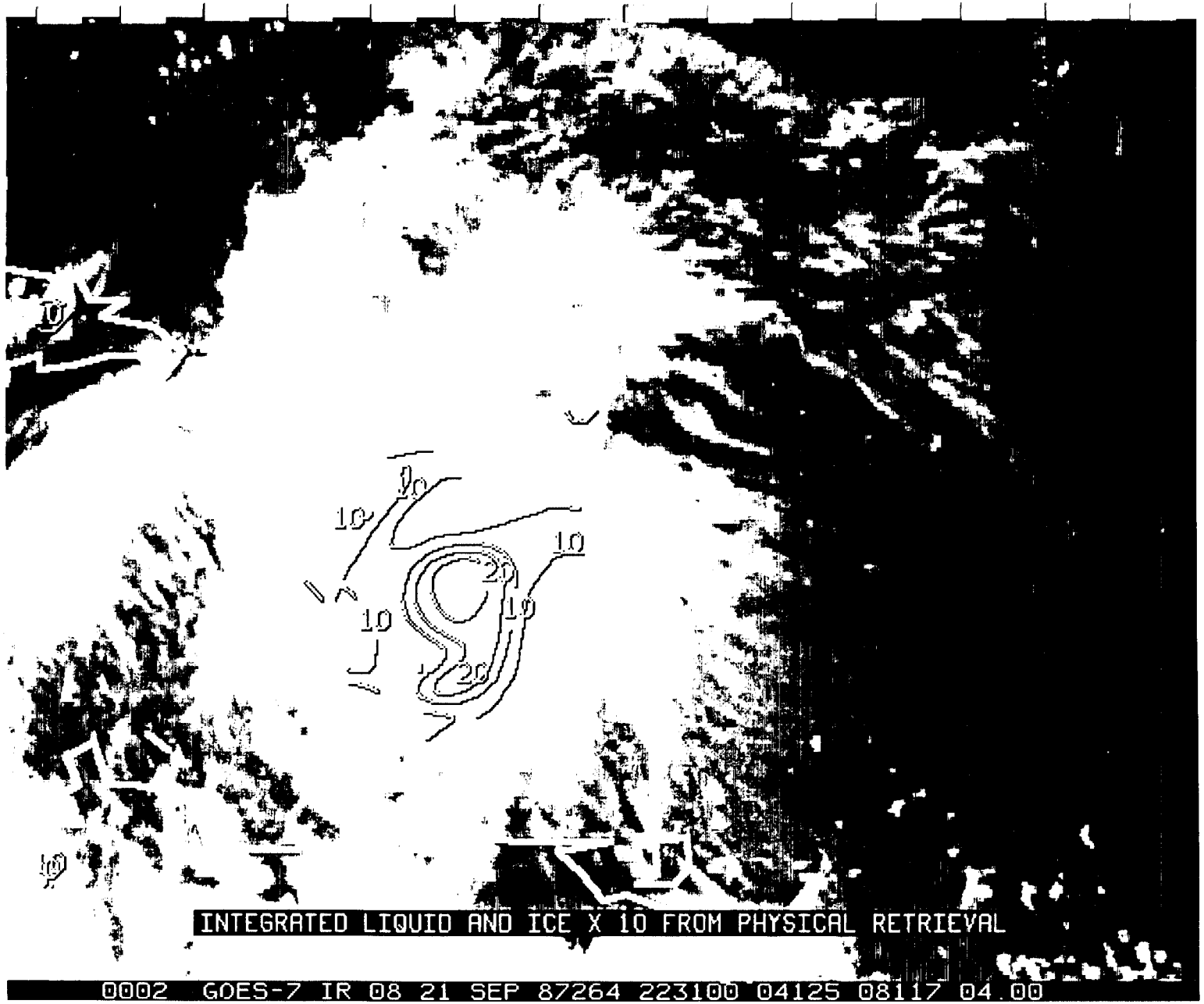
10
10
10
10
20
10
20
10
INTEGRATED LIQUID AND ICE X 10 FROM PHYSICAL RETRIEVAL
0002 GOES-7 IR 08 21 SEP 87264 223100 04125 08117 04.00

Fig 19

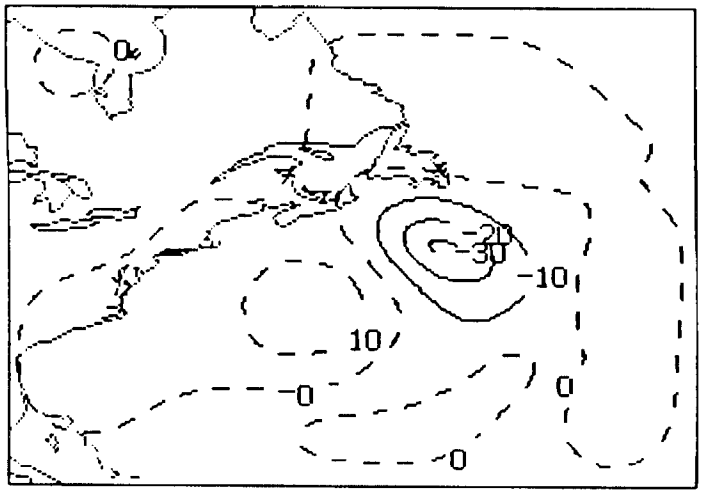

DMGP TIME 0. DAY 890120. 700. MB

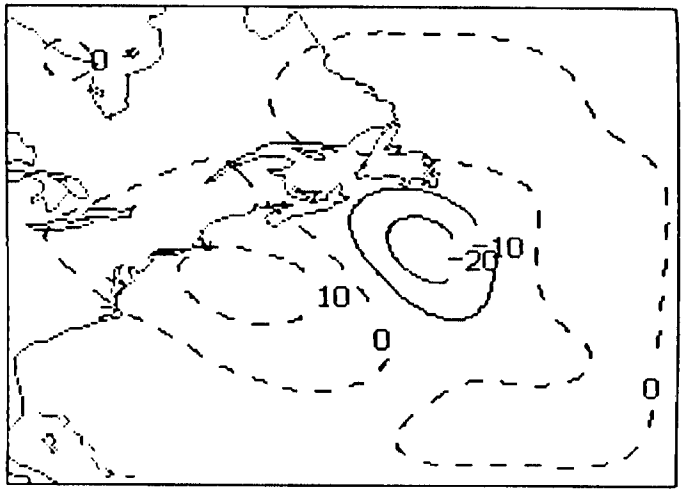

DMGP TIME 0. DAY 890120. 400. MB

ADIABATIC INITIALIZATION

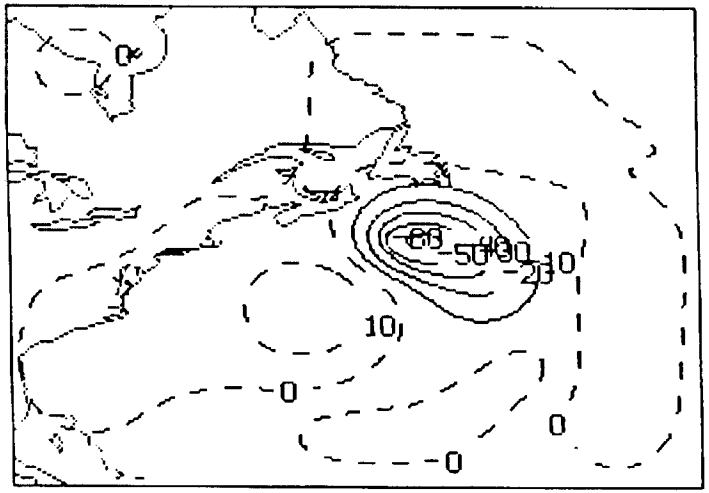

DMGP TIME 0. DAY 890120. 700. MB

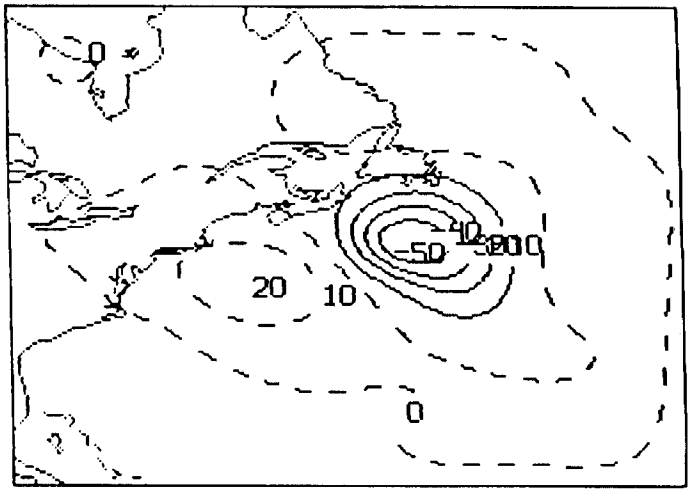

DMGP TIME 0. DAY 890120. 400. MB

DIABATIC INITIALIZATION

Fig. 20

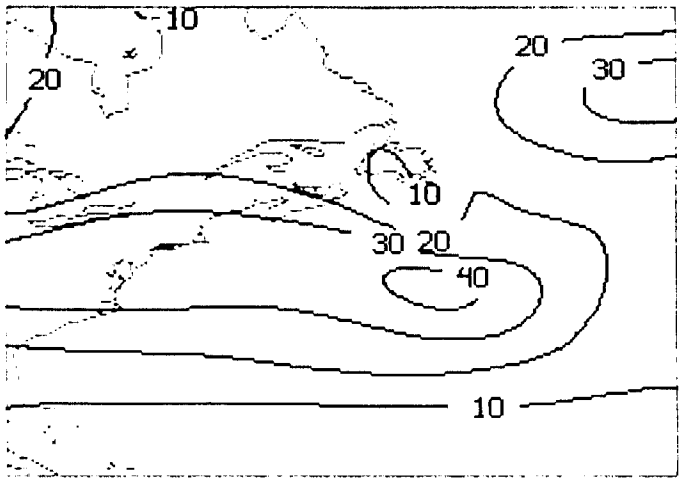

SPD (MPS) TIME 12. DAY 890120. 500. MB 24H FORECAST

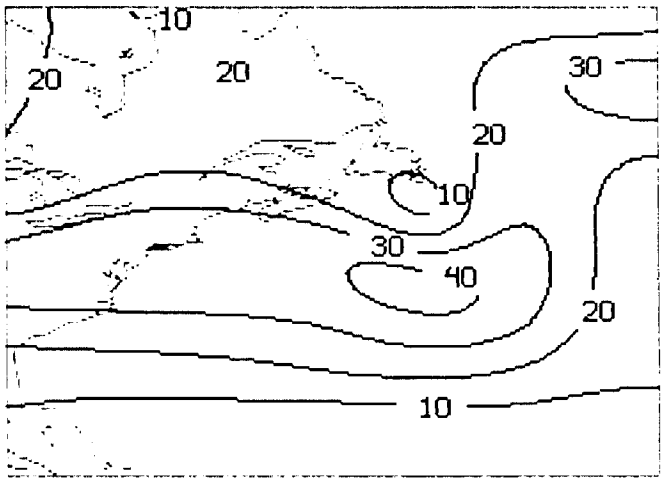

SPD (MPS) TIME 12. DAY 890120. 500. MB 12H FORECAST COLD

WINDSPEED

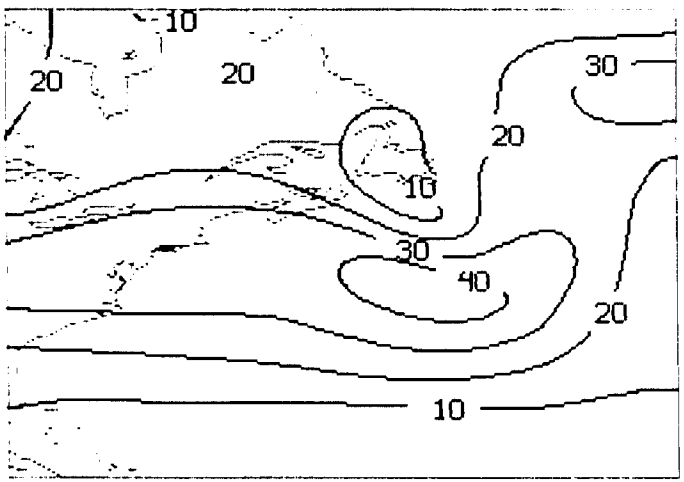

SPD (MPS) TIME 12. DAY 890120. 500. MB EXTERNALLY FORCED 2H

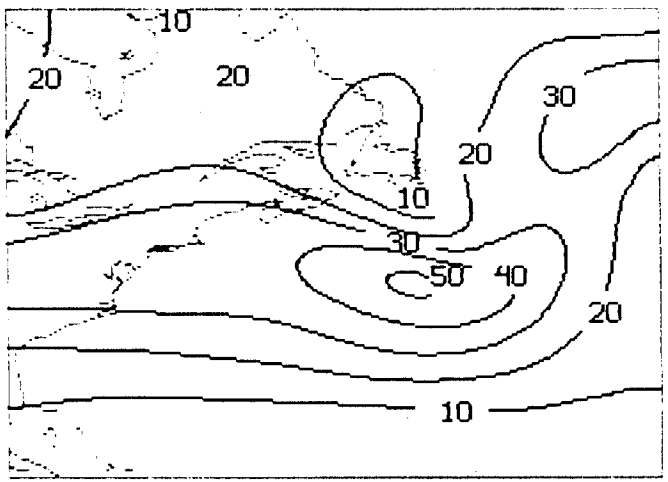

SPD (MPS) TIME 12. DAY 890120. 500. MB EXTERNALLY FORCED 4H

Fig 21

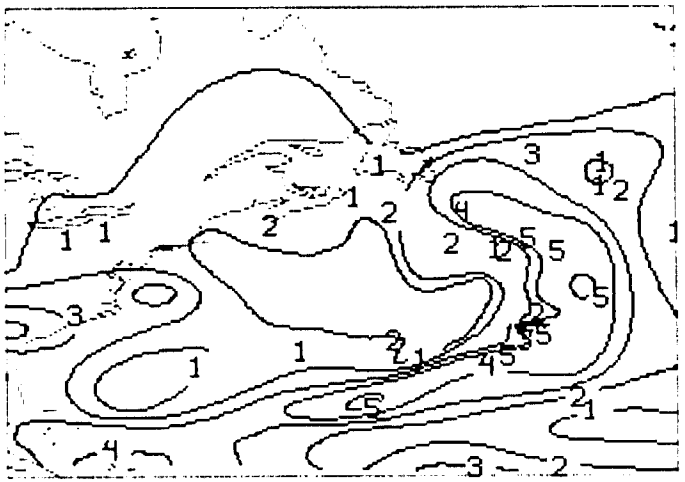

MIXR (6PK6) TIME 12. DAY 890120. 700. MB 24H FORECAST

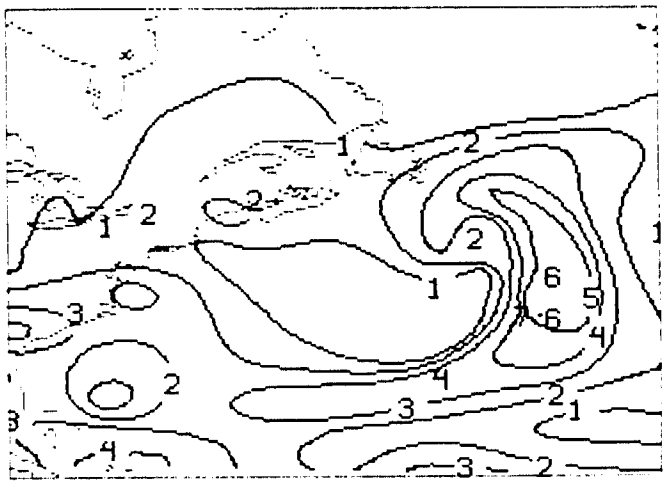

MIXR (6PK6) TIME 12. DAY 890120. 700. MB 12H FORECAST COLD

MIXING RATIO

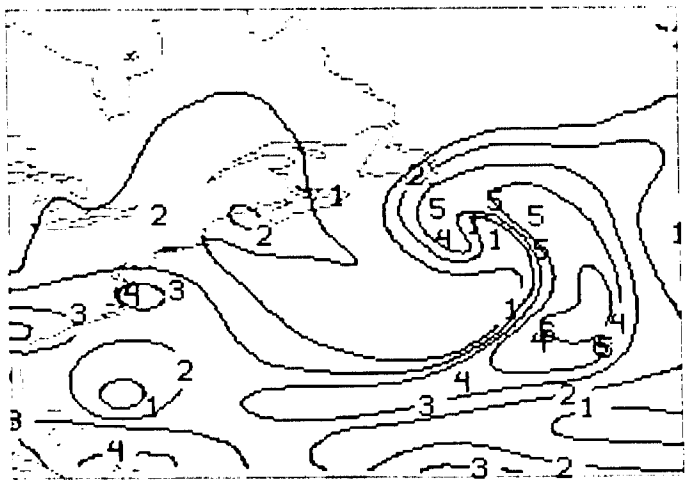

MIXR (6PK6) TIME 12. DAY 890120. 700. MB EXTERNALLY FORCED 2H

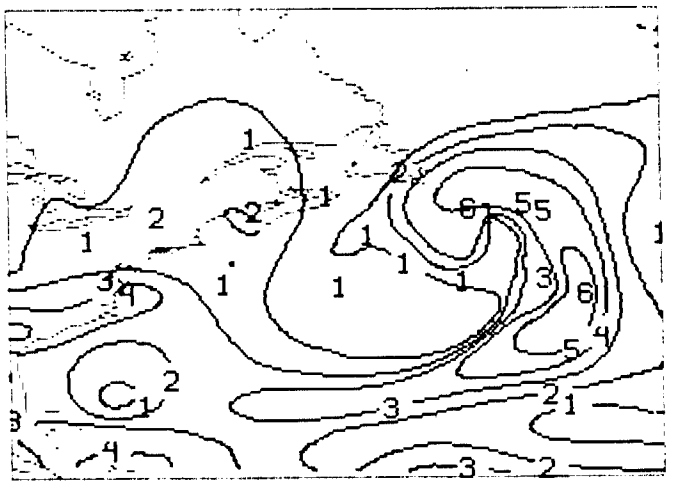

MIXR (6PK6) TIME 12. DAY 890120. 700.MB EXTERNALLY FORCED 4H

Fig 22

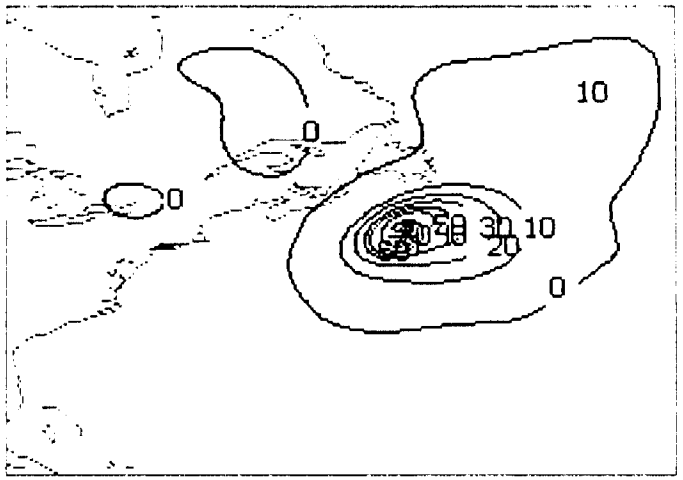

PPTN (MM) TIME 12. DAY 890120. 24H FORECAST

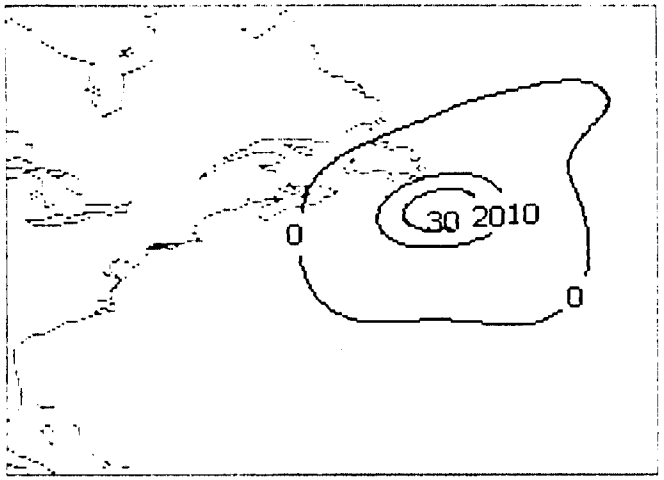

PPTN (MM) TIME 12. DAY 890120. 12H FORECAST COLD START

RAINFALL

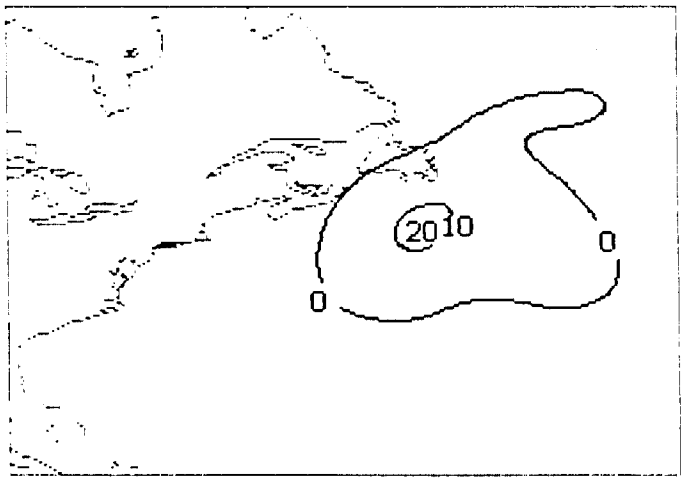

PPTN (MM) TIME 12. DAY 890120. EXTERNALLY FORCED 2H

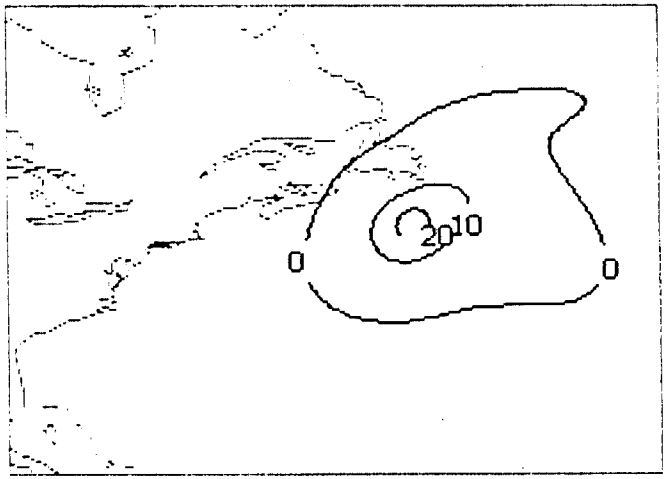

PPTN (MM) TIME 12. DAY 890120. EXTERNALLY FORCED 4H

Fig 23

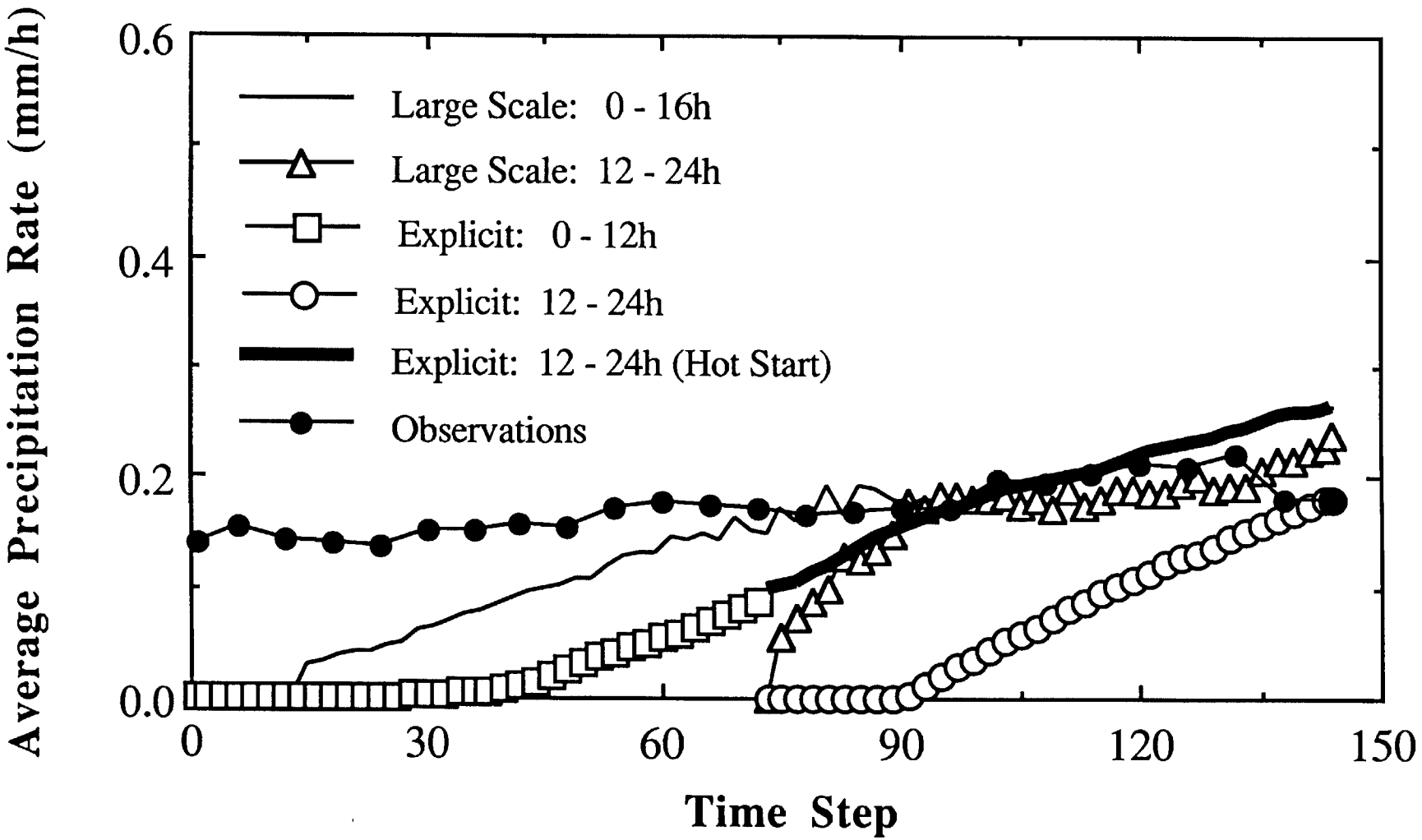
Average Precipitation Rate (mm/h)
0.6
0.4
0.2
0.0
0
30
60
90
120
150
Time Step
Large Scale: 0 - 16h
Large Scale: 12 - 24h
Explicit: 0 - 12h
Explicit: 12 - 24h
Explicit: 12 - 24h (Hot Start)
Observations

Fig 24

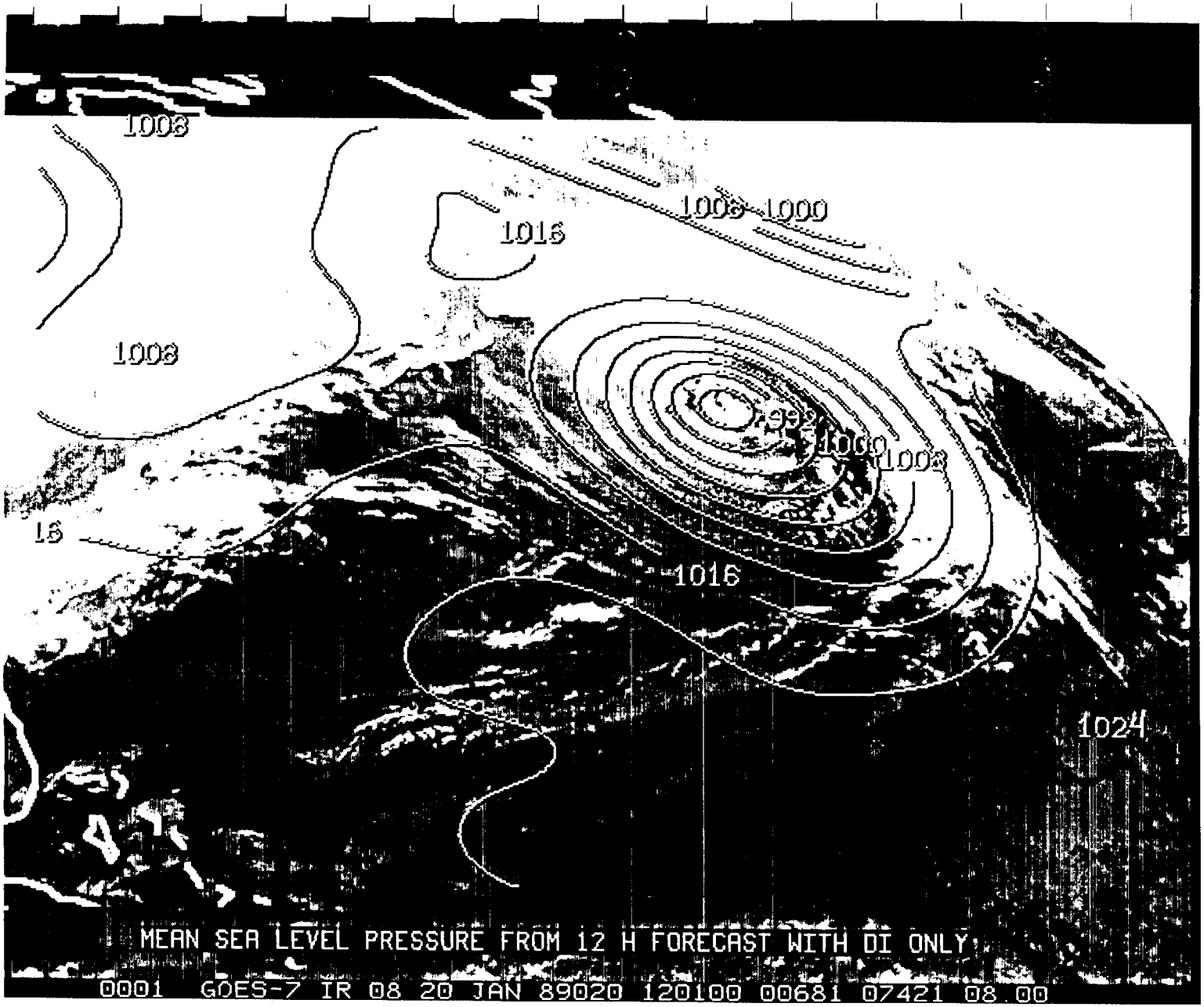
1008
1000
1016
1008
1000
1008
1016
1024
MEAN SEA LEVEL PRESSURE FROM 12 H FORECAST WITH DI ONLY
0001 GOES-7 IR 08 20 JAN 89020 120100 00681 07421 08 00

Fig 25

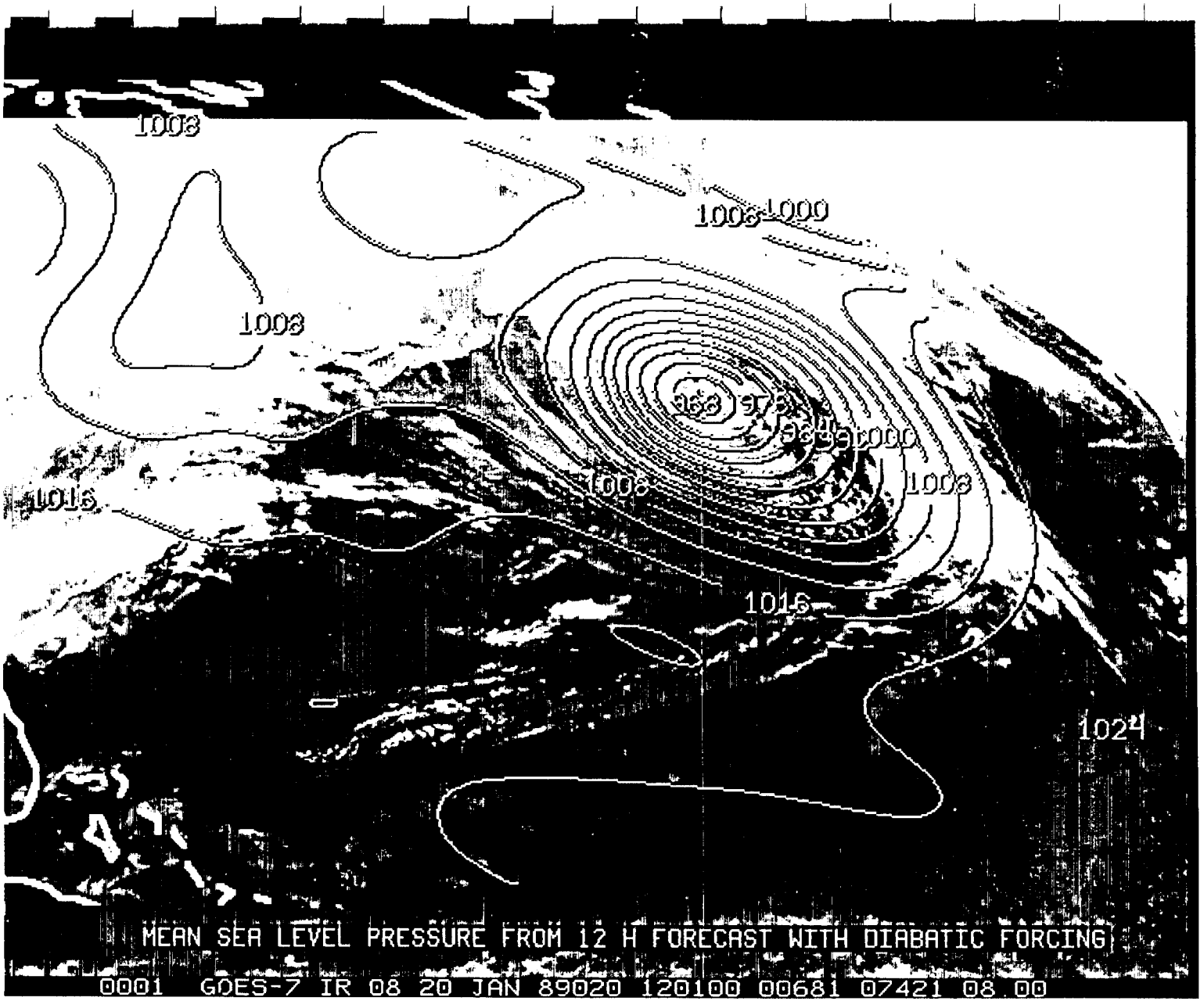
1008
1008
1000
1008
1008
1016
1008
1016
1024
MEAN SEA LEVEL PRESSURE FROM 12 H FORECAST WITH DIABATIC FORCING
0001 GOES-7 IR 08 20 JAN 89020 120100 00681 07421 08.00

Fig 3c

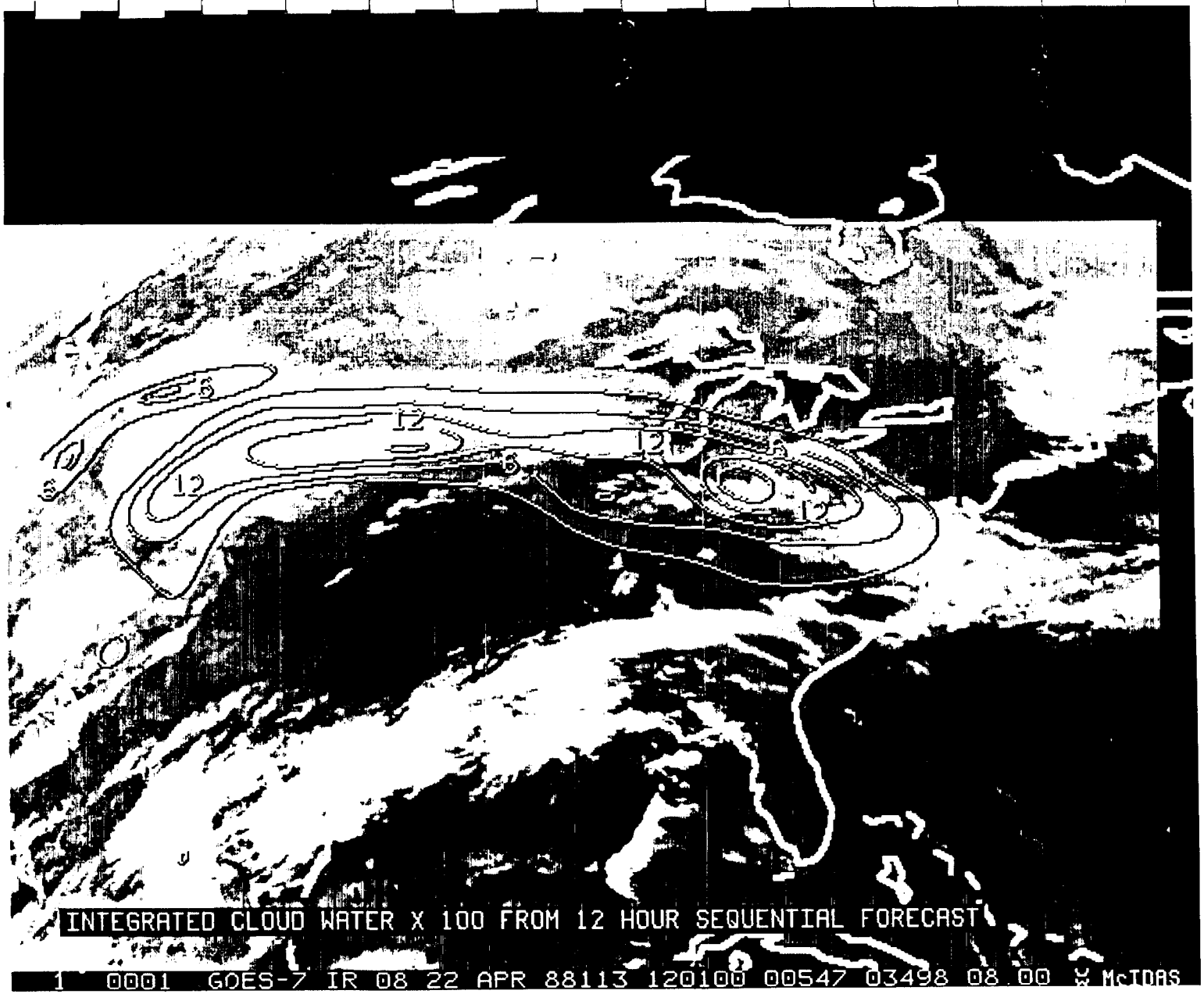
6
12
12
6
12
12
6
INTEGRATED CLOUD WATER X 100 FROM 12 HOUR SEQUENTIAL FORECAST
1 0001 GOES-7 IR 08 22 APR 88113 120100 00547 03498 08 00 McIDAS

Fig 27

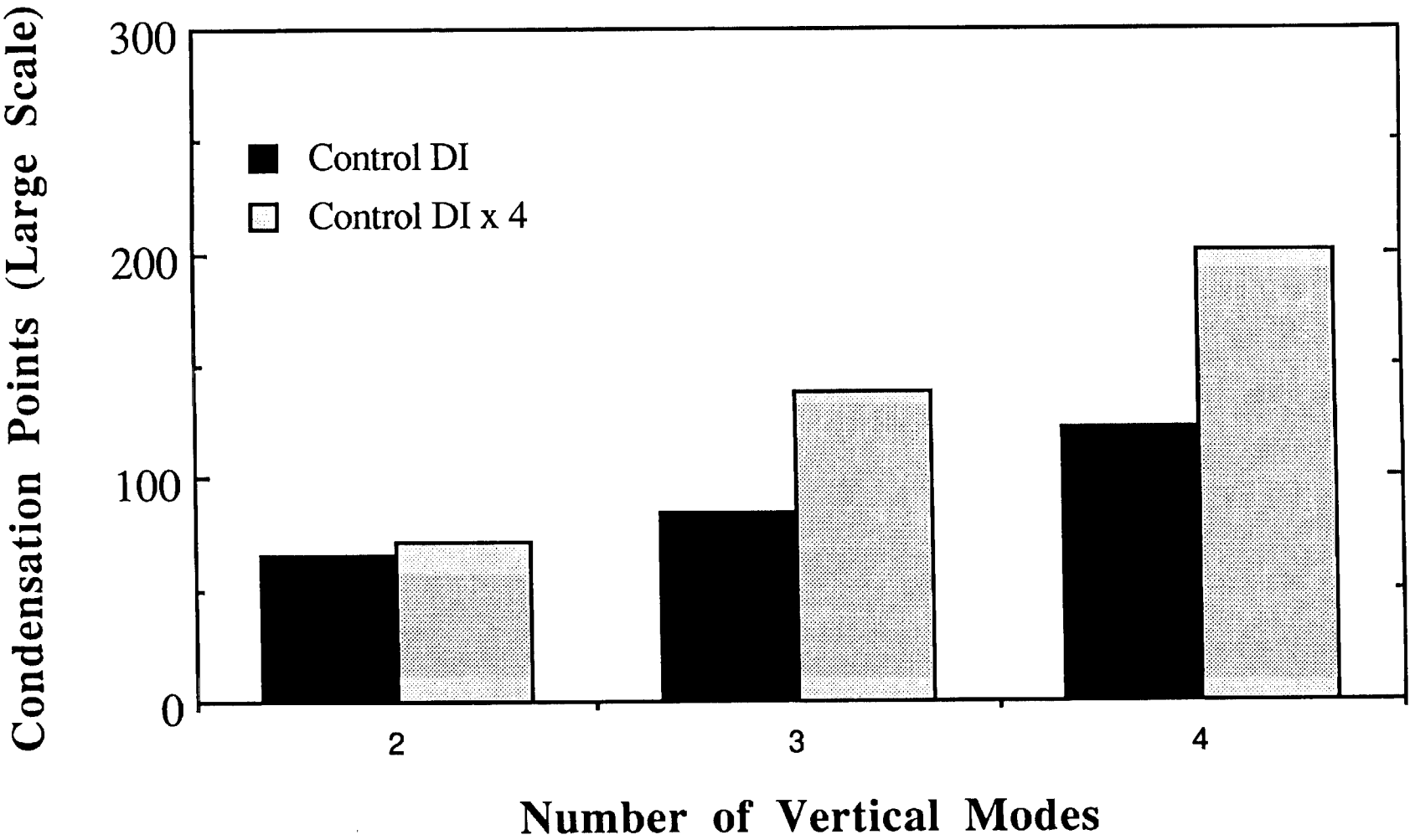
Condensation Points (Large Scale)
300
200
100
0
Control DI
Control DI x 4
2
3
4
Number of Vertical Modes

Fig 28

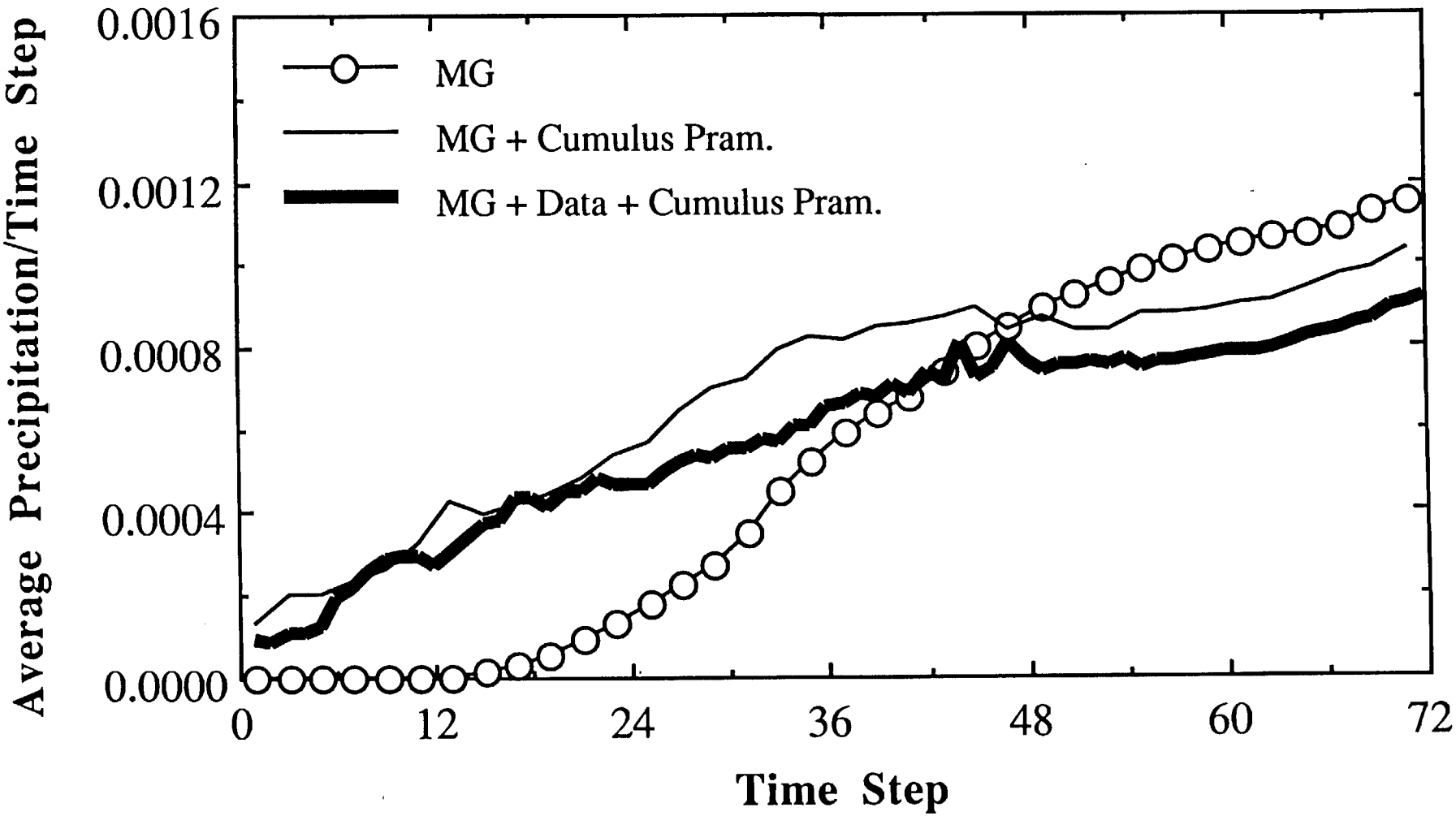
Average Precipitation/Time Step
0.0016
0.0012
0.0008
0.0004
0.0000
MG
MG + Cumulus Pram.
MG + Data + Cumulus Pram.
0
12
24
36
48
60
72
Time Step

Fig 27

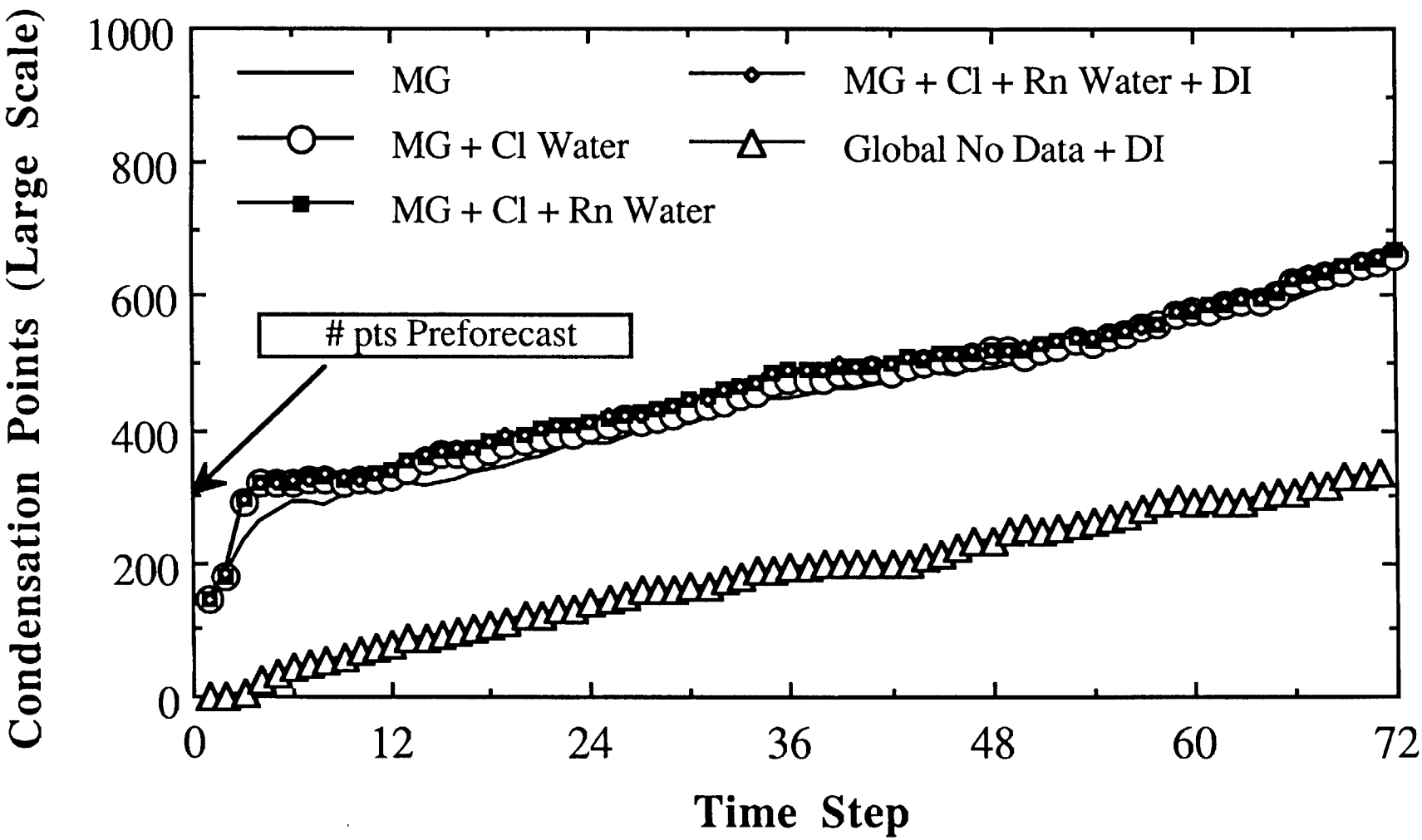
Condensation Points (Large Scale)
1000
800
600
400
200
0
0
12
24
36
48
60
72
Time Step
MG
MG + Cl Water
MG + Cl + Rn Water
MG + Cl + Rn Water + DI
Global No Data + DI
pts Preforecast

Fig 30

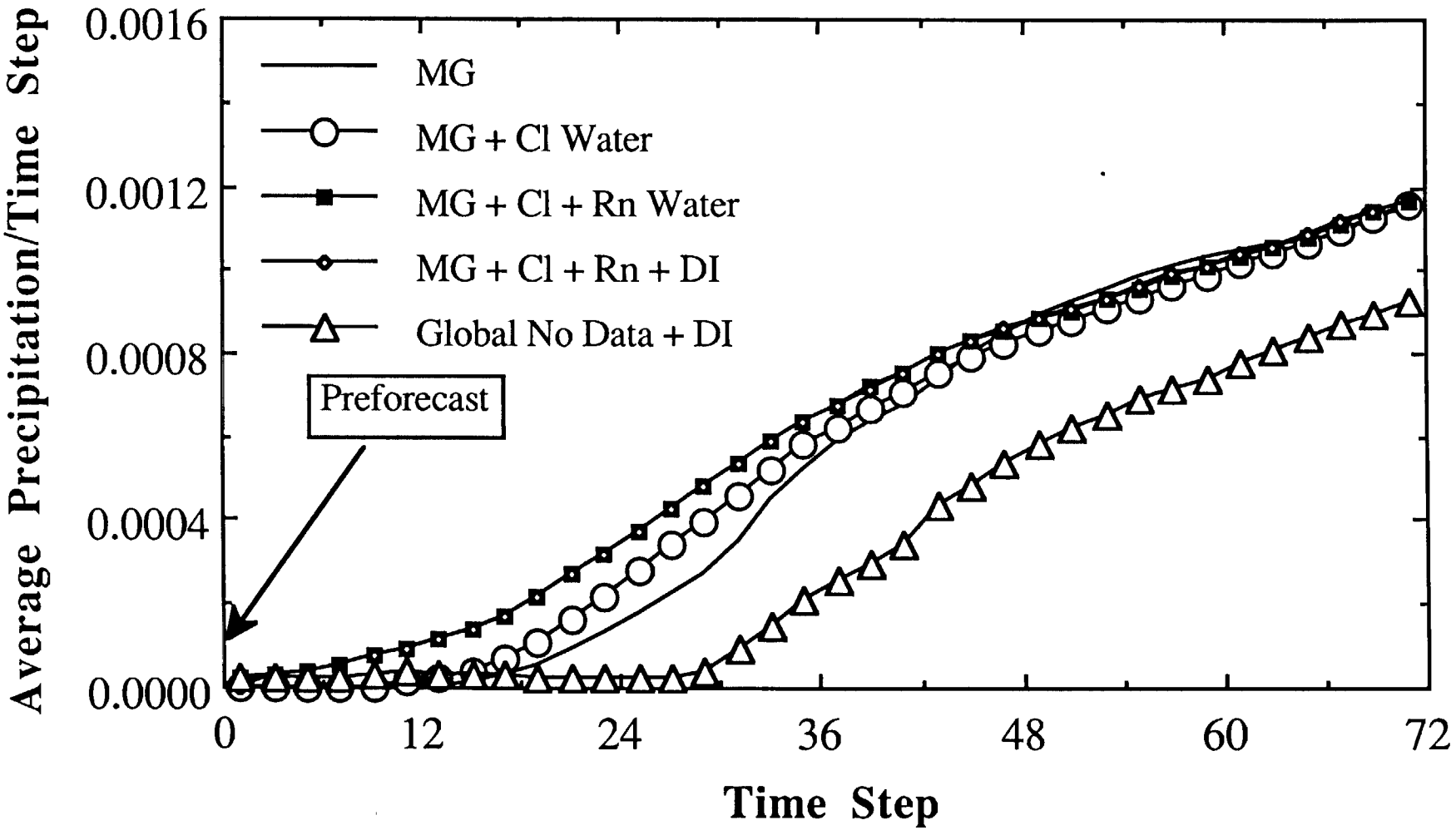
Average Precipitation/Time Step
0.0016
0.0012
0.0008
0.0004
0.0000
MG
MG + Cl Water
MG + Cl + Rn Water
MG + Cl + Rn + DI
Global No Data + DI
Preforecast
0
12
24
36
48
60
72
Time Step

Fig 31

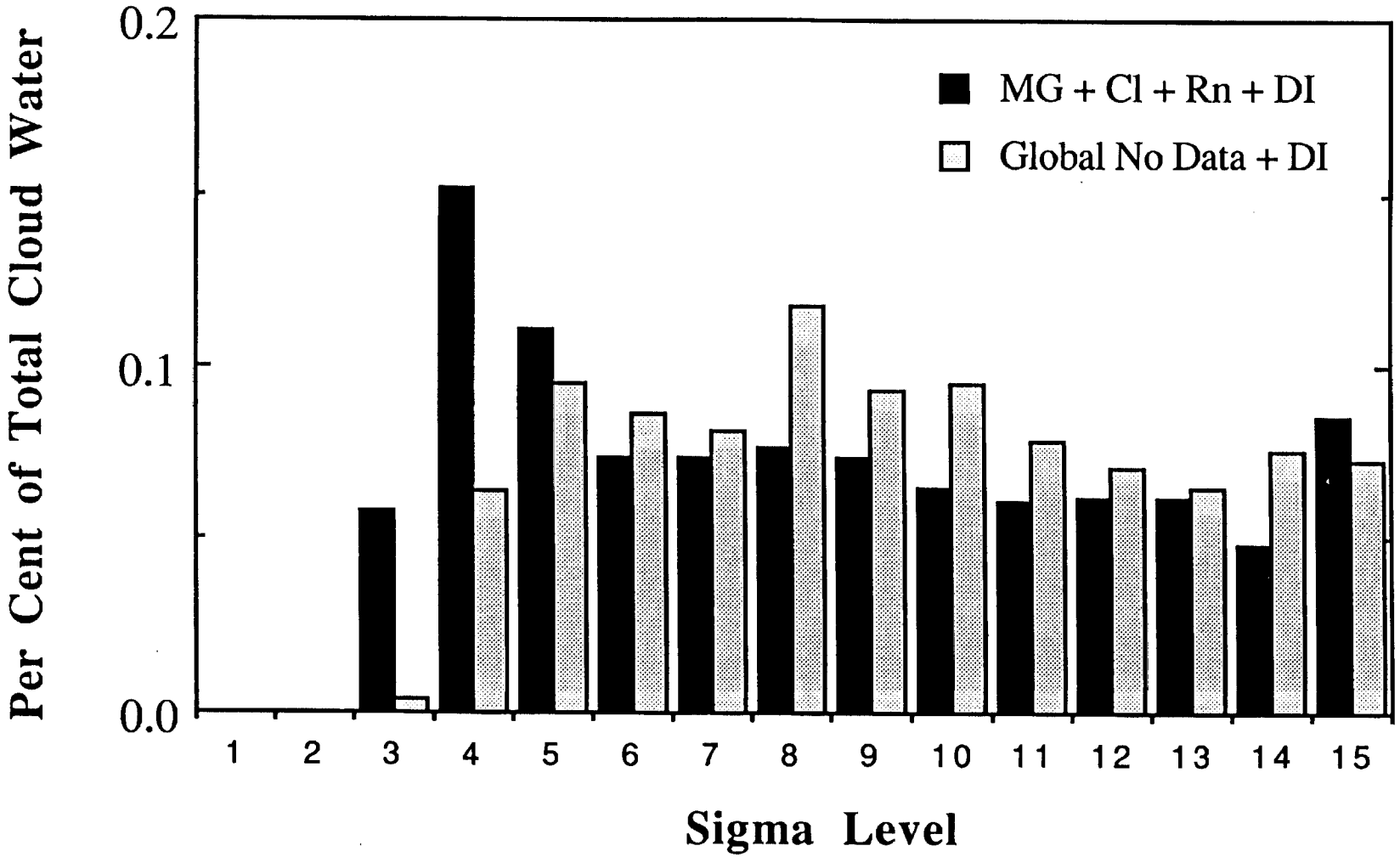
Per Cent of Total Cloud Water
0.2
0.1
0.0
MG + Cl + Rn + DI
Global No Data + DI
1
2
3
4
5
6
7
8
9
10
11
12
13
14
15
Sigma Level

Fig 32

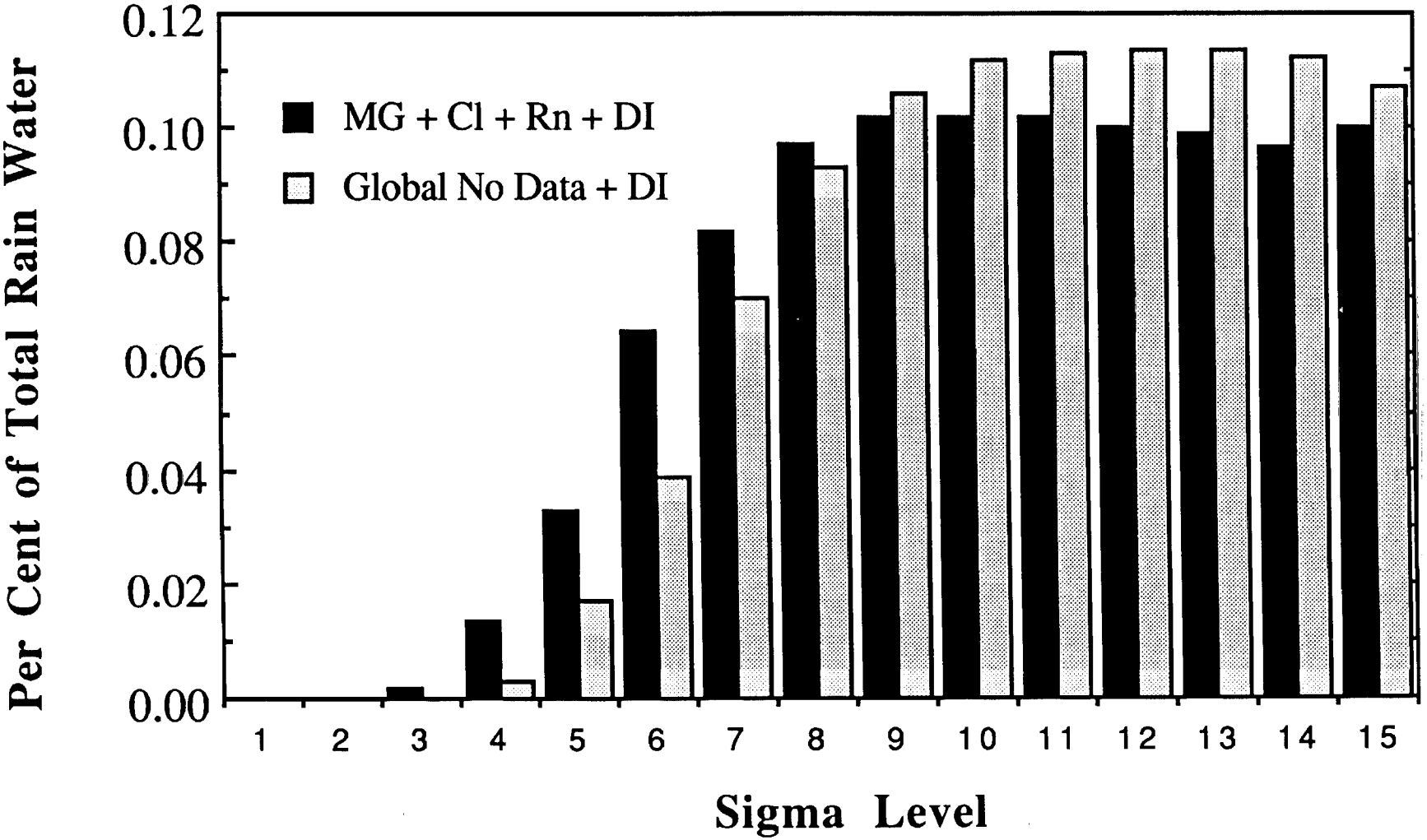
Per Cent of Total Rain Water
0.12
0.10
0.08
0.06
0.04
0.02
0.00
MG + Cl + Rn + DI
Global No Data + DI
1
2
3
4
5
6
7
8
9
10
11
12
13
14
15
Sigma Level

Fig 33

PHYSICAL RETRIEVAL OF PRECIPITATION WATER CONTENTS FROM SPECIAL SENSOR MICROWAVE/IMAGER (SSM/I) DATA-PART I: A CLOUD ENSEMBLE/RADIATIVE PARAMETERIZATION FOR SENSOR RESPONSE (report version)

by

William S. Olson and William H. Raymond

Cooperative Institute for Meteorological Satellite Studies

1225 West Dayton Street

University of Wisconsin

Madison, Wisconsin 53706

To be modified and submitted to *J. Appl. Meteor.*

PHYSICAL RETRIEVAL OF PRECIPITATION WATER CONTENTS FROM SPECIAL SENSOR MICROWAVE/IMAGER (SSM/I) DATA- PART I: A CLOUD ENSEMBLE/RADIATIVE PARAMETERIZATION FOR SENSOR RESPONSE (report version)

by

William S. Olson and William H. Raymond

1. INTRODUCTION

The physical retrieval of geophysical parameters based upon remotely sensed data requires a sensor response model which relates the upwelling radiances that the sensor observes to the parameters to be retrieved. In the retrieval of precipitation water contents from satellite passive microwave observations, the sensor response model has two basic components. First, a description of the radiative transfer of microwaves through a precipitating atmosphere must be considered, because it is necessary to establish the physical relationship between precipitation water content and upwelling microwave brightness temperature. Also the spatial response of the satellite microwave sensor (or antenna pattern) must be included in the description of sensor response, since precipitation and the associated brightness temperature field can vary over a typical microwave sensor resolution footprint.

Olson (1989) utilized a simple cuboidal, radiative transfer cloud model to describe the upwelling brightness temperatures at the Scanning Multichannel Microwave Radiometer (SMMR) frequencies. Upwelling brightness temperatures were convolved by approximate radiometer antenna patterns to simulate the antenna temperatures measured by the SMMR. More recently, in applications to aircraft microwave data, Kummerow, et al. (1989) calculated upwelling microwave brightness temperatures for a collection of vertical precipitation profiles, allowing for variations in the total vertically-integrated precipitation by scaling the selected profile. In applications of this method to Special Sensor Microwave/Imager (SSM/I) data, vertically integrated precipitation water contents were assumed to vary lognormally in space within the raining fraction of the radiometer footprint

(Kummerow, 1992). Sensor resolution effects were accomodated by preprocessing the SSM/I data using an antenna pattern matching technique (Robinson, et al., 1992). Xiang, et al. (1992) utilized three-dimensional cloud model simulations as the basis for upwelling brightness temperature calculations at the SSM/I frequencies. The retrieved profiles of cloud and precipitation profiles were those associated with modeled microwave brightness temperatures most consistent with SSM/I observations. An antenna pattern matching technique was utilized to account for the differing spatial resolution of the SSM/I channels; ref. Farrar and Smith (1992).

In the present study, a "population" of convective cells, as well as stratiform clouds, are simulated using a computationally-efficient multi-cylinder cloud model. Ensembles of clouds selected at random from the population, distributed over a 25 km x 25 km model domain, serve as the basis for radiative transfer calculations of upwelling brightness temperatures at the SSM/I frequencies. Sensor spatial response is treated explicitly by convolving the upwelling brightness temperatures by domain-integrated SSM/I antenna patterns. The sensor response model is utilized in precipitation water content retrievals, which is the subject of Part II in this series.

2. DEFINITIONS

The sensor response model describes the physical relationship between the values of geophysical parameters **P** in the earth-atmosphere system, and the antenna temperatures **TA** which the sensor measures. A single antenna temperature measurement TA may respond to variations in several geophysical parameters at different locations; therefore the response model is written $\mathbf{TA(P)}_{mod}$ to represent this multivariate dependency.

It is assumed that the field of geophysical parameters **P** over the sensor swath can be represented by an array of values at discrete grid locations. The gridded domain for SSM/I retrievals is illustrated in Fig. 1. Rectangular grid "boxes" are defined on the grid, such that the center of each box coincides with the earth location of an all-channel antenna

temperature measurement from the SSM/I. The boxes are oriented along the SSM/I A-scans (which contain the all-channel measurements) at a regular spacing of 25 km. Since the cross-scan separation of succeeding A-scan lines varies along the scan line, the cross-scan dimension of the grid boxes also varies, with a maximum dimension of 25 km in the center of the swath, and decreasing towards swath edge. In the discretization of the antenna patterns (Section 3) and brightness temperature fields (Section 4), the variation of the grid box dimension with scan position is taken into account.

In the grid system depicted in Fig. 1, an element of $\mathbf{TA(P)}_{mod}$ is defined by

$$TA(P)_p = A_c^T\, TB(P)_p + A_x^T\, TB(P)_{p'} + \delta_p\, Tbb, \qquad (1)$$

where A_c and A_x are the co- and cross-polarized antenna patterns of the radiometer, $\mathbf{TB(P)}_p$ and $\mathbf{TB(P)}_{p'}$ are the modeled brightness temperatures in the polarization p and orthogonal polarization p' with respect to the plane of polarization of the measurement, and δ_p is the fraction of the radiometer feedhorn pattern not subtended by the antenna. Tbb is the cosmic background radiance (2.7 K). Each antenna temperature is modeled as the convolution of the upwelling brightness temperature field by the spatial response pattern of the sensor (see section 3 below). In this way, measurements at different channel frequencies or from different sensors which have different sampling / spatial resolution can be accommodated.

In the following sections, the components of the sensor response model, Eq. (1), are described.

3. SENSOR SPATIAL RESPONSE FUNCTIONS

SSM/I measurements are diffraction-limited because the channel wavelengths (1.55 cm to 0.35 cm) are not small in comparison to the antenna dimensions (61 cm x 66 cm); from Hollinger (1991). Aperture diffraction effects cause the breadth of the sensor antenna

patterns to decrease with increasing frequency. The result is a large variation in the effective spatial resolution of the SSM/I.

Measurements of the SSM/I antenna patterns and a detailed description of the SSM/I scan geometry were provided by Poe (1988). Based upon this information, the co- and cross-polarized SSM/I antenna patterns at the earth's surface are calculated for each SSM/I scan position and channel. The patterns are then area-integrated over each grid box in the swath grid and then normalized over all grid boxes to yield spatial response functions. Thus, the sensor spatial response functions $\mathbf{A_C}$ and $\mathbf{A_X}$ give the mean response, for each SSM/I measurement, to brightness temperatures upwelling from each grid box in the swath grid of Fig. 1. Representative normalized spatial response functions at 19.35, 37, and 85.5 GHz are illustrated in Fig. 2. It may be noted from the figure that the sensor spatial response at 19.35 GHz is spread over several grid boxes in the swath grid, indicating relatively low spatial resolution at the grid scale (25 km). In contrast, the spatial response at 85.5 GHz is concentrated almost entirely in a single grid box, indicating high spatial resolution. The spatial response patterns are included in the sensor response model to accomodate the disparity in spatial resolution exhibited by the different channels of SSM/I.

4. CLOUD ENSEMBLE/RADIATIVE MODEL

The relationship between the geophysical parameters **P** and the brightness temperatures $\mathbf{TB_p}$ and $\mathbf{TB_{p'}}$ upwelling from an individual grid box is described using a cloud ensemble/radiative model. The model geometry is illustrated in Fig. 3. The horizontal dimensions of the domain are 25 km x 25 km, the nominal grid box dimension, with a vertical dimension of 20 km. Typically, within a region of these dimensions, an array of convective clouds as well as anvil-type or stratiform cloud may coexist. Both types of cloud are simulated in this study, with a brief summary given below.

4.1 Model Description

Individual cloud simulations are performed using two versions of the multi-cylinder cloud model of Ridout (1991, 1993). Ridout's original model (ref. 1991, 1993) is utilized for convective cloud simulations. It is a time-dependent, non-hydrostatic cloud model which utilizes six concentric, quasi-cylindrical regions to represent the horizontal exchange of heat and moisture between the core region of the modeled convective cell and its immediate environment. The vertical momentum equation is represented explicity only in the innermost cylinder (core) of the cloud model, thereby reducing computational requirements substantially. The model includes a parameterization for the effects of vertical wind shear on the entrainment/detrainment of liquid water and other cloud variables.

The treatment of microphysics follows the development by Lin, et al. (1983), with some modifications by Ferrier (1988). The model predicts the distributions of cloud water and cloud ice, rain, snow, and graupel/hail at levels separated by 300 m in the vertical, averaged over each cylindrical region.

A model cloud is initially forced by a prescribed sub-cloud vertical velocity distribution over a prescribed period (900 s in the current study), after which time the forcing is removed and the cloud continues to develop according to model dynamics. This method of initiation is used to simulate gust-front forcing of convective clouds. Cloud development is also controlled by a prescribed minimum updraft radius which is the radial dimension of the updraft (third cylinder) at midlevels in the troposphere. The radii of the other cylinders are all scaled according to the prescribed updraft radius.

A second version of the Ridout (1992) model is developed to simulate stratiform anvil-type precipitation distributions in this study. In this version of the model, the five surrounding cylinders are eliminated, and it is assumed that the distributions of all cloud variables both inside and outside the remaining cylinder are identical. In other words, a strictly one-dimensional simulation is performed. In addition, the vertical velocity distribution is prescribed to be a double-parabolic profile, with a downdraft below the

freezing level and an updraft aloft. This type of vertical velocity profile is generally consistent with observations documented by Leery and Houze (1979), Gamache and Houze (1982), Marks and Houze (1987), and Rutledge and Houze (1987), who observed mesoscale updrafts and downdrafts in several tropical and midlatitude storms. The Lin/Ferrier cloud microphysical parameters are altered to reflect the variability of particle size distributions noted by Houze, et al. (1979) and Stewart, et al. (1984). Stratiform cloud simulations are performed by integrating the model forward in time until equilibrium distributions of all cloud variables are obtained, usually after 10 hours of simulation time.

4.2 Cloud Environment

The cloud environment for both convective and stratiform cloud simulations is taken from the GATE Day 261 rawinsonde profile; ref. Ferrier and Houze (1989). Profiles of pressure, temperature, water vapor mixing ratio, and horizontal wind components are interpolated to levels at 150 m altitude spacing in the Ridout model.

4.3 Generation of Ensembles - Convective Clouds

By varying the minimum updraft radius and the basal updraft vertical velocity in the Ridout model, a variety of clouds ranging from shallow to deep convection are simulated. Combinations of eight cloud radii between 0.5 and 5 km and four basal updrafts between 2 and 8 m/s are used to generate 32 different cloud simulations. For each cloud simulation an effective cloud lifetime is computed. For the purpose of this study the lifetime of a simulated cloud is defined as the period over which the average reflectivity of the cloud core volume (a cylindrical region 2.43 km in radius and 9.49 km in height) exceeds 30 dBZ. Effectively, these are the cloud radar echo lifetime criteria that were used by López (1977) in his study of tropical clouds. The core volume dimensions are designed to simulate the radar volume of the airborne APS-20 radar utilized in López' study.

Based upon the radar echo lifetime statistics compiled by López (1977), a "population" of simulated clouds is created. In López' study, tropical clouds were found to have echo lifetimes that were lognormally distributed. A plot of this observed lifetime

distribution is reproduced in Fig. 4. A simulated cloud with a given lifetime is assumed to occur with the same relative frequency as a cloud with the same observed lifetime in López' radar study.

A random number generator is utilized to select simulated clouds from the population and create an ensemble within the 25 km x 25 km model domain (see Fig. 3). Once a cloud is selected from the population, a cloud lifestage is also randomly selected. The cloud from that stage of the simulation is then positioned at random within the model domain. Another cloud is then selected at random from the assumed population, and the procedure is repeated. The only restriction on cloud placement is that the updrafts of no two simulated clouds may overlap. By varying the number of clouds selected for the ensemble, a wide range of cloud configurations with different water and ice contents can be simulated. In this study, 350 different cloud ensembles containing between 8 and 56 clouds are created using the procedure outlined above. One such ensemble based upon 48 simulated clouds is depicted in Fig. 5. In the figure, image intensity is proportional to the slant-path integrated water contents at the SSM/I viewing incidence angle (53.1 degrees from zenith).

4.4 Generation of Ensembles - Stratiform Clouds

Different stratiform clouds are generated by varying the amplitude of the prescribed updraft and downdraft distributions. Following the diagnostics studies of Gamache and Houze (1982), in which the magnitudes of updraft and downdraft velocities were estimated for tropical anvils, a range of representative updraft and downdraft amplitudes are selected. Updraft amplitudes are varied from 0.05 to 0.50 m/s, while downdraft amplitudes are varied from 0.00 to -0.50 m/s, to create a total of 42 stratiform simulations.

4.5 Radiance Calculations

Both convective and stratiform cloud ensembles are located within the model domain depicted in Fig. 3. The 25 km x 25 km x 20 km model domain is subdivided into a grid with a horizontal grid spacing of 0.500 km, and a vertical grid spacing of 0.375 km.

Pressure, temperature, water vapor density, and the equivalent water contents of precipitating and non-precipitating particles from the simulated clouds are interpolated to grid locations within the domain. In addition, cloud latent heating rates are evaluated at grid locations. The average surface rainfall rate over the domain is also computed.

The cloud and environmental parameters at each grid location are used to calculate the associated microwave radiative properties (i.e., the extinction coefficients, single-scatter albedoes, and asymmetry factors). Molecular oxygen and water vapor extinction coefficients are computed using the Liebe (1985) model. Microwave radiative parameters for precipitating liquid and ice hydrometeors are computed using the formulae of Kummerow and Weinman (1988). Rayleigh theory is employed to calculate the extinction coefficients of nonprecipitating cloud particles. At the base of the grid a surface skin temperature and microwave emissivities characteristic of both land and ocean surfaces are assigned. The downwelling cosmic background brightness temperature (2.7 K) is specified at the top of the model domain.

A forward radiative transfer calculation is performed to determine the distribution of microwave brightness temperatures upwelling from each cloud ensemble domain. A radiative transfer solution based upon Eddington's second approximation is utilized to accomodate the multiple scattering effects of precipitating hydrometeors at microwave frequencies. Brightness temperatures are computed at the SSM/I frequencies (19.35, 22.235, 37, and 85.5 GHz) in both vertical and horizontal polarizations at an incidence angle of 53.1 degrees. Since radiance paths at oblique incidence can exit the sides of the model domain, it is assumed that the domain, and all cloud and environmental properties, are periodic in the horizontal.

Fields of brightness temperatures upwelling from the convective cloud ensemble of Fig. 5 are depicted in Fig. 6 (over a low-emissivity background characteristic of the ocean), and in Fig. 7 (over a high-emissivity backgound characteristic of a land surface). Comparing the figures, it may be noted that the ocean background provides a good

radiative contrast to regions of greater emission from liquid precipitation, while the higher-emissivity land background provides less contrast. Over either background, the low brightness temperatures at 85.5 GHz associated with scattering by precipitating ice particles are evident. The basic differences between liquid and ice precipitation signatures provide the motivation for the radiative parameterization described in the next section.

Ensemble-average, horizontally-polarized brightness temperatures are plotted against the corresponding ensemble-average slant path-integrated precipitating liquid water contents for the four SSM/I frequencies in Fig. 8. The brightness temperature calculations in these plots utilize an emissivity of 0.3, characteristic of an ocean surface. Both convective and stratiform ensemble calculations are included in the figure. Plotted numbers in the figure are the ensemble-average slant-path integrated ice water contents, thresholded at integral values.

It may be noted from the figure that there is a significant spread of brightness temperatures corresponding to a given liquid precipitation path, due to variations in ice water content, precipitation area, non-precipitating cloud amount, and cloud geometry. The scattering effect of ice precipitation is most obvious at 37 and 85.5 GHz, leading to somewhat lower brightness temperatures for a given precipitating liquid path. At 85.5 GHz, the stratiform ensembles yield brightness temperatures which are significantly lower than the convective ensemble brightness temperatures, due to the relatively high amounts of precipitating ice (relative to precipitating liquid) in the stratiform clouds. The focus of the next section will be to parameterize the ensemble-average upwelling brightness temperatures as functions of the precipitating liquid and ice paths.

5. RADIATIVE PARAMETERIZATION OF CLOUD ENSEMBLE/ RADIATIVE CALCULATIONS

The cloud ensemble/radiative calculations provide a fairly detailed and accurate description of the upwelling brightness temperature field for a given cloud ensemble configuration. However, the sensor response model (Eq. 1) requires a functional

relationship between the grid box average brightness temperatures ($\mathbf{TB_p}$ and $\mathbf{TB_{p'}}$) and properties of the cloud field and its environment (geophysical parameters **P**). This functional relationship, or parameterization, must include a meaningful description of the precipitation field and produce an accurate representation of the detailed cloud ensemble/radiative calculations. However, since the sensor response model will ultimately be utilized in retrievals, the number of geophyical parameters **P** must be consistent with the sampling of the SSM/I. The SSM/I provides only 13 brightness temperture measurements per grid box in the swath grid of Fig. 1., and it is likely that some of the information in these measurements is redundant. Thus the number of parameters must be kept small in order to avoid ambiguous retrievals; i.e. the number of unknown parameters **P** in the retrieval must be less than the number of independent measurements. Our strategy is to select parameters which describe the mean cloud and environmental characteristics of each grid box, and then parameterize smaller scale variability.

Figures 5 through 7 illustrate the basic relationships between precipitating liquid and ice contents and upwelling microwave brightness temperatures. There is a strong correlation between the path-integrated precipitating water content and the upwelling brightness temperature at 37 GHz. The same correlation is observed in the 19.35 and 22.235 GHz simulations (not shown). At 85.5 GHz, the path-integrated precipitating ice content is strongly anticorrelated with upwelling brightness temperature.

These relationships suggest a simple parameterization for the average upwelling brightness temperature from a given swath grid box. The full three-dimensional radiative calculation is replaced by four one-dimensional calculations. The first calculation is performed for the brightness temperature upwelling from the cloud-free environment of the grid box. The second assumes that only precipitating liquid is present in the model atmosphere; the third only precipitating ice, and the fourth for a model atmosphere containing both precipitating liquid and ice. Vertical profiles of precipitating liquid and ice in the one-dimensional radiative calculations are represented by analytical curve fits to the

horizontally-averaged profiles of both the convective and stratiform cloud ensembles. Both precipitating liquid and ice equivalent water contents are given by

$$\mathrm{PLWC} = \begin{cases} 0, & z > \mathrm{zmax} \\ A \cdot \sin\left(\pi\,(z - \mathrm{zmin})/(\mathrm{zmax} - \mathrm{zmin})\right) & \\ \quad \cdot \exp\left(-\{B1 + B2/\mathrm{PLWP}\} \cdot (z - \mathrm{zmin})/(\mathrm{zmax} - \mathrm{zmin})\right), & \\ \qquad \mathrm{zmin} < z < \mathrm{zmax} & \\ 0, & z < 0 \end{cases} \tag{2}$$

Here, PLWC is the precipitating liquid or ice equivalent water content, PLWP is the slant path-integrated precipitating liquid or ice depth, zmin and zmax are the lower and upper altitude bounds of the water content profile, and B1 and B2 are fitting constants. Given the slant path-integrated precipitating liquid water or ice depth, the constant A is set such that the integrated analytical profile yields the same depth. The constants zmin, zmax, B1, and B2 are all optimized to yield the minimum mean-square difference between the water content profiles generated by the cloud ensembles and those calculated using Eq. (2). Values of the adjustable parameters and statistics of the analytical profile approximation are listed in Table 1.

The mean profiles and analytical curve fits for convective liquid and ice precipitation are shown in Figs. 9 and 10, respectively. Similar curve fits are obtained for the stratiform cloud ensembles. The mean error standard deviation in the estimated water contents from the analytical profiles is about 0.03 g/m^3.

The four one-dimensional calculations are combined in proportion to the fractional coverage of liquid and ice precipitation that are observed along the oblique viewing angle of the SSM/I. Although it is assumed that precipitating liquid and ice occupy specified fractions, no assumption is made concerning the relative positions of the liquid and ice

fractions with respect to one another inside the grid box. If f_l and f_i are the fractions of precipitating liquid and ice, respectively, then the parameterized upwelling brightness temperature at a given frequency and polarization is given by

$$TB(P) = (1 - f_l)(1 - f_i)\,TB_c + f_l(1 - f_i)\,TB_l + (1 - f_l)\,f_i\,TB_i + f_l\,f_i\,TB_{li}\,. \quad (3)$$

Here, TB_c, TB_l, TB_i, and TB_{li} are the brightness temperatures upwelling from a cloud-free model atmosphere, an atmosphere containing only precipitating liquid, an atmosphere containing only preciptating ice, and an atmosphere containing both precipitating liquid and ice, respectively.

Although Eq. (3) is a fairly good approximation to the brightness temperatures upwelling from the stratiform cloud ensembles, the small-scale variability of precipitation water paths in the convective ensembles leads to discrepancies which cannot be parameterized so easily. To account for the variability of water paths, the presence of nonprecipitating clouds, and other factors, the liquid and ice precipitation water contents in the analytical profiles are adjusted to obtain better agreement with the detailed brightness temperature calculations. This strategy follows the modeling efforts of Short and North (1990), and Hinton, et al. (1992), who noted that the brightness temperature response to the average precipitation rate is less if the rain rates are gamma or lognormally distributed, rather than uniformly distributed. Thus, the effective liquid and ice precipitation water contents are expressed as power-law functions of the original water contents (from the analytical profiles), to accomodate the difference in response.

$$PLWC' = \alpha\ PLWC^{\beta} \quad (4)$$

Here PLWC is the original liquid or ice water content. The power-law constants α and β are adjusted to minimize the difference between the parameterized brightness temperatures, Eq. (3), and those computed from the cloud ensemble/radiative calculations. Separate power-law constants are computed for the convective and stratiform ensembles. Best-fit power law constants and parameterization errors are summarized in Table 2. Also scatterplots of the parameterized brightness temperatures vs. the cloud ensemble brightness temperatures at the four SSM/I frequencies are presented in Fig. 11.

It may be noted from Table 2 that the power-law constants used to modify the convective precipitating liquid water contents at 19.35, 22.235, and 37 GHz are all significantly less than 1, indicating a substantial reduction in the effective water content utilized in the radiative parameterization. This result is consistent with the study of Hinton, et al. (1992), who noted a reduced response of upwelling brightness temperature to mean rainfall rate if the rainfall rates within a given region are gamma-distributed. The power-law constants used to modify the stratiform precipitating liquid water contents are closer to 1, which is reasonable since the parameterization appoximates the precipitation field by a horizontally-uniform field, and the stratiform cloud ensembles have horizontally-uniform structure.

The power-law constants for convective ice precipitation defy a simple physical interpretation; however, the power-law constants used to modify the stratiform precipitating ice equivalent water contents are close to 1. Again, the horizontally-uniform clouds in the radiative parameterization are a good approximation to the true structure of the stratiform cloud ensembles, so only a slight modification of the water contents is required.

The statistics in Table 2 and the scatterplots in Fig. 11 indicate parameterization errors which are typically small, but which increase with increasing frequency. It should be noted that the absolute accuracy of SSM/I antenna temperature measurements is on the order of $\pm$ 3 K (Hollinger, 1991). The most serious parameterization errors are attributed to the strongly convective ensembles which produce brightness temperatures between 180 K and

200 K at 85.5 GHz (see Fig. 11d). Scattering by precipitation-sized ice particles is strongest for these convective clouds at 85.5 GHz, and the horizontally-homogeneous cloud approximation utilized in the parameterization is least suitable under these conditions.

In the retrieval scenario it will not be known *a priori* whether a given brightness temperature is upwelling from a convective or stratiform cloud field. Therefore, a simple discriminant based upon the relative proportions of liquid and ice precipitation is devised. The distribution of ice vesus liquid preciptation paths of the convective and stratiform ensembles is shown in Figure 12. It may be noted that the ratio of ice to liquid paths is much smaller in the convective ensembles than in the stratiform ensembles. In the convective ensembles, the ratio of ice precipitation path to the total path, designated r_{ice}, is always less than 0.5, while in the stratiform ensembles it typically exceeds 0.8. In this study it is assumed that if r_{ice} is less than 0.5, the convective parameterization for brightness temperature is used. If r_{ice} is greater than 0.8, then the stratiform parameterization is employed. For ratios between 0.5 and 0.8, it is assumed that the precipitation water paths have both convective and stratiform components, the proportion of each being determined by linear interpolation.

6. CONCLUDING REMARKS

The cloud ensemble/radiative parameterization described herein provides a computationally-efficient means of simulating microwave antenna temperatures at the SSM/I frequencies. The parameterization is therefore useful in physical retrieval applications where many thousands of antenna temperature computations must be performed over a single solution domain (see Part II of this series). The partitioning of cloud fields into separate convective and stratiform components is an obvious simplification, since generally speaking there are dynamical and thermodynamic interactions between the convective and stratiform regions of an organized precipitating storm; ref. Rutledge and Houze (1987). The cloud ensemble/radiative parameterization

could be generalized by simulating cloud fields in a fully 3-dimensional cloud model and parameterizing the bulk precipitation structure and radiance fields as in the current study.

Other data from the SSM/T, SSM/T-2, and infrared sensors could be included in physical retrievals by specifying the appropriate sensor spatial response characterisitics and channel frequencies in the cloud ensemble/radiative parameterization. The addition of these sensor data will be the subject of future study.

Acknowledgments

The authors wish to thank Robert Aune, Scott Braun, George Diak, Brad Ferrier, Barry Hinton, James Hollinger, Robert Houze, Jr., Christian Kummerow, Lynn McMurdie, Gene Poe, Robert Rabin, James Ridout, David Short, Bill Smith, Matthias Steiner, James Weinman, Mark Whipple and Harold Woolf for their help and inspiration during various phases of this study. This work was supported by NASA Grant NAGW-1855. One author (WHR) was supported in part by National Science Foundation Grant ATM-8920508.

REFERENCES

Farrar, M.R., and E.A. Smith, 1992: Spatial resolution enhancement of terrestrial features using deconvolved SSM/I microwave brightness temperatures. IEEE Trans. Geosci. Remote Sens., 30, 349-355.

Ferrier, B.S., 1988: One-dimensional time-dependent modeling of squall-line convection. Ph.D. thesis, University of Washington, Seattle, Washington, 259 pp.

Ferrier, B.S., and R.A. Houze, Jr., 1989: One-dimensional time-dependent modeling of deep convection. Part I: Model dynamics and simulations of GATE cumulonimbus clouds. J. Atmos. Sci., 46, 330-352.

Gamache, J.F., and R.A. Houze, Jr., 1982: Mesoscale air motions associated with a tropical squall line. Mon. Wea. Rev., 110, 118-135.

Hinton, B.B., W.S. Olson, D.W. Martin, and B. Auvine, 1992: A passive microwave algorithm for tropical oceanic rainfall. J. Appl. Meteor., 31, 1379-1395.

Hollinger, J.P. (ed.), 1991: DMSP Special Sensor Microwave/Imager Calibration/Validation Final Report Volume I. Naval Research Laboratory, Washington, D.C.

Houze, R.A., Jr., P.V. Hobbs, P.H. Herzegh, and D.B. Parsons, 1979: Size distributions of precipitation particles in frontal clouds. J. Atmos. Sci., 36, 156-162.

Kummerow, C.D., and J.A. Weinman, 1988: Radiative properties of deformed hydrometeors at commonly used passive microwave frequencies. IEEE Trans. Geosci. Remote Sens., 26, 629-638.

Kummerow, C., R.A. Mack, and I.M.Hakkarinen, 1989: A self-consistency approach to improve microwave rainfall rate estimation from space. J. Appl. Meteor., 28, 869-884.

Kummerow, C., 1992: personal communication. Currently with Goddard Space Flight Center, Greenbelt, Maryland.

Leery, C.A., and R.A. Houze, Jr., 1979: Melting and evaporation of hydrometeors in precipitation from the anvil clouds of deep tropical convection. J. Atmos. Sci., 36, 669-679.

Liebe, H.J., 1985: An updated model for millimeter wave propagation in moist air. Radio Science, 20, 1069-1089.

López, R.E., 1977: The lognormal distribution and cumulus cloud populations. Mon. Wea. Rev., 105, 865-872.

Lorenc, A.C., 1986: Analysis methods for numerical weather prediction. Quart. J. R. Met. Soc., 112, 1177-1194.

Lin, Y.-L., R.D. Farley, and H.D. Orville, 1983: Bulk parameterization of the snow field in a cloud model. J. Climate Appl. Meteor., 22, 1065-1092.

Marks, F.D., and R.A. Houze, Jr., 1987: Inner core structure of Hurricane Alicia from airborne doppler radar observations. J. Atmos. Sci., 44, 1296-1317.

Olson, W.S., 1989: Physical retrieval of rainfall rates over the ocean by multispectral microwave radiometry- application to tropical cyclones. J. Geophys. Res. - Atmospheres, 94, 2267 - 2280.

Poe, G., 1988: personal communication. Currently with Aerojet Electronics Systems Division, Azusa, California.

Ridout, J.A., 1991: A Parameterized Quasi-Five-Cylinder Convective Cloud Model and Its Application to Remote Sensing of Rainfall. Ph.D. thesis, University of Wisconsin, Madison, Wisconsin, 278 pp.

Ridout, J.A., 1992: personal communication. Currently with Naval Research Laboratory-West, Monterey, California.

Ridout, J. A., 1993: A quasi-five-cylinder model of deep convection. Part I: Updraft growth in non-sheared environments. Submitted to J. Atmos. Sci..

Robinson, W.D., C. Kummerow, and W.S. Olson, 1992: A technique for matching and enhancing the resolution of microwave measurements from the SSM/I instrument. IEEE Trans. Geosci. Remote Sens., 30, 419-429.

Rutledge, S.A., and R.A. Houze, 1987: A diagnostic modeling study of the trailing stratiform region of a midlatitude squall line. J. Atmos. Sci., 44, 2640-2656.

Short, D.A., and G.R. North, 1990: The beam filling error in the Nimbus 5 Electronically Scanning Microwave Radiometer observations of Global Atlantic Tropical Experiment rainfall. J. Geophys. Res., 95, 2187-2193.

Simpson, J., R.F. Adler, G.R. North, 1988: A proposed Tropical Rainfall Measuring Mission (TRMM) Satellite. Bull. Amer. Met. Soc., 69, 278-295.

Stewart, R.E., J.D. Marwitz, J.C. Pace, and R.E. Carbone, 1984: Characteristics through the melting layer of stratiform clouds. J. Atmos.Sci., 41, 3227-3237.

Xiang, X., E.A. Smith, and G.J. Tripoli, 1992: A cloud and radiation model-based algorithm for rainfall retrieval from SSM/I multispectral microwave measurements. Proceedings of the Sixth Conference on Satellite Meteorology and Oceanography, Atlanta, Georgia, 286-289.

Table 1. Parameters of the best-fit analytical precipitating water content profiles, based upon the convective and stratiform cloud ensemble simulations. Adjustable parameters zmin and zmax are in units of kilometers, B1 is dimensionless, and B2 has units of m^2/kg. Parameters associated with the liquid and ice precipitation profiles are listed separately. The analytical convective profiles have a combined bias of -2.6×10^{-5} g/m^3, and an error standard deviation of 0.037 g/m^3. The analytical stratiform profiles have a combined bias of 1.1×10^{-4} g/m^3, and and error standard deviation of 0.028 g/m^3.

	zmin	zmax	B1	B2
Convective liquid:	-0.84	6.19	1.81	1.67
Convective ice:	3.75	15.20	5.25	3.22
Stratiform liquid:	-0.77	5.07	0.99	-0.29
Stratiform ice:	3.13	10.70	3.21	-0.37

Table 2. Best-fit power-law constants in the cloud ensemble/radiative parameterization at the SSM/I frequencies. Constants are listed separately for convective and stratiform cloud ensembles. Also listed are the bias and error standard deviation of the parameterized brightness temperatures with respect to the brightness temperatures generated from the cloud ensembles.

	α_{liq}	β_{liq}	α_{ice}	β_{ice}
19.35 GHz				
convective:	.350	.400	1.428	.857
stratiform:	.937	.953	.930	.855
bias = -.138 K				
σ_{err} = 1.693 K				
22.235 GHz				
convective:	.327	.393	1.284	.950
stratiform:	.795	.874	.920	.857
bias = -.208 K				
σ_{err} = 1.036 K				
37 GHz				
convective:	.244	.356	.820	.864
stratiform:	.916	.959	.982	.924
bias = -.766 K				
σ_{err} = 2.430 K				
85.5 GHz				
convective:	.883	1.464	.187	.417
stratiform:	.988	1.023	1.021	.982
bias = -.538 K				
σ_{err} = 3.165 K				

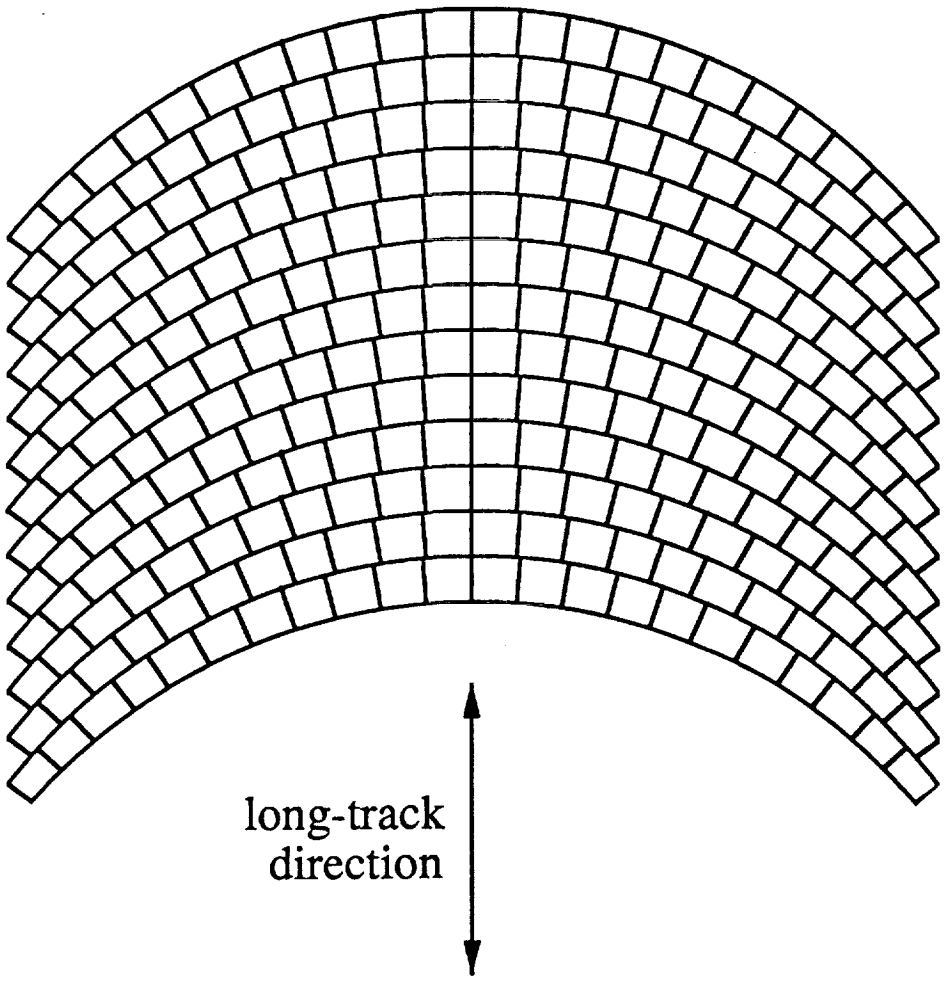

Fig. 1. Schematic of the SSM/I swath grid. For clarity, grid box sizes have been magnified by a factor of three.

(a) 19.35 GHz normalized response

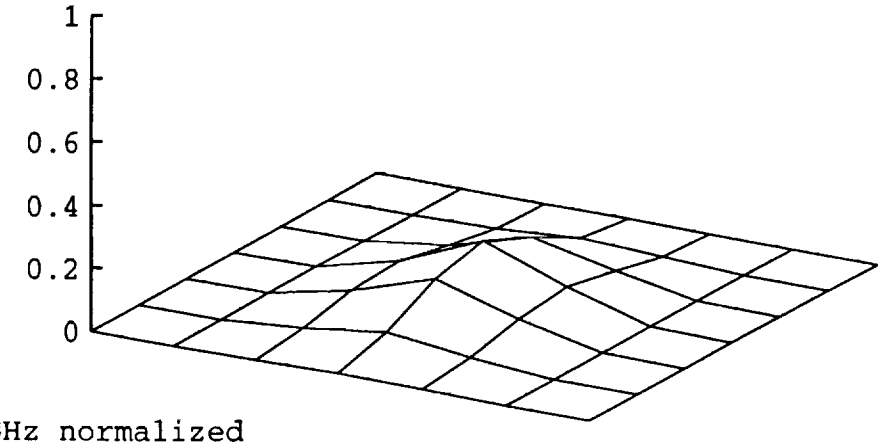

(b) 37 GHz normalized response

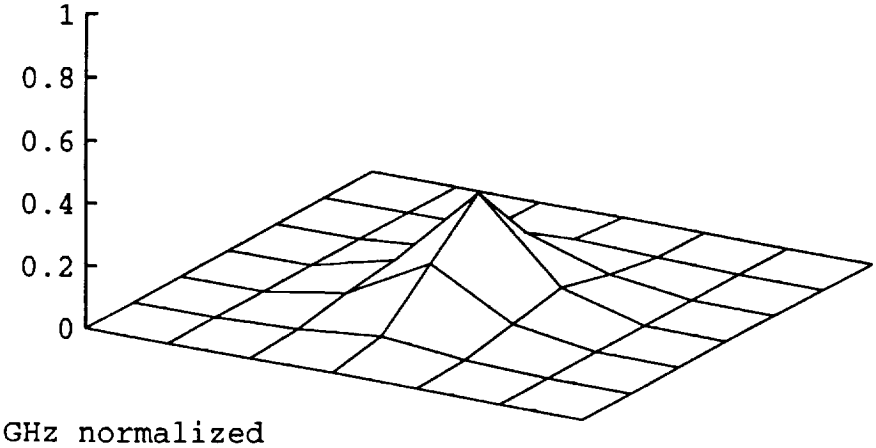

(c) 85.5 GHz normalized response

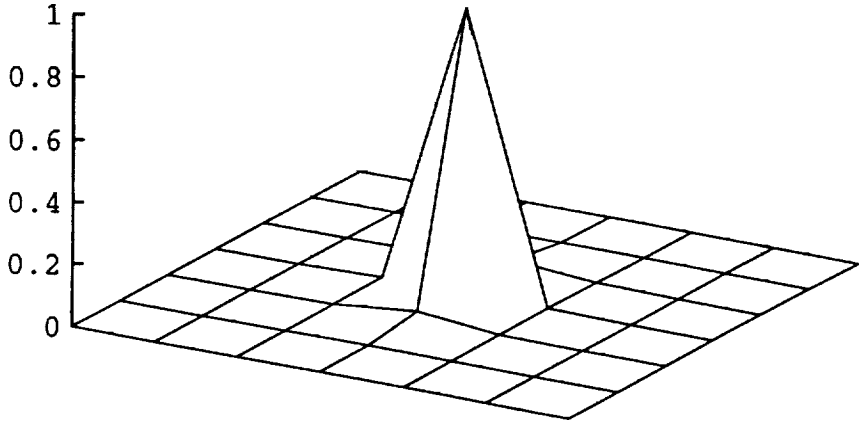

Fig. 2. Co-polarized SSM/I response functions at (a) 19.35 GHz, (b) 37 GHz, and (c) 85.5 GHz in the vertical polarization channels.

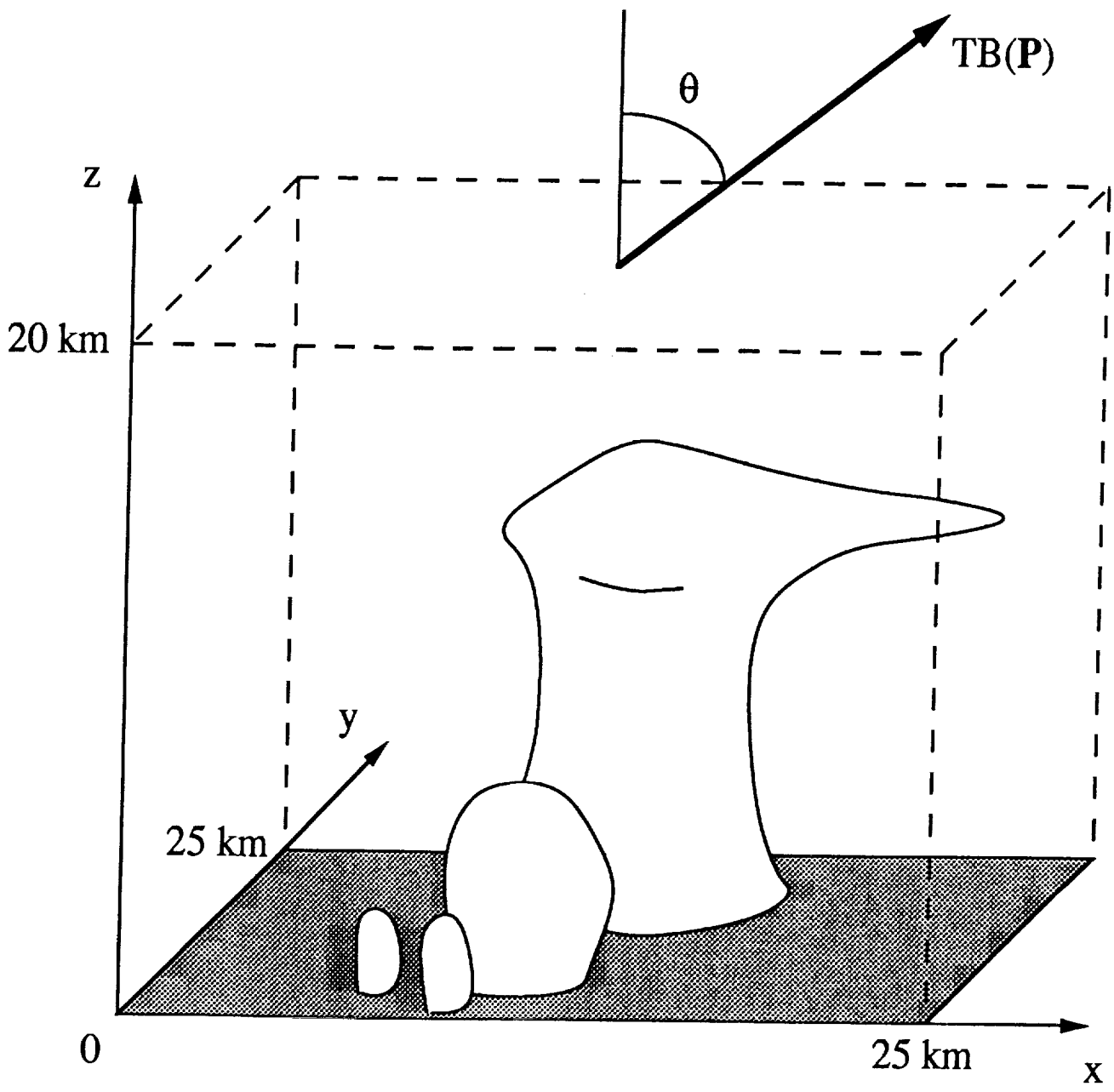

Fig. 3 Domain of the cloud ensemble/radiative model. Model dimensions are 25 km x 25 km x 20 km. Upwelling brightness temperatures are computed along an oblique path at angle $\theta = 53.1$ from zenith.

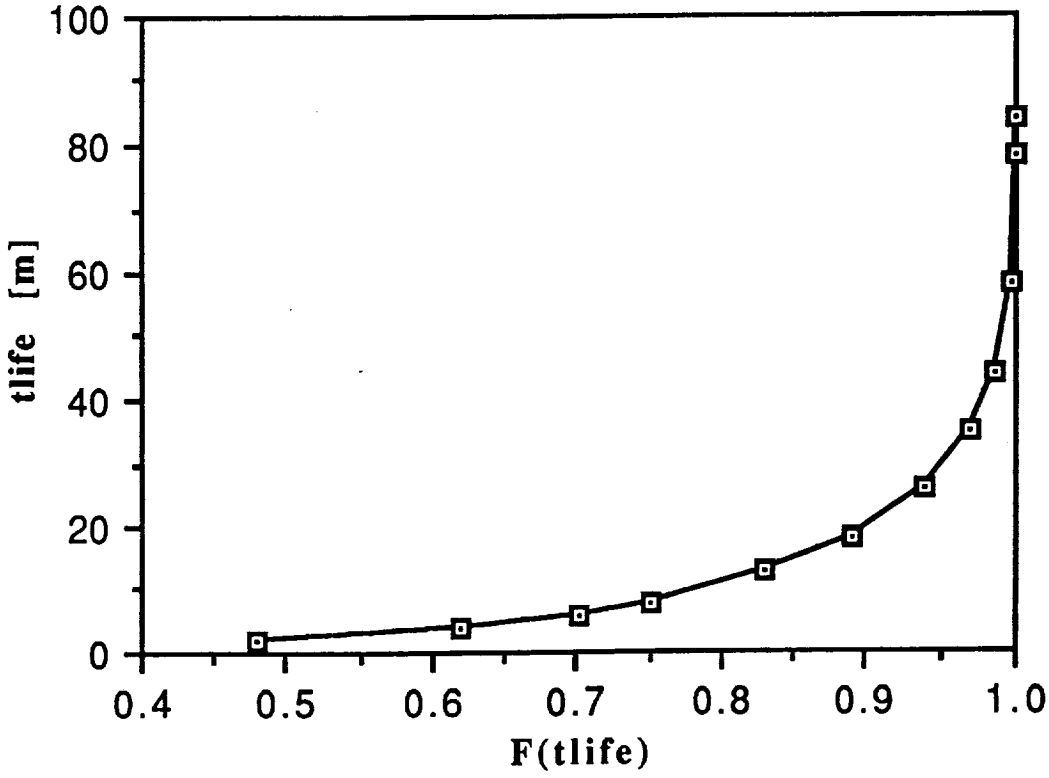

Fig. 4. Radar echo lifetime cumulative distribution from López (1977). The cloud radar echo lifetime tlife, in minutes, is plotted against the cumulative fraction of clouds F with lifetimes less than tlife.

(a)

(b)

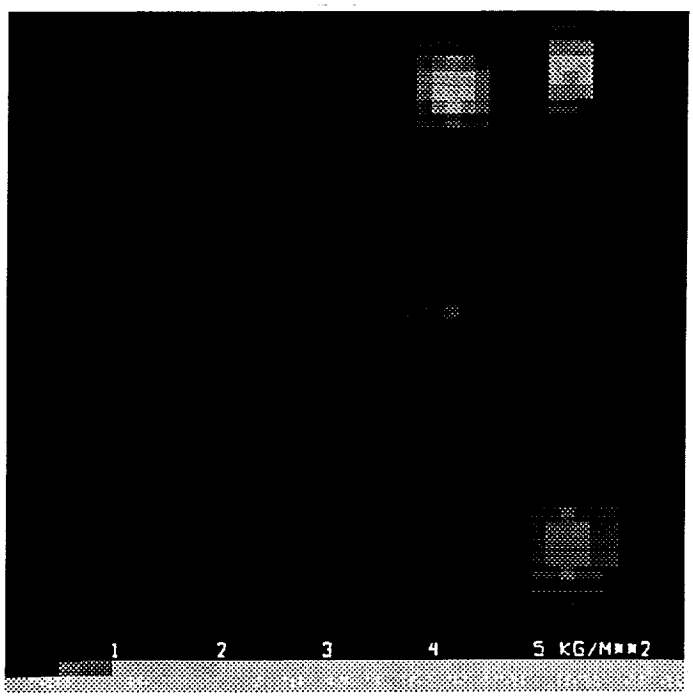

Fig. 5. Imagery of (a) path integrated precipitating liquid water and (b) path integrated precipitating ice from the cloud ensemble/radiative model. The precipitation path distributions are generated from an ensemble of 48 convective cloud simulations. The area represented by each panel is 25 km x 25 km.

(a)

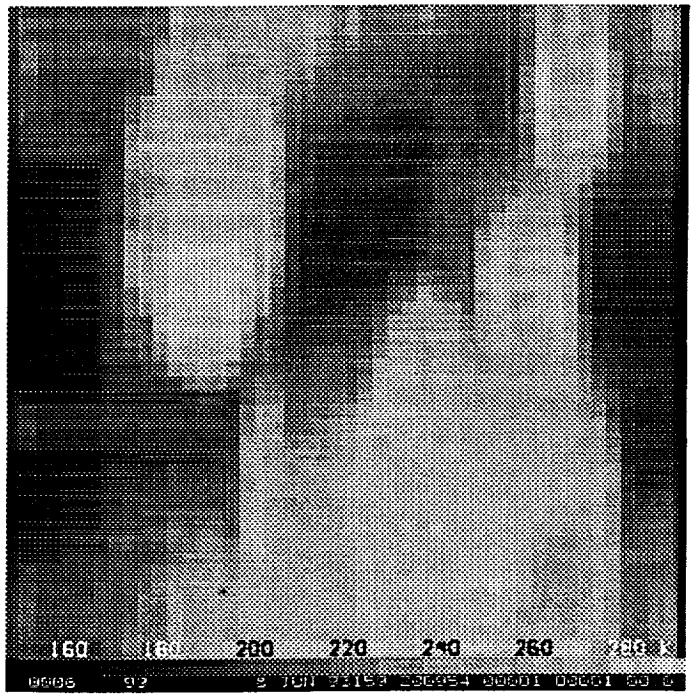

(b)

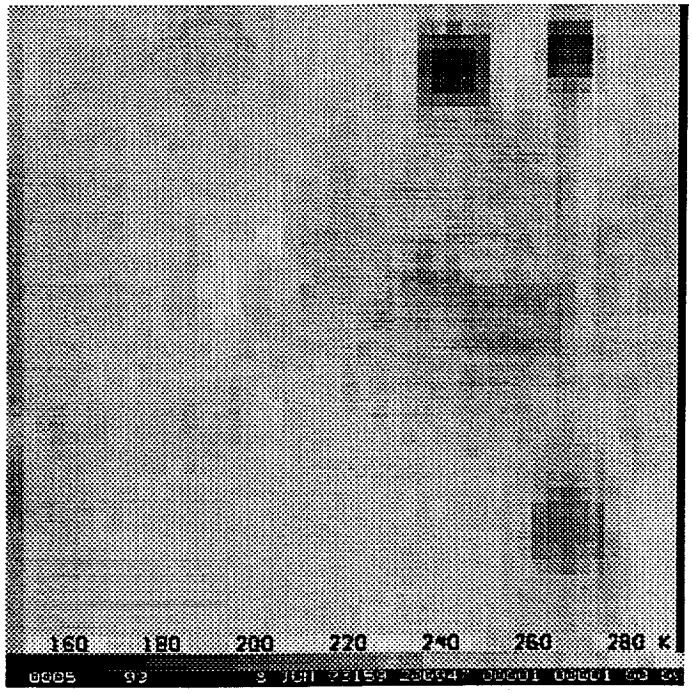

Fig. 6. Computed brightness temperature field at (a) 37 GHz, and (b) 85.5 GHz, upwelling from the convective cloud ensemble shown in Fig. 5. A surface emissivity of 0.30 is assumed. The area represented by each panel is approximately 25 km x 25 km.

(a)

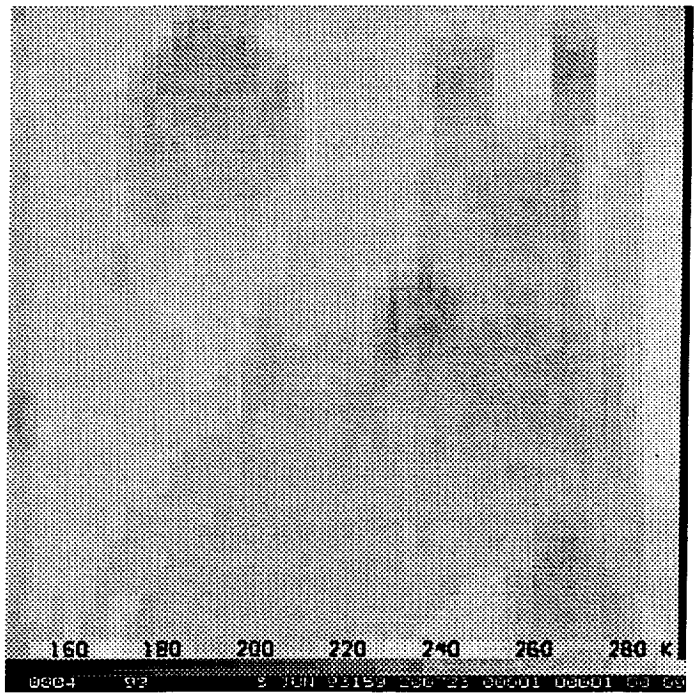

(b)

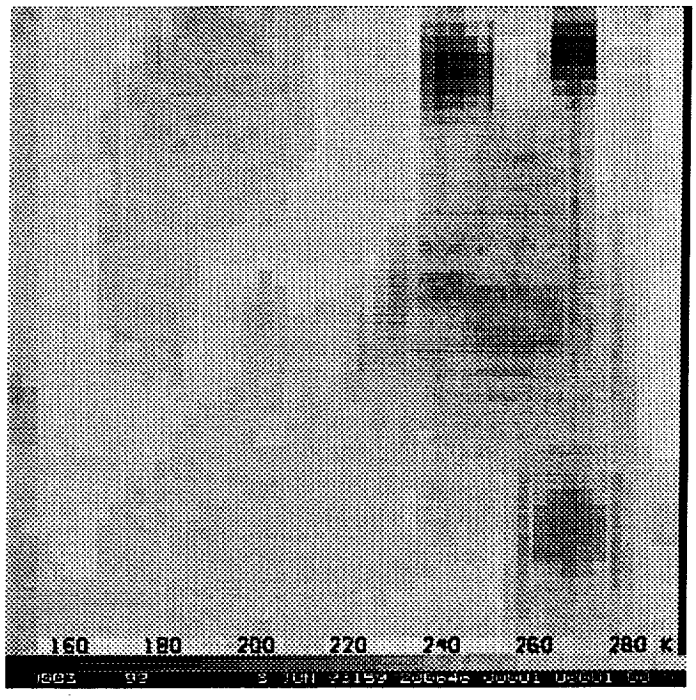

Fig. 7. Computed brightness temperature field at (a) 37 GHz, and (b) 85.5 GHz, upwelling from the convective cloud ensemble shown in Fig. 5. A surface emissivity of 0.95 is assumed. The area represented by each panel is approximately 25 km x 25 km.

(a)

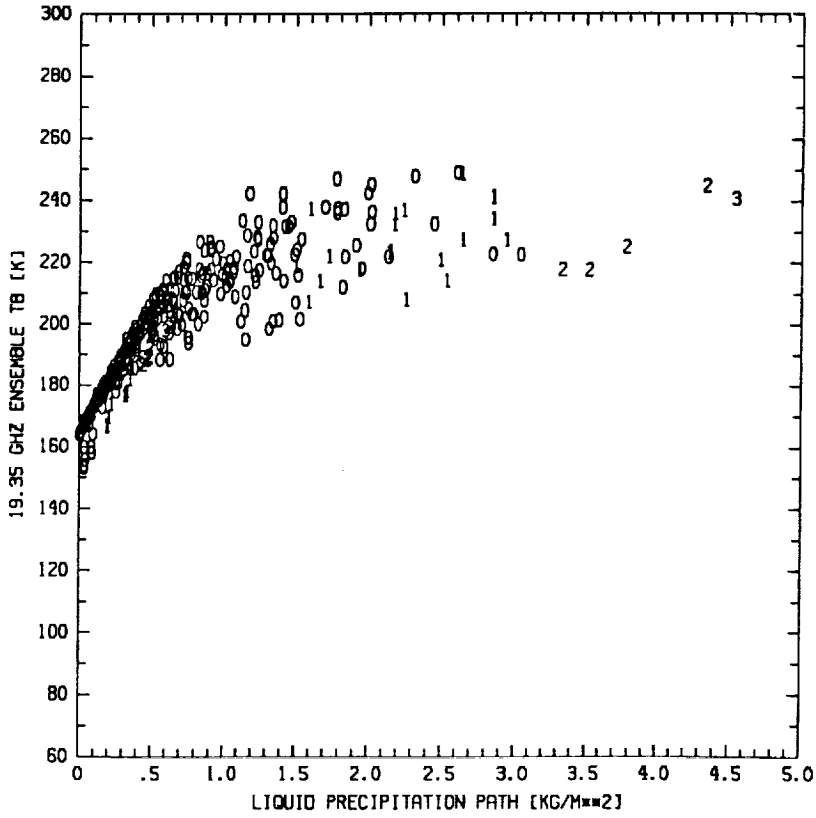

(b)

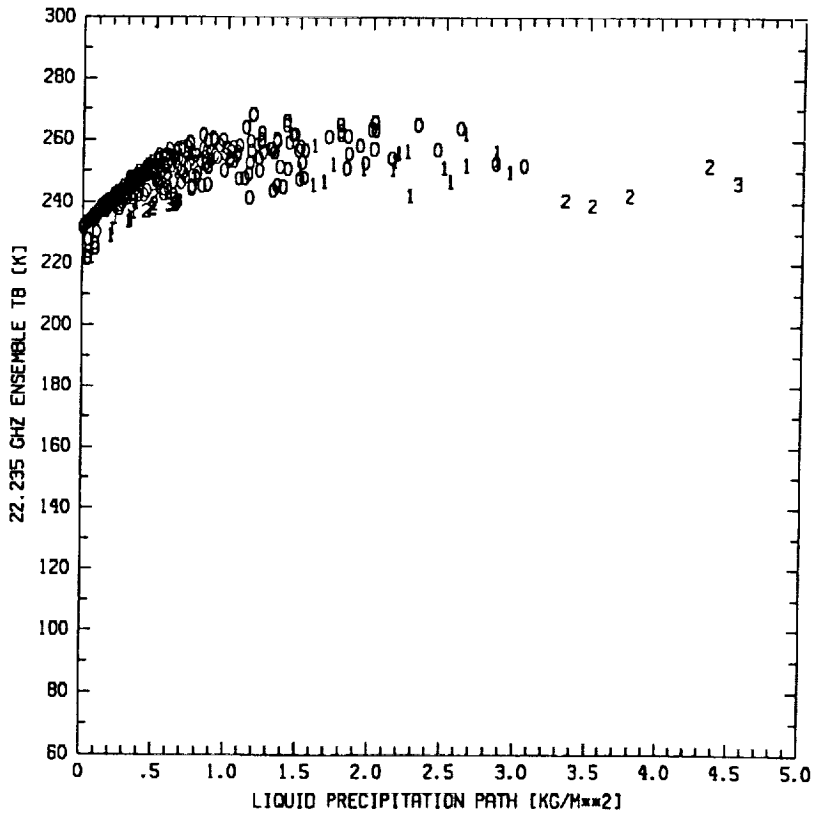

Fig. 8. Plot of cloud ensemble/radiative model brightness temperatures vs. ensemble-average precipitating liquid water paths at (a) 19.35 GHz and (b) 22.235 GHz. Plotted numbers are ensemble-average precipitating ice water paths thresholded at integral values.

(c)

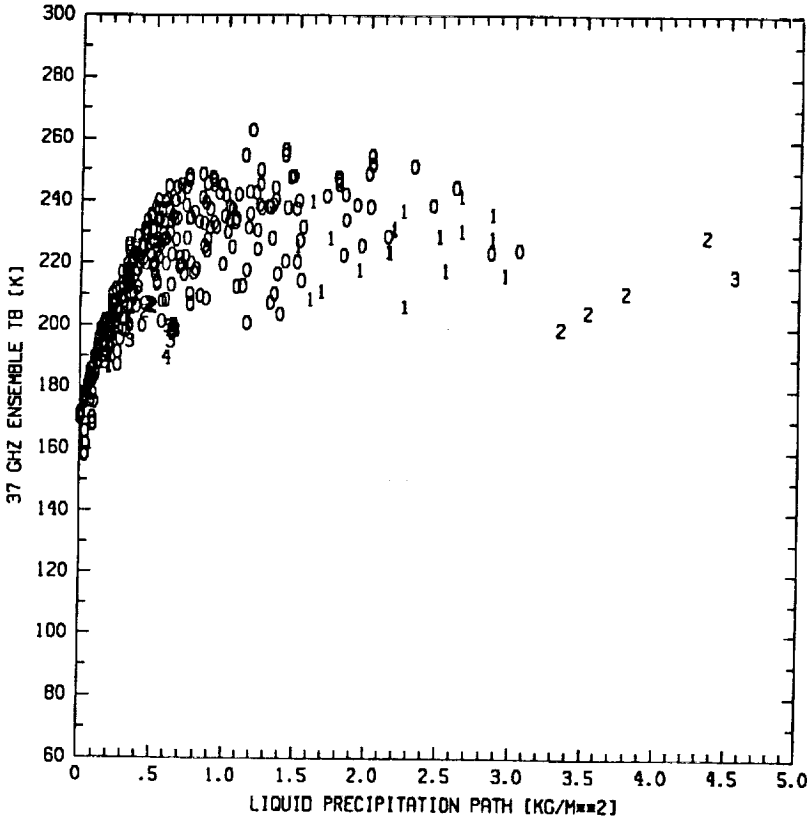

(d)

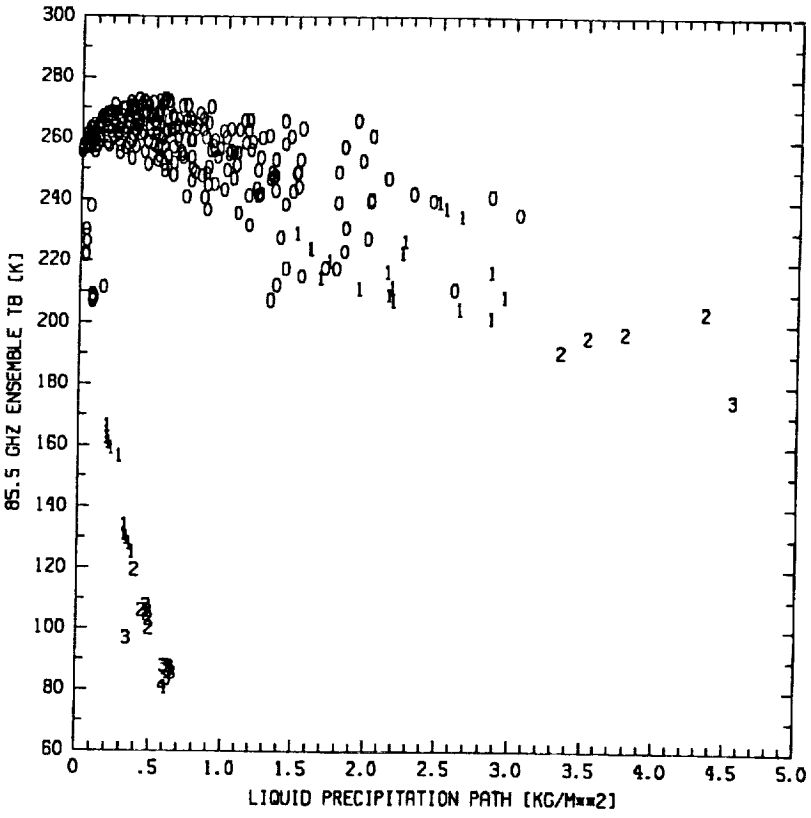

Fig. 8. (cont.) Plot of cloud ensemble/radiative model brightness temperatures vs. ensemble-average precipitating liquid water paths at (c) 37 GHz and (d) 85.5 GHz. Plotted numbers are ensemble-average precipitating ice water paths thresholded at integral values.

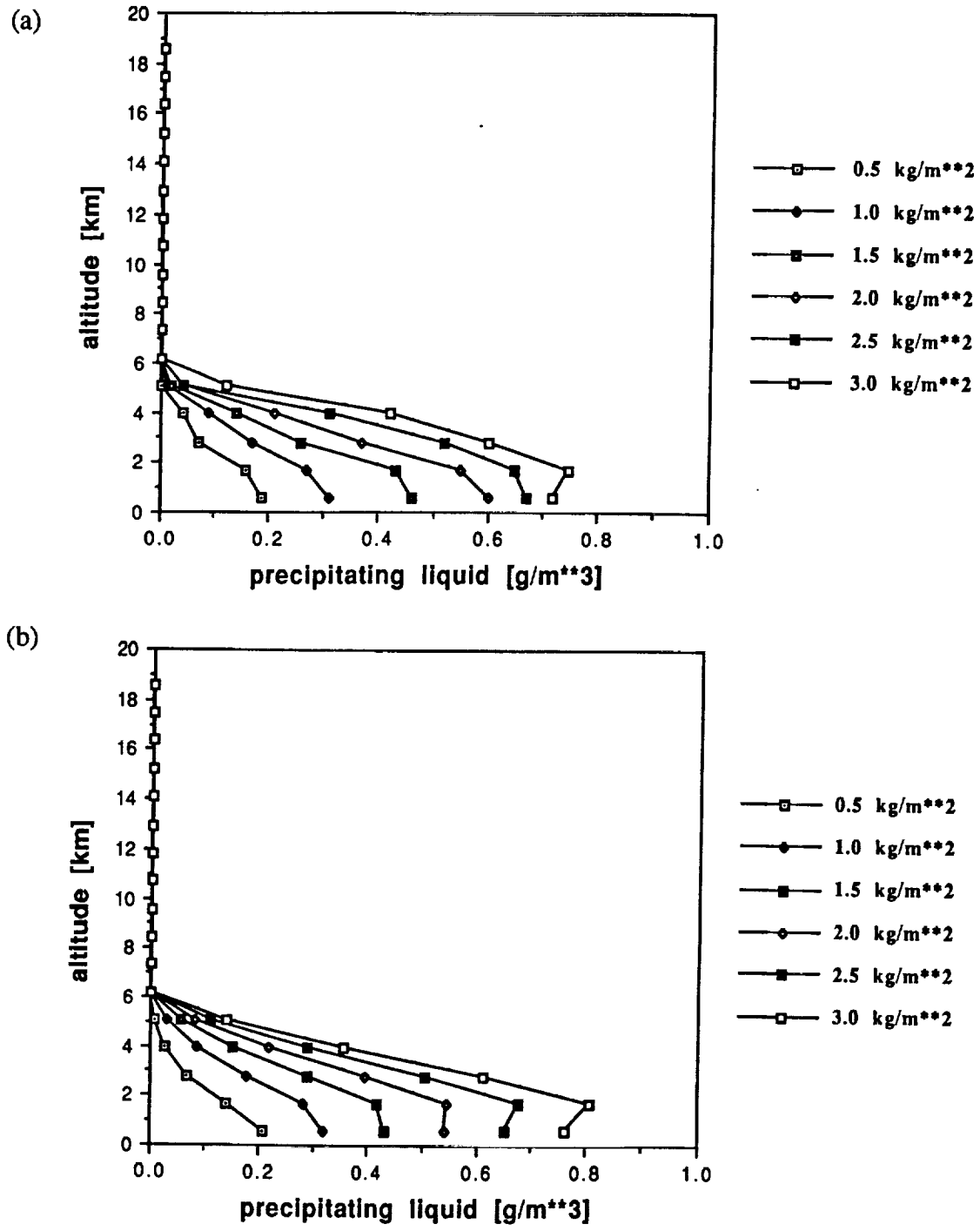

Fig. 9. Mean profiles of precipitating liquid water from (a) the convective cloud ensemble simulations, and (b) the analytical curve fits described in the text. Profiles are shown for precipitating liquid paths of 0.5, 1.0, 1.5, 2.0, 2.5, and 3.0 kg/m^2.

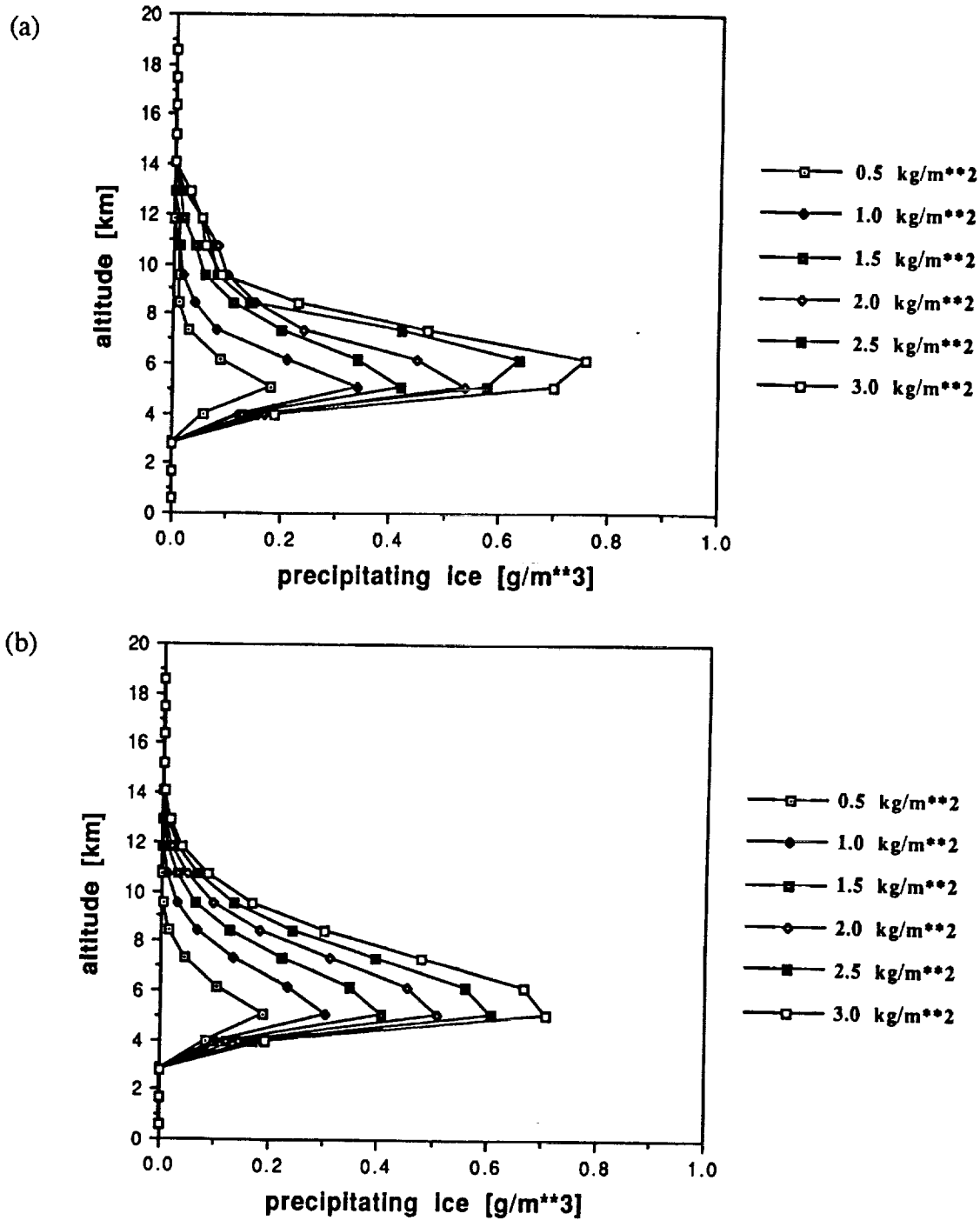

Fig. 10. Mean profiles of precipitating ice from (a) the convective cloud ensemble simulations, and (b) the analytical curve fits described in the text. Profiles are shown for precipitating ice paths of 0.5, 1.0, 1.5, 2.0, 2.5, and 3.0 kg/m^2.

(a)

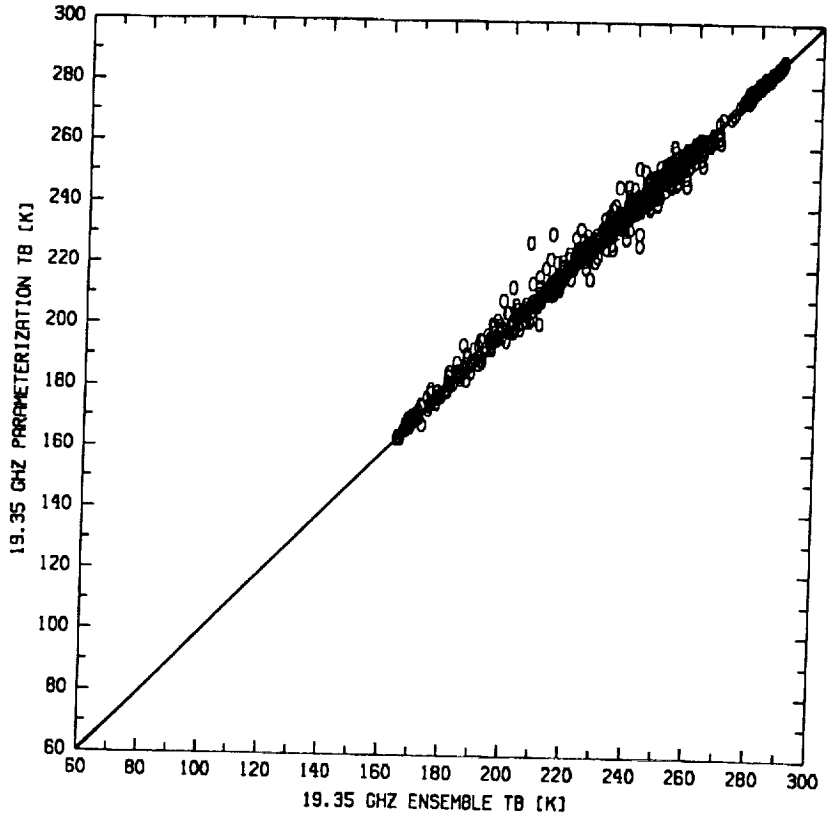

(b)

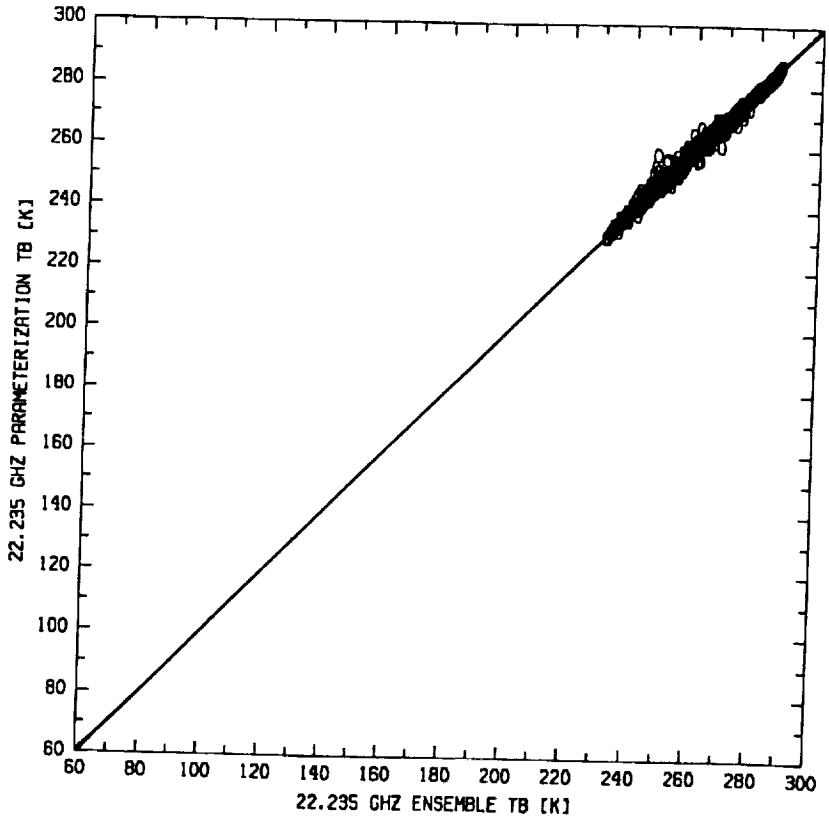

Fig. 11. Plot of parameterized brightness temperatures vs. cloud ensemble/radiative model brightness temperatures at (a) 19.35 GHz and (b) 22.235 GHz. For reference, the solid line in each panel represents a perfect correlation.

(c)

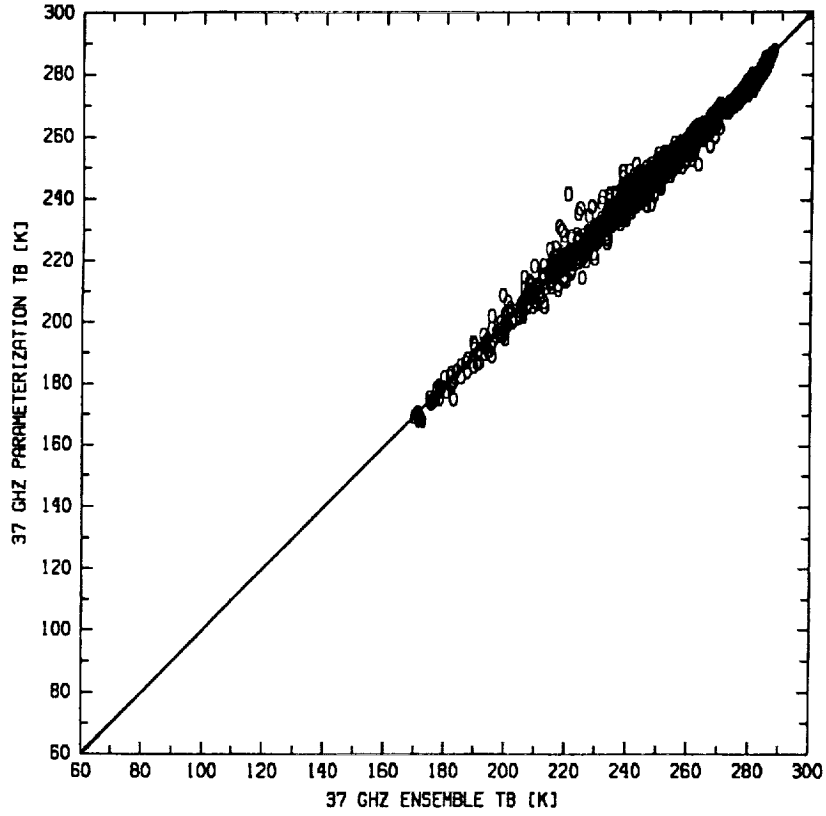

(d)

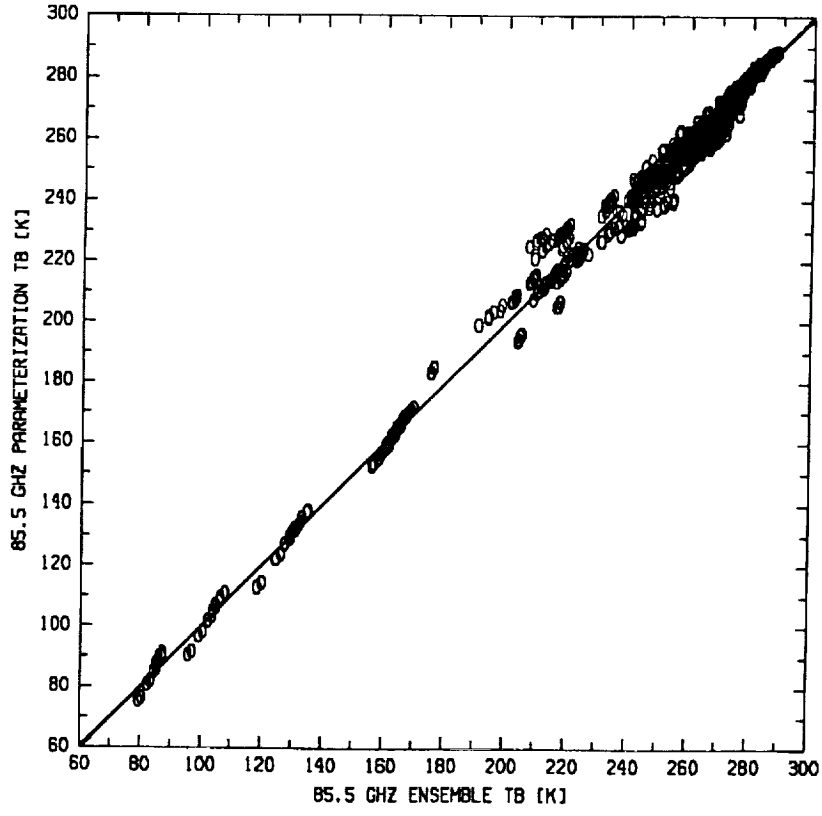

Fig. 11. (cont.) Plot of parameterized brightness temperatures vs. cloud ensemble/radiative model brightness temperatures at (c) 37 GHz and (d) 85.5 GHz. For reference, the solid line in each panel represents a perfect correlation.

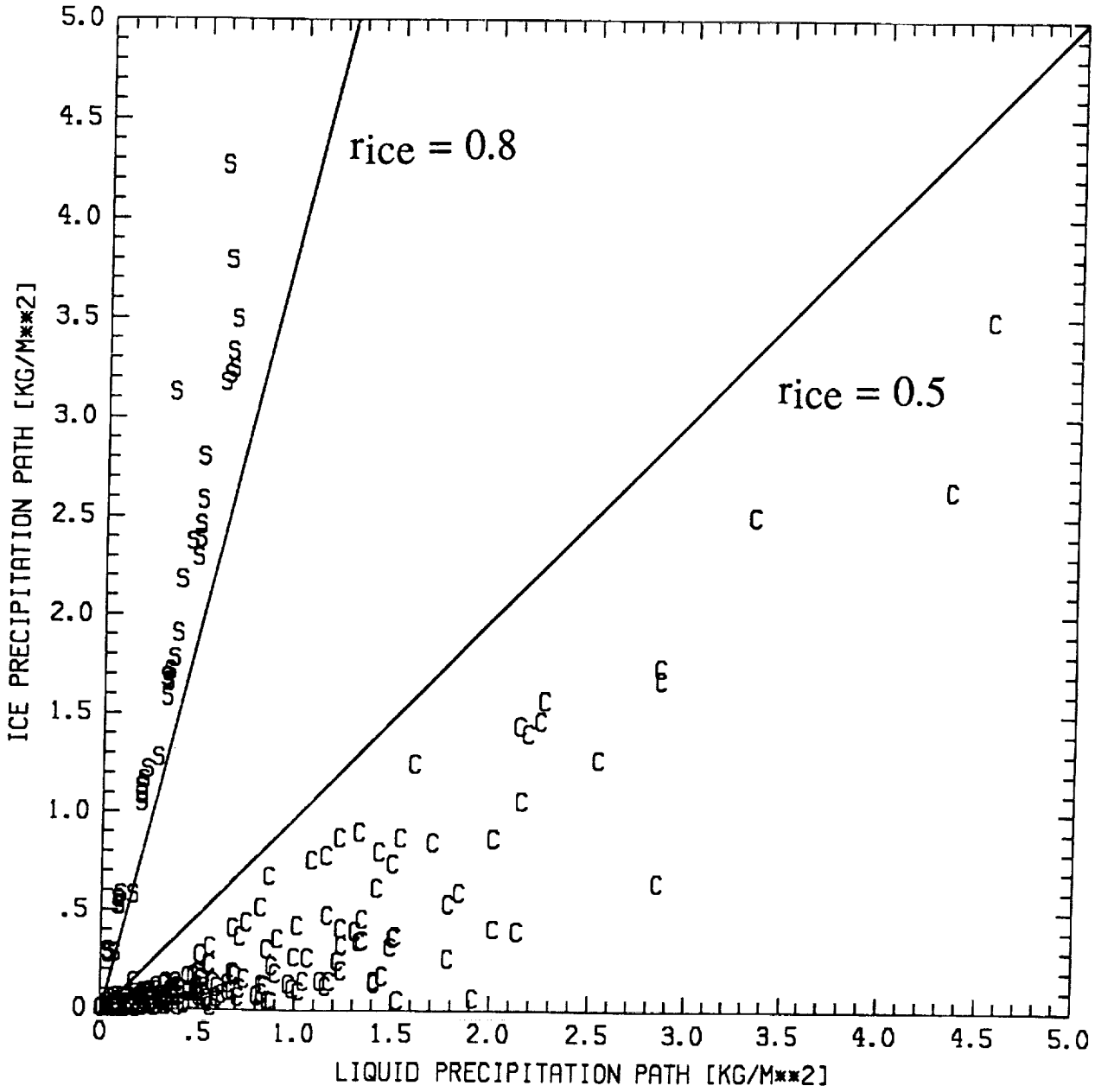

Fig. 12. Scatterplot of ice precipitation path versus liquid precipitation path from both the convective cloud ensemble (C) and stratiform cloud ensemble (S) simulations. Ice to total precipitation path ratios of 0.5 and 0.8 are indicated by solid lines.

PHYSICAL RETRIEVAL OF PRECIPITATION WATER CONTENTS FROM SPECIAL SENSOR MICROWAVE/IMAGER (SSM/I) DATA-PART II: RETRIEVAL METHOD AND APPLICATIONS (report version)

by

William S. Olson

Cooperative Institute for Meteorological Satellite Studies

1225 West Dayton Street

University of Wisconsin

Madison, Wisconsin 53706

To be modified and submitted to *J. Appl. Meteor.*

PHYSICAL RETRIEVAL OF PRECIPITATION WATER CONTENTS FROM SPECIAL SENSOR MICROWAVE/IMAGER (SSM/I) DATA- PART II: RETRIEVAL METHOD AND APPLICATIONS (report version)

by

William S. Olson

1. INTRODUCTION

The retrieval of precipitation distributions by passive microwave techniques has been an area of study in satellite remote sensing for well over a decade. The recent initiative to estimate both the horizontal and vertical distributions of precipitating liquid water in the tropics, i.e. the Tropical Rainfall Measuring Mission or TRMM, has further stimulated interest in this area; see Simpson, et al. (1988). The proposed TRMM satellite will carry a suite of sensors including passive and active microwave instruments, as well as visible and infrared radiometers. In addition to TRMM, a combination of microwave and visible/IR sensors has also been proposed for the Earth Observing System (EOS) platforms for the purpose of retrieving rainfall rates and other geophysical parameters; ref. Schoeberl, et al. (1992). Methods for determining precipitation distributions based upon data from several instruments having different spectral and resolution characteristics will therefore be required.

Currently multispectral microwave observations from the Special Sensor Microwave/Imager (SSM/I), borne by the DMSP-F8, F10, and F11, have provided researchers with the means for retrieving rainfall rates; see Hollinger (1991), Kummerow, et al. (1989), Petty and Katsaros (1990), Xiang, et al. (1992). The SSM/I is a multichannel, dual-polarization, passive microwave radiometer with channels at 19.35, 22.235, 37, and 85.5 GHz. The diffraction limitation of the SSM/I antenna causes the spatial resolution of measurements to increase with frequency, such that the minimum footprint dimension decreases from 43 km at 19.35 GHz to 13 km at 85.5 GHz. The DMSP-F8, F10, and F11 also carry the Special Sensor Microwave/Temperature (SSM/T) sounder with channels at 50.5, 53.2, 54.35, 54.9, 58.4, 58.825, and 59.4 GHz, and a

footprint dimension of approximately 180 km at nadir view. In addition the DMSP F11 carries the Special Sensor Microwave/Temperature -2 (SSM/T-2) sounder, with channels at 91.665, 150, and 183.3 ± 1, ± 3, ± 7 GHz, and a minimum footprint dimension of 48 km at nadir view. The SSM/T and SSM/T-2 can provide temperature and humidity information not available from the SSM/I alone.

In the present study, a physical retrieval method for estimating precipitating water distributions and other geophysical parameters based upon measurements from the DMSP-F8 SSM/I is developed. Three unique features of the retrieval method are (1) sensor antenna functions are explicitly included to accommodate varying channel resolution, (2) precipitation-brightness temperature relationships are quantified using the cloud ensemble/radiative parameterization described in Part I, and (3) spatial constraints are imposed for certain background parameters, such as humidity, which vary more slowly in the horizontal than the cloud and precipitation water contents. The general framework of the method will facilitate the incorporation of measurements from the SSM/T, SSM/T-2 and geostationary infrared measurements, as well as information from conventional sources (e.g. radiosondes) or numerical forecast model fields.

2. METHOD

The basis of the retrieval method is the minimum variance solution as described in Lorenc (1986). An error functional which expresses the deviation of the observed satellite antenna temperatures from model-derived values, plus an additional constraint which represents the deviation of retrieved geophysical parameters from *a priori* estimates, is derived.

$$E = (\mathbf{TA}_{obs} - \mathbf{TA(P)}_{mod})^T \Sigma^{-1} (\mathbf{TA}_{obs} - \mathbf{TA(P)}_{mod}) + (\mathbf{P} - \mathbf{P}_{apriori})^T \Delta^{-1} (\mathbf{P} - \mathbf{P}_{apriori}) \quad (1)$$

Here, $\mathbf{TA}_{obs}$ is a vector of antenna temperature measurements, $\mathbf{TA(P)}_{mod}$ are antenna temperature estimates based on the sensor response model (see Part I of this series), **P** is a vector of geophysical parameters to be retrieved, and $\mathbf{P}_{apriori}$ are estimates of the parameters based upon *a priori* knowledge. Σ and Δ are covariance matrices representing observational plus model errors (Σ), and errors in the *a priori* estimates (Δ). In the present study all off-diagonal elements of these matrices are neglected.

The retrieval of precipitating liquid water contents and other geophysical parameters is accomplished by iteratively perturbing the geophysical parameters until the error functional Eq. (2) is minimized. Unlike Lorenc (1986), the error functional is minimized using the memoryless, quasi-Newton method described by Shanno (1978). The quasi-Newton approach is computationally efficient when the retrieval problem requires the simultaneous optimization of a large number of unknown geophysical parameters. In this situation, matrix inversion methods are impractical.

3. APPLICATION OF THE RETRIEVAL METHOD TO SSM/I DATA

3.1 Retrieval Parameters and Constraints

In Part I of this series, a sensor response model was developed for SSM/I to relate measured microwave antenna temperatures to variations in geophysical parameters in the earth/atmosphere system. The sensor response model is designated $\mathbf{TA(P)}_{mod}$ in Eq. (1). The explicit dependence of antenna temperature on slant path-integrated liquid and ice-phase precipitation, fractional coverage of liquid and ice precipitation within a 25 km x 25 km grid box, atmospheric temperature and water vapor, and surface temperature and emissivity were discussed in Part I. Although each of these geophysical parameters can have a significant effect on SSM/I antenna temperatures, only a limited number of unknown parameters can be allowed in the minimization of the error functional Eq. (1). Otherwise, ambiguous solutions can result.

Of primary interest are the distributions of precipitating liquid and ice over the swath grid, and therefore the slant path-integrated preciptitating liquid and ice, and the associated grid-box fractions are allowed to vary in the retrievals. Although variations in surface skin temperature and emissivity can affect microwave surface emission, climatological variations of surface skin temperature are relatively small. Surface skin temperature over the ocean varies by less than ± 5 K in the tropics, up to about ± 10 K at midlatitudes (Pickard and Emery, 1982). Any error in the retrieved value of skin temperature can easily be compensated by a change in the surface emissivity to produce nearly the same surface emission. Therefore, in this study the value of surface skin temperature is prescribed at a climatological value representative of the tropics (300.15 K). A somewhat better estimate could be obtained from infrared retrieval composites, but a climatological value is found to be sufficiently accurate for the purpose of demonstrating the retrieval method. Surface emissivities are parameterized according to the model of Grody (1988). The emissivity in each polarization has a frequency dependence given by

$$e = a + b \cdot \ln(\nu) \tag{2}$$

where ν is the channel frequencey and a and b are free parameters. Separate emissivity parameters describing the emissivities of land and ocean surfaces are allowed to vary in the retrieval, but it is assumed that these parameters are the same for every grid box of the swath grid. To account for the mixture of emissivities in grid boxes which contain both land and water surfaces, an additional land fraction parameter, f_{land}, is also allowed to vary in the retrieval. The effective emissivity is given by

$$e_{effective} = f_{land} \cdot e_{land} + (1 - f_{land}) \cdot e_{ocean} \tag{3}$$

In the retrieval method, profiles of atmospheric temperature and water vapor mixing ratio are represented by a mean profile and a set of profile eigenfunctions. The mean profiles and eigenfunctions are derived from a global radisonde data base of 1200 profiles developed by Smith, et al. (1974).

A link between the atmospheric profiles and cloud ensemble/radiative parameterization is established as follows. A profile of temperature and humidity (water vapor mixing ratio) is selected to serve as the environment for the cloud model simulations and ensemble generation described in Part I. The relationship between the generated ensembles and the computed upwelling microwave brightness temperatures is parameterized, and a set of fitting constants is calculated for that particular environment (see also Part I). Additional profiles of atmospheric temperature and humidity can be selected to generate cloud ensemble/radiative parameterizations appropriate for other climatologies.

In the retrieval, an initial guess profile is compared to all of the profiles utilized to generate cloud ensemble/radiative parameterizations. The parameterization associated with the profile which best matches the initial guess profile (in the mean-square sense) is selected for the retrieval of precipitation amounts in a given grid box. The guess profiles are allowed to deviate from the parameterization profiles by allowing the weighting of the first eigenfunctions of temperature and mixing ratio (in an eigenfunction decomposition of the guess profiles) to vary in the retrieval.

In the present study, the GATE Day 261 profile (ref. Ferrier and Houze, 1989) is selected to yield a cloud ensemble/radiative parameterization representative of tropical conditions. This single profile is selected for the demonstration of the precipitation retrieval method, since the applications herein include SSM/I observations of a tropical squall line and a developing tropical storm. However, cloud ensemble/radiative parameterizations corresponding to other temperature and humidity environments could be added to represent midlatitude conditions or other climatologies.

Physical retrieval tests in which the temperature and mixing ratio eigenfunction weights were allowed to vary in each grid box resulted in a lack of constraint on solutions and ambiguous retrievals. Ambiguous solutions were due to the fact that temperature variations and mixing ratio variations over land produce only a very small signal in upwelling microwave brightness temperatures at the SSM/I frequencies, and these signals are generally indistinguishable from variations in background emissivity or precipitation amount.

The ambiguities are removed by prescibing the first eigenfunction weight of temperature over the entire swath grid, and allowing the first eigenfunction weight of water vapor mixing ratio to vary only over oceanic regions. Over land, the first eigenfunction weight of mixing ratio is again prescribed.

Regarding the retrieval of precipitation parameters, preliminary testing also revealed an ambiguity between slant path-integrated precipitating ice and the fraction of precipitating ice within each grid box. The ambiguity in these retrieved quantities is removed by setting the fraction of precipitating ice equal to the fraction of precipitating liquid. This constraint is likely to introduce some error into retrieved precipitation amounts, since precipitating ice, which is associated with stronger convective updrafts and organized mesoscale motions (see Part I), generally has an areal extent which is different from the areal extent of precipitating liquid. The ice content/fraction ambiguity might be removed with the addition of higher-frequency ice sensitive channels on future microwave sensors.

A summary of parameters **P** in the SSM/I physical retrieval and the associated constraints on the parameters is summarized in Table 1.

In the initial demonstration of the retrieval method which is documented here, only the cloud ensemble/radiative parameterization based upon the GATE Day 261 profile is considered. This parameterization is appropriate since only retrievals of precipitation in the tropics are considered here. Precipitation retrieval applications in other climatic

environments, and the selection of alternative cloud ensemble/radiative parameterizations appropriate to those environments, will be the subject of a future study.

Estimates of observational and cloud ensemble/radiative parameterization errors are specified in the diagonal elements of Σ of Eq. (1). The observational error standard deviations of each SSM/I measurement are taken to be 3 K as suggested by Hollinger, et al. (1991) for absolute calibration errors. Parameterization error standard deviations are assumed to be 6 K in the 85.5 GHz channels and 3.6 K in the remaining channels. These figures reflect the greater residual errors in the 85.5 GHz parameterization fits to the cloud ensemble/radiative calculations of brightness temperatures (see Part I). An additional weighting factor of 0.25 is applied to the 85.5 GHz terms in Eq. (1) to compensate for the SSM/I 85.5 GHz sampling, which is four times as great as the sampling in the other channels.

The minimization of E in Eq. (1) requires the evaluation of finite difference derivatives of brightness temperatures with respect to the parameters **P**. Efficient convergence to a minimum requires that these derivatives be scaled to compensate for variations in sensitivity of brightness temperature to a particular parameter. Appropriate scaling factors for each parameter are selected based upon extensive retrieval tests.

3.2 Darwin Case Study

The physical retrieval method, Eq. (1), is applied to SSM/I observations of a tropical squall line at 0906 UTC on February 9, 1988 in the vicinity of Darwin, Australia. SSM/I observation of the squall line at 37 GHz and 85.5 GHz in the horizontal polarization are shown in Figs. 1a and 1b, respectively. In the panels of the figure, the northern coast of Australia and the outlines of Bathurst and Melville Islands are indicated by white lines, and the grayscale of brightness temperature values in K is displayed at the bottom. Each panel has dimensions of approximately 240 km x 240 km. The convective leading edge of the squall line parallels the coast of Australia, and is indictated by a line of relatively low brightness temperatures in the 85.5 GHz channel. These depressed brightness

temperatures are induced by the scattering of microwave radiances by precipitation-sized ice particles which are held aloft by relatively strong updrafts within the convective zone. A sequence of radar imagery from the Darwin/TOGA radar bracketing the SSM/I overpass time indicates a general southeast to northwest motion of the squall line (Steiner, 1992). A broad, trailing stratiform precipitation region to the south and east of the convective leading edge is seen as a relatively uniform depression in the 37 and 85.5 GHz brightness temperatures extending beyond the lower edge of each panel. The brightness temperatures in the trailing stratiform region tend to be higher than in the convective zone, which suggests that the concentrations of scattering ice particles are not as high in the stratiform zone. Regions of smaller-scale convective precipitation are seen as scattering depressions in the 85.5 GHz imagery to the northwest of the squall line, between Bathurst and Melville Islands, and also to the west of the convective line.

The SSM/I retrieval method is applied to a 64 x 64 section of the swath grid centered on the Darwin/TOGA radar site, located at the center of the panels in Fig. 1. All seven of the SSM/I channels are included in the retrieval. After 21 iterations of the quasi-Newton procedure the error functional E in Eq. (1) is effectively minimized without any additional constraints (second term equal to zero) to produce the retrievals of average slant path-integrated precipitating liquid and precipitating ice depicted in Figs. 2a and 2b, respectively. The image intensity in these panels is proportional to the equivalent column-integrated liquid water or ice from the retrieval. A grayscale relating depth-integrated water in kg/m^2 to image intensity is shown at the bottom of each panel.

From Fig. 2, it may be noted that the highest concentrations of integrated liquid precipitation occur along the convective leading edge of the squall line, with lower values spread almost uniformly over the trailing stratiform region. Peak values are close to 4 kg/m^2 in the convective leading edge, with typical values between 1 and 2 kg/m^2 in the trailing stratiform region. Regions of liquid precipitation associated with the convective zones west and northwest of Darwin are also seen in the retrieval. Retrievals of the

column-integrated precipitating ice in Fig. 2b exhibit relatively high values in both the convective leading edge and stratiform zones, on the order of 1 to 1.5 kg/m^2. The retrievals in the convective and stratiform zones have roughly the same magnitude, in contrast to the retrievals of liquid precipitation, which exhibit greater values along the convective leading edge. Also, the maximum ice amounts in the stratiform zone tend to be concentrated to the southeast of Darwin. Precipitating ice amounts are significantly less in the convective regions northwest and west of Darwin, with maximum values of about 0.8 kg/m^2.

A nearly concident radar volume scan from the 5-cm Darwin/TOGA radar starting at 0850 UTC on February 9, 1988 is processed to obtain comparative estimates of integrated liquid and ice precipitation amounts. The radar reflectivities from the volume scan are first interpolated to a cartesian grid with overall dimensions 240 km x 240 km x 18 km. The grid spacings are 2 km in the horizontal and 1.5 km in the vertical. The radar data in elevation/azimuth/range format are interpolated to grid locations using the method of Mohr and Vaughan (1979).

Within the convective leading edge of the squall line, the fractions of liquid and ice precipitation associated with a given radar reflectivity are estimated using the temperature-dependent partitioning scheme of Moss and Johnson (1992). Within the trailing stratiform region, it is assumed that the radar reflectivity is due entirely to ice-phase hydrometeors above the freezing level, and below the 6 C level the radar reflectivity is due entirely to liquid hydrometeors. A linear transition from ice to liquid between 0 C and 6 C is assumed. This stratiform precipitation partitioning scheme is based upon model simulations of anvil clouds using a one-dimensional version of the Ridout (1991, 1993) model. The vertical profile of environmental temperatures is obtained from the Darwin sounding at 2200 UTC on February 9, 1988.

Slant path-integrated liquid and ice-phase precipitation fields derived from the Darwin volume scan are shown in Figs. 3a and 3b, respectively. Fig. 3a may be compared to the

SSM/I retrieval of integrated liquid precipitation in Fig. 2a. Precipitation amounts in the convective leading edge and trailing stratiform regions of the tropical squall line have roughly the same magnitudes in both the SSM/I and radar estimates. A small positive bias in liquid precipitation estimates is evident in the SSM/I retrievals, however. Also, there appear to be spurious retrievals of light preciptation north of the squall line and along the lower edge of Melville Island. The high bias and spurious retrievals may be due, in part, to the lack of explicit nonprecipitating clouds in the cloud ensemble/radiative parameterization. The effect of nonprecipitating clouds is imbedded in the relationships between precipitation amount and upwelling brightness temperature, but the cloud liquid water content does not vary as an independent variable. A region containing significant nonprecipitating cloud can therefore be interpreted as a region of light precipitation in the retrieval. Spurious retrievals of liquid precipitation in coastal regions could also be due to slight errors in SSM/I data geolocation, coupled with the very low sensitivity of the SSM/I channels to variations in precipitating water in coastal regions. Although the SSM/I geolocation was checked and adjusted to match up with a coastline data base, any small error which would move the SSM/I data from land over ocean would require a large adjustment in the land fraction, f_{land}, to compensate. An increase in the amount of liquid precipitation in the retrieval solution could also provide this compensation. In addition, the derivative scaling for liquid precipitation in the vicinity of coastlines must be adjusted to compensate for the lack of sensitivity of upwelling brightness temperatures to variations in precipitating liquid amount. This is because the derivative goes through a change of sign and actually vanishes at a coastal boundary, and therefore derivative magnitudes are relatively small. The scaling of derivatives heightens the sensitivity of the parameterized brightness temperatures to changes in precipitating liquid, and leads to exaggeration of errors in the liquid precipitation retrievals arising from noise or improper geolocation.

The radar-derived slant path-integrated precipitating ice in Fig. 3b may be compared to the SSM/I retrieval in Fig. 2b. There is a fairly good correspondence between the radar and SSM/I retrieved fields, both in pattern and magnitude of precipitating ice. The figures suggest only a slight high bias of the SSM/I retrieved ice amounts over the radar estimates. Note that within about 20 km of the radar site there is a conical data-void region in the radar-derived field, due to the 25° limiting elevation angle of the radar (Keenan, et al., 1988).

3.3 Tropical Storm Emily - 1004 UTC Overpass

The physical retrieval method is applied to SSM/I observations of the incipient Tropical Storm Emily at 1004 UTC on September 21, 1987, as it was developing over the Windward Islands off the northeast coast of South America. The SSM/I 37 GHz and 85.5 GHz horizontal polarization images of Emily on this date are shown in Fig. 4a and 4b, respectively. The northern coast of South American and Caribbean Islands are indicated by white lines, and a brightness temperature grayscale is displayed at the bottom of each panel. The panel dimensions are approximately 1400 km x 1400 km. The most intense convective development in Emily is seen just north of the island of Trinidad and Tobago. This oblong convective zone spans about 250 km, with 37 GHz horizontal polarization antenna temperatures near 255 K, indicating strong absorption and emission from precipitating liquid. Embedded in the convective zone are smaller regions of microwave scattering at 85.5 GHz, especially to the north-northeast of Trinidad and Tobago. The more intense scattering regions are associated with precipitating ice held aloft by the stronger updrafts of the convective zone, and the 85.5 GHz horizontal polarization antenna temperatures reach a minimum of 150 K. To the north and northwest of the convective zone are semi-circular bands in the antenna temperature imagery arising from developing bands of precipitation. Most of these bands contain significant amounts of precipitating ice, identified by scattering depressions in the 85.5 GHz antenna temperatures.

The retrieval algorithm is applied to a 64 x 64 swath grid section centered on Emily. After 21 iterations the error functional in Eq. (1) is minimized to yield the retrievals of grid box average, slant-path integrated precipitating liquid and ice in Figs. 5a and 5b. It may be noted that the pattern of precipitating liquid in Fig. 5a closely follows the pattern of 37 GHz emission in Fig. 4a. Maximum values of integrated liquid occur in the convective core area of Emily, with magnitudes close to 2.6 kg/m^2, and lesser amounts, on the order of 1 kg/m^2, in developing rainbands. Retrievals of precipitating liquid along the coast of South America are spurious, for the most part, since coincident infrared imagery (not shown) at the time of the SSM/I overpass does not show significant cloud along the coast. The precipitation artifacts are likely due to a compensation in the retrieval for variations in land surface emissivity.

Integrated precipitating ice concentrations in the retrieval of Fig. 5b coincide with regions of strong scattering in the 85.5 GHz SSM/I imagery. Precipitating ice retrievals exhibit maximum values close to 3 kg/m^2 in the convective core region, with values up to 1 kg/m^2 in the outer bands. The overall extent and magnitude of the precipitating ice amounts are generally less than those of precipitating liquid in Emily at the overpass time.

3.4 Tropical Storm Emily- 2242 UTC overpass

The SSM/I retrieval procedure is repeated for a subsequent overpass of Emily at approximately 2242 UTC on September 21, 1987. SSM/I imagery from this overpass in the 37 GHz and 85.5 GHz horizontal polarization channels is shown in Figs. 6a and 6b, respectively. These may be compared to the imagery of Emily roughly 12 hours earlier, shown in Figs. 4a and 4b. It may be noted from the figures that the core region of Emily had moved about 400 km to the west-northwest of its original position in the Windward Islands. Also, the storm had taken on the classical structure of a hurricane, with spiral bands and an apparent eye which can be seen in the 85.5 GHz imagery. At the time of the second SSM/I overpass, Emily was still classified as a tropical storm, but was deepening

rapidly, and the storm attained hurricane status early the following day (ref. Case and Gerrish, 1988).

Retrievals of slant-path integrated precipitating liquid and ice from the second overpass of Emily are diplayed in Figs. 7a and 7b, respectively. A correspondence between precipitating liquid and 37 GHz emission patterns (Figs. 6a and 7a) is evident. Also there is a strong correlation between scattering depressions in brightness temperature and retrieved precipitating ice amounts (Figs. 6b and 7b), as it was noted in the 1004 UTC Emily retrievals. Maximum retrieved values of precipitating liquid and ice within Emily are on the order of 2 kg/m^2, although liquid precipitation amounts tend to be higher in general.

4. EXTENSION OF CURRENT WORK AND APPLICATIONS

Work will continue to further improve the representation of clouds and their environments in the sensor response model. Greater variability in the solution fields of emissivity, air temperature, and water vapor may also be allowed if additional sensor data and/or constraints are utilized in the retrieval. Future tests will include the lower-frequency SSM/I data as well as SSM/T, SSM/T-2, and geostationary infrared measurements. Retrievals will be validated using volume-scan radar measurements and conventional weather data.

The sequence of Emily retrievals is utilized in the latent heating analysis and numerical weather prediction model forecasts in Section 4 of this report. Rates of latent heating are inferred from the liquid and ice precipitation distributions and are assimilated into the forecast model fields using a new technique. This application is important because the development or "spin-up" of storms in numerical model forecasts is often retarded due to a lack of fine-scale initial data. The SSM/I-derived latent heating information can partially compensate for this lack of fine-scale data.

Latent heating information may help to improve short-term numerical weather prediction model forecasts of storms, but forecast model fields may also be used to help

improve retrievals through the constraint term in Eq. (1). The interplay between forecast models and retrievals is a subject of further study by the author.

Acknowledgments

The authors wish to thank Robert Aune, John Derber, Brad Ferrier, George Diak, Barry Hinton, James Hollinger, Christian Kummerow, Lynn McMurdie, Grant Petty, Gene Poe, Robert Rabin, James Ridout, David Short, Bill Smith, James Weinman, Mark Whipple and Harold Woolf for their help and inspiration during various phases of this study. This work was supported by NASA Grant NAGW-1855.

REFERENCES

Case, R.A., and H.P. Gerrish, 1988: Annual Summary Atlantic Hurricane Season of 1987. Mon. Wea. Rev., 116, 939-949.

Ferrier, B.S., and R.A. Houze, Jr., 1989: One-dimensional time-dependent modeling of deep convection. Part I: Model dynamics and simulations of GATE cumulonimbus clouds. J. Atmos. Sci., 46, 330-352.

Grody, N.C., 1988: Surface identification using satellite microwave radiometers. IEEE Trans. on Geoscience and Rem. Sensing, 26, 850-859.

Hollinger, J.P. (ed.), 1991: DMSP Special Sensor Microwave/Imager Calibration/Validation Final Report Volume I. Naval Research Laboratory, Washington, D.C.

Keenan, T.D., G.J. Holland, M.J. Manton, and J. Simpson, 1988: TRMM ground truth in a monsoon environment: Darwin, Australia. Aust. Met. Mag., 36, 81-90.

Kummerow, C., R.A. Mack, and I.M.Hakkarinen, 1989: A self-consistency approach to improve microwave rainfall rate estimation from space. J. Appl. Meteor., 28, 869-884.

López, R.E., 1977: The lognormal distribution and cumulus cloud populations. Mon. Wea. Rev., 105, 865-872.

Lorenc, A.C., 1986: Analysis methods for numerical weather prediction. Quart. J. R. Met. Soc., 112, 1177-1194.

Petty, G.W., and K.B. Katsaros, 1990: New geophysical algorithms for the Special Sensor Microwave Imager. Fifth International Conference on Satellite Meteorology and Oceanography, September 3-7, London, England, 247-251.

Pickard, G.L. and W.J. Emery, 1982: Descriptive Physical Oceanography. Pergamon Press, New York, 249 pp.

Ridout, J.A., 1991: A Parameterized Quasi-Five-Cylinder Convective Cloud Model and Its Application to Remote Sensing of Rainfall. Ph.D. thesis, University of Wisconsin, Madison, Wisconsin, 278 pp.

Ridout, J. A., 1993: A quasi-five-cylinder model of deep convection. Part I: Updraft growth in non-sheared environments. Submitted to J. Atmos. Sci..

Shanno, D.F., 1978: Conjugate gradient methods with inexact searches. Math. Oper. Res., 3, 244-256.

Schoeberl, M., J. Pfaendtner, R. Rood, A. Thompson, and B. Wielicki, 1992: Atmospheres panel report to the payload panel. Paleogeography, Paleoclimatology, Paleoecology (Global and Planetary Change Section), 98, 9-23.

Short, D.A., 1988: A statistical-physical interpretation of ESMR-5 brightness temperatures over the GATE area. In Tropical Rainfall Measurements, Proceedings of the International Symposium on Tropical Precipitation Measurements, Tokyo. A. Deepak Publishing, Hampton, Virginia.

Simpson, J., R.F. Adler, G.R. North, 1988: A proposed Tropical Rainfall Measuring Mission (TRMM) Satellite. Bull. Amer. Met. Soc., 69, 278-295.

Smith, W.L., H.M. Woolf, P.G. Abel, C.M. Hayden, M. Chalfant, and N. Grody, 1974: Nimbus-5 sounder data processing system Part I: Measurement characteristics and data reduction procedures. NOAA Technical Memorandum NESS 57, 99 pp.

Xiang, X., E.A. Smith, and G.J. Tripoli, 1992: A cloud and radiation model-based algorithm for rainfall retrieval from SSM/I multispectral microwave measurements. Proceedings of the Sixth Conference on Satellite Meteorology and Oceanography, Atlanta, Georgia, 286-289.

Table 1. Retrieved geophysical parameters (P) and associated spatial constraints in the SSM/I physical retrieval method.

Parameter	Spatial Constraints
land fraction within each grid box	none
land emissivity parameters from Grody (1988) parameterization	uniform over grid
ocean emissivity parameters from Grody (1988) parameterization	uniform over grid
first eigenfunction weight of water vapor mixing ratio profile	uniform over land, no constraint over ocean
precipitation fraction within each grid box	none
mean slant path depth of precipitating liquid within the precipitation fraction	none
mean slant path depth of precipitating ice within the precipitation fraction	none

(a)

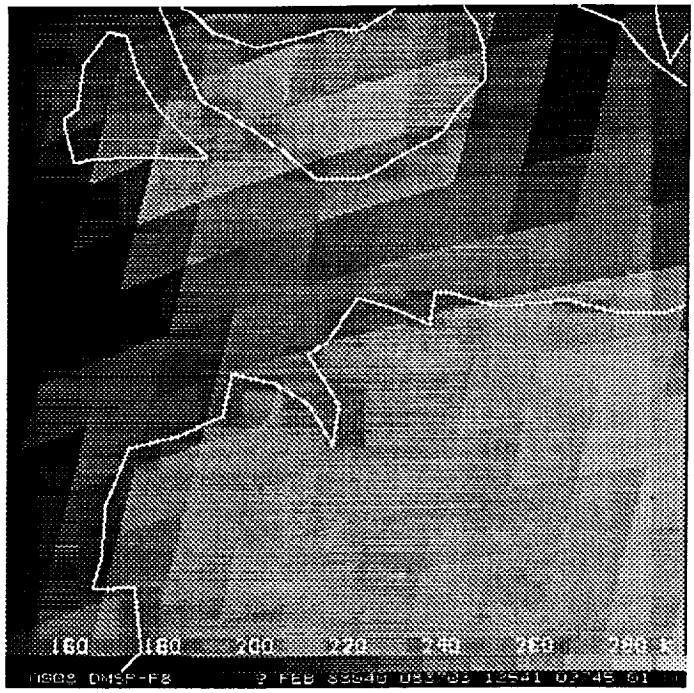

(b)

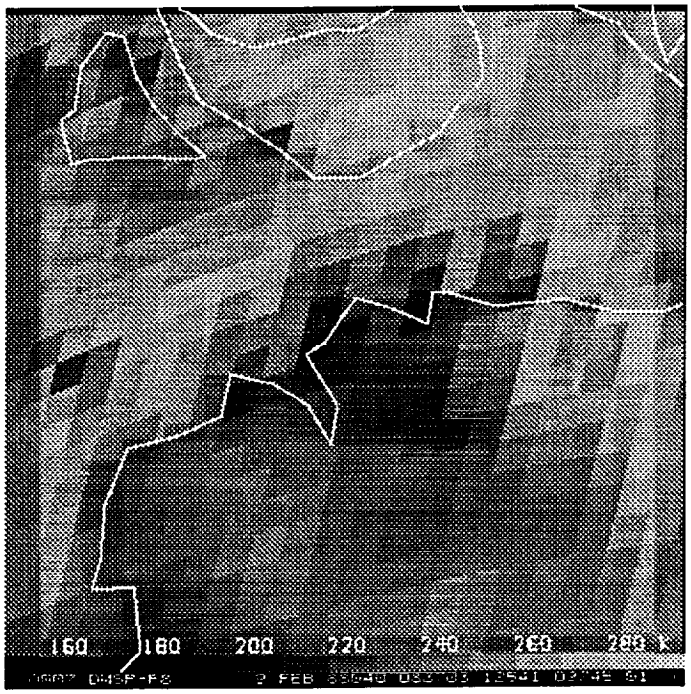

Fig. 1. SSM/I antenna temperature imagery of a tropical squall line in the vicinity of Darwin, Australia at 0906 UTC on February 9, 1988. The 37 GHz horizontal polarization imagery is shown in panel (a), and the 85.5 GHz horizontal polarization imagery is shown in panel (b). Coastlines are indicated by solid white lines. The area represented by each panel is approximately 250 km x 250 km.

(a)

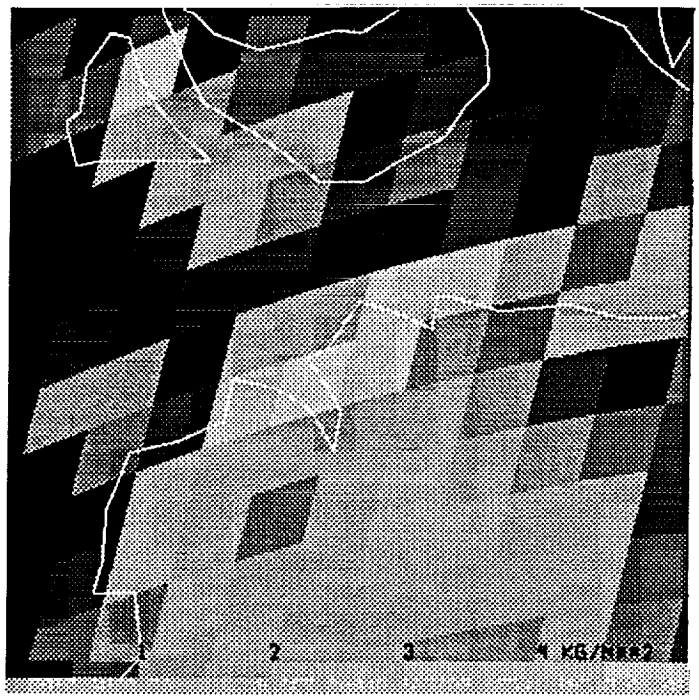

(b)

Fig. 2. Retrieved distributions of slant path-integrated precipitating liquid (a) and ice (b) derived from the SSM/I overpass of Darwin, Australia at 0906 UTC on February 9, 1988.

(a)

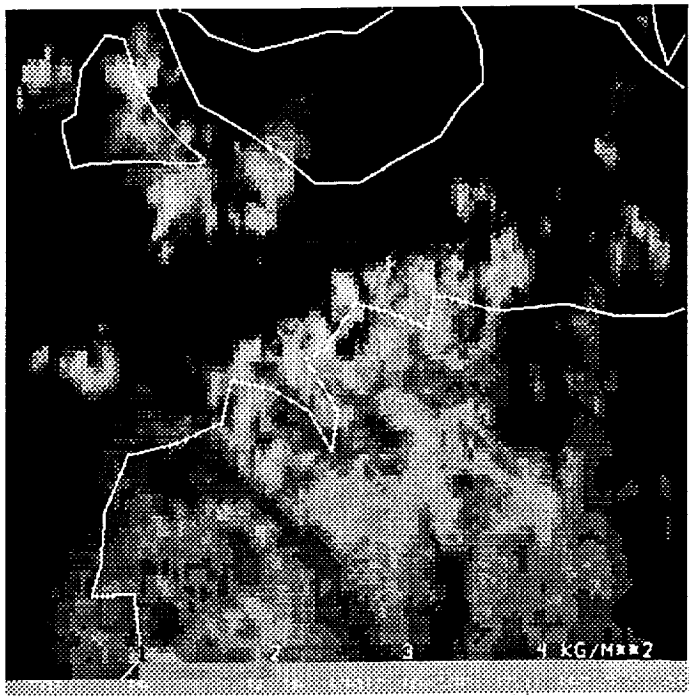

(b)

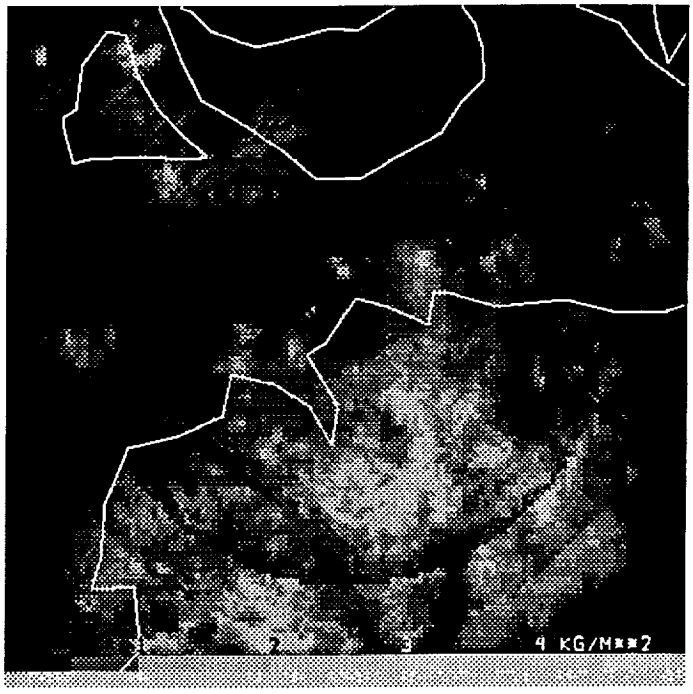

Fig. 3. Distributions of slant path-integrated precipitating liquid (a) and ice (b) derived from a volume scan of the Darwin/TOGA radar starting at 0850 UTC on February 9, 1988.

(a)

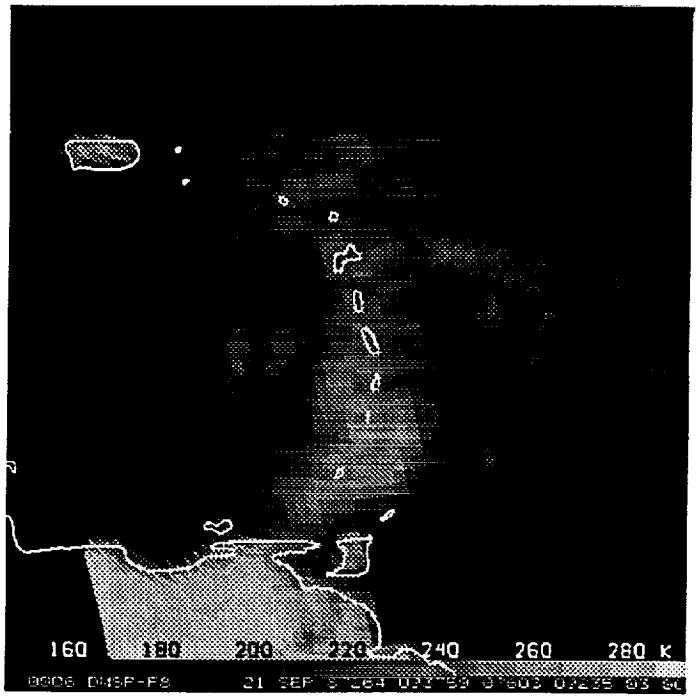

(b)

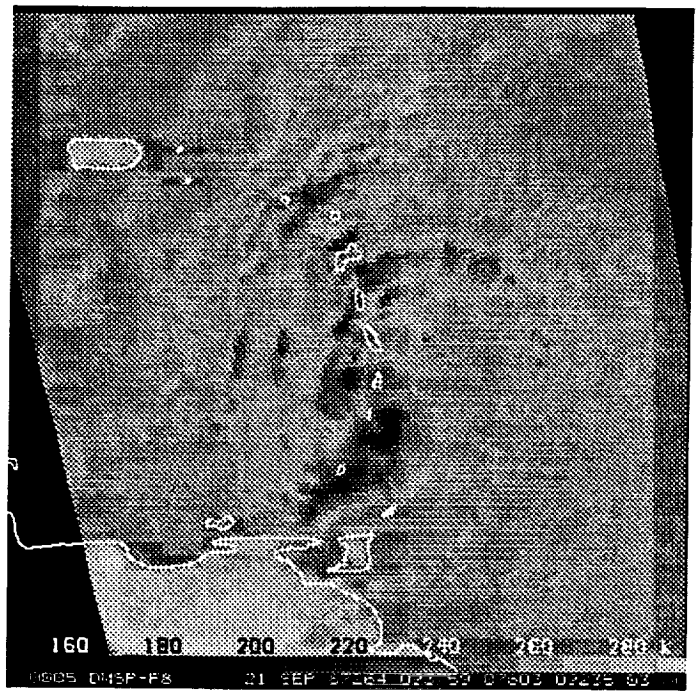

Fig. 4. SSM/I antenna temperature imagery of Tropical Storm Emily in the Windward Islands at 1004 UTC on September 21, 1987. The 37 GHz horizontal polarization imagery is shown in panel (a), and the 85.5 GHz horizontal polarization imagery is shown in panel (b). Coastlines are indicated by solid white lines. The area represented by each panel is approximately 1500 km x 1500 km.

(a)

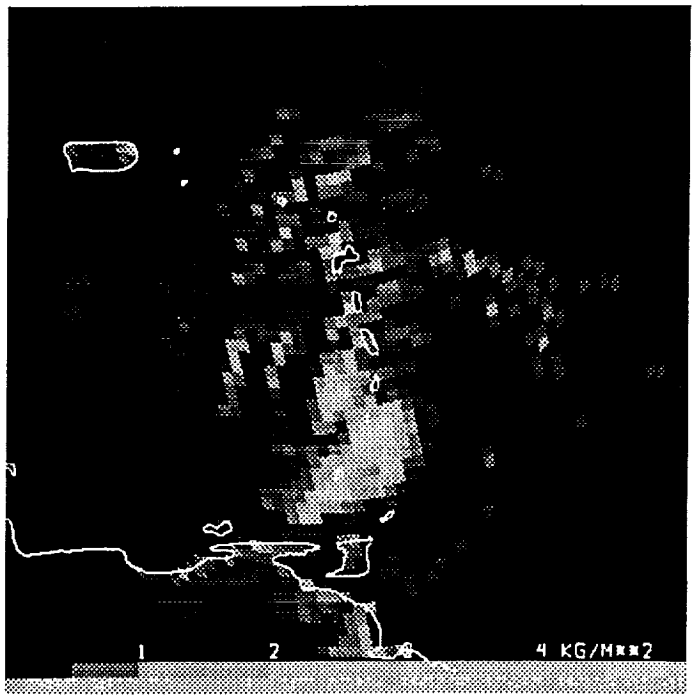

(b)

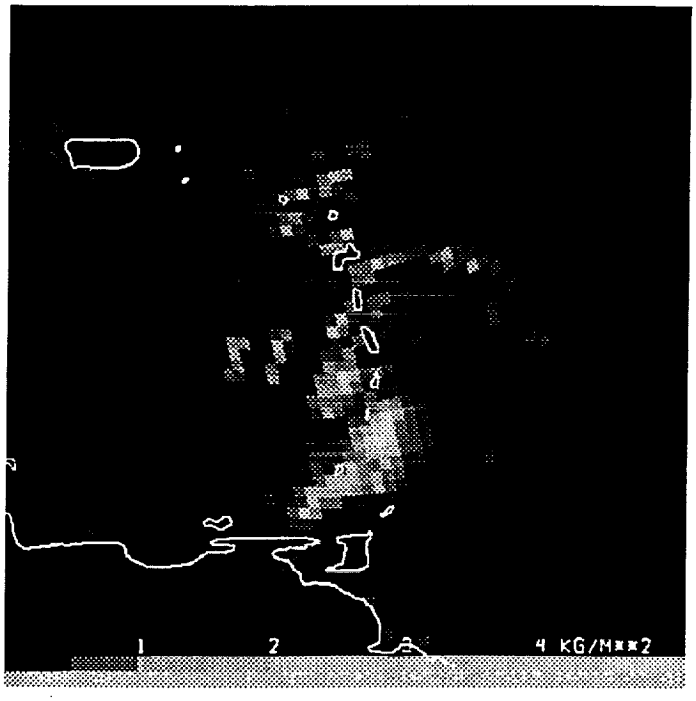

Fig. 5. Retrieved distributions of slant path-integrated precipitating liquid (a) and ice (b) derived from the SSM/I overpass of Tropical Storm Emily at 1004 UTC on September 21, 1987.

(a)

(b)

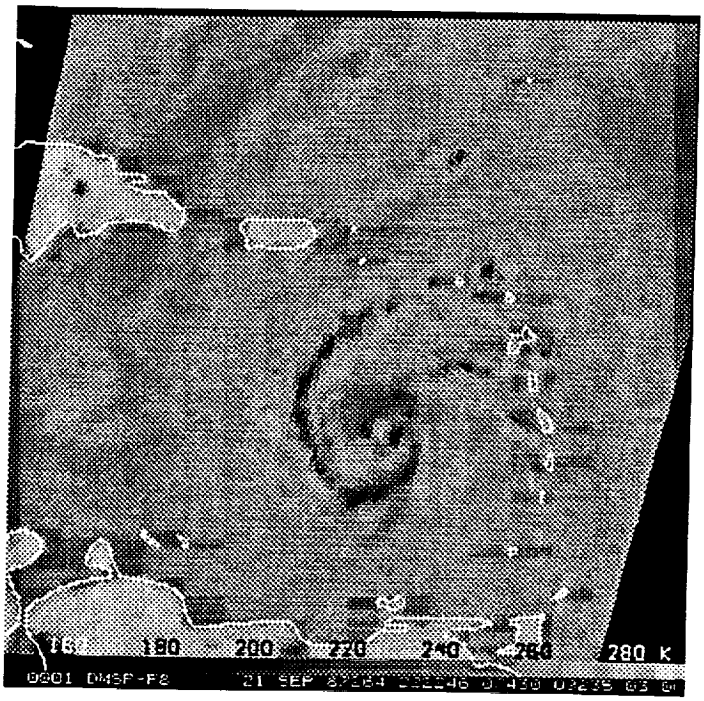

Fig. 6. SSM/I antenna temperature imagery of Tropical Storm Emily north of Venezuela at 2242 UTC on September 21, 1987. The 37 GHz horizontal polarization imagery is shown in panel (a), and the 85.5 GHz horizontal polarization imagery is shown in panel (b). Coastlines are indicated by solid white lines. The area represented by each panel is approximately 1500 km x 1500 km.

(a)

(b)

Fig. 7. Retrieved distributions of slant path-integrated precipitating liquid (a) and ice (b) derived from the SSM/I overpass of Tropical Storm Emily at 2242 UTC on September 21, 1987.

Forecast Model Applications of Retrieved Three Dimensional Liquid Water Fields

By

William H. Raymond and William S. Olson

Cooperative Institute for Meteorological Satellite Studies

1225 West Dayton Street

University of Wisconsin

Madison, Wisconsin 53706

To be modified and submitted to *J. Appl. Meteor.*

Abstract

Retrieved three dimensional liquid water fields are used in a regional mesoscale forecast model to help induce storm development and enhance the early production of precipitation. Vertical layer-mean heating rates are regressed against slant path-integrated liquid and ice precipitating water contents, based upon a cloud ensemble model. This procedure yields a best fit two-parameter regression formula for each vertical layer. The regression formulae are used to estimate latent heating values from the slant-path integrated liquid and ice precipitation water contents from SSM/I retrievals. In the forecast model, diabatic temperature contributions are calculated and used in a diabatic forcing procedure with or without diabatic initialization. We find that the time needed to spin-up precipitation processes in tropical storm Emily is greatly accelerated, and the horizontal distribution of the forecast fields is improved through the application of the data.

1. Introduction

Mesoscale forecasts must go through a development stage when initial conditions do not adequately resolve mesoscale circulations. This spin-up is common in numerical weather prediction since much of the data is obtained from synoptic scale observations. Also, the failure to include cloud, rain and ice fields in the assimilation procedure means than this spin-up process is repeated with the next sequential forecast. This neglect is a natural consequence since cloud and rain water data have been unavailable. There has been some effort to circumvent this problem through the use of diabatic or cumulus initialization techniques (Errico and Rasch 1988; Donner 1988; Turpeinen et al. 1990; Tarbell et al 1981; Salmon and Warner 1986, etc.). These procedures have been somewhat successful, but the vertical distribution of the diabatic heating remains a major problem since raingauge reports give a measure of surface precipitation depth, and visible/infrared remote sensing methods typically yield estimates of surface rain rate.

Some success in assimilating explicit cloud and rain water information, and initializing diabatic processes was demonstrated in chapter one of this report. A continuation of these procedures is presented here, but using radiance data measured by the Special Sensor Microwave/Imager (SSM/I) to estimate the heating rates. SSM/I-derived estimates of integrated precipitating liquid and ice are optimized using physical information supplied by a cloud ensemble/radiative model of convective and stratiform clouds. Vertical layer-mean latent heating rates from the cloud ensemble model are regressed against the slant path-integrated liquid and ice precipitation water contents to determine the best fit two parameter regression coefficients for each vertical layer. Given SSM/I retrievals of path integrated liquid and ice precipitation amounts, the regression formulae yields a vertical distribution of heating rates for our forecast model applications.

In this final report only the data associated with tropical storm Emily is evaluated. This will be expanded in the near future for a proposed journal article. Forecasts are made using the National Meteorological Centre's (NMC) initialized global analyses. When only an adiabatic initialization is used, our forecasts produce no development in the vicinity of the Emily disturbance. This result

suggests that the initial data are missing most of the mesoscale information needed to begin the storm development. Forecasts are dramatically different when either diabatic forcing or diabatic forcing combined with diabatic initialization is used. These findings are presented and discussed in this portion of the final report, but first, additional details about the three dimensional diabatic heating rate data are presented.

2. Latent Heating Rates for Emily at 1004 UTC, September 21, 1987

Latent heating rates in Emily at 1004 UTC, September 21, 1987 are derived from the SSM/I retrieval of the slant path-integrated precipitation liquid and ice distributions discussed in chapter 3 of this report. The latent heating analysis is based upon regression formulae which are applied to the retrieved precipitation fields. The regression formulae are derived as follows.

Latent heating rates from the convective and stratiform cloud simulations in each of the cloud ensembles of chapter 2 are interpolated to grid points within the 25 km x 25 km x 20 km domain shown in Fig 3 of that section. The heating rates are then averaged in 1.1 km thick layers over the 25 km x 25 km domain to obtain layer-mean estimates at 17 levels for each cloud ensemble. The layer-mean latent heating rates are regressed against the slant path-integrated liquid and ice precipitation water contents in the same ensemble using the formula

$$H_{lat}=a_1*PLWP + a_2*PIWP , \qquad (1)$$

where H_{lat} is the latent heating rate in joules/m^3-s, PLWP is the slant path-integrated liquid precipitation averaged over the grid box, PIWP is the slant path-integrated ice precipitation averaged over the grid box, and a_1 and a_2 are the best-fit regression coefficients. Both the slant path-integrated liquid and ice amounts are assumed to have units of kgm^{-2} in (1). PLWP and PIWP are chosen as predictors of the latent heating rate, since these parameters are estimated in the SSM/I physical retrieval method (see chapter 3). Note that H_{lat} in the above formula equals zero if both

PLWP and PIWP are zero, which is a constraint on the regression formula since it is assumed that their is no latent heating if no cloud or precipitation exist.

A total of 213 convective cloud ensembles and 42 stratiform cloud ensembles based upon the GATE day 261 environment (1200 UTC sounding from Quadra research vessel) are utilized in the regression analysis. The regression coefficients and formula errors for each of the 17 standard levels are summarized in Table 1. Note that at levels below the freezing level (4km), latent heating rates increase with the path-integrated precipitation liquid amount and decrease with the path-integrated precipitating ice amount. The negative correlation between latent heating rates and ice amount (negative values of a_2) can be linked to the differences between the thermodynamics of convection and stratiform precipitation. Low level heating is normally associated with convective precipitation events (Tao et al. 1990). However, if precipitating ice concentrations are high relative to precipitating liquid amounts, then a stratiform precipitation event is indicated. Stratiform precipitation is usually associated with cooling at altitudes below the freezing level, due to melting of precipitating ice and evaporation of rain.

At levels between 5.70 km and 10.70 km, the latent heating rate is positively correlated with both the liquid and ice precipitation amounts. At higher altitudes the magnitude of the latent heating rate fall off substantially, and it is difficult to infer any systematic trends. Latent heating rates at 17.45 km and 18.58 km are so low that meaningful regressions are not possible. It may also be noted that correlations between latent heating rate regression estimates and the true heating rates are significant at and below 10.70 km, with the exception of the 2.82 km and 3.94 km levels.

The latent heating rates are inferred from the slant-path integrated precipitating liquid and ice estimates obtained from the SSM/I physical retrieval method, upon inserting these estimates into the regression formula (1) above. The latent heating rates at the standard levels (see Table 1) are then interpolated to levels at 50 mb increments between 1000 mb and 100 mb inclusive. These vertically-interpolated values are then interpolated in the horizontal from the 25 km resolution swath grid to the 40 km resolution forecast model grid. The contour plot in Fig 1, superimposed on the GOES IR image valid at 1001 UTC 21 September 1987, shows the distribution of temperature

increase associated with latent heating at sigma level 10, approximately the 700 mb level, inferred from the 1004 UTC Emily retrieval (also see Figs 5a and 5b of chapter 3). Here the maximum latent heating produces a temperature change of 0.07 C per 300 s^{-1}. The bi-modal vertical distribution of the latent heating is largest at sigma levels 12 and 6, approximately at the 850 and 500 mb levels, where the maximum diabatic activity is equivalent to 0.44 C and 0.37 C per 300 s^{-1}, respectivity.

3. The Diabatic Procedure

A diabatic initialization and/or diabatic forcing procedure is installed into the CIMSS forecast model to take full advantage of the semi-implicit method, as previously described in chapter 1. This is accomplished by modifying the semi-implicit average temperature $T^{2\tau}$, computed from the thermodynamic equation (McGregor et al 1978; Leslie et al 1985), by adding the externally determined temperature contribution T_{ex}. This redefines the average temperature at the appropriate grid points according to

$$T^{2\tau} \equiv T^{2\tau} + T_{ex} , \tag{2}$$

where

$$T_{ex} = (L\Delta t/\rho c_p)H_{lat} , \tag{3}$$

and

$$T^{2\tau} = [T^{\tau+1} + T^{\tau-1}]/2 . \tag{4}$$

Here c_p is the specific heat for constant pressure, H_{lat} the remotely sensed heating rate determined by (1), L is the latent heat of condensation or evaporation and the superscripts signify the time step.

During the diabatic forcing or diabatic initialization process, which is designed to initialize the mesoscale circulation, the mixing ratio can be altered as desired To avoid excessive evaporation, some upward adjustment of the mixing ratio may be required, namely

$$q_v = q_v + \Delta q_v \,. \tag{5}$$

In our calculations Δq_v is set to give the equivalent of the amount of moisture needed in the condensation process to achieve the observed heating rates.

During the vertical mode initialization procedure (Bourke and McGregor 1983) T_{ex} is held constant at the selected grid points. The application early in the forecast period of an external diabatic forcing represents a natural extension of the diabatic initialization. This procedure requires at each time step that the grid point average temperature is modified by the difference between the external contribution T_{ex} and the model produced diabatic temperature $T_{IN} = |\Delta t L Q / c_p|$, yielding

$$T^{2\tau} \equiv T^{2\tau} + (T_{ex} - T_{IN}) \,. \tag{6}$$

Here Q is the model produced liquid water condensation at each grid point over one time step. In our study the quantity in parenthesis in (6) is taken to be non-negative. Equation (6) can be interpreted as a blending over time, between the forcing and the model diabatic production. If all precipitating grid locations have sufficient condensation, then the external forcing is reduced to zero. Even though this is the desired result it is not explicitly required before the termination of the forcing at a preselected forecast time. This application of the external forcing is somewhat modified from the procedure used in Newtonian nudging (Hoke and Anthes 1976).

Note that (2) and (6) are similar, except model produced condensation reduces the external forcing in (6). This reduction removes the potential for over forcing. The external diabatic forcing is a natural continuation of diabatic contributions introduced in the initialization. The forcing is

applied starting with the first time step after the vertical mode initialization and continued until the model produces an equivalent temperature change or until a preselected termination time is exceeded. With each passing time step, T_{ex} is advected by the model horizontal winds according to

$$\partial(T_{ex})/\partial t + u\partial(T_{ex})/\partial x + v\partial(T_{ex})/\partial y = 0. \qquad (7)$$

In regions with strong vertical shear it may be advantageous to advect T_{ex} using a vertically averaged horizontal wind. The advection process will ultimately smooth and diffuse the heating if (7) is used over a sufficiently large time period. Normally the diabatic forcing lasts only a few hours. In any event, some tapering must be used to terminate the diabatic forcing, provided (6) is not reduced to zero by model generated condensation processes. Remotely sensed time variations in T_{ex} could also be allocated for if known. In our calculations, T_{ex} is assumed to remain unchanged except for horizontal advection.

An alternative approach is to apply the external diabatic forcing at the satellite observation time. Then, a gradual transition into and exit from the external diabatic forcing regime greatly avoids the production of noise and gravity waves during the forecast. The time span needed to produce gradual changes depends upon the magnitude of the external forcing. The length of time period used in the forcing can be varied to achieve the desired result. Excessively long periods of forcing should be avoided since they can can lead to some negative consequences. For example, too much diabatic forcing can cause a build up of excessive amounts of liquid water that can eventually lead to large amounts of precipitation drag which cause downbursts that choke off the convergence and the moisture supply. Events of this type can reduce the overall storm development because they may produce storm-wide low level divergence that chokes off the moisture supply.

4. Forecasting Emily

In Figs 2 and 3 are 700 mb geopotential heights and divergence fields from a twenty four hour forecast beginning at 0000 UTC 21 September 1987. These fields are super-imposed over the

GOES infrared (IR) image for the region containing tropical storm Emily valid at 0001 UTC 22 September 1987. This simulation uses an adiabatic initialization with 4 vertical modes. Note in Figs 2 and 3 that the height and divergence fields show no development whatsoever in the immediate vicinity of Emily. No precipitation is associated with this flow. However, some precipitation does occur over elevated topographical features in association with changes in the diurnal cycle.

Retrieved heating rates for Emily, based on the physical retrieval and regression procedures described in section 2, provides a knowledge of both the horizontal and vertical distribution of the diabatic heating. This information is then used directly in the CIMSS model diabatic initialization and diabatic forcing procedures, as described in section 3. Diabatic forcing, beginning at time step 120, i.e., at 1000 UTC 21 September 1987, and ending at time step 165, is applied during a forecast according to (2) through (7). The introduction contains a one and one-half hour ramp-up, with one and one-quarter hours of constant forcing, and a one hour ramp-down procedure. Thus, the diabatic forcing begins slowly ten hours into the forecast and shuts down 3.75 hours later. The length of the ramps can be adjusted based on model response. A tapered introduction and exit is necessary to keep gravity and inertia wave noise to a minimum.

At the end of the twenty-four hour forecast, or fourteen hours after the start of the forcing, the 700 mb geopotential heights contain several closed contour centers, as seen in Fig 4. Some indication of the development of a warm core is provided by the center containing the 3200 m contours. The convergence (negative divergence) at 700 mb (Fig 5) has a maximum of approximately -8×10^{-5} s^{-1} directly over the location of Emily. Also, the positive vorticity reaches a magnitude of 24×10^{-5} s^{-1} at 700 mb, as illustrated in Fig 6. The integrated precipitating liquid water, fourteen hours after the start of the diabatic forcing, has a maximum of 4.0 kgm^{-2} (Fig 7). However, smaller magnitudes are found in the SSM/I physical retrieval, shown in Fig 8, which contains a maximum near 2.5 kgm^{-2} of precipitating liquid and ice. Also, the spatial distribution for the retrieved precipitating field shows a comma shape. The lack of spatial structure in the forecasted quantity is though to be linked to a common feature among models, namely, a tendency to over-

develop precipitation situations. Too much condensation occurs in grid scale explicit cloud calculations because moist and dry downdrafts, which help to restrict the total condensation, are not correctly parameterized. Inadequacies in the vertical and horizontal mixing or turbulence parameterization, too coarse of a grid resolution, and other deficiencies in the cloud and rain water parameterizations may also be contributing factors. To help keep the storm from over developing or developing too rapidly, in our calculations the maximum amount condensed at any one time step at any grid location is restricted by requiring that $0< |Q/fq| <0.5$, where f is the Coriolis parameter and q the mixing ratio. Conservation of moisture is retained since the excess is carried in the slightly super saturated mixing ratio. This is thought to be a better alternative than using artificial diffusion, which is non-conservative, in our 40 km resolution simulations.

The remotely retrieved heating rate information described in section 2 is used in a fourteen hour forecast containing a diabatic initialization followed by two hours (24 time steps) of diabatic forcing. Four vertical modes are used in this simulation since, as described in our earlier work, the combined diabatic initialization and diabatic forcing is not sensitive to the choice of the vertical wave number in the vertical mode initialization (Bourke and McGregor 1983).

Results from the fourteen hour forecast are shown in Figs 9 through 12. The forecasted 700 mb height field contains two centers with closed contours (Fig 9). For the same time period, convergence (-1.2×10^{-5} s^{-1}) is found over this region (Fig 10) associated with a positive vorticity that has a maximum value of 16×10^{-5} s^{-1} (Fig 11). This development, that coincides with Emily, is somewhat less than that shown in Figs 4 through 8 primarily because the length of the forcing is less. This weaker signal is also evident in the integrated rain water shown in Fig 12, when compared with the values shown in Fig 7. Dispite having less integrated rain water, the weaker system has more rainfall at the surface during the first few hours of its existence, presumely because the clouds are closer to the surface and because the weaker vertical motions do not greatly impede the precipitating liquid.

5. Summary

Vertical heating profiles (1000 UTC 21 September 1987) are constructed using the vertical layer-mean latent heating rates from a cloud ensemble model and the slant path-integrated liquid and ice precipitating water contents retrieved from the SSM/I. This information is then used in a diabatic initialization and/or diabatic forcing procedure to help encourage the spin-up the precipitation and the development of tropical storm Emily. The robust nature of the diabatic forcing procedure, as described and tested in chapter 1 of this final report, is evident by the successful generation of a disturbance in both the twenty four and fourteen hour forecasts. One additional case study should be done to complete our investigation, after which the diabatic forcing procedure should be tested in an operational setting where many different meteorological situations can occur. The physical retrieval technique for estimating the vertical structure of the latent heating looks extremely promising.

Acknowledgments. This work was supported by NASA Grant NAGW-1855. One author (WHR) was supported in part by National Science Foundation Grant ATM-8920508.

References

Bourke, W. and J. L. McGregor, 1983: A nonlinear vertical mode initialization scheme for a limited area prediction model. *Mon. Wea. Rev.*, **111**, 2285-2297.

Donner, L. J., 1988: An initialization for cumulus convection in numerical weather prediction models. *Mon. Wea. Rev.*, **116**, 377-385.

Errico, R. and P. J. Rasch, 1988: A comparison of various normal-mode initialization schemes and the inclusion of diabatic processes. *Tellus*, **40A**, 1-25.

Fiorino, M and T.T. Warner, 1981: Incorporating surface winds and rainfall rates into the initialization of a mesoscale hurricane model. *Mon. Wea. Rev.*, **109**, 1914-1929.

Hoke, J. E. R. A. Anthes, 1976: The initialization of numerical models by a dynamical initialization technique. *Mon. Wea. Rev.*, **104**, 1551-1556.

Leslie, L. M., G. A. Mills, L. W. Logan, D. J. Gauntlett, G. A. Kelly, J. L. McGregor and M. J. Manton, 1985: A high resolution primitive equation NWP model for operations and research. *Aust. Meteor. Mag.*, **33**, 11-35.

McGregor, J. L., L. M. Leslie and D. J. Gauntlett, 1978: The ANMRC limited-area model: consolidated formulation and operational results. *Mon. Wea. Rev.*, **106**, 427-438.

Salmon, E. M., and T. T. Warner, 1986: Short-term numerical precipitation forecasts initialized using a diagnosed divergent-wind component. *Mon. Wea. Rev.*, **114**, 2122-2132.

Tao, W-K., J. Simpson, S. Lang, M. McCumber, R Adler and R. Penc, 1990: An algorithm to estimate the heating budget from vertical hydrometer profiles. *J. Appl. Meteor.*, **29**, 1232-1244.

Tarbell, T. C., T. T. Warner and R. A. Anthes, 1981: An example of the initialization of the divergent wind component in a mesoscale numerical weather prediction model. *Mon. Wea. Rev.*, **109**, 77-95.

Turpeinen, O. M., L. Garand, R. Benoit and M. Roch, 1990: Diabatic initialization of the Canadian regional finite-element (RFE) model using satellite data. Part I: Methodology and application to a winter storm. *Mon. Wea. Rev.*, **118**, 1381-1395.

Table 1. Latent heating rate regression formulae coefficients and statistics. Note that there are insufficient data to perform a regression at the two highest levels. Units of altitude are kilometers, and bias and σ_{err} are in joules/m^3-s.

altitude	a_1	a_2	bias	σ_{err}	r
0.56	0.370	-0.251	-0.073	0.430	0.617
1.69	0.909	-0.355	-0.087	0.942	0.528
2.82	0.108	-0.122	0.066	0.478	0.229
3.94	0.227	-0.119	0.018	0.532	0.305
5.07	0.344	0.044	0.007	0.289	0.607
6.19	0.166	0.168	0.008	0.185	0.786
7.32	0.045	0.181	0.007	0.139	0.841
8.45	0.059	0.123	0.007	0.112	0.809
9.57	0.044	0.072	0.009	0.062	0.853
10.70	0.038	0.025	0.006	0.054	0.650
11.82	0.045	-0.003	0.006	0.065	0.436
12.95	0.170	-0.022	0.022	0.162	0.576
14.08	0.041	-0.007	0.002	0.049	0.461
15.20	-0.002	0.000	-0.000	0.002	0.545
16.33	-0.000	0.000	0.000	0.000	0.443
17.45	----	----	----	----	----
18.58	----	----	----	----	----

List of Figures

Fig. 1. Temperature values (C) x 100 used in the diabatic initialization and/or diabatic forcing routine at sigma level 8 (approximately 700 mb).

Fig. 2. Height field at 700 mb from the twenty four hour forecast with adiabatic initialization conditions and no diabatic forcing. Contour interval is 4 m.

Fig. 3. Same as Fig 2 but for the divergence field. Contour interval is 1 x 10^{-5} s^{-1}.

Fig. 4. The 700 mb height field from the twenty four hour forecast with diabatic forcing applied beginning 10 hours into the forecast and lasting for 3.75 hours. Contour interval is 4 m.

Fig. 5. Same as Fig 4 but showing the divergence field. The contour interval is 1 x 10^{-5} s^{-1}.

Fig. 6. Same as Fig 4 but showing the vorticity. Contour interval is 4 x 10^{-5} s^{-1}.

Fig. 7. Vertically integrated rain water x 10 associated with the fields shown in Figs 4, 5 and 6. Contour interval is 0.5 kgm^{-1}.

Fig. 8. Retrieved estimates of the integrated precipitating liquid and ice from SSM/I radiances (Olson, 1993).

Fig. 9 The 700 mb heights from the fourteen hour forecast that used diabatic initialization and two hours of diabatic forcing. Contour interval is 4 m.

Fig. 10. Same as Fig 9 but showing the divergence. Contour interval is 1 x 10^{-5} s^{-1}.

Fig. 11. Same as Fig 9 but showing the vorticity. Contour interval is 4 x 10^{-5} s^{-1}.

Fig. 12. The vertically integrated rain water x 10 associated with the fields shown in Fig 9, 10 and 11. Contour interval is 0.5 kgm^{-1}.

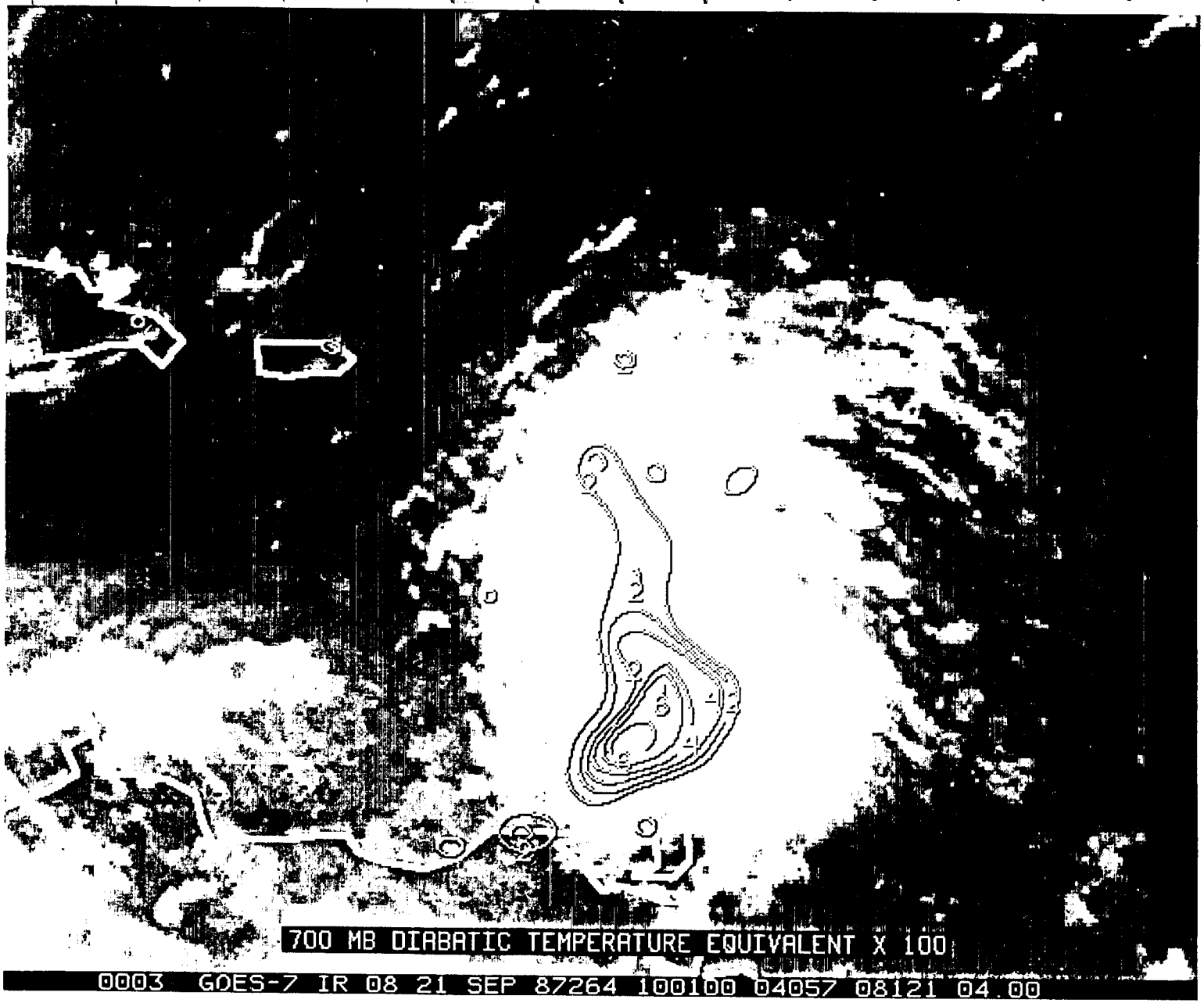
700 MB DIABATIC TEMPERATURE EQUIVALENT X 100
0003 GOES-7 IR 08 21 SEP 87264 100100 04057 08121 04.00

Fig. 1

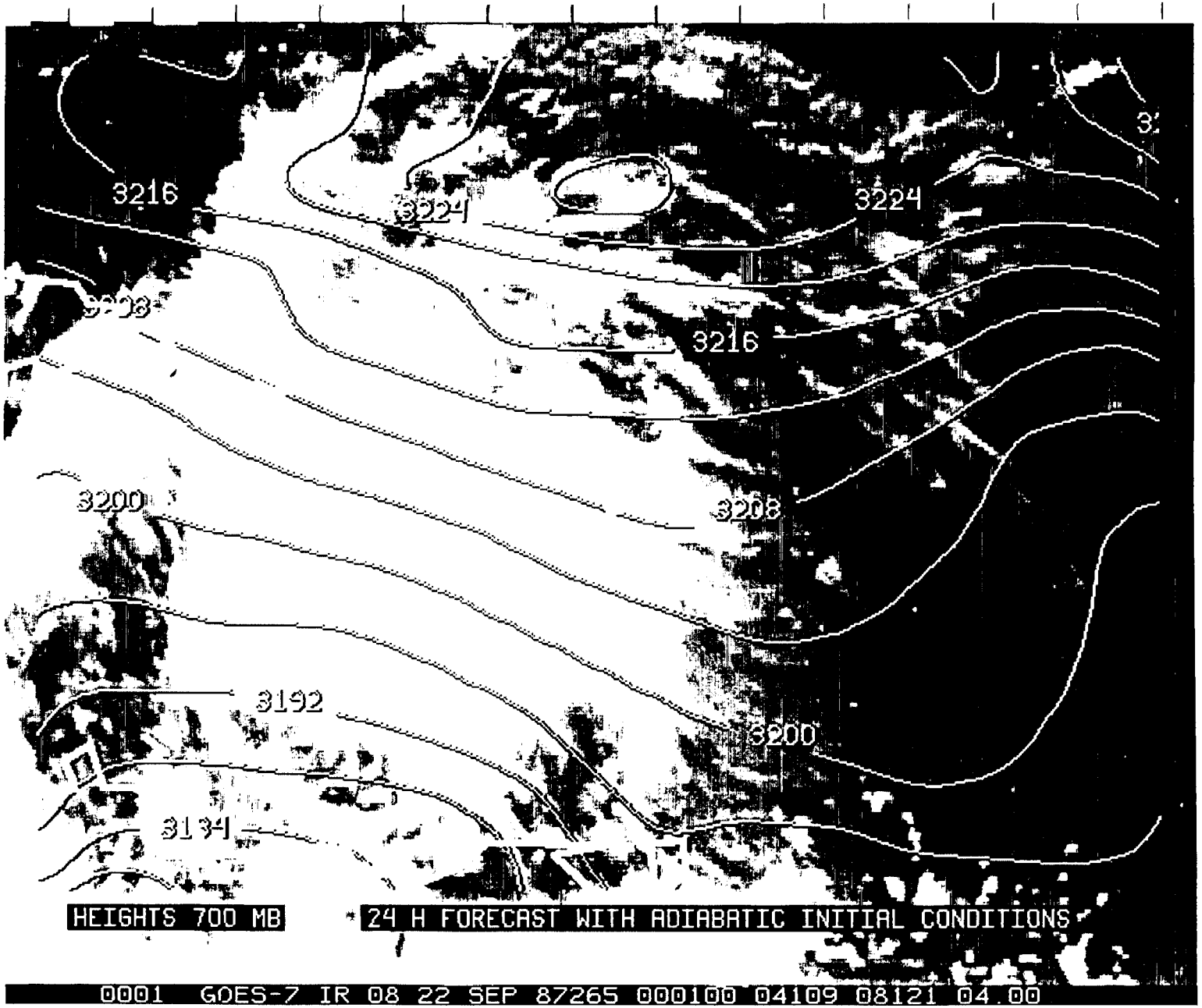
3216
3224
3224
3216
3200
3208
3192
3200
3184
HEIGHTS 700 MB
24 H FORECAST WITH ADIABATIC INITIAL CONDITIONS
0001 GOES-7 IR 08 22 SEP 87265 000100 04109 08121 04 00

Fig 2

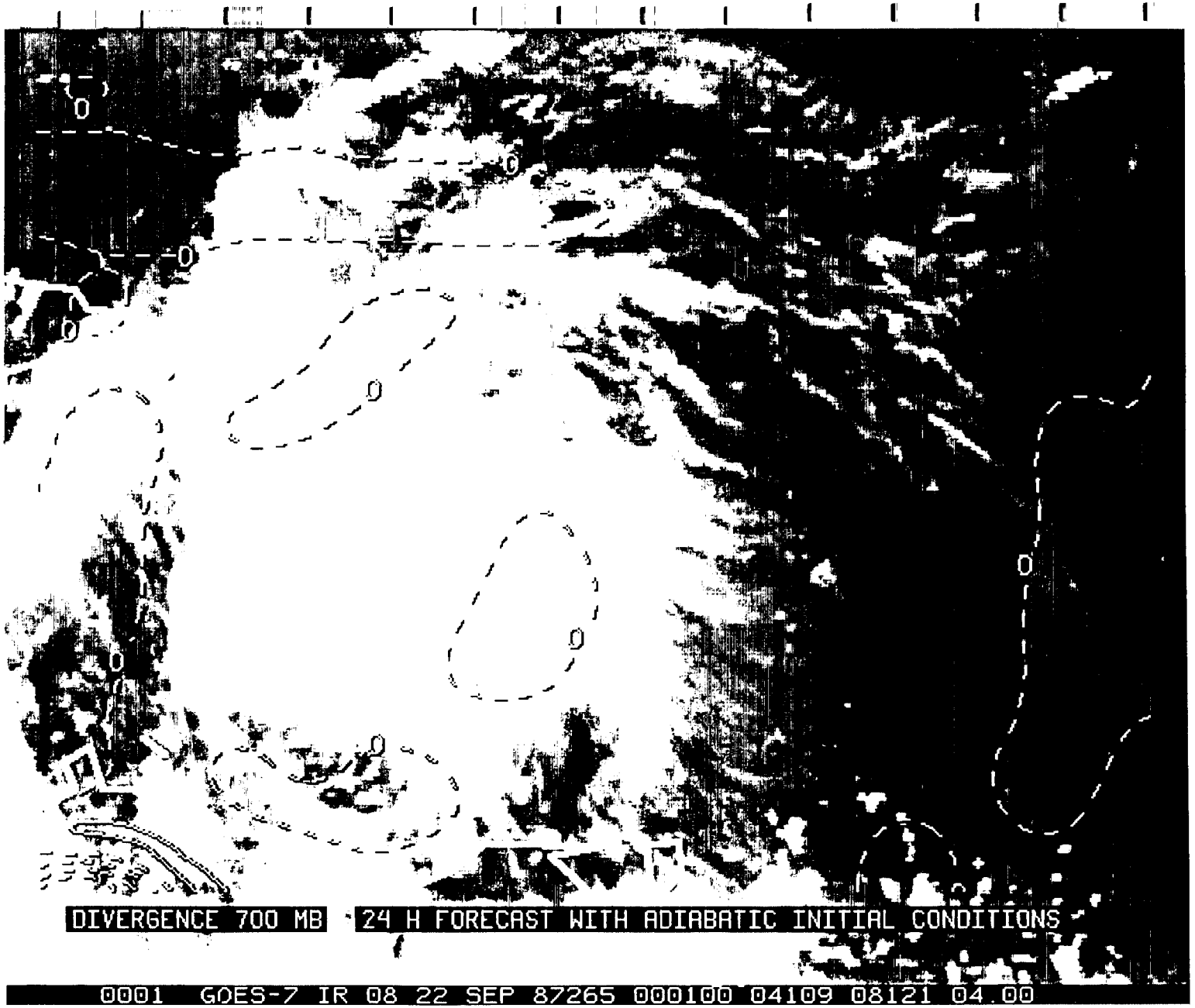
0
0
0
0
0
0
0
0
0
0
DIVERGENCE 700 MB
24 H FORECAST WITH ADIABATIC INITIAL CONDITIONS
0001 GOES-7 IR 08 22 SEP 87265 000100 04109 08121 04.00

Fig 3

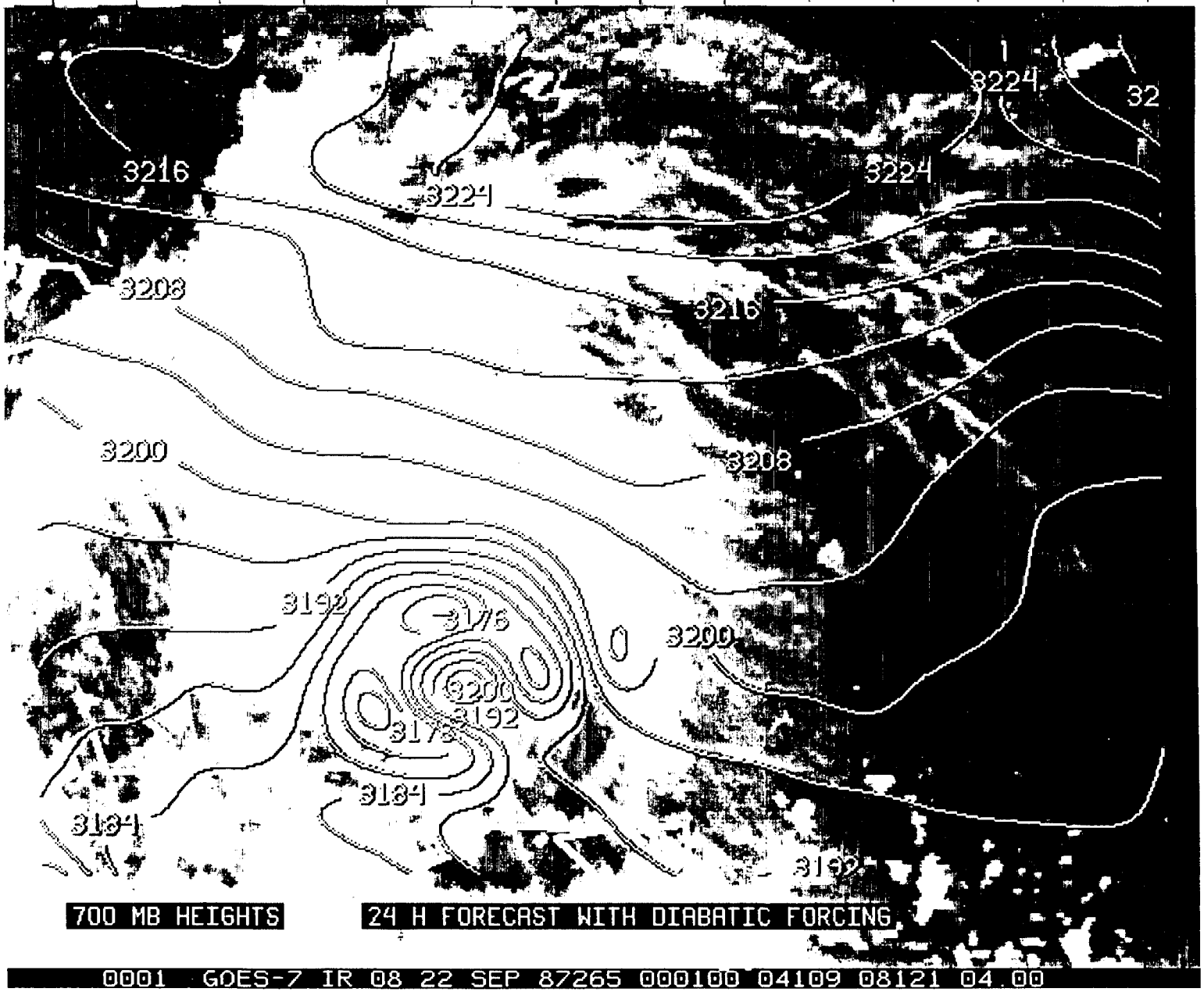
3224
32
3216
3224
3224
3208
3216
3200
3208
3192
3176
3200
3200
3192
3176
3184
3184
3192
700 MB HEIGHTS
24 H FORECAST WITH DIABATIC FORCING
0001 GOES-7 IR 08 22 SEP 87265 000100 04109 08121 04.00

Fig 4

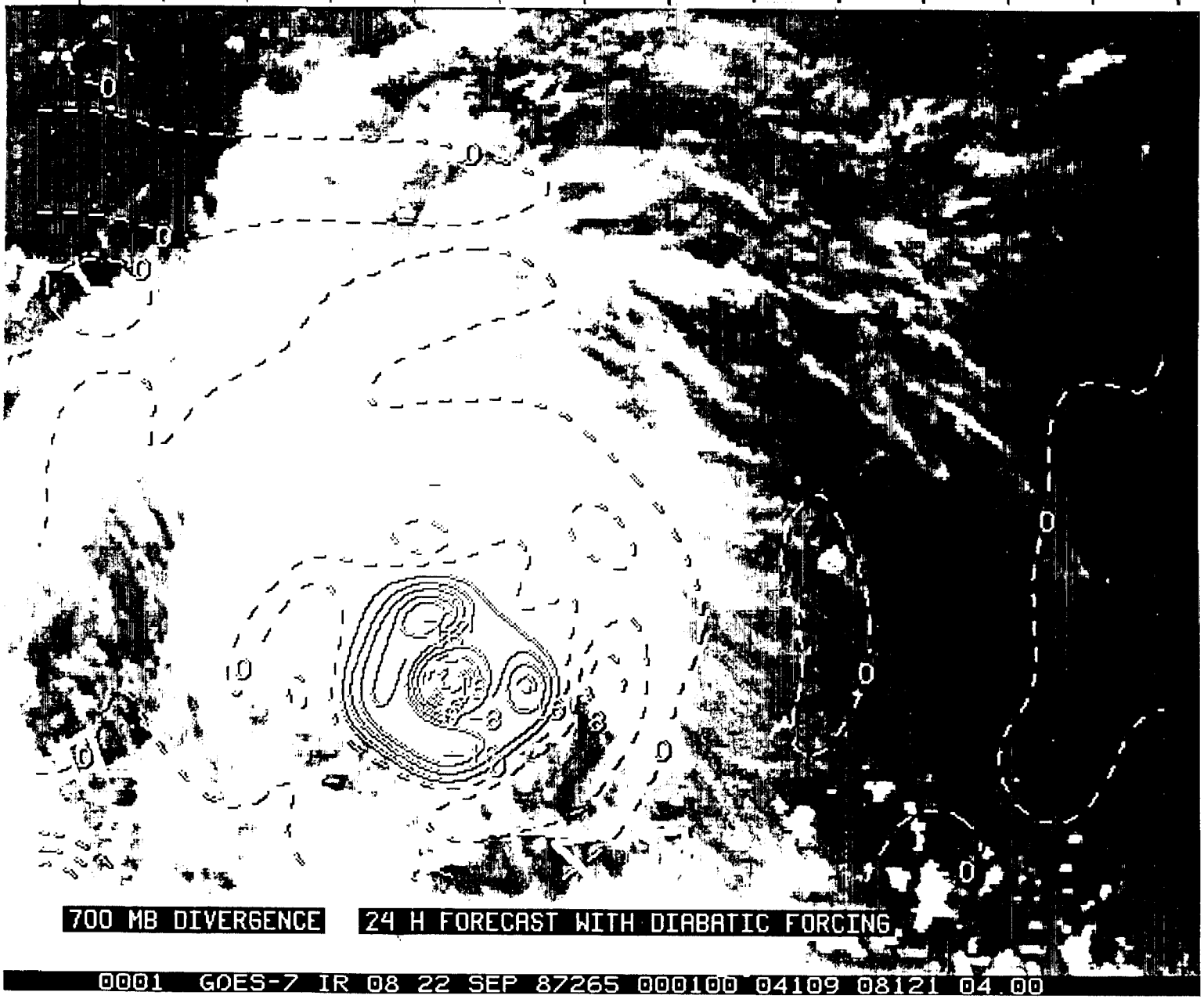
700 MB DIVERGENCE
24 H FORECAST WITH DIABATIC FORCING
0001 GOES-7 IR 08 22 SEP 87265 000100 04109 08121 04.00

Fig 5

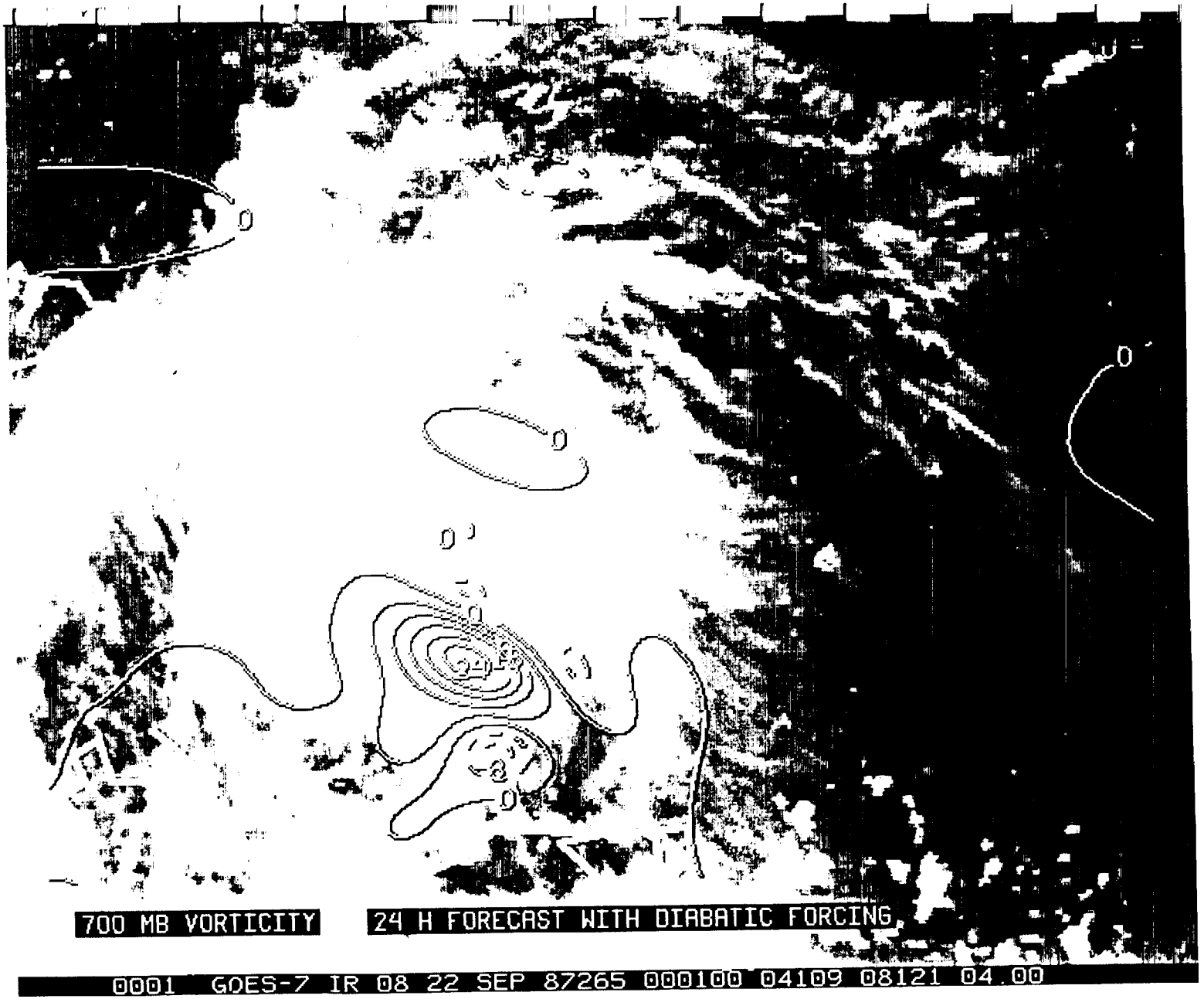
700 MB VORTICITY
24 H FORECAST WITH DIABATIC FORCING
0001 GOES-7 IR 08 22 SEP 87265 000100 04109 08121 04.00

Fig 6

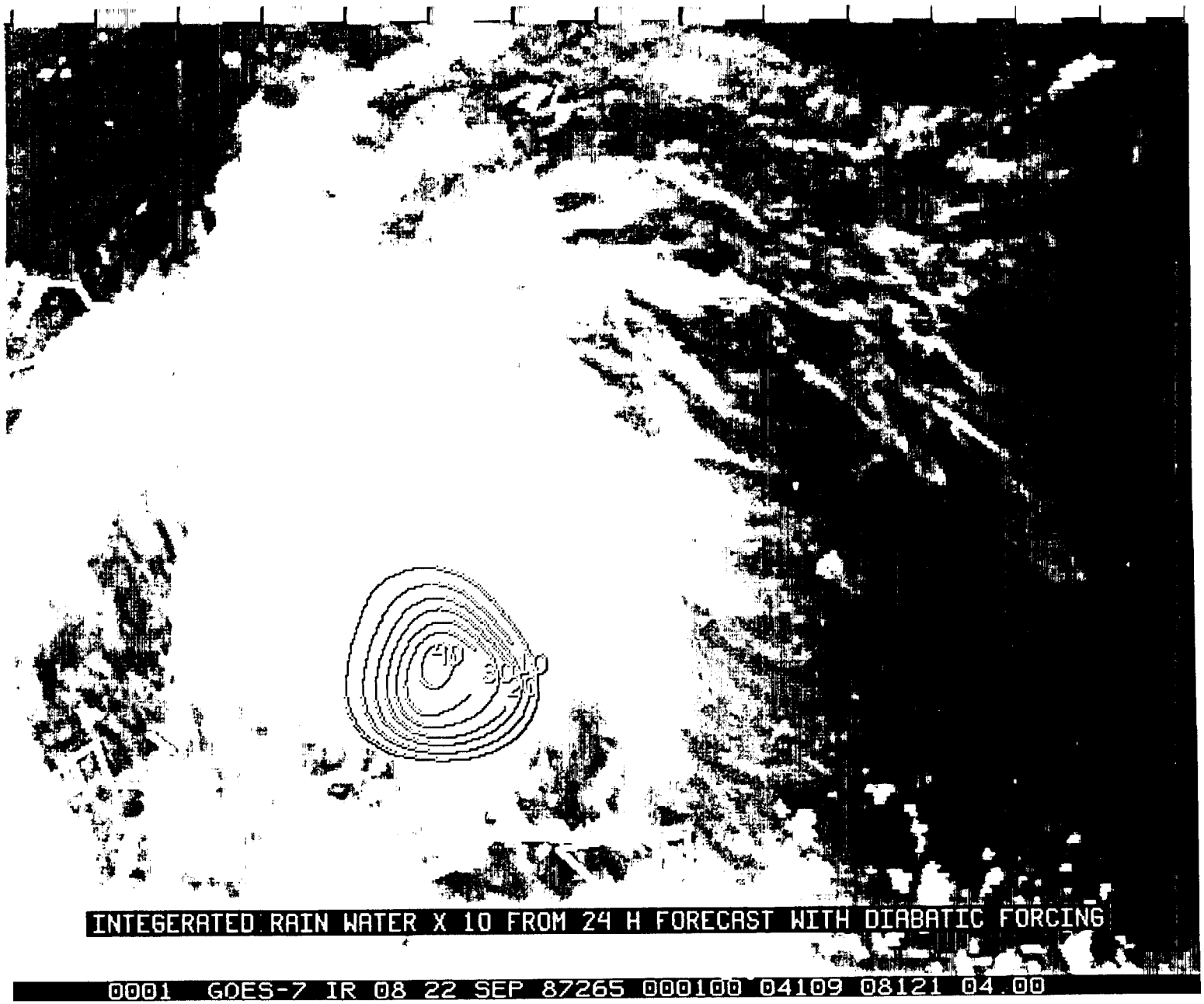
INTEGERATED RAIN WATER X 10 FROM 24 H FORECAST WITH DIABATIC FORCING
0001 GOES-7 IR 08 22 SEP 87265 000100 04109 08121 04 00

Fig 7

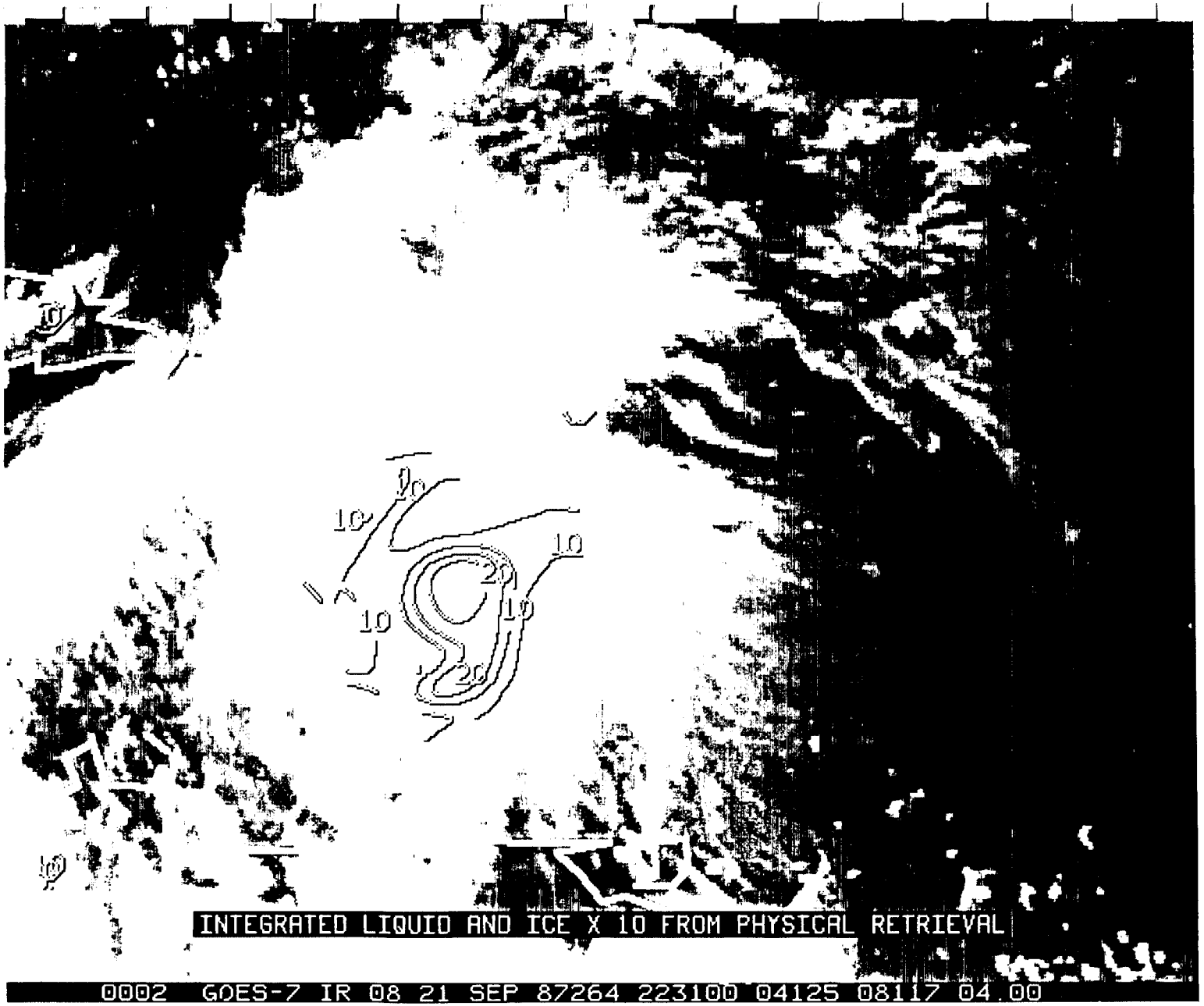
10
10
10
10
10
20
20
10
INTEGRATED LIQUID AND ICE X 10 FROM PHYSICAL RETRIEVAL
0002 GOES-7 IR 08 21 SEP 87264 223100 04125 08117 04.00

Fig 8

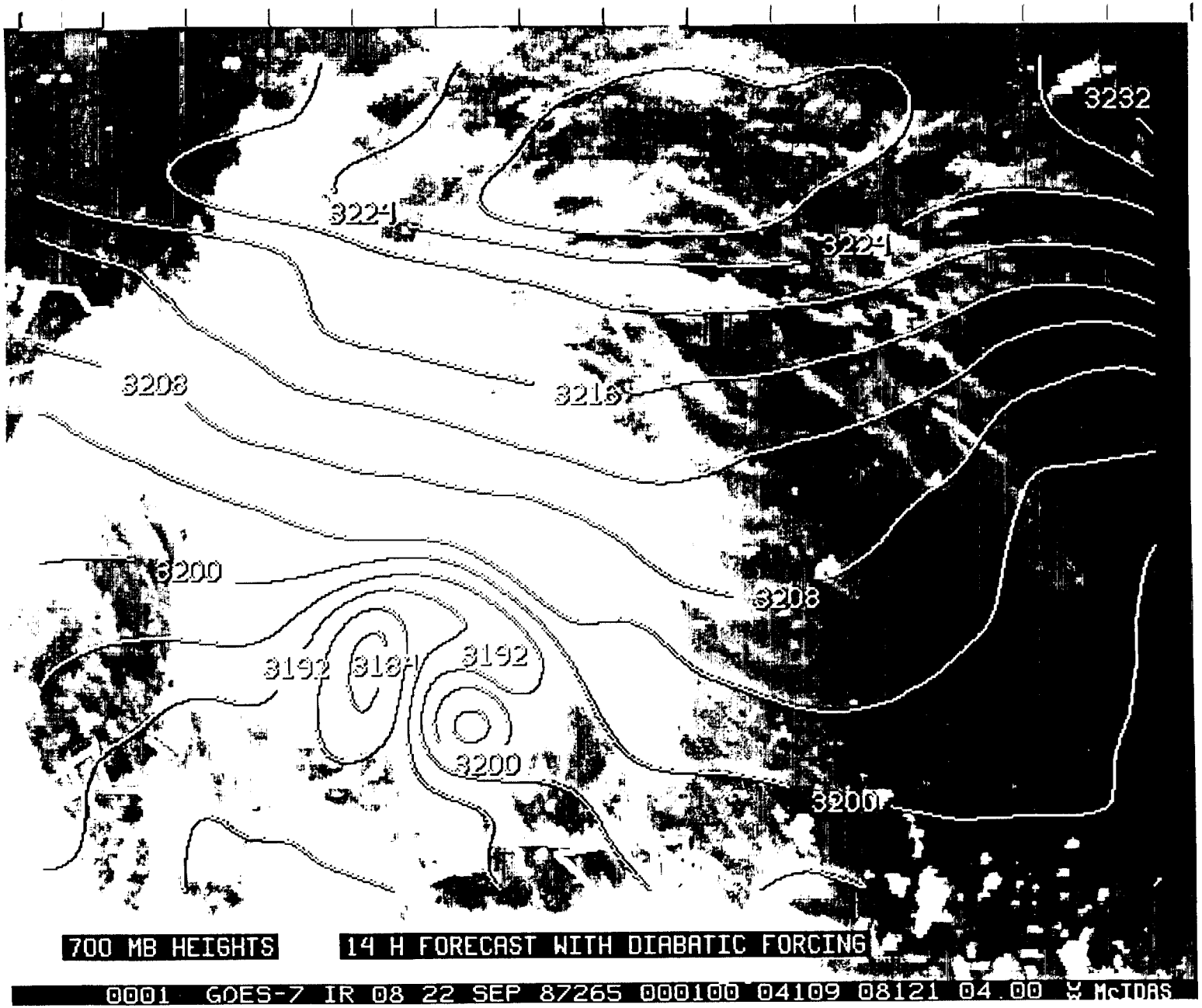
3232
3224
3224
3208
3216
3200
3208
3192
3184
3192
3200
3200
700 MB HEIGHTS
14 H FORECAST WITH DIABATIC FORCING
0001 GOES-7 IR 08 22 SEP 87265 000100 04109 08121 04.00 McIDAS

Fig 9

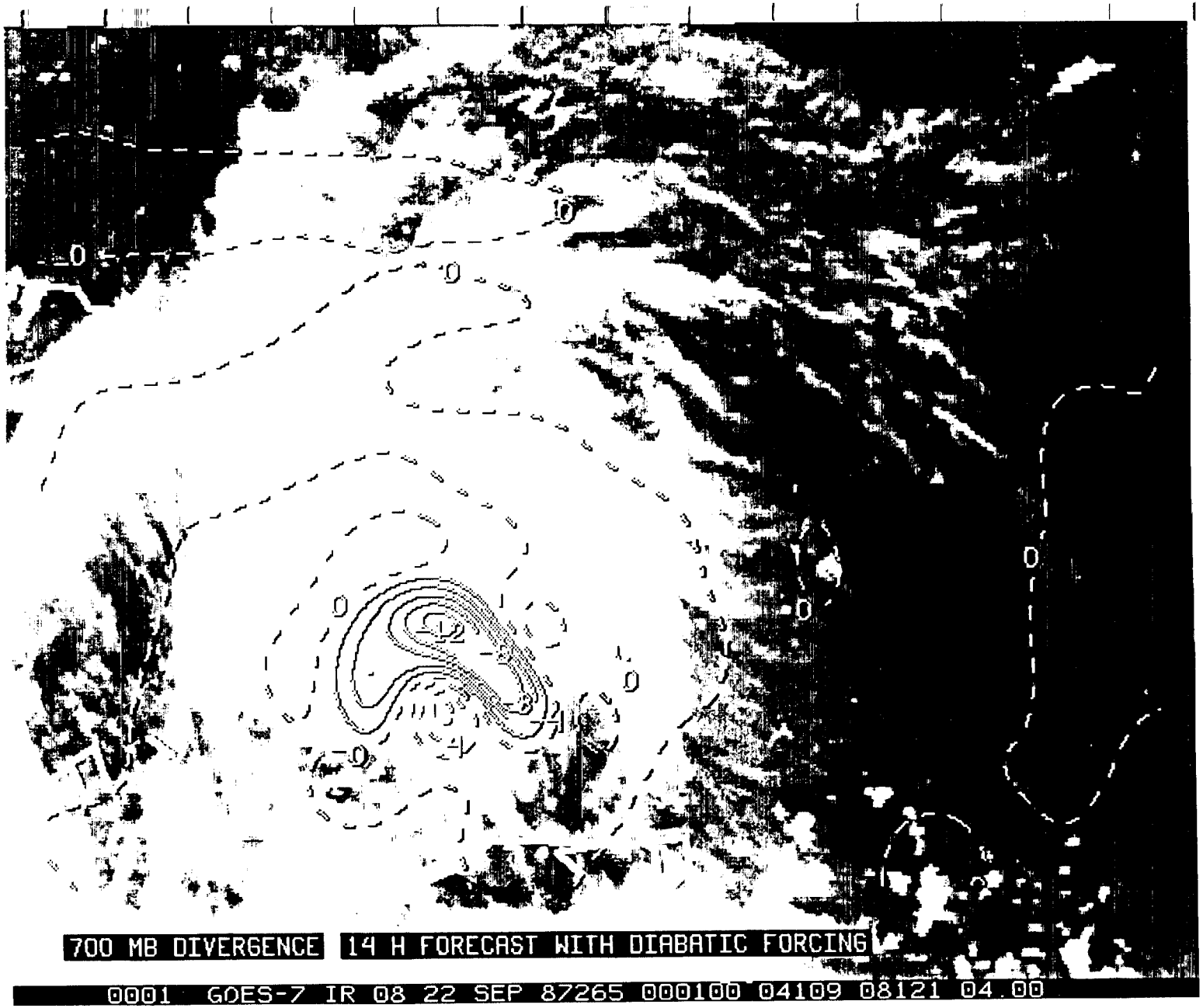
700 MB DIVERGENCE
14 H FORECAST WITH DIABATIC FORCING
0001 GOES-7 IR 08 22 SEP 87265 000100 04109 08121 04.00

Fig 10


700 MB VORTICITY
14 H FORECAST WITH DIABATIC FORCING
0001 GOES-7 IR 08 22 SEP 87265 000100 04109 08121 04 00

Fig 11

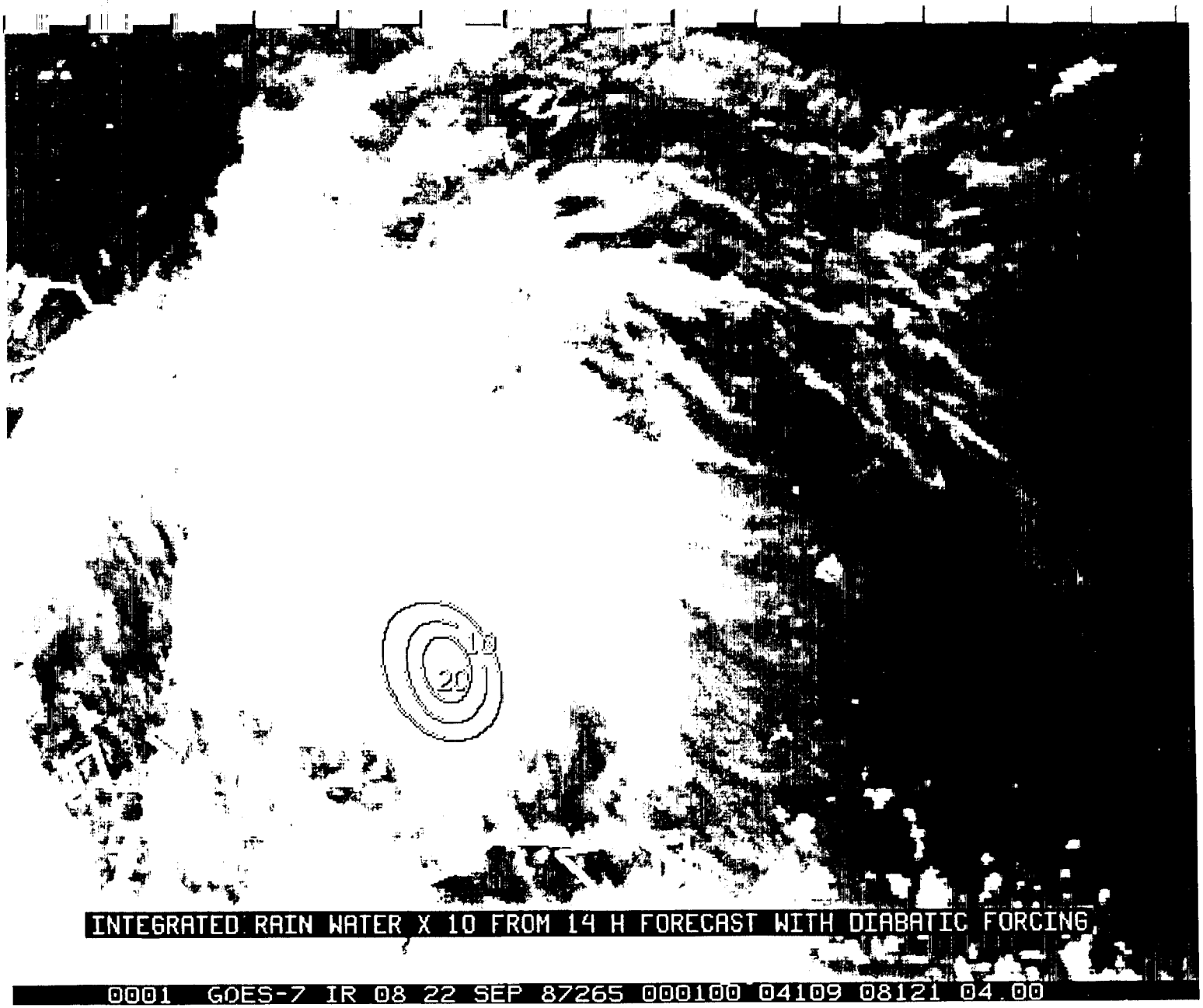
10
20
INTEGRATED RAIN WATER X 10 FROM 14 H FORECAST WITH DIABATIC FORCING
0001 GOES-7 IR 08 22 SEP 87265 000100 04109 08121 04.00

Fig 12

Reprinted from MONTHLY WEATHER REVIEW, Vol. 121, No. 7, July 1993
American Meteorological Society

Moist Wind Relationships

WILLIAM H. RAYMOND

Cooperative Institute for Meteorological Satellite Studies, University of Wisconsin, Madison, Wisconsin

(Manuscript received 24 July 1992, in final form 8 January 1993)

ABSTRACT

Equations describing the temporal and spatial behavior of the kinematic moisture and heat flux are introduced in this study. In these nonlinear equations, the contribution by diabatic processes to the large-scale flux is composed of two parts. One part is associated with a Rayleigh damping term, while the other arises from temporal and spatial changes in the pressure gradient term.

The influence of diabatic processes on the large-scale moisture fluxes depends greatly on the degree of balance between forcing and damping terms in the governing equations. The existence of a near balance requires a reduction in the large-scale horizontal geostrophic wind speed. From a scale analysis of the moisture flux equations it is argued that reductions in the large-scale horizontal wind speed, observed within major cumulus cloud systems, help conserve large-scale moisture fluxes. The deviation of the wind from geostrophic conditions is easily estimated. This wind modification induces secondary vertical circulations that contribute to the convergence, creating or supporting long-lived mesoscale flows. In the tropics the wind modification has an antitriptic relationship.

These diagnostic findings suggest possible modifications to the wind field in the application of cumulus parameterization, and may be important in diabatic initialization of numerical weather prediction models.

1. Introduction

In the extratropics, the large-scale atmospheric flow fluctuates about known balance conditions. Away from the major centers of cyclonic and anticyclonic activity, the horizontal wind components closely approximate geostrophy in the free atmosphere. Within strong cyclonic centers the flow is modified by curvature and by diabatic effects. To forecast the wind field in the presence of diabatic activity would require solutions of the complete equations of motion with physical processes included, which is not always practical. Otherwise, to get a snapshot of the instantaneous horizontal wind field requires solving the nonlinear diabatic balance equations. The simple wind laws, like the gradient-wind approximation, do include the effect of curvature and some indirect consequences of diabatic heating. This study outlines a simplified approach derived from first principles that identifies how diabatically induced modifications in the horizontal wind components influence the moisture and sensible heat fluxes. This study provides necessary additional information about the effect of diabatic processes on the atmospheric dynamics for use in model initialization and cumulus parameterization.

Many years of observations have shown that diabatic processes can significantly enhance cyclonic development and influence the general circulation. Many journal articles and textbooks testify to this. A small subset includes Petterssen (1956), Riehl and Malkus (1958), Kuo (1965, 1974), Yanai et al. (1973), Riehl (1979), Donner et al. (1982), Houze and Hobbs (1982), and Konig and Ruprecht (1989). Modeling studies also have verified that moist processes are important for rapid development (Kuo and Reed 1988; Reed et al. 1988). Additionally, diabatic initialization techniques are used to enhance cyclonic circulations and low-level convergence to help speed up precipitation processes in numerical forecast models (e.g., Tarbell et al. 1981; Krishnamurti et al. 1983; Krishnamurti et al. 1984; Donner 1988; Wang and Warner 1988; Turpeinen et al. 1990; Daley 1991).

There also are many studies on the effect of clouds on the large-scale dynamics, including Malkus (1952), Schneider and Lindzen (1976), Sui and Yanai (1986), Cho (1985), and Konig and Ruprecht (1989). The vertical transport of atmospheric properties in clouds is important because the cloud vertical velocity is much larger than that found in the environment, especially in the tropics. In contrast, the magnitudes of the horizontal flow in the cloud and environment are of the same order, but according to the above studies, mixing, vertical transport, and other processes are responsible for some deceleration of the mean flow by "cumulus friction" (Malkus 1952; Schneider and Lindzen 1976). Several articles propose parameterizations of cumulus convection effects on the large-scale vorticity or momentum. Approaches include mass entrainment and

Corresponding author address: Dr. William H. Raymond, CIMMS/University of Wisconsin, 1225 West Dayton St., Madison, WI 53706.

detrainment concepts (Ooyama 1971), vertical transport and properties from simple cloud models (Shapiro and Stevens 1980), the introduction of drag terms (Esbensen et al. 1987; Austin and Houze 1973), and other representations of cumulus friction (Schneider and Lindzen 1976). In this study a different method is proposed to estimate the cumulus friction process.

Gill (1980) has examined tropical circulation forced by localized heating, while Heckley and Gill (1984) have studied transient features in the tropics when the heating is impulsively started. In these studies the role of diabatic heating on the large-scale flow is modeled by adding a forcing term to the continuity equation in the linearized shallow-water model. The forcing modifies the pressure and its gradients, which in turn modify the horizontal wind field. This model is conceptually simple yet captures the essence of the large-scale response to diabatic forcing arising from thermal changes. Gill (1980) heuristically added a Rayleigh damping term with constant coefficient over the entire domain of his linear model, which produced a steady state, but this was not intended to represent the cumulus friction process, and it provided no insight on why cumulus friction occurs, its region of influence, or consequences. Holton and Colton (1972) in their linear vorticity model also found that damping was needed to obtain agreement with observations.

Lorenz (1978) has identified some optimal atmospheric energetic arrangements, but local optimal relationships remain unknown if they exist at all. One can speculate that cumulus friction is partially an atmospheric response for conserving basic large-scale atmospheric properties or optimizing fundamental parameters like the kinetic energy, enthalpy, etc. Clearly, temporal and advective changes in moisture flux, heat flux, and entropy are influenced by cumulus friction.

In this diagnostic study it is found that mesoscale moist processes introduce into the moisture and heat flux equations a Rayleigh damping term that depends upon the condensation and evaporation rate. This friction allows changes in the large-scale moisture fluxes to remain relatively small provided a near balance exists between the forcing and damping terms. Scale analysis shows that this balance involves the pressure gradient, Coriolis, and Rayleigh damping term. Balance further requires a reduction in the large-scale horizontal geostrophic wind speed, that is, the creation of an ageostrophic wind. Clearly, if the horizontal wind is reduced excessively, then the balance condition breaks down. Our hypothesis is that for long-lived mesoscale convection the large-scale horizontal winds do not differ greatly from that needed to establish a near balance between the pressure gradient, Coriolis, and Rayleigh damping terms. It is found diagnostically and in numerical applications that the ageostrophic wind enhances the existing convergence and establishes a mesoscale vertical circulation within the large-scale flow to help balance the modified horizontal wind.

To illustrate our hypothesis we examine the behavior of the kinematic moisture and heat flux. The derivation of these equations is quite simple, but they yield surprising information. In these equations the contribution of diabatic heating to the horizontal wind components is naturally partitioned into two parts. One diabatic contribution is contained within the geostrophic wind component (pressure gradient term), while the remaining one is associated with the Rayleigh damping (condensation) or forcing (evaporation) term. To examine the importance of the terms in the flux component equations, a scale analysis is preformed and simplified solutions are found. For nontropical regions our approximate solutions are given in terms of the geostrophic flow. In some of our illustrative examples a time scale less than the inverse of the Coriolis parameter is required; however, the flux equations are valid even when this is not true. In tropical regions any tendency toward moisture flux conservation enhances the relationship between the pressure gradient term and the Rayleigh damping term. This induces secondary antitriptic circulations. A simple hurricane model is presented to illustrate the wind modifications associated with any enhancement toward moisture flux conservation. Also tested are applications in cumulus parameterization.

2. The equations

The inviscid equations (Haltiner and Williams 1980, pp. 16, 17, and 308) for large-scale flow describing horizontal wind components u and v, the temperature T, potential temperature θ, the mixing ratio q, and pressure p are

$$\frac{du}{dt} = -\frac{1}{\rho}\frac{\partial p}{\partial x} + fv, \tag{1}$$

$$\frac{dv}{dt} = -\frac{1}{\rho}\frac{\partial p}{\partial y} - fu, \tag{2}$$

$$\frac{d\theta}{dt} = -\frac{L\theta Q}{Tc_p}, \tag{3}$$

$$\frac{dq}{dt} = Q. \tag{4}$$

The total derivative $d(\ )/dt$, x, y, z, and t have the standard definitions. The Coriolis parameter f satisfies $f = 2\Omega \sin\phi$, where Ω is the angular velocity of the earth and ϕ is the latitude. Here ρ is the density, g is the acceleration due to gravity, c_p is the specific heat for constant pressure, L is the latent heat of condensation or evaporation, and Q is the condensation or evaporation rate. Here Q is a sink for condensation and a source for evaporation and sublimation from saturated air; otherwise, $Q = 0$ when q is below saturation. This is expressed formally by

$$Q = \frac{dq_s}{dt}. \tag{5}$$

Evaporation from the earth's surface is not explicitly included in the foregoing inviscid model. Adding the continuity equation to the four preceding equations enables the vertical motion to also be computed. For large-scale flow the hydrostatic and ideal gas laws complete the list of equations.

The transfer of moisture or heat per unit area per unit time represents the moisture or heat flux. The kinematic flux form is consistent with atmospheric measurements of temperature, mixing ratio, and wind speed and direction (Stull 1988). For example, the kinematic moisture flux has components qu, qv, and qw, while the same quantities for the kinematic sensible heat flux are θu, θv, and θw. To find the component equations governing the temporal and spatial distribution of the horizontal kinematic moisture flux, multiply (1) and (2) by the mixing ratio q and rearrange by application of the chain rule and (4). (A similar process involving the potential temperature yields the kinematic heat flux equations described in the Appendix.) The equations for the horizontal components of the total moisture flux are

$$\frac{d(qu)}{dt} = -\frac{q}{\rho}\frac{\partial p}{\partial x} + qfv + Aqu, \tag{6}$$

$$\frac{d(qv)}{dt} = -\frac{q}{\rho}\frac{\partial p}{\partial y} - qfu + Aqv. \tag{7}$$

Along with the total derivative, note that each nonlinear flux component equation contains a pressure gradient term, a term containing the Coriolis parameter, and a term that includes the factor $A = Q/q$. The A coefficient[1] is negative for condensation, making Aqu and Aqv Rayleigh damping terms. Thus, regardless of the sign of qu and qv, the damping term always reduces the magnitude of the flux. In contrast, evaporation induces a forcing response that enhances the magnitude of the flux. In tropical regions the term containing the Coriolis parameter f is small and may be ignored without introducing large errors. Then, changes to the kinematic flux depend on the residual of the pressure gradient and damping terms.

Away from the tropics the pressure gradient can be expressed in terms of the large-scale geostrophic wind

$$v_g = \frac{1}{f\rho}\frac{\partial p}{\partial x}, \tag{8}$$

$$u_g = \frac{-1}{f\rho}\frac{\partial p}{\partial y}. \tag{9}$$

It should be noted that diabatic contributions to the pressure field are implicitly included in the definition of the geostrophic wind. In addition, the Rayleigh damping term is important, while other indirect and feedback diabatic influences on the large-scale flow occur, but are not considered in this study. Using the geostrophic approximation simplifies (6) and (7), yielding

$$\frac{d(qu)}{dt} = -qf(v_g - v) + Aqu, \tag{10}$$

$$\frac{d(qv)}{dt} = qf(u_g - u) + Aqv. \tag{11}$$

The moisture flux is conservative in (10) and (11) for adiabatic and frictionless conditions, and for geostrophic flow. If the wind components were to remain geostrophic during a condensation event, then significant reductions in the kinematic moisture flux would occur because of the cumulative effects of the Rayleigh damping. The exact nature of any optimal *local* response in the moisture flux, heat flux, energy, or other basic atmospheric state is unknown. Scale analysis (given below), however, suggests that the large-scale moisture flux is nearly conserved. Even though the surface evaporation process slowly builds up the atmospheric water vapor, condensation can quickly deplete local supplies unless there exists a mesoscale circulation to help replenish the local reservoir. Any hypotheses that say there is a tendency toward conservation of moisture flux must also include some mechanism for generating vertical circulations.

One way to make the left-hand sides of (10) and (11) small in magnitude is to alter the wind components u and v so that the right-hand sides are closer to being balanced but not necessarily identically balanced. It is our hypothesis that the reduction in the large-scale horizontal wind components observed during major long-lived precipitating events help preserve the large-scale moisture flux. This reduction in velocity speed decreases the change in the synoptic-scale kinematic moisture flux that would otherwise occur if the wind speed remained unchanged. As will be shown in the example and applications in sections 3 and 4, this modification also enhances the longevity of the disturbance and minimizes loss in the moisture flux by creating a mesoscale vertical circulation that helps restore or pump additional moisture into the storm. Much of the discussion that follows examines the nature of the changes in the large-scale horizontal wind components that are needed to support our hypothesis.

A scale analysis of (1) and (2) shows that for large-scale conditions the pressure gradient and Coriolis force terms are larger in magnitude than the contribution from the total derivative (Holton 1979). In a similar

[1] Both the moisture and heat flux have a term containing the condensation or evaporation rate. Rayleigh damping reduces the moisture flux, while the heat flux is enhanced by diabatic forcing during precipitating events. In magnitude, A is significantly larger than the B coefficient associated with the forcing in the sensible heat flux equations given in the Appendix.

TABLE 1. A scale analysis* of the terms in the u moisture wind [Eq. (8)].

	$\frac{d(qu)}{dt}$	qfv	$\frac{q}{\rho}\frac{\partial p}{\partial x}$	Aqu
Scaling	$\frac{qU^2}{L}$	$q2\Omega U$	$\frac{q}{\rho}\frac{\Delta p}{L}$	$\frac{U^2q}{L_c}$
Magnitude				
(extratropics)	$q \times 10^{-4}$	$q \times 10^{-3}$	$q \times 10^{-3}$	$\leqslant q \times 10^{-3}$
(tropics)	$q \times 10^{-4}$	$\leqslant q \times 10^{-4}$	$q \times 10^{-3}$	$\leqslant q \times 10^{-3}$

* $U \sim 10$ m s^{-1}, $A \sim \frac{U}{L_c}$ s^{-1}, $L \sim 10^6$ m, L_c (precipitation scale) $\sim\geqslant 10^5$ m, $\Delta p \sim 10^3$ N m^{-2}.

analysis for (6) and (7) the term containing diabatic processes is an order of magnitude more important than the contribution from the total derivative, provided A is scaled with Q proportional to 10^{-7} g g^{-1} s^{-1}, a magnitude common to mesoscale precipitation events. Table 1 illustrates our findings for large-scale circulations containing a long-lived mesoscale diabatic process, of length scale L_c, for tropical and nontropical situations. In Table 1 the derivative term yields a magnitude U^2q/L, while the diabatic term gives U^2q/L_c, where Q is scaled by Uq/L_c and $L_c = 10^5$ m. In tropical regions the Coriolis parameter is reduced; thus, the pressure gradient and the damping terms dominate provided A is sufficiently large. This scale analysis suggests that the large-scale fluid flow is nearly balanced by the right-hand sides in (6) and (7). This is consistent with our stated hypothesis. Clearly, different scaling will provide different magnitudes; for example, short duration or microscale diabatic processes are of much less importance to the large-scale flow. However, the Rayleigh damping term remains important provided $L_c/L \sim 0.1$. Convective parameterizations assume a similar ratio between grid and diabatic scales. However, the total derivative in (10) and (11) becomes important as the scale size is reduced.

In this study (10) and (11) or (6) and (7) are evaluated *diagnostically*. The right-hand sides of these equations are assumed to be nearly in balance, but some contribution from the total derivative is allowed. A simplified analysis is used to trace how the nonconservative total derivative contributes. As an example, assume that the deviation from conservation is known to be a small fraction of the flux; then for nonzero values of q, u, and v there exist coefficients α_u and α_v such that

$$\frac{d(qu)}{dt} = \alpha_u qu, \tag{12}$$

$$\frac{d(qv)}{dt} = \alpha_v qv. \tag{13}$$

This is a generalization of the approximation for the partial time derivative used in Gill (1980) and Matsuno (1966). To get a grasp of the magnitude of the coefficient assume that the flux qu experiences a complete reversal of sign for the synoptic flow within a time period of Δt; then the coefficient α_u would have magnitude $2/\Delta t$. Generally the magnitude is less than this. The coefficients α_u and α_v, however, are locally functions of time and the independent spatial variables. For long-lived large-scale diabatic situations these coefficients vary slowly in space. Within mesoscale disturbances they should vary in a pattern consistent with the disturbance. For example, the convection may moisten the upper atmosphere, giving α_u and α_v a positive sign, while drying lower levels making the coefficients negative. Equations (12) and (13) allow a climatological estimate of the nonconservative property of the horizontal kinematic moisture fluxes to be easily determined from model calculations. A more complete solution procedure that makes no simplifying assumptions will be presented elsewhere in an independent study.

Substituting (12) and (13) into (10) and (11) gives

$$-fv_g + fv + u(A - \alpha_u q) = 0, \tag{14}$$

$$fu_g - fu + v(A - \alpha_v q) = 0. \tag{15}$$

Note that A, $\alpha_u q$, and $\alpha_v q$ couple the two algebraic equations together. Dividing (14) and (15) by f and solving the coupled system for u and v yields

$$u_m \equiv u = \frac{u_g + M_v v_g}{1 + M_u M_v}, \tag{16}$$

$$v_m \equiv v = \frac{v_g - M_u u_g}{1 + M_u M_v}. \tag{17}$$

Here the subscript m denotes the moist solution. Note that $u_m = u_g$ and $v_m = v_g$ when $M_u \equiv (A - \alpha_u)f^{-1}$ and $M_v \equiv (A - \alpha_v)f^{-1}$ are set to zero. Here A is negative for condensation, so a positive value of α_u and α_v would enhance the magnitude of M_u and M_v. For some circumstances—for example, for large hourly condensation rates in a hurricane—the magnitude of the nondimensional number $R_1 \equiv Af^{-1}$ can exceed unity. A condensation rate of $Q \approx -0.8 \times 10^{-7}$ g g^{-1} s^{-1} yields $R_1 = -0.408$, provided $f = 10^{-4}$ and an average q satisfies $q = 2$ g kg^{-1}. Magnitudes for R_1 of 0.2 and less, however, are probably more common for large areas.

For tropical flow the moist wind is computed using (6), (7), (12), and (13). This yields

$$u_m \equiv u = \left(-\frac{1}{\rho}\frac{\partial p}{\partial x}\right)\left(\frac{1}{\alpha_u - A}\right), \tag{18}$$

$$v_m \equiv v = \left(-\frac{1}{\rho}\frac{\partial p}{\partial y}\right)\left(\frac{1}{\alpha_v - A}\right), \tag{19}$$

provided neither $\alpha_u - A$ nor $\alpha_v - A$ is equal to zero. The perturbation in the horizontal velocity is found

using the pressure gradient computed from the diabatic heating. If the total derivative term; that is, in (6) and (7) is small, then the perturbation flow induced by the diabatic process is antitriptic; that is, there is a near balance between the Rayleigh damping term and the pressure gradient term. An example of antitriptic flow is found in Raymond (1986), illustrating topographically induced mesoscale circulations in barotropic flow around an isolated mesoscale obstacle. Similar circulations containing positive and negative couplet pairs of convergence–divergence and cyclonic–anticyclonic flows are produced by this antitriptic mechanism.

For extratropical flow an examination of (16) and (17) expanded in powers of R_1 provides a clearer picture. Assuming that $u_m = u_L + u_{\text{pert}}$ and $v_m = v_L + v_{\text{pert}}$, where u_L and v_L are the horizontal wind components in the large-scale flow, and assigning all terms involving Q to the perturbation, yields for the perturbation and large-scale flow the expressions

$$u_{\text{pert}} = R_1 v_g - R_1^2 u_g + \frac{R_1(\alpha_u + \alpha_v)u_g}{f} + \cdots, \quad (20a)$$

$$u_L = u_g - \frac{\alpha_v v_g}{f} + \frac{\alpha_u \alpha_v u_g}{f^2} + \cdots, \quad (20b)$$

$$v_{\text{pert}} = -R_1 u_g - R_1^2 v_g + \frac{R_1(\alpha_u + \alpha_v)v_g}{f} + \cdots, \quad (21a)$$

$$v_L = v_g + \frac{\alpha_u u_g}{f} - \frac{\alpha_u \alpha_v v_g}{f^2} + \cdots. \quad (21b)$$

Note that the large-scale flow is nearly balanced if $|\alpha_v|/f \ll 1$ and $|\alpha_u|/f \ll 1$. Also the series in (20b) and (21b) converge rapidly, provided these ratios are much less than 1. When this is not the case, this series expansion should not be used.

In the Northern Hemisphere, given $R_1 < 0$ (condensation) with $u_g > 0$ and $v_g > 0$, (20a) and (21a) imply that the magnitude of a westerly flow is reduced, since $u_g/u_m > 1$, while the magnitude of a southerly flow is enhanced, since $v_g/v_m < 1$. Repeating this thought experiment with an easterly flow leads to the reverse conclusions. In the Southern Hemisphere, $u_g > 0$ implies that a northerly flow is enhanced because the coriolis parameter changes sign making $R_1 > 0$. As will be shown in the hurricane example given below, the diabatic perturbation terms [(20a) and (21a)] add significantly to the local convergence.

The diabatic contribution alters the speed $V_m = (u_m^2 + v_m^2)^{1/2}$. Writing the definition of speed in terms of the large-scale wind and the diabatic perturbation gives

$$V_m = [V_L^2 + 2u_L u_{\text{pert}} + 2v_L v_{\text{pert}} + (u_{\text{pert}})^2 + (v_{\text{pert}})^2]^{1/2}. \quad (22a)$$

Here $V_L = (u_L^2 + v_L^2)^{1/2}$. Approximating the large-scale flow by factoring out V_L but replacing all occurrences of V_L in the denominator by V_g yields

$$V_m = V_L\left[1 + 2\left(\frac{u_L}{V_g^2}\right)u_{\text{pert}} + 2\left(\frac{v_L}{V_g^2}\right)v_{\text{pert}} + \left(\frac{u_{\text{pert}}}{V_g}\right)^2 + \left(\frac{v_{\text{pert}}}{V_g}\right)^2\right]^{1/2}, \quad (22b)$$

where $V_g = (u_g^2 + v_g^2)^{1/2}$. Substituting from (20) and (21) into (22b) gives

$$V_m = V_g\left[1 - R_1^2 + \frac{2R_1(\alpha_u + \alpha_v)}{f} - \frac{2R_1(\alpha_u u_g^2 + \alpha_v v_g^2)}{fV_g^2} + \frac{2R_1 u_g v_g(\alpha_v - \alpha_u)}{fV_g^2} + \frac{2R_1 u_g v_g(\alpha_u + \alpha_v)(\alpha_v - \alpha_u)}{f^2 V_g^2} + \cdots\right]^{1/2} + \cdots. \quad (22c)$$

Note that $V_m = V_g(1 - R_1^2)^{1/2}$ when $\alpha_u = \alpha_v = 0$. All terms in the brackets except for the first two tend to nullify each other or make small contributions provided $|\alpha_v|/f \ll 1$ and $|\alpha_u|/f \ll 1$. Thus, (22c) implies that the speed associated with moist cyclonic activity is less than the geostrophic value.

For comparison purposes, note that the relationship between the geostrophic and gradient wind speed V_{gr} is

$$V_{\text{gr}} = V_g\left(1 + \frac{V}{fR}\right)^{-1}, \quad (23)$$

where R is the radius of curvature (Holton 1979). For cyclonic situations ($fR > 0$) the ratio V_{gr}/V_g is less than 1. Thus, the speed is reduced from geostrophic values by the gradient wind primarily because curvature effects are included. In regions having condensation, the rate needed to sustain a specific curvature can be determined approximately by equating (22c) and (23), and solving for Q. Approximating the solution by the first two terms in (22c) gives

$$Q = -fq\left[1 - \left(1 + \frac{V}{fR}\right)^{-2}\right]^{1/2}. \quad (24)$$

As an example, if $f = 10^{-4}$, $V/fR = 0.2$, and $q = 2$ g kg^{-1}, then $Q = -1.1055 \times 10^{-7}$ g g^{-1} s^{-1}. Note that Q is proportional to fq.

3. An example

Idealized flow in a hurricane is used to illustrate the diabatic influence on the wind field. An idealized axisymmetric vortex flow was selected because of its interesting theoretical properties and because of the initialization difficulties encountered when inserting a diabatic vortex flow in a numerical model. Following the procedure presented in section 2, but for cylindrical

coordinates and for axisymmetric flow, allows the moist radial wind component u_m to be written in terms of the tangential velocity v according to

$$u_m = vM_v\left(1 + \frac{v}{fr}\right)^{-1}. \tag{25}$$

It is assumed that the contribution from $\alpha_v f^{-1}$ in M_v is small. Near the vortex core $v/fr \gg 1$; thus, u_m simplifies to

$$u_m = frM_v, \tag{26}$$

while far from the core $v/fr \ll 1$, so

$$u_m = vM_v. \tag{27}$$

The divergence is

$$\frac{\partial u_m}{\partial r} + \frac{u_m}{r} = M_v\left(1 + \frac{v}{fr}\right)^{-1}\left(\frac{\partial v}{\partial r} + \frac{v}{r}\right) + v\left(1 + \frac{v}{fr}\right)^{-1} \times \frac{\partial M_v}{\partial r} - M_v\left(1 + \frac{v}{fr}\right)^{-2}\left(\frac{\partial v}{\partial r} - \frac{v}{r}\right)\frac{1}{fr}. \tag{28}$$

For $v/fr \gg 1$, the divergence [(28)] simplifies to

$$\frac{\partial u_m}{\partial r} + \frac{u_m}{r} = 2fM_v + \frac{rf\partial M_v}{\partial r}, \tag{29a}$$

while when $v/fr \ll 1$ the expression is

$$\frac{\partial u_m}{\partial r} + \frac{u_m}{r} = M_v\left(\frac{\partial v}{\partial r} + \frac{v}{r}\right) + \frac{v\partial M_v}{\partial r}. \tag{29b}$$

In (29a) the sign depends upon M_v and its radial variation. In (29b) the divergence depends upon the vorticity $(\partial v/\partial r + v/r)$ and the radial variation in M_v. In both (29a) and (29b) $M_v < 0$ contributes toward the convergence, provided the magnitude of M_v is increasing radially outward and $v > 0$. Positive vorticity, averaged over the hurricane inner core, of 10^{-2} s^{-1} is common. Thus, as indicated by (29), substantial convergence is generated by diabatic processes when M_v is sufficiently large in magnitude and of negative sign. Negative vorticity with $M_v < 0$ and decreasing outward implies divergence. Evaporation near the cloud tops also encourages divergence.

To express the radial velocity as a function of distance from the vortex center, it is necessary to know M_v, or Q when $\alpha_v f^{-1}$ is small, and its radial distribution. Near the vortex center a constant value for M_v would imply, following (27), a flow that is proportional to r (solid rotation), while if M_v were linear in r, then u would be proportional to r^2. Far from the vortex center the radial component [(28)] is proportional to the tangential component v and to M_v. In the outer reaches of a hurricane the radial distribution of v decreases approximately as $r^{-1/2}$ (Riehl 1963). Thus, the radial variation in u_m is considerable but depends a great deal upon the radial variation of the net condensation rate Q.

In the absence of condensation or evaporation ($Q = 0$) our solutions satisfy $u = 0$ unless $\alpha_v \neq 0$. Thus, radial velocities associated with condensation bands in hurricanes should be localized and exist in addition to a dynamically induced large-scale convergence associated with $\alpha_v \neq 0$. These bands in the radial velocity are seen in both numerical model simulations and in observations of hurricanes (Willoughby 1979).

With a balance between the centrifugal and pressure gradient forces that characterizes intense atmospheric vortices, cyclostrophic flow leads to a tangential velocity defined by

$$v_c = \left(\frac{r}{\rho}\frac{\partial p}{\partial r}\right)^{1/2}. \tag{30}$$

Therefore, solving for the moist tangential velocity $v_m = v$, in the cylindrical moisture flux equations, using a procedure analogous to that developed in earlier sections, gives

$$v_m^2 + frv_m + fru_mM_u = v_c^2. \tag{31}$$

Ignoring the dependence of u_m on v_m yields a moisture-modified gradient wind expression

$$v_m = -\frac{fr}{2} \pm \frac{fr}{2}\left[1 - \frac{4u_mM_u}{fr} + \frac{4v_c^2}{(fr)^2}\right]^{1/2}. \tag{32}$$

Retaining the dependence of v_m on u_m developed above [(25)] requires solving the cubic equation

$$v_m^3 + 2frv_m^2 + [(1 + M_vM_u(fr)^2 - v_c^2]v_m = frv_c^2 \tag{33}$$

for v_m. Note that (33) remains cubic even when $M_v = M_u = 0$, implying than an extraneous real root[2] has been introduced by the algebra.

Results are presented in Fig. 1 to illustrate the differences between (32) and (33). The axisymmetric tangential flow is taken from the analytical expression given in (6) of Fiorino and Elsberry (1989), with maximum velocity $V_{max} = 35$ m s^{-1}. In their formula for the tangential wind the radius of maximum tangential winds is set to $r_{max} = 100$ km and the parameter $b = 0.96$. For simplicity, in our experiments this radial profile is assumed to be in cyclostrophic balance, and is illustrated by the thick line in Fig. 1. Adding the influence of the Coriolis parameter (gradient wind) for a dry case [$u_m = 0$, (32)] produces reductions in the tangential velocity of approximately 4 m s^{-1} at r_{max}, with larger values outside the radius of maximum winds. Willoughby (1990) indicates that the gradient balance condition closely approximations the axisymmetric tangential winds observed in hurricanes. However, it should be remembered that measured pressure

[2] For the v_c used, (33) has three real roots, two of which are negative.

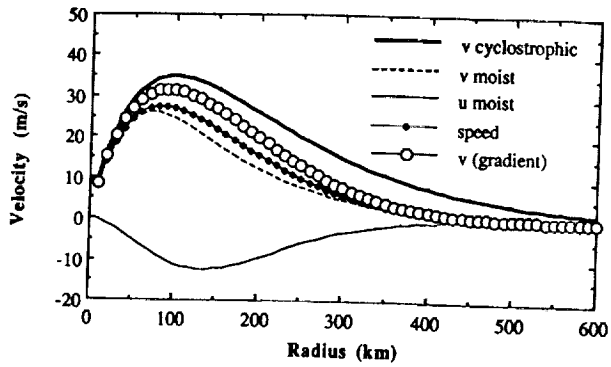

FIG. 1. Idealized axisymmetric hurricane cyclostrophic, gradient, and moist tangential velocities (m s^{-1}) as a function of radius. Speed and radial component also illustrated for the moist wind.

gradients already contain diabatic contributions. This could explain the discrepancy between these observational findings (Willoughby 1990) and the theoretical and numerical findings that intense vortices react strongly to specified heat sources (Hank and Schubert 1986; Delden 1989). Note that our moist wind solution, as illustrated by the divergence in (29), is also dependent upon the intensity of the vortex.

To solve (33) for v_m, the nondimensional values of M_v and M_u (Fig. 2) are assigned to be proportional to v_c so that each is -2 at r_{max}. This large magnitude for M_v and M_u is used to dramatize the response of the drag terms. The roots of (33) give one real positive solution for v_m that can be used to evaluate (25), yielding a radial inflow of approximately 12 m s^{-1}. As expected, the diabatic influence reduces the speed and shifts the radius of maximum tangential velocity from 100 to 80 km, while generating the maximum magnitude of the radial velocity at $r = 140$ km. The maximum reduction in the tangential velocity component is about 8 m s^{-1}, but the overall reduction in the speed is less since a strong radial inflow is present. Considering that our estimates of M_v and M_u are inflated in magnitude and in areal coverage, we can probably infer that the tangential velocities are not greatly altered by the diabatic drag term.

Magnitudes of M_v and M_u dictate the radius of maximum heating (RMH). Figure 2 shows a curve for $M = M_v = M_u$ where the RMH is at 100 km, and another M that is positive between 0 and 50 km, illustrating possible modifications (exaggerated) because of inner core evaporation. These M's are used in the calculation of u_m to show the importance of the divergence as a function of the RMH, as illustrated in Fig. 3. In every case the balanced solutions show that the greatest convergence is located interior to the circle with the prescribed RMH. Whether this would result in a change in the location of the RMH depends on the availability of moisture and other factors. However, in these calculations the radius of the maximum cyclostrophic wind was held fixed at 100 km. Otherwise, little change occurs in the magnitude or location of the maximum value of v_m as a function of RMH.

Observations or results from model simulations of intense vortices are needed to complete the evaluation of the moisture-modified horizontal winds and the evaluation of the diabatic and total derivative terms. The contribution from the total derivative would be expected to vary spatially, but the pattern should be consistent between similar types of situations and should change in time somewhat slowly.

4. Applications

Cumulus initialization and parameterization of long-lived convection in the extratropics are areas that could benefit from the knowledge contained in (16), (17), (18), and (19). The following discussion highlights some simple tests to investigate this potential in cumulus parameterization. These tests are presented to illustrate possible applications and do not represent a completely definitive study of the topic.

Cumulus parameterization schemes—for example, Kuo (1965, 1974)—estimate subgrid-scale moist con-

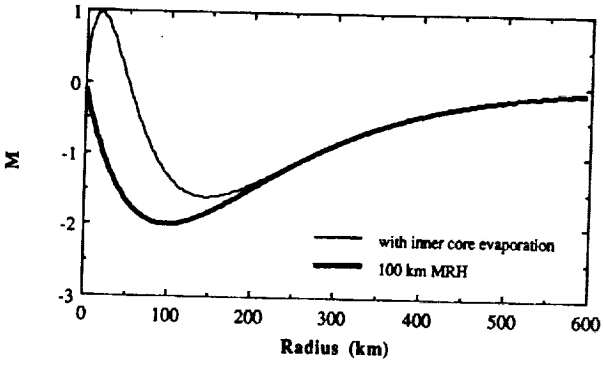

FIG. 2. Radial profiles of M illustrating (exaggerated) radial distribution of the condensation or evaporation rate.

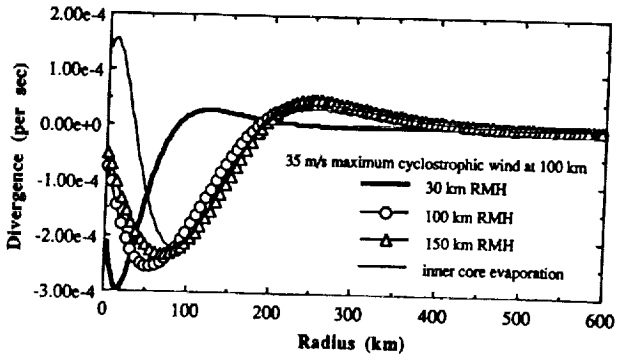

FIG. 3. Radial distribution of the moist divergence (s^{-1}) as a function of M.

vective activity using the instantaneous state of the grid-scale variables and moisture or cloud properties. This information is then used to modify the large-scale temperature and moisture fields. Because cumulus clouds contain a large vertical component of motion, relative to their environment, they also are responsible for significant vertical momentum transport. Several schemes based on cumulus friction concepts have been introduced to adjust the grid-scale momentum (Ooyama 1971; Shapiro and Stevens 1973; Schneider and Lindzen 1967; Shapiro and Stevens 1980; Zhang and Cho 1991). These approaches introduce a cloud velocity that requires an additional determination, usually from a cloud model. In contrast, the terms in (20a) and (21a) that represent approximate changes in the large-scale wind introduce no cloud-scale dependent variables but require calculation of the geostrophic wind.

To test the momentum adjustment suggested by the perturbation terms in (20a) and (21a), they were added to the Kuo cumulus parameterization scheme in the local [Cooperative Institute for Meteorological Satellite Studies (CIMSS)] version of the Australian Bureau of Meteorology Research Centre's (BMRC) finite-area model (Leslie et al. 1985). Thus, $u_{new} = u_{old} + u_{pert}$ where (20a) defines u_{pert}; similarly, $v_{new} = v_{old} + v_{pert}$ where (21a) defines v_{pert}. Our configuration of this semi-implicit regional model has 15 sigma levels. A 12-h control forecast, 0000–1200 UTC 22 April 1988, with 150-km horizontal resolution and 600-s time steps was performed using the standard Kuo cumulus parameterization scheme (1965) without any momentum adjustment. In the test forecast the first two terms in (20a) and (21a) are used to modify the horizontal wind components u and v, with the added requirement that $|R_1| < 0.5$. (Smaller magnitudes for R_1 may be more acceptable.) This large magnitude for R_1 was used to highlight the differences between the two schemes in a short forecast. Even though the convection may vary slightly in location and intensity between model time steps, it is still assumed that the convection is long lived. Spatially isolated convection will not result in introducing numerical noise because such noise is removed efficiently by the high-order low-pass tangential or sine filters (Raymond 1988; Raymond and Garder 1991). In Fig. 4 the differences between the forecasts for the 500-mb mixing ratios (g kg^{-1}) are superimposed upon the infrared satellite image. Note that small increases in the mixing ratio occur over cloudy regions,

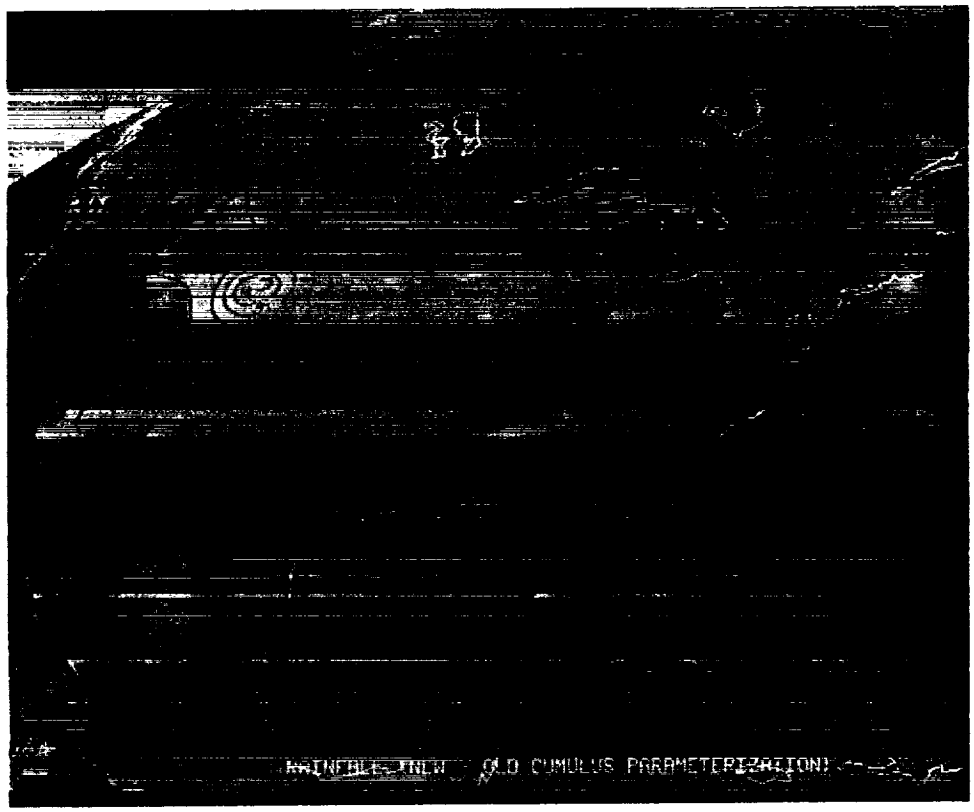

FIG. 4. Difference (×10) in the mixing ratio (g kg^{-1}) for a 12-h forecast (0000–1200 UTC 22 April 1988) with and without the perturbation wind [Eqs. (20a) and (21a)] application in the cumulus cloud parameterization scheme. Differences are superimposed upon the VAS infrared image.

but decreases occur over regions associated with descending vertical motion. In this figure the band of clouds to the north and west is associated with a cold front, while the band over the Gulf coast is high clouds streaming in over Mexico from the Pacific Ocean. (These bands are separated by a strong wind jet.) Our tests show that the first term in (20a) and (21a) is responsible for most of enhanced vertical circulation.

The convective rainfall from the cumulus scheme with momentum adjustment was slightly less than that produced by the traditional Kuo procedure because the restriction $|R_1| < 0.5$ limited the amount of condensation. This made the parameterization more realistic since too much condensation was occurring too rapidly in some localities with the standard scheme. It is known—for example, Krishnamurti et al. (1980)—that the original Kuo (1965) scheme gives excessive moistening of the atmosphere. Sundqvist et al. (1989) introduced a special factor to govern the vertical distribution of convective heating to help correct that problem. Nevertheless, a maximum increase in the nonconvective rainfall of 4 mm in 12 h was also observed. This increase (Fig. 5) occurred because of the enhanced vertical circulation that resulted from the application of the momentum adjustment [(20a) and (21a)].

Initialized National Meteorological Center global analyses valid over North America between 1200 UTC 9 March and 1200 UTC 12 March 1988 were used as initial and boundary conditions in a 72-h forecast made by the CIMSS regional model using 190.5-km resolution on a 41 × 37 horizontal grid with a 720-s time step. The control forecast uses no momentum adjustment. In the test case the momentum adjustment uses the first two terms given in (20a) and (21a) with the restriction that $|R_1| < 0.25$. Also, the sixth-order implicit tangent filter (Raymond 1988) is applied with a filter factor of either $\epsilon = 0.05$ or $\epsilon = 0.64$. The latter value gives moderate to heavy filtering. The u velocity component rms differences between verifying initialized analysis and forecast are shown as a function of time in Figs. 6a–c. The momentum adjustment at sigma level 3 (approximately 230 mb) results in a small improvement in the statistics except at 24 h. Increasing the filter factor from 0.05 to 0.64 has a larger impact than the adjustment, primarily because all grid points are involved. In contrast, the maximum number of occurrences for cumulus parameterization is no more

FIG. 5. Same as Fig. 4 but illustrating the 12-h difference in the total rainfall (mm) between the two 12-h forecasts.

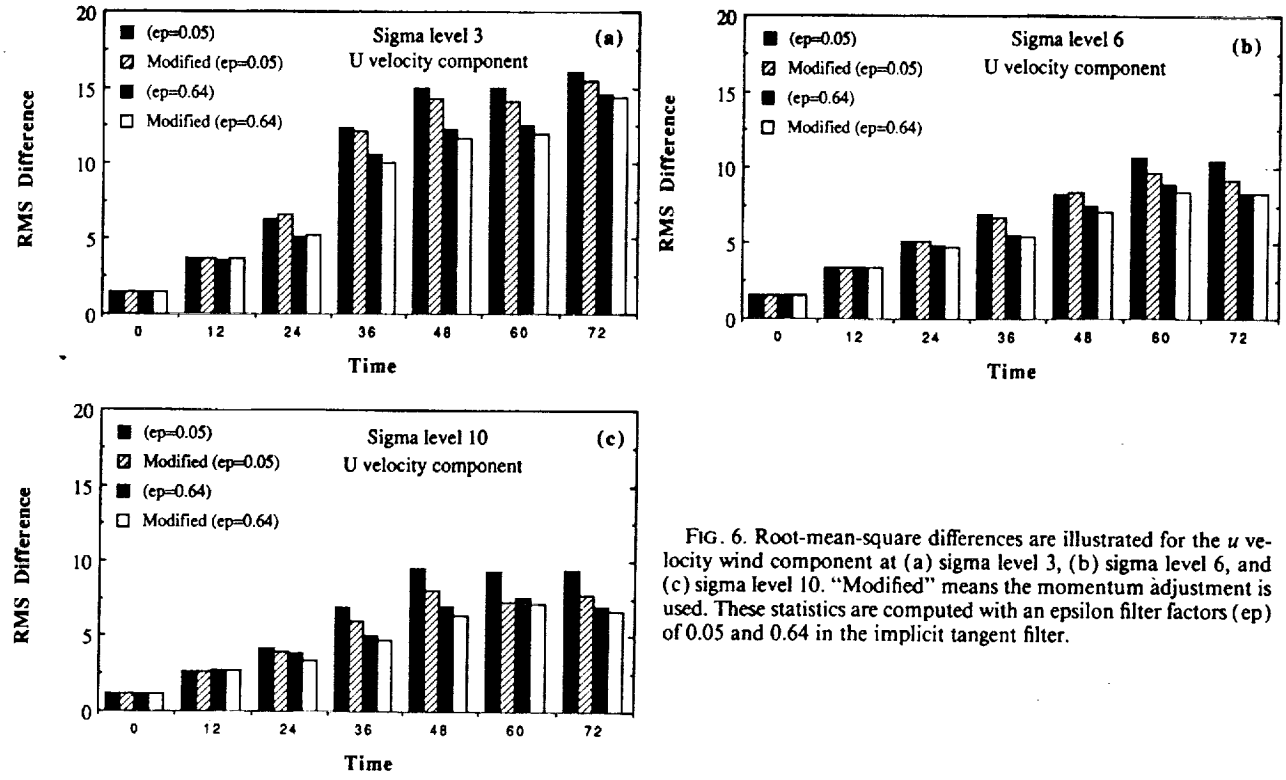

FIG. 6. Root-mean-square differences are illustrated for the u velocity wind component at (a) sigma level 3, (b) sigma level 6, and (c) sigma level 10. "Modified" means the momentum adjustment is used. These statistics are computed with an epsilon filter factors (ep) of 0.05 and 0.64 in the implicit tangent filter.

than 527 vertical profiles out of about 1500 possible locations (see Fig. 8). At sigma level 6 (Fig. 6b, approximately 440 mb) the major improvement occurs late in the forecast. Lower levels (approximately 720 mb) respond best to the momentum adjustment, as illustrated in Fig. 6c. In all cases, heavy filtering always reduces the contribution from the adjustment. The v velocity wind component rms differences are shown in Fig. 7. Again, sigma level 10 shows the most improvement at 60 and 72 h. Upper-level contributions average out to near neutral or slightly on the negative side. This may reflect shortcomings in the cumulus parameterization or in the momentum adjustment process or in both. The lack of entrainment or vertical mixing by turbulence in the cumulus parameterization is clearly a deficiency. How case dependent the adjustment procedure is remains unknown, as do estimates for α_u and α_v.

The number of active cumulus parameterizations versus time step is shown for a 36-h period in Fig. 8. It shows that cumulus convective activity is slightly enhanced early in the forecast and experiences less $2\Delta t$ and other high-frequency oscillations with the momentum adjustment.

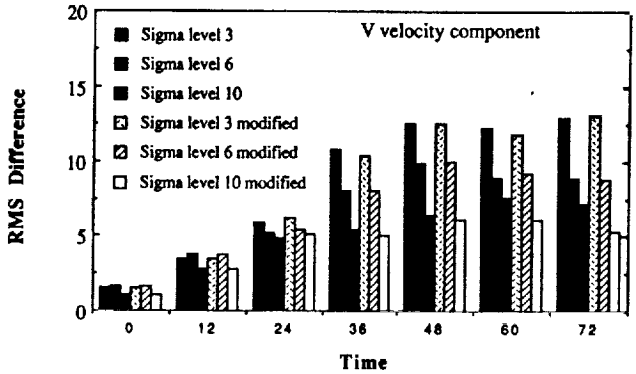

FIG. 7. Same as Fig. 6 but for the v velocity wind component and with the smaller filter factor.

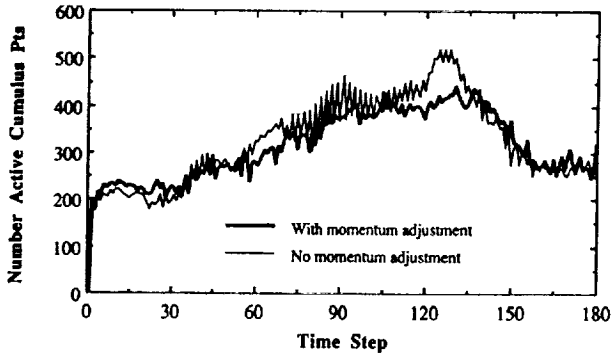

FIG. 8. Number of grid points experiencing cumulus parameterization as a function of the time step.

5. Summary

A diabatically induced term is present in the equations describing the moisture flux and heat flux. This term has the form of damping (forcing) for condensation (evaporation). Diabatic processes also influence the horizontal flux through the pressure gradient term. In this study the influence of the damping term is evaluated, but the characteristics associated with diabatic changes to the geostrophic wind are not analyzed.

This study finds that mild reductions in the large-scale wind speed caused by cumulus friction can contribute to the near conservation of the large-scale horizontal components of the moisture flux. This is the consequence of an establishment of a near balance between the pressure gradient, Coriolis, and Rayleigh damping terms in the moisture flux equations. This balance is identified by scale analysis. This outcome is independent of the mechanism responsible for the reduction in wind speed.

Estimates of diabatically related changes to the horizontal wind are easily obtained from the balanced relationship. For realistic condensation rates, these wind estimates are consistent with the gradient wind approximation. When these estimates are used in a simple hurricane model they predict a radial inflow with convergence, provided the rotation is cyclonic. In contrast, divergence is associated with anticyclonic rotation and evaporation. When the predicted wind perturbations are used as a momentum adjustment in a Kuo cumulus parameterization scheme they improve the 72-h forecast rms u velocity component error statistics and enhance mesoscale vertical circulations. In the tropics any movement toward conservation of moisture flux enhances an antitriptic relationship, cementing a near balance between a Rayleigh damping term and the pressure gradient term. Note that it is necessary to have the condensation before the wind-related processes can be activated. In this way this process is similar to conditional instability of the second kind (CISK).

Our equations (20a) and (21a) are approximations of the influence from one diabatic source on the wind. A more rigorous study using the vorticity and divergence concept will be described elsewhere. The terms in the flux equations are also being analyzed using mesoscale model calculations. This is the subject of continuing study.

Acknowledgments. This work was supported by National Science Foundation ATM-8920508 and NASA NAGW-1855. The author thanks Arthur Garder (Professor Emeritus, Southern Illinois University, Edwardsville, Illinois), Barry Hinton (SSEC, University of Wisconsin), and Robert Rabin (NSSL, Normal, Oklahoma) for helpful suggestions. Leo Donner (GFDL, Princeton, New Jersey), Robert Merrill (CIMSS, University of Wisconsin), and Franklin Robertson (NASA/Marshall, Huntsville, Alabama) are thanked for suggesting specific references.

APPENDIX

The Sensible Heat Flux Equations

The equations describing the temporal and spatial distribution of the horizontal components of the sensible heat flux can be constructed from (1), (2), and (4). They are

$$\frac{d(\theta u)}{dt} = -\frac{\theta}{\rho}\frac{\partial p}{\partial x} + \theta f v - B\theta u, \qquad \text{(A1)}$$

$$\frac{d(\theta v)}{dt} = -\frac{\theta}{\rho}\frac{\partial p}{\partial y} - \theta f u - B\theta v. \qquad \text{(A2)}$$

In these equations the damping coefficient $B = LQ/(Tc_p)$; here, T is temperature, c_p is the specific heat at constant pressure, and L is the latent heat of vaporization. For condensation processes B is negative but smaller in magnitude than the coefficient A in (8) and (9).

REFERENCES

Austin, P. M., and R. A. Houze, 1973: A technique for computing vertical transports by precipitating cumuli. *J. Atmos. Sci.*, **30**, 1100–1111.

Cho, H. R., 1985: Rates of entrainment and detrainment of momentum of cumulus clouds. *Mon. Wea. Rev.*, **113**, 1920–1932.

Daley, R., 1991: *Atmospheric Data Analysis.* Cambridge University Press, 457 pp.

Delden, A. van, 1989: On the deepening and filling of balanced cyclones by diabatic heating. *Meteor. Atmos. Phys.*, **41**, 127–145.

Donner, L. J., 1988: An initialization for cumulus convection in numerical weather prediction models. *Mon. Wea. Rev.*, **116**, 377–385.

——, H. L. Kuo, and E. J. Pitcher, 1982: The significance of thermodynamic forcing by cumulus convection in a general circulation model. *J. Atmos. Sci.*, **39**, 2159–2181.

Esbensen, S. K., L. J. Shapiro, and E. I. Tollerud, 1987: The consistent parameterization of the effects of cumulus clouds on the large-scale momentum and vorticity fields. *Mon. Wea. Rev.*, **115**, 664–669.

Fiorino, M., and R. L. Elsberry, 1989: Some aspects of vortex structure related to tropical cyclone motion. *J. Atmos. Sci.*, **46**, 975–990.

Gill, A. E., 1980: Some simple solutions for heat-induced tropical circulations. *Quart. J. Roy. Meteor. Soc.*, **106**, 447–462.

Hack, J. J., and W. H. Schubert, 1986: Nonlinear response of atmospheric vortices to heating by organized cumulus convection. *J. Atmos. Sci.*, **43**, 1559–1573.

Haltiner, G. J., and R. T. Williams, 1980: *Numerical Prediction and Dynamic Meteorology.* Wiley, 477 pp.

Heckley, W. A., and A. E. Gill, 1984: Some simple analytical solutions to the problem of forced equatorial long waves. *Quart. J. Roy. Meteor. Soc.*, **110**, 203–217.

Holton, J. R., 1979: *An Introduction to Dynamic Meteorology.* Academic Press, 391 pp.

——, and D. E. Colton, 1972: A diagnostic study of the vorticity balance at 200 mb in the tropics during the northern summer. *J. Atmos. Sci.*, **29**, 1124–1128.

Houze, R. A., and P. V. Hobbs, 1982: Organization and structure of precipitating cloud systems. *Advances in Geophysics*, No. 24, Academic Press, 225–315.

Konig, W., and E. Ruprecht, 1989: Effects of convective clouds on the large-scale vorticity budget. *Meteor. Atmos. Phys.*, **41**, 213–229.

Krishnamurti, T. N., S. Low-Nam, and R. Pasch, 1983: Cumulus parameterization and rainfall rates II. *Mon. Wea. Rev.*, **111**, 815–828.

——, K. Ingles, S. Cocke, T. Kitade, and R. Pasch, 1984: Details of low latitude medium range numerical weather prediction using a global spectral model. *J. Meteor. Soc. Japan*, **62**, 613–648.

——, Y. Ramanathan, H.-L. Pan, R. J. Pasch, and J. Molinari, 1980: Cumulus parameterization and rainfall rates. *Mon. Wea. Rev.*, **108**, 456–464.

Kuo, H. L., 1965: On formation and intensification of tropical cyclones through latent heat release by cumulus convection. *J. Atmos. Sci.*, **22**, 40–63.

——, 1974: Further studies of the parameterization of the influence of cumulus convection on large-scale flow. *J. Atmos. Sci.*, **31**, 1232–1240.

Kuo, Y. H., and R. S. Reed, 1988: Numerical simulation of an explosively deepening cyclone in the eastern Pacific. *Mon. Wea. Rev.*, **116**, 2081–2105.

Leslie, L. M., G. A. Mills, L. W. Logan, D. J. Gauntlett, G. A. Kelly, J. L. Mcgregor, and M. J. Manton, 1985: A high resolution primitive equation NWP model for operations and research. *Aust. Meteor. Mag.*, **33**, 11–35.

Lorenz, E. N., 1978: Available energy and the maintenance of a moist circulation. *Tellus*, **30**, 14–31.

Malkus, J. S., 1952: The slopes of cumulus clouds in relation to external wind sheer. *Quart. J. Roy. Meteor. Soc.*, **78**, 530–542.

Matsuno, T., 1966: Quasi-geostrophic motions in the equatorial area. *J. Meteor. Soc. Japan*, **44**, 25–43.

Ooyama, K., 1971: Convection and convection adjustment: A theory on parameterization of cumulus convection. *J. Meteor. Soc. Japan*, **49** (special issue), 744–756.

Petterssen, S., 1956: *Weather Analysis and Forecasting*. McGraw-Hill, 428 pp.

Raymond, W. H., 1986: Topographical-induced mesoscale motions in antitriptically balanced barotropic flow. *Tellus*, **38A**, 251–262.

——, 1988: High-order low-pass implicit tangent filters for use in finite area calculations. *Mon. Wea. Rev.*, **116**, 2132–2141.

——, and A. Garder, 1991: A review of recursive and implicit filters. *Mon. Wea. Rev.*, **119**, 477–495.

Reed, R. J., A. J. Simmons, M. D. Albright, and P. Unden, 1988: The role of latent heat release in explosive cyclogenesis: Three examples based on ECMWF operational forecasts. *Wea. Forecasting*, **3**, 217–229.

Riehl, H., 1963: Some relations between the wind and thermal structure of steady-state hurricanes. *J. Atmos. Sci.*, **20**, 276–287.

——, 1979: *Climate and Weather in the Tropics*. Academic Press, 611 pp.

——, and J. S. Malkus, 1958: On the heat balance of the equatorial trough zone. *Geophysica*, **6**, 503–538.

Schneider, E. K., and R. S. Lindzen, 1976: A discussion of the parameterization of momentum exchange by cumulus convection. *J. Geophys. Res.*, **81**, 3158–3160.

Shapiro, L. J., and D. E. Stevens, 1980: Parameterization of convective effects on the momentum and vorticity budgets of synoptic-scale Atlantic tropical waves. *Mon. Wea. Rev.*, **108**, 1816–1826.

Stull, R. B., 1988: *An Introduction to Boundary Layer Meteorology*. Kluwer Academic Publishers, 666 pp.

Sui, C. H., and M. Yanai, 1986: Cumulus ensemble effects on the large-scale vorticity and momentum fields of GATE. Part I: Observational evidence. *J. Atmos. Sci.*, **43**, 1618–1642.

Sundqvist, H., E. Berge, and J. E. Kristjansson, 1989: Condensation and cloud parameterization studies with a mesoscale numerical weather prediction model. *Mon. Wea. Rev.*, **117**, 1641–1657.

Tarbell, T. C., T. T. Warner, and R. A. Anthes, 1981: An example of the initialization of the divergent wind component in a mesoscale numerical weather prediction model. *Mon. Wea. Rev.*, **109**, 77–95.

Turpeinen, O. M., T. L. Garand, R. Benoit, and M. Roach, 1990: Diabatic initialization of the Canadian regional finite-element (RFE) model using satellite data. Part I: Methodology and application to a winter storm. *Mon. Wea. Rev.*, **116**, 2593–2613.

Wang, W., and T. T. Warner, 1988: Use of four-dimensional data assimilation by Newtonian relaxation and latent-heat forcing to improve a mesoscale-model precipitation forecast: A case study. *Mon. Wea. Rev.*, **116**, 2593–2613.

Willoughby, H. E., 1979: Excitation of spiral bands in hurricanes by interaction between the symmetric mean vortex and a shearing environment steering current. *J. Atmos. Sci.*, **36**, 1226–1238.

——, 1990: Gradient balance in tropical cyclones. *J. Atmos. Sci.*, **47**, 265–274.

Yanai, M., S. Esbense, and J.-H. Chu, 1973: Determination of bulk properties of tropical cloud clusters from large-scale heat and moisture budgets. *J. Atmos. Sci.*, **30**, 611–627.

Zhang, G. J., and H.-R. Cho, 1991: Parameterization of the vertical transport of momentum by cumulus clouds. Part I: Theory. *J. Atmos. Sci.*, **48**, 1483–1492.

Preprints, Ninth Conference on Numerical Weather Prediction, Denver, C0, Oct. 10-15, American Meteorological Society, 430-433.

INITIALIZATION AND ASSIMILATION OF CLOUD AND RAINWATER IN A REGIONAL MODEL

William H. Raymond and William S. Olson
Cooperative Institute for Meteorological Satellite Studies
The University of Wisconsin
Madison, Wisconsin 53706

1. INTRODUCTION

In this study we examine the initialization and assimilation of cloud and rainwater quantities in a mesoscale regional model. In our study forecasts of explicit cloud and rainwater are made using conservation equations. The physical processes include condensation, evaporation, autoconversion, accretion and the removal of rainwater by fallout. These physical processes, some of which are parameterized, represent source and sink terms in the conservation equations. The question of how to initialize the explicit liquid water calculations in numerical models and how to retain information about precipitation processes during the 4-D assimilation cycle are important issues that will be addressed.

With increasing computer speed there has been a slow but study enhancement in model horizontal grid resolution. Current NWP models are approaching the spatial resolution where time-dependent cloud variables are physically relevant. In our pilot study we examine the feasibility of initializing and assimilating cloud and rainwater using explicit cloud conservation equations within a regional mesoscale model. The knowledge of cloud and rainwater fields as a function of time and space provides information, such as model heating rates and vertical distributions, that are more difficult to obtain from conventional cloud parameterization approaches where cloud properties are not retained from one time step to the next. Global models will soon routinely solve explicit cloud and rainwater conservation equations, but limited area mesoscale models can be utilized to examine this topic now.

Cloud and rainwater are the cumulative products of the transport of atmospheric moisture, both vapor and liquid, plus the physical processes included in cloud development and decay. By their very nature cumulative processes are difficult to initiate in numerical models, and it is common for precipitation to be absent during the first few hours of a numerical forecast. One reason for this deficiency is the resolution of the data. Conventional surface and upper air reports are known not to capture the mesoscale circulations that have the enhanced convergence necessary to support mesoscale precipitation processes. The missing mesoscale circulations also influence the moisture and thermal fields (Turpeinen 1990). Consequently, in order to initiate precipitation and assimilate cloud parameters it is necessary to know additional information beyond the conventional synoptic data base. This might include accurate estimates of the vertical heating rates and the low level convergence and/or the high level divergence that produces the cloud-sustaining vertical motion field. Also, model generated inaccuracies or shortcomings, e.g., phase errors and inadequate physics, must be accommodated in some manner.

When the heating rates are known or can be approximated, then either diabatic or cumulus initialization is possible (Errico and Rasch 1988; Donner 1988). These initialization procedures help establish circulation patterns consistent with latent heating processes that are otherwise not resolved in synoptic scale data. For a review of recent studies using diabatic initialization schemes, see Table 1 in Turpeinen et al. (1990). Without the heating rate information each forecast must go through a short time period where the precipitation processes must 'spin-up' before rainfall can be produced. In regional mesoscale models this spin-up usually occurs during the first 2 to 6 hours. Diabatic initialization should reduce the degree and duration of the spin-up. In contrast, normal mode or dynamic initialization procedures, designed to help with the removal of gravity waves during initialization, only provide slight or no assistance in speeding up precipitation processes (Lejenas 1980).

Cloudwater and rainwater data are generally not available. Rain gauge reports imply information about the total amount of liquid water reaching the surface, but no knowledge about the instantaneous vertical distribution is recoverable. Most microwave satellite measurements of instantaneous cloud quantities only resolve the vertically integrated cloud and/or integrated rainwater. Thus it is necessary to make some assumption about the vertical distribution of the heating rate. New physical retrieval methods that combine observed microwave satellite radiances with known meteorological fields and/or physical constraints should provide some insight into the vertical partitioning of the liquid water. These techniques are just beginning to be examined.

The use of diabatic initialization requires an answer to the question of how the latent heating is going to be distributed in the vertical. Some studies have used representative profiles (Fiorino and Warner 1981); others assume a general parabolic profile (Tarbell et al 1981; Salmon and Warner 1986, etc.) while some have tried to use the forecast model itself in some fashion (Wergen 1988: Danard 1985: Turpeinen et al. 1990). Donner (1988) used a variational formulation to optimize the vertical distribution with respect to the methodology of the Kuo cumulus parameterization. In all but the Donner study it has been

customary to use either the diabatic omega equation or a diabatic form of the normal mode initialization scheme. Earlier pioneering work by Krishnamurti et al. (1984) suggested that a reanalysis of the moisture and wind field is also needed.

In this study we will incorporate in the initialization the heating rates, cloudwater, and rainwater predicted by a forecast beginning 12 hours before the assimilation process. This information will be combined with new information from observations, and heating rates will be utilized in a diabatic form of the vertical mode initialization scheme of Bourke and McGregor (1983). Theoretically, if data is always available then cloud and rainwater could be treated much like other meteorological variables, i.e., updated and modified during the 4D assimilation process. Caution is however required when making large changes to existing model cloud fields, or to the dynamics that support the precipitation process. Testing and experience with explicit cloud initialization will dictate what the correct procedure should be.

Results from only a few experiments are presented here. An evaluation of the contribution of the satellite data will be given at the conference.

2. MODELING CONSIDERATIONS

A modified version of the Bureau of Meteorology Research Centre (BMRC) operational incremental O/I analysis (Mills and Seaman 1990), vertical mode initialization or VMI (Bourke and McGregor 1983), and semi-implicit forecast model (Leslie, et al. 1985) are used in this investigation. The incremental analysis is set to preserve the irrotational wind field while the rotational component of the differences between data and model guess wind and other fields are evaluated by the O/I. In our initial tests the horizontal resolution is 120 km, while the vertical sigma coordinate is subdivided into 15 levels. We selected the low resolution 120 km grid spacing on a 35x35 horizontal grid configuration to specifically examine problems that are relevant or commonly encountered in today's centers for numerical weather prediction.

In our present study the Kuo cumulus parameterization is turned off and the conventional large scale precipitation procedure is replaced with explicit conservation equations for cloudwater and rainwater. The explicit cloud physics contains processes modeled using a modified Kessler type scheme (Kessler 1974), while the condensation and fall velocity calculations are similar to that described in Anthes, et al. (1987). The 'fallout' term is calculated by a semi-Lagrangian method to allow for the 10 minute time steps used in the semi-implicit model calculations. Ice phase cloud particles have not yet been included in the model.

Part of the goal of the current study is to modify the model cloud and rainwater fields using SSM/I retrievals of integrated total liquid water or vertical distributions of water. These observed quantities will be used to perturb existing model cloud and rainwater fields. Heating rates, lagged by one time step (Δt=10 min) or based on the total liquid water from the 12h pre-forecast, are used in the initialization. Many different types of model experiments are to be conducted, including those related to the model's response to diabatic and initial information.

Because of horizontal scale considerations, our explicit cloud calculations do not model individual clouds but do approximate average values for a system or complex of clouds. This was the motivation behind the modifications made to the Kessler (1974) cloud physics formulation. It is known that the lifetime of individual clouds is less than one hour while a cloud complex exists for many hours with remnants lasting for days. Thus Kessler's accretion (collection) process was modified to slow greatly the conversion from cloud to rainwater when the cloud water C is below a preset critical value C_{crit}. Also incorporated is a vertical dependence on temperature that follows the scheme suggested by Schlesinger (1990). This latter change helps retain and enhance anvil or cloud top features. In mixing ratio units (gg^{-1}), the contribution to the rate of change from accretion is

$$ACC \equiv 0.88 C_1 C_2 \, C \, R^{0.875} \qquad (1)$$

where $C_1 = \min[\,1.0,\ 1.0 - (C_{crit} - C)/C_{crit}\,]$,

$C_2 = \min[\,1.0, (T - 233)/40\,]$,

$C_2 = \max[\,1.0, C_2\,]$.

Here R is rainwater in mixing ratio units, T is the temperature in degrees Kelvin, and C_{crit}=1 gkg^{-1}. Initial experiments give promising results, but additional tests and verifications will be made to further evaluate computed cloud water quantities. These will include comparisons between model cloud water fields and SSM/I retrievals of cloud water distributions.

To facilitate the large time step size used in the semi-implicit forecast model the fallout term in sigma coordinates is rewritten as two terms, one of which represents vertical advection,

$$g\partial(\rho v_t R)/\partial\sigma \equiv A\partial(p^* R)/\partial\sigma + (p^* R g/p^*)\partial(\rho v_t)/\partial\sigma . \qquad (2)$$

Here ρ is the air density, v_t (ms^{-1}) is the terminal velocity of raindrops, p^* is the surface pressure, g is the acceleration of gravity and A (s^{-1}) is equivalent to a velocity in the vertical σ coordinate system, that is

$$A = g\rho v_t / p^* . \qquad (3)$$

The time tendency for A using (2) now can be found by semi-Lagrangian procedures.

3. DISCUSSION OF RESULTS

Super-imposed over the GOES 7 IR image in Fig. 1 are contours of cloudwater (solid) and rainwater (dashed) for sigma level 4 (approx. 300 mb) from a 12h forecast. The contour interval is 0.1 gkg^{-1}. The initial field for this ERICA (Experiment on Rapidly Intensifying Cyclones over the Atlantic) IOP-5 case is obtained from NMC's initialized global analysis. For the most part, the forecasted cloud fields assume the horizontal comma-shape shown in the

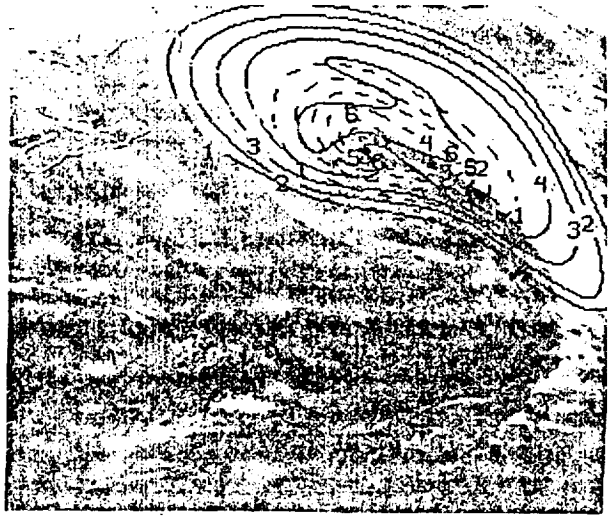

Fig. 1. Contours (0.1 gkg^{-1}) of cloudwater (solid) and rainwater (dashed) from a 12h forecast (0000 to 1200UTC, 20 Jan 1989) are superimposed over the GOES IR image.

image. In this forecast no diabatic initialization was used. When the modifications to the accretion term proposed in Eq. (1) are removed, the amount of cloud water is reduced to just one short contour (not shown) while the rainwater is enhanced slightly beyond that shown in Fig. 1. Cloudwater amounts at lower sigma levels also are much reduced when the original Kessler formulation is used. With either method the total rainfall is nearly identical in magnitude and areal coverage. The maximum rainfall over 12 hours was 33 mm for the modified approach and 34 mm for the original Kessler formulation.

In Fig. 2 the area averaged precipitation rate at each time step is plotted versus the time step for forecasts between 1200UTC, 19 Jan and 1200UTC, 20 Jan 1989. In the two forecasts without explicit clouds (labeled "large scale"), all excess water vapor exceeding saturation falls out immediately. This approach is known to produce rainfall rapidly. In contrast, note that the precipitation in the explicit

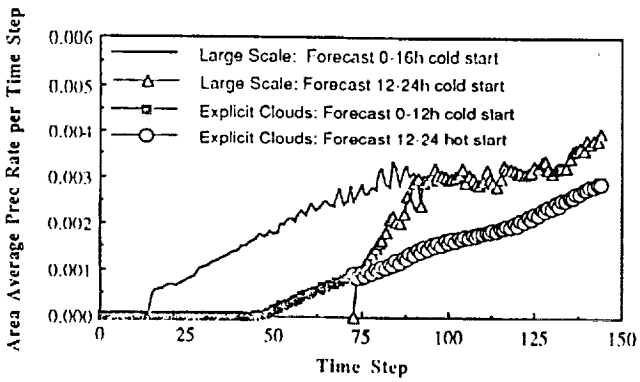

Fig. 2. Area average precipitation rate (cm) is plotted versus the time step for 4 forecasts. Forecasts with and without explicit clouds illustrate the differences in the precipitation spin-up time.

cloud calculations is delayed. This is because the autoconversion threshold, used to model the water holding capacity of clouds, is not triggered until the cloudwater exceeds 0.5 gkg^{-1}.

After 12h or 72 time steps, the forecast fields generated by the explicit cloud calculations are assimilated to begin a second 12-hour forecast. Note in Fig. 2 that the precipitation rate remains unchanged following the assimilation step as illustrated by the continuous curve between steps 72 (square) and 73 (circle). However, the precipitation rate can incur irregular behavior if the irrotational wind or dynamics are significantly changed. The incremental analysis in our assimilation preserves the irrotational wind component from the previous forecast. But, our current VMI initialization can alter the convergence and/or divergence. Thus, some consideration is being given to installing an incremental initialization procedure.

In Fig. 3 we expand the view of the second 12h period presented earlier in Fig. 2. Two of the curves from Fig. 2 are reproduced for comparison purposes. They include the cold started large scale calculations represented by the triangle curve, and the assimilated hot start shown with circles. Additionally, cold and hot started explicit cloud calculations beginning with the global initialized analysis are presented. The hot started forecasts utilize cloudwater and rainwater forecasted by the 12h pre-forecast. The heating rate at time step 72 is also used in the diabatic vertical mode initialization.

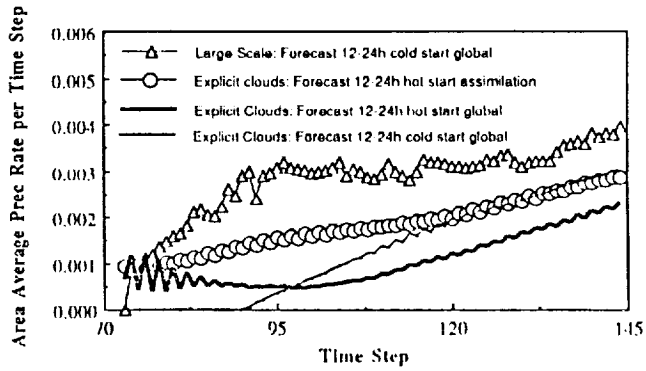

Fig. 3. Same as Fig. 2 except for initialization. All forecasts begin at time step 72.

It is clear that when the previous forecast model fields are used, as in the assimilation process, there is dynamics to support the cloud and rainwater. Thus the forecasted precipitation rate behaves properly (circle curve). When the supporting mesoscale dynamics and moisture supply are missing, as in the global initialized analysis, then adding cloud and rainwater initially can result in less realistic behavior as illustrated by the heavy solid curve in Fig. 3. This curve illustrates our worst-case scenario. For this latter case, improvement is obtained when the heating rates are also used to force or nudge the dynamics (Wang and Warner

1988) toward the desired goal (not shown). We discovered that enhanced development can become too strong in a reduced area when only the heating rates from time step 72 in the 12h pre-forecast are used. Approximating the heating rates from the total cloudwater and rainwater fields gives better results.

Many additional experiments are required before the best strategy or strategies are identified. But, the assimilation approach using incremental changes clearly is indicated to be a powerful technique that could solve the spin-up problem. However, remotely sensed cloudwater and rainwater data, and information about their vertical distribution, is still required if the forecast is to correctly simulate the atmosphere.

Acknowledgements. This work was supported by NASA Grant NAGW-1855. One author (WHR) was supported in part by National Science Foundation Grant ATM-8920508.

References

Anthes, R. A., E-Y Hsie and Y-H Kuo, 1987: Description of the Penn State/NCAR mesoscale model version 4 (MM4). NCAR Technical Note NCAR/TN-282+STR. National Center for Atmospheric Research, Boulder, Colorado, 66pp.

Bourke, W. and J. L. Mcgregor, 1983: A nonlinear vertical mode initialization scheme for a limited area prediction model. *Mon. Wea. Rev.*, **111**, 2285-2297.

Danard, M., 1985: On the use of satellite estimates of precipitation in initial analyses for numerical weather prediction. *Atmosphere-Ocean*, **23**, 23-42.

Donner, L. J., 1988: An initialization for cumulus convection in numerical weather prediction models. *Mon. Wea. Rev.*, **116**, 377-385.

Errico, R. and P. J. Rasch, 1988: A comparison of various normal-mode initialization schemes and the inclusion of diabatic processes. *Tellus*, **40A**, 1-25.

Fiorino, M and T.T. Warner, 1981: Incorporating surface winds and rainfall rates into the initialization of a mesoscale hurricane model. *Mon. Wea. Rev.*, **109**, 1914-1929.

Kessler, E., 1974: Model of precipitation and vertical air currents. *Tellus*, **26**, 519-542.

Krishnamurti, T. N., K. Ingles, S. Cocke, R. Pasch, and T. Kitade, 1984: Details of low latitude medium range weather prediction using a global spectral model II. Effect of orography and physical initialization. *J Meteor. Soc. Japan*, **62**, 613-649.

Lejenas, H., 1980: On the influence of the technique of nonlinear normal mode initialization on the nonconvective precipitation rate. *Mon. Wea. Rev.*, **108**, 1465-1468.

Leslie, L. M., G. A. Mills, L. W. Logan, D. J. Gauntlett, G. A. Kelly, J. L. McGregor and M. J. Manton, 1985: A high resolution primitive equation NWP model for operations and research. *Aust. Meteor. Mag.*, **33**, 11-35.

Mills, G. A. and R. S. Seaman, 1990: The BMRC regional data assimilation system. *Mon. Wea. Rev.*, **118**, 1217-1237.

Salmon, E. M., and T. T. Warner, 1986: Short-term numerical precipitation forecasts initialized using a diagnosed divergent-wind component. *Mon. Wea. Rev.*, **114**, 2122-2132.

Schlesinger, R. E., 1990: Feedback of deep moist convection to its near environment as diagnosed from three-dimensional numerical model output: Results from an early experiment. *J. Atmos. Sci.*, **47**, 1390-1412.

Tarbell, T. C., T. T. Warner and R. A. Anthes, 1981: An example of the initialization of the divergent wind component in a mesoscale numerical weather prediction model. *Mon. Wea. Rev.*, **109**, 77-95.

Turpeinen, O. M., L. Garand, R. Benoit and M. Roch, 1990: Diabatic initialization of the Canadian regional finite-element (RFE) model using satellite data. Part I: Methodology and application to a winter storm. *Mon. Wea. Rev.*, **118**, 1381-1395.

Wang, W. and T. T. Warner, 1988: Use of four-dimensional data assimilation by newtonian relaxation and latent-heat forcing to improve a mesoscale-model precipitation forecast: A case study. *Mon. Wea. Rev.*, **116**, 2593-2613.

Wergen, W., 1988: The diabetic ECMWF normal mode initialization scheme. *Beitr. Phys. Atmosph.*, **61**, 274-302.

Preprints, Sixth Conference on Satellite Meteorology and Oceanography, Atlanta, GA, Jan 5-10, American Meteorological Society, 313-316.

PHYSICAL RETRIEVAL OF PRECIPITATION WATER CONTENTS USING MULTISENSOR MICROWAVE DATA AND MODEL CONSTRAINTS

William S. Olson and William H. Raymond

CIMSS / Space Science and Engineering Center
University of Wisconsin
Madison, Wisconsin

1. INTRODUCTION

The retrieval of precipitation distributions by passive microwave techniques has been an area of study in satellite remote sensing for well over a decade. The recent initiative to estimate both the horizontal and vertical distributions of precipitating liquid water in the tropics (i.e. the Tropical Rainfall Measuring Mission or TRMM) has further stimulated interest in this area; see Simpson, et al. (1988). The proposed TRMM satellite will carry a suite of sensors including passive and active microwave instruments, as well as visible and infrared radiometers. A combination of microwave and visible/IR sensors has also been proposed for one of the Earth Observing System (EOS) platforms for the purpose of retrieving rainfall rates and other geophysical parameters; ref. Murphy (1987). Methods for determining precipitation distributions based upon data from several instruments having different spectral and resolution characteristics will therefore be required.

Currently multispectral microwave observations from the Special Sensor Microwave/Imager (SSM/I), borne by the DMSP-F8, have provided researchers with the means for retrieving rainfall rates; see Hollinger (1991), Kummerow and Liberti (1990), Petty and Katsaros (1990). The SSM/I is a multichannel, dual-polarization, passive microwave radiometer with channels at 19.35, 22.235, 37, and 85.5 GHz. The diffraction limitation of the SSM/I antenna causes the spatial resolution of measurements to increase with frequency, such that the minimum footprint dimension decreases from 43 km at 19.35 GHz to 13 km at 85.5 GHz. The DMSP also carries the Special Sensor Microwave/Temperature sounder with channels at 50.5, 53.2, 54.35, 54.9, 58.4, 58.825, and 59.4 GHz, and a footprint dimension of approximately 180 km at nadir view. In the present study, a physical retrieval method for estimating precipitation water distributions and other geophysical parameters based upon measurements from the DMSP-F8 SSM/I is developed. Three unique features of the retrieval method are (1) sensor antenna functions are explicitly included to accommodate varying channel resolution, (2) an embedded one-dimensional cloud model is utilized to generate vertical distributions of precipitating and nonprecipitating water, and (3) spectral solutions are sought for certain background parameters, such as humidity, which vary more slowly in the horizontal than the cloud and precipitation water contents. The general framework of the method will allow us to incorporate measurements from the SSM/T and geostationary infrared measurements, as well as information from conventional sources (e.g. radiosondes) or numerical forecast model fields.

2. RETRIEVAL METHOD

The basis of the retrieval method is the minimum variance solution as described in Lorenc (1986). An error functional which expresses the deviation of the observed satellite antenna temperatures from model-derived values, plus an additional constraint which represents the deviation of retrieved geophysical parameters from *a priori* estimates, is derived.

$$E = (TA_{obs} - TA(P)_{mod})^T \Sigma^{-1} (TA_{obs} - TA(P)_{mod}) + (P - P_{apriori})^T \Delta^{-1} (P - P_{apriori}) \quad (1)$$

Here, TA_{obs} is a vector of antenna temperature measurements, $TA(P)_{mod}$ are antenna temperature estimates based on a physical model, P is a vector of geophysical parameters to be retrieved, and $P_{apriori}$ are estimates of the parameters based upon *a priori* knowledge. Σ and Δ are covariance matrices representing observational plus model errors (Σ), and errors in the *a priori* estimates (Δ). In this study all off-diagonal elements of these matrices are neglected.

The antenna temperature model, $TA(P)_{mod}$, embodies the physical relationship between the geophysical parameters to be retrieved and the antenna temperatures measured by the radiometer. An element of $TA(P)_{mod}$ may be written

$$TA(P)_p = A_c^T TB(P)_p + A_x^T TB(P)_{p'} + \delta_p Tbb, \quad (2)$$

where A_c and A_x are the co- and cross-polarized antenna patterns of the radiometer, $TB(P)_p$ and $TB(P)_{p'}$ are the modeled brightness temperatures in the polarization p and orthogonal polarization p' with respect to the plane of polarization of the measurement, and δ_p is the fraction of the radiometer feedhorn pattern not subtended by the antenna. Tbb is the cosmic background radiance (2.7 K). Thus each antenna temperature is modeled as the convolution of the upwelling brightness temperature field by the antenna response pattern of the sensor. In this way, measurements at different channel frequencies or from different sensors which have different sampling / spatial resolution can be accommodated.

The retrieval of preciptation liquid water contents and other geophysical parameters is accomplished by iteratively perturbing the geophysical parameters until the error functional Eq. (1) is minimized. Unlike Lorenc (1986), we minimize the error functional using the memoryless, quasi-Newton method described by Shanno (1978).

3. SENSOR RESPONSE MODEL

In this section, the components of the sensor antenna temperature model, Eq. (2), are described.

3.1 Model Grid

Both the antenna response functions and brightness temperature fields are discretized on a model grid. Rectangular grid "boxes" are defined on the grid, such that the center of each box coincides with the earth location of an all-channel antenna temperature measurement from the SSM/I. The boxes are oriented along the SSM/I A-scans (which contain the all-channel measurements) at a regular spacing of 25 km. Since

the cross-scan separation of succeeding A-scan lines varies along the scan line, the cross-scan dimension of the grid boxes also varies, with a maximum dimension of 25 km in the center of the swath, and decreasing towards swath edge. In the discretization of the antenna response functions and brightness temperature fields, the variation of the grid box dimension with scan position is taken into account.

3.2 Antenna Response Functions

Measurements of the SSM/I antenna reponse functions and a detailed description of the SSM/I scan geometry were provided by Gene Poe (currently with Aerojet Electrosystems Co.). Using this information the integrated co- and cross-polarized antenna responses over each grid box for all SSM/I measurements are computed.

3.3 Radiative Transfer / Cloud Model

The model for the average polarized brightness temperature, $TB(P)_p$, upwelling from a grid box is described here. The earth's surface is characterized by a skin temperature and an emissivity. The emissivity in each polarization is represented using the two-parameter formula of Grody (1988). The downwelling brightness at the top of the atmosphere is set equal to the cosmic background value (2.7 K).

The model atmosphere is divided into 50 mb layers, starting from an assumed top of the atmosphere at 100 mb. Atmospheric temperature falls off linearly with height at a fixed lapse rate of 5.4 K/km from a variable surface value. The surface relative humidity (and the associated water vapor density) is also allowed to vary in the retrieval. It is assumed that the water vapor density falls off exponentially with height, with a scale height of 2.0 km. The temperature lapse rate and vapor scale height reflect the tropical climatological values compiled by Jordan (1958).

Clouds are assumed to occupy a variable cloud fraction within each grid box. Within the cloud fraction, the vertical profiles of precipitating liquid water and ice hydrometeors, as well as nonprecipitating cloud droplets and ice, are determined using a one-dimensional, steady-state cloud model. The updraft in the cloud model is an adaptation of the plume model described in Anthes (1977), which utilizes the water substance conservation equations of Kessler (1965). In light of the arguments by Schlesinger (1990), the rate of accretion of cloud water by rain drops is reduced by a factor of three from the original formulation in Kessler. For a given cloud

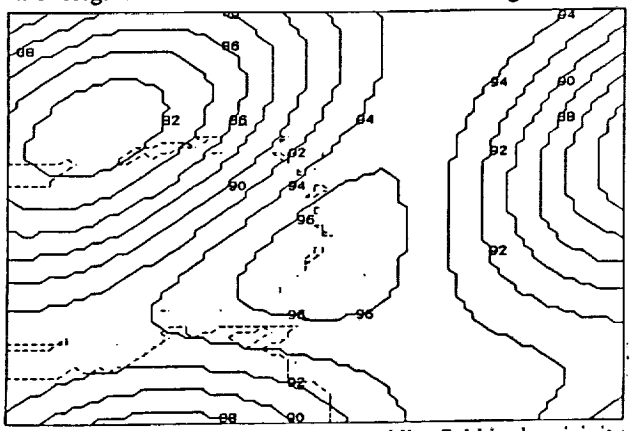

Fig. 1. Retrieved surface relative humidity field in the vicinity of Emily at 10 UTC on September 21, 1987. Values are in percent; coastlines are dashed.

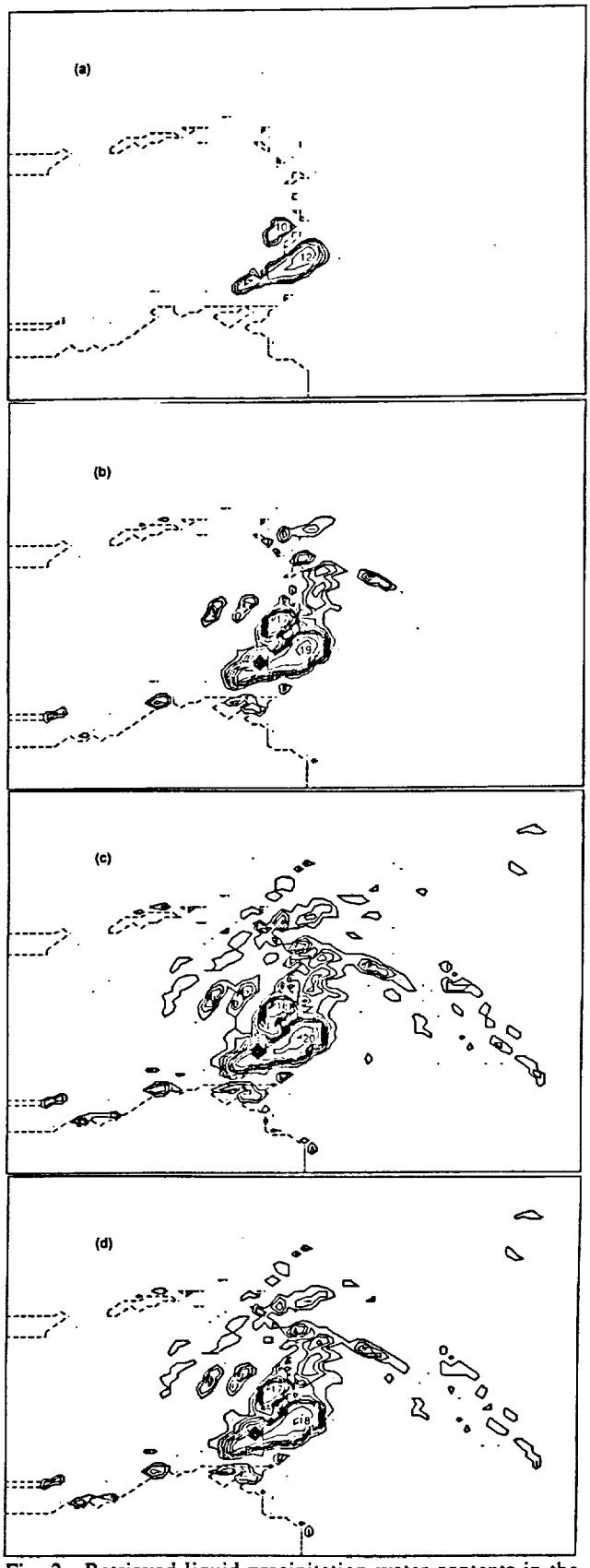

Fig. 2. Retrieved liquid precipitation water contents in the vicinity of Emily at 10 UTC on September 21, 1987. Fields are shown at pressure levels of (a) 550 mb, (b) 700 mb, (c) 850 mb, and (d) at the surface. Contours are drawn at increments of 0.2 g/m^3, starting with a minimum contour of 0.2 g/m^3. Maximum values are in tenths of a g/m^3; coastlines are dashed.

environment, vertical development of the cloud is controlled by a single parameter, the horizontal mass entrainment rate. The entrainment rate is assumed to be inversely proportional to the cloud updraft radius, as in Simpson and Wiggert (1969). The updraft radius is allowed to vary in the retrieval. The transition from liquid to ice phase water substance is linear in the model, beginning at the 273 K isotherm and ending at 253 K, above which the cloud is completely glaciated. Precipitation fallout is assumed to occupy a separate downdraft region, which has the same horizontal cross-sectional area as the updraft. Therefore, within the area determined by the cloud fraction, the liquid water contents of the various cloud water constituents at each level are the averages of the updraft and downdraft values.

Absorption coefficients for molecular oxygen and water vapor are computed using the formulae of Liebe (1985), and cloud absorption coefficients are computed based upon Rayleigh theory. Extinction coefficients, single-scatter albedoes, and asymmetry factors for liquid and ice hydrometeors are determined using fits to detailed calculations by Kummerow and Weinman (1988).

Brightness temperatures upwelling from each grid box are computed using a multiple-scattering radiative transfer code. The radiative transfer solution is based upon Eddington's second approximation for a vertically-layered atmosphere. Separate radiances are computed for the clear and cloudy regions of the grid box, and then averaged with a weight equal to the fractional coverage of each region within the grid box.

4. APPLICATION OF THE RETRIEVAL METHOD TO SSM/I DATA

The physical retrieval method is applied to SSM/I observations of the incipient Hurricane Emily at 10 UTC on September 21, 1987, as it was developing over the Windward Islands off the northeast coast of South America. A total of eight geophysical parameters are optimized in the retrieval: four emissivity parameters (two for each polarization), surface air temperature, surface relative humidity, cloud fraction, and cloud updraft radius. Since only thirteen observations per grid box are available from the SSM/I, band-limited spectral solutions for the emissivity parameters, air temperature, and relative humidity are sought in order to greatly reduce the number of degrees of freedom in the problem. Only the DC components of the emissivity parameters (one for land and one for ocean regions) and surface air temperature are utilized to represent these parameters over the solution grid. A linear trend, the DC, and first wavenumber are used to represent horizontal variations of the surface relative humidity field. A separate cloud fraction and effective updraft radius for each grid box are also determined. Also, only the 37 and 85.5 GHz SSM/I data are utilized in the retrieval to be presented.

After 15 iterations the error functional Eq. (1) without any additional constraints (second term equal to zero) is effectively minimized to produce the surface relative humidity and precipitation liquid water content fields in Figs. 1 and 2, respectively. The retrieved fields in this first test case appear reasonable, although the precipitation in the core region of Emily is extreme (equivalent surface precipitation water content greater than 1 g/m^3 or 18 mm/hr covering a large area), and the vertical development of the associated cloud is limited.

5. EXTENSION OF CURRENT WORK AND APPLICATIONS

Work will continue to further improve the representation of clouds and their environments in the sensor response model. The relatively rapid convergence of the retrieval method (all fields had essentially converged in less than 10 iterations) using only four channels of sensor data suggests that more degrees of freedom may be allowed in the retrieval solutions. Investigations by Short (1988) and others have indicated that the representation of clouds by a statistical distribution over each grid box rather than by a single vertical profile may be superior for remote sensing applications. Greater variability in the solution fields of emissivity, air temperature, and water vapor may also be allowed if additional sensor data and/or constraints are utilized in the retrieval. Future tests will include the lower-frequency SSM/I data as well as SSM/T and geostationary infrared measurements. Retrievals will be validated using volume-scan radar measurements and conventional weather data.

One of the goals of the present investigation is to utilize retrievals of precipitation water contents as a proxy for latent heating in rapidly developing storms. Latent heating information may help to improve short-term numerical weather prediction model forecasts of storms, but forecast model fields may also be used to help improve retrievals through the constraint term in Eq. (1). The interplay between forecast models and retrievals is a subject of further study by the authors.

Acknowledgments

The authors wish to thank Robert Aune, John Derber, George Diak, Barry Hinton, James Hollinger, Christian Kummerow, Lynn McMurdie, Grant Petty, Gene Poe, Robert Rabin, James Ridout, David Short, Bill Smith, James Weinman, Mark Whipple and Harold Woolf for their help and inspiration during various phases of this study. This work was supported by NASA Grant NAGW-1855. One author (WHR) was supported in part by National Science Foundation Grant ATM-8920508.

6. REFERENCES

Anthes, R.A., 1977: A cumulus parameterization scheme utilizing a one-dimensional cloud model. Mon. Wea. Rev., 105, 270-286.

Grody, N.C., 1988: Surface identification using satellite microwave radiometers. IEEE Trans. on Geoscience and Rem. Sensing, 26, 850-859.

Hollinger, J.P. (ed.), 1991: DMSP Special Sensor Microwave/Imager Calibration/Validation Final Report Volume II. Naval Research Laboratory, Washington, D.C.

Jordan, C.L., 1958: Mean soundings for the West Indies area. J. of Meteor., 15, 91-97.

Kessler, E. III, 1965: Microphysical parameters in relation to tropical cloud and precipitation distributions and their modifications. Geofis. Intern., 5, 79-88.

Kummerow, C.D., and G.L. Liberti, 1990: Precipitating cloud vertical structure derived from passive microwave radiometery. Seventh Conference on Atmospheric Radiation, July 23-27, San Francisco, California, J72-J76.

Kummerow, C.D., and J.A. Weinman, 1988: Radiative properties of deformed hydrometeors at commonly used passive microwave frequencies. IEEE Trans. on Geoscience and Rem. Sensing, 26, 629-638.

Liebe, H.J., 1985: An updated model for millimeter wave propagation in moist air. Radio Science, 20, 1069-1089.

Lorenc, A.C., 1986: Analysis methods for numerical weather prediction. Quart. J. R. Met. Soc., 112, 1177-1194.

Murphy, R. (ed.), 1987: HMMR High-Resolution Multifrequency Microwave Radiometer Instrument Panel Report, National Aeronautics and Space Administration, 59 pp.

Petty, G.W., and K.B. Katsaros, 1990: New geophysical algorithms for the Special Sensor Microwave Imager. Fifth International Conference on Satellite Meteorology and Oceanography, September 3-7, London, England, 247-251.

Schlesinger, R.E., 1990: Feedback of deep moist convection to its near environment as diagnosed from three-dimensional numerical model output: Results from an early experiment. J. Atmos. Sci., 47, 1390-1412.

Shanno, D.F., 1978: Conjugate gradient methods with inexact searches. Math. Oper. Res., 3, 244-256.

Short, D.A., 1988: A statistical-physical interpretation of ESMR-5 brightness temperatures over the GATE area. In Tropical Rainfall Measurements, Proceedings of the International Symposium on Tropical Precipitation Measurements, Tokyo. A. Deepak Publishing, Hampton, Virginia.

Simpson, J., R.F. Adler, G.R. North, 1988: A proposed Tropical Rainfall Measuring Mission (TRMM) Satellite. Bull. Amer. Met. Soc., 69, 278-295.

Simpson, J., and V. Wiggert, 1969: Models of precipitating cumulus towers. Mon. Wea. Rev., 97, 471-489.

Abstrasts, Fourth International Conference on Precipitation, Iowa City, Iowa, April 26-28.

SSM/I Physical Retrieval of Precipitation Distributions and Numerical Model Forecast Applications

William S. Olson and William H. Raymond

CIMSS/Space Science and Engineering Center,
University of Wisconsin, Madison, Wisconsin 53706

The Special Sensor Microwave/Imager (SSM/I) is a passive microwave radiometer with channels at 19.35, 22.235, 37, and 85.5 GHz. At the lower three frequencies, absorption and re-emission of microwaves by liquid precipitation produces a measurable signal which is strongly related to the vertically-integrated liquid water within the radiometer field of view. At 85.5 GHz, liquid precipitation also has an absorption/emission signature, but the upwelling microwave radiances are strongly modulated by scattering off precipitation-sized ice particles which occur at greater altitudes. The combination of channels can therefore be utilized to infer approximate vertical distributions of precipitation water contents.

A physical retrieval method based upon a minimum variance estimator is applied to the SSM/I measured radiances to deduce the vertical distributions of precipitation water contents in different weather systems. The retrieval method incorporates a radiative parameterization for computing upwelling microwave radiances at the SSM/I frequencies as functions of the non-homogeneous distributions of precipitating liquid and ice hydrometeors over a 25 km x 25 km area (the sampling resolution of the SSM/I). The radiative parameterization is based upon detailed calculations of the propagation of microwaves through simulated cloud fields. Both convective and stratiform cloud fields are generated using a numerical model. The spatially inhomogeneous response of the SSM/I instrument to the upwelling radiance field (an antenna diffraction effect) is also explicitly modeled in the physical retrieval method.

Retrieved precipitation water distributions are compared to volume radar scans from Darwin, Australia and Kwajalein, Marshall Islands.

Latent heating rates inferred from SSM/I retrieved precipitation water distributions can be assimilated into numerical weather prediction model forecasts. This kind of information is especially important in data-sparse regions (i.e., over the oceans) where the development of new storms may not be captured by the traditional observational network. Latent heating fields have been assimilated into CIMSS Subsynoptic Scale Model forecasts using a new method, and have shown significant impact on the "spin-up" and subsequent evolution of rapidly deepening storms.

Latent heating information is used in the model's diabatic initialization and in the Newtonian nudging of the temperature field early in the model forecast. The nudging commences with the initial guess and is modified through time by the forecasted wind field

and condensation rates. The Newtonian nudging of the model temperature field at locations experiencing latent heating represents an external forcing that enhances rapid deepening in model forecasts. Our findings show that diabatic initialization using two vertical modes gives a small response, while four vertical modes can produce large changes that on occasion generate model instability. Important factors influencing the outcome include the model grid size, mesoscale content of the initial model fields and the model physics. By introducing an estimated latent heating field into a numerical simulation of the ERICA IOP-5 storm, 24 hour forecasts of central pressure decreased as much as 20 mb.

Preprints, 26th International Conference on Radar Meteorology, Norman, Oklahoma, 24-28 May 1993.

SIMULATION OF SSM/I OBSERVATIONS OF TROPICAL PRECIPITATION BASED UPON DARWIN RADAR DATA

William S. Olson

CIMSS/SSEC, University of Wisconsin
Madison, Wisconsin 53706

Matthias Steiner

Department of Atmospheric Sciences, AK-40
University of Washington, Seattle, Washington 98195

1. INTRODUCTION

In the physical retrieval of precipitation amounts using the satellite-borne Special Sensor Microwave/Imager (SSM/I), an accurate radiative transfer model relating liquid and ice-phase precipitation water contents to upwelling, cloud top radiances is required. One such model that has been used to retrieve precipitation amounts from SSM/I (ref. Olson and Raymond, 1992) is based upon Eddington's second approximation, which includes the effect of multiple scattering of microwave radiances off precipitating hydrometeors. In the present study radar-derived hydrometeor distributions will serve as input to this radiative transfer model, to determine whether or not consistency between the model-output radiances and SSM/I observations can be achieved, and under what modeling assumptions. This study should lead to an improved radiative model and more accurate SSM/I physical retrievals.

2. RADAR DATA AND PROCESSING

Volume radar reflectivity data from the 5-cm Darwin/TOGA installation recorded during the passage of a squall line at 18:20 UTC on February 9, 1988 are interpolated to a cartesian grid with dimensions 240 km x 240 km x 18 km. The grid spacings are 2 km in the horizontal and 1.5 km in the vertical. The radar data in elevation/azimuth/range format are interpolated to grid locations based on the method of Mohr and Vaughan (1979).

Within the convective leading edge of the squall line, the fractions of liquid and ice precipitation associated with a measured reflectivity are estimated using the temperature-dependent partitioning scheme of Moss and Johnson (1992). Within the trailing stratiform precipitation region, it is assumed that the radar reflectivity is due entirely to ice-phase hydrometeors above the freezing level, and below the 6 C level the radar reflectivity is due entirely to liquid hydrometeors. A linear transition from ice to liquid between 0 C and 6 C is assumed. This stratiform precipitation partitioning scheme is based upon model simulations of anvil clouds using a one-dimensional version of the Ridout (1991) model. The vertical profile of environmental temperatures is obtained from the Darwin sounding at 22:00 UTC on February 9, 1988.

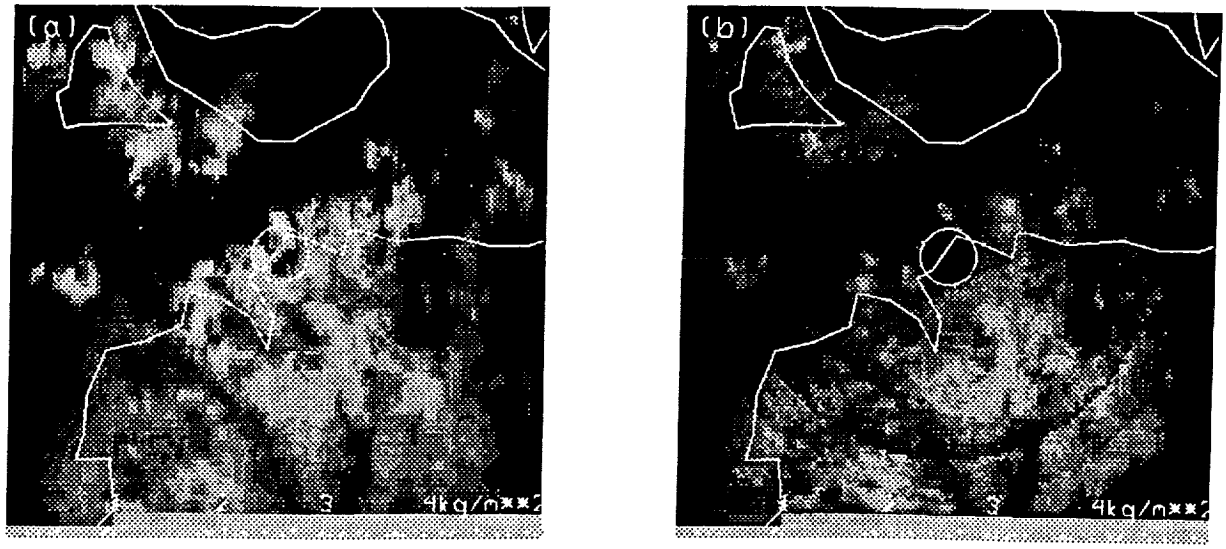

Fig. 1. Fields of slant path-integrated liquid precipitation (a) and ice precipitation (b) derived from the Darwin/TOGA radar at 18:20 UTC on February 9, 1988. Coastlines are indicated by white lines, and the white circle indicates a data-void region in the radar volume scan. Each panel covers an area of 240 km x 240 km.

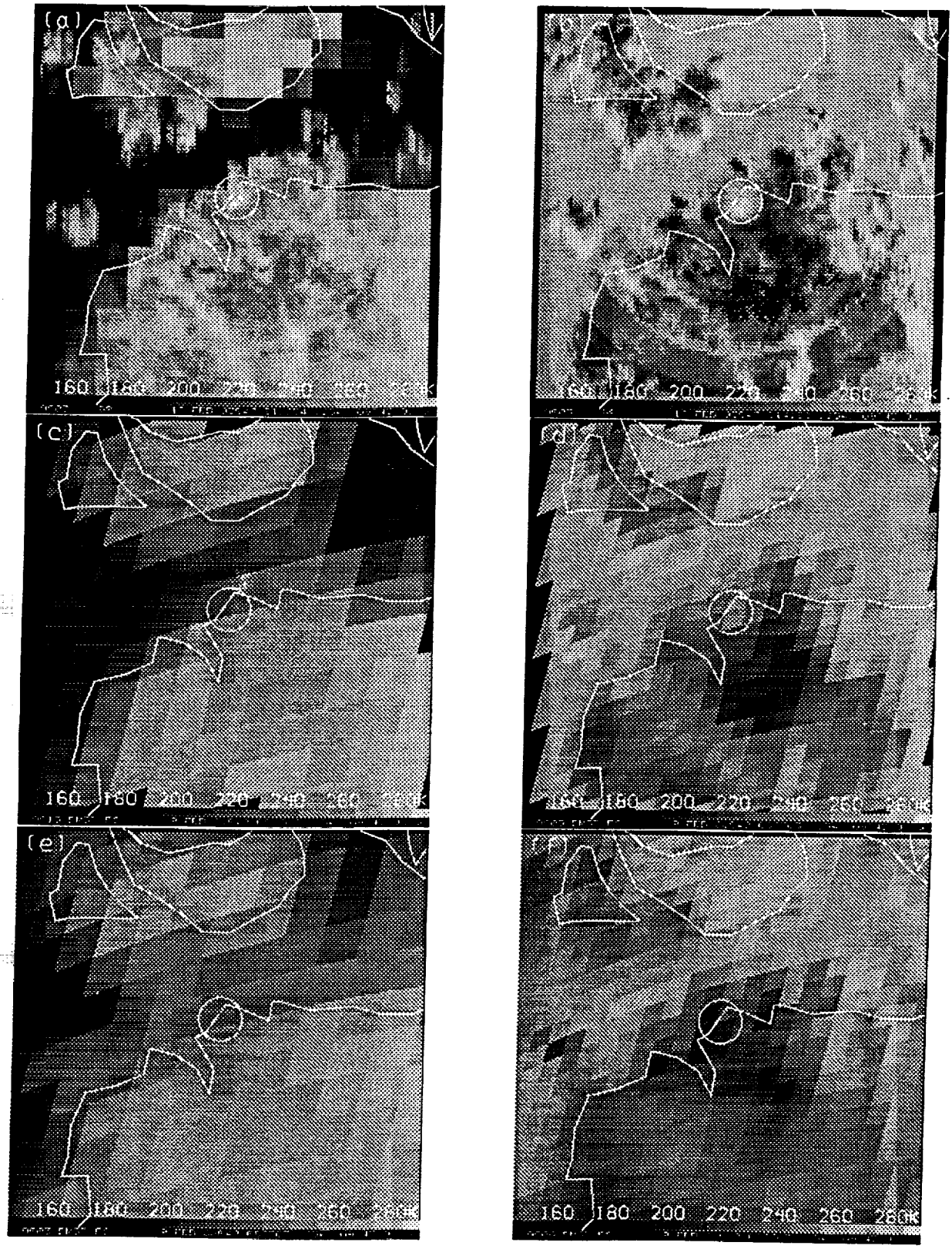

Fig. 2. Simulated brightness temperature fields at 37 GHz and 85.5 GHz are shown in panels (a) and (b), respectively. Simulated antenna temperature fields at 37 GHz and 85.5 GHz are shown in panels (c) and (d), while SSM/I observed antenna temperatures at 37 GHz and 85.5 GHz are shown in panels (e) and (f).

Integrated liquid and ice-phase precipitation fields derived from the Darwin volume scan are shown in Figs. 1a and 1b, respectively. The convective leading edge of the squall line is seen crossing the Darwin radar site along the northern coast of Australia. The region of trailing stratiform precipitation is primarily to the south of the leading edge. Northwest of the radar site, convective precipitation between Bathurst and Melville Islands is also observed. The white circle in the precipitation images indicates a data-void zone in the radar volume scan.

3. SSM/I SIMULATIONS

3.1 Radiative Transfer Calculations

The liquid and ice precipitation water contents derived from the radar are converted to values of extinction coefficient, single-scatter albedo, and asymmetry factor at the SSM/I frequencies (19.35, 22.235, 37, and 85.5 GHz) using the parameterizations in Kummerow and Weinman (1988). Absorption coefficients for molecular oxygen and water vapor are computed using the formulae of Liebe (1985). Microwave absorption by non-precipitating clouds is neglected in the present development. A surface skin temperature of 300 K and emissivities characteristic of land and ocean surfaces, where appropriate, are assumed.

The upwelling microwave radiances at the SSM/I frequencies in two orthogonal planes of polarization at an incidence angle of 53.1^{o} are computed using Eddington's second approximation along individual ray paths through the radar volume. The resulting field of microwave brightness temperatures at 2 km resolution at 37 GHz and 85.5 GHz in the horizontal polarization are shown in Figs. 2a and 2b, respectively.

3.2 Sensor Response

The spatial resolution of the SSM/I varies from about 55 km at 19.35 GHz to 14 km at 85.5 GHz, and antenna temperatures are sampled at intervals of 12.5 km at 85 GHz, and at 25 km at all other frequencies. In order to simulate SSM/I resolution effects, the 2 km resolution images in Figs. 2a and 2b are convolved by the SSM/I 37 GHz and 85.5 GHz antenna patterns. The resulting images are then resampled at the SSM/I measurement locations. The final simulated antenna temperature images at 37 GHz and 85.5 GHz are presented in Figs. 2c and 2d, respectively. Coincident antenna temperature measurements from the SSM/I are shown in Figs. 2e and 2f.

4. RESULTS AND DISCUSSION

A general correspondence between precipitation regions in the simulated and observed SSM/I imagery is evident, and the magnitudes of the antenna temperatures are fairly consistent. However, the simulated antenna temperatures in the convective regions tend to be higher than those observed, while minimum simulated antenna temperatures over the stratiform precipitation region tend to be lower than those observed. These differences are most obvious in the 85.5 GHz imagery, for which scattering by precipitation-sized ice particles, and the associated lowering of upwelling radiances, is more pronounced than at 37 GHz. Errors in the partitioning of the liquid and ice precipitation components in the simulations might account for these discrepancies. Also it may be noted that simulated antenna temperatures at 37 GHz over the ocean tend to be somewhat lower than those observed. The lack of nonprecipitating clouds in the simulations might account for less emission and lower antenna temperatures over the low-emissivity ocean background. The sensitivity of simulated antenna temperatures to modeling assumptions will be the subject of future study.

Acknowledgments

The authors wish to thank Tom Keenan for providing the Darwin radiosonde data utilized in this study, and also Robert Houze, Jr. for providing helpful commentary. Gene Poe kindly provided the SSM/I measured antenna patterns. Ken Bywaters assisted in producing the figures in this paper.

5. REFERENCES

Kummerow, C. D., and J. A. Weinman, 1988: Radiative properties of deformed hydrometeors for commonly used passive microwave frequencies. *IEEE Trans. on Geoscience and Remote Sensing*, **26**, 629-638.

Liebe, H. J., 1985: An updated model for millimeter wave propagation in moist air. *Radio Science*, **20**, 1069-1089.

Mohr, C. G., and R. L. Vaughan, 1979: An economical procedure for cartesian interpolation and display of reflectivity factor data in three-dimensional space. *J. Appl. Met.*, **18**, 661-670.

Moss, S. J., and D. W. Johnson, 1992: Aircraft measurements to validate and improve numerical model parameterizations of the ice and water ratios in clouds. Proceedings of the 11th International Conference on Clouds and Precipitation, Montreal, Canada.

Olson, W.S., and W.H. Raymond, 1992: Physical retrieval of precipitation water contents using multisensor microwave data and model constraints. Proceedings of the Sixth Conference on Satellite Meteorology and Oceanography, Atlanta, Georgia, 4 pp.

Ridout, J. A., 1991: A parameterized quasi-five-cylinder convective cloud model and its application to remote sensing of rainfall. Ph.D. thesis, University of Wisconsin-Madison, 278 pp.